The Preparation and Characterization of Graphene-based Nanoparticles and Carbon Nanodots with Tunable Photoluminescent Properties

Xiangshuai Geng

Supervised by Prof. Biqiong Chen, Dr. Simon Hayes and Dr. Joel Foreman

Department of Materials Science and Engineering

July 2019

A thesis submitted to the University of Sheffield for the degree of Doctor of Philosophy

In loving memory of my grandmother

Always on my mind

Forever in my heart

Declaration

I hereby declare that the thesis has been done by myself and has not been submitted in any degree application before. The work has been conducted by myself, except where due acknowledgement has been given.

Some cooperation published works:

1. Yan Liu, Yawen Xu, Xiangshuai Geng, Yingying Huo, Dexin Chen, Kang Sun, Guangdong Zhou, Biqiong Chen and Ke Tao, Synergistic Targeting and Efficient Photodynamic Therapy Based on Graphene Oxide Quantum Dot-Upconversion Nanocrystal Hybrid Nanoparticles[J]. Small, 2018, 14(19): 1800293.
2. Richard Justin, Sabiniano Román, Dexin Chen, Ke Tao, Xiangshuai Geng, Richard T. Grant, Sheila MacNeil, Kang Sun and Biqiong Chen, Biodegradable and conductive chitosan–graphene quantum dot nanocomposite microneedles for delivery of both small and large molecular weight therapeutics[J]. Rsc Advances, 2015, 5(64): 51934-51946.
3. Richard Justin, Ke Tao, Sabiniano Román, Dexin Chen, Yawen Xu, Xiangshuai Geng, Ian M. Ross, Richard T. Grant, Andrew Pearson, Guangdong Zhou, Sheila MacNeil, Kang Sun and Biqiong Chen, Photoluminescent and superparamagnetic reduced graphene oxide–iron oxide quantum dots for dual-modality imaging, drug delivery and photothermal therapy[J]. Carbon, 2016, 97: 54-70.

Abstract

Recently, luminescent carbon-based dots (CDs) have received more and more attention because of their excellent performance, such as tunable photoluminescence (PL), simple synthesis, easy surface functionalization, good biocompatibility, no heavy metal element and various potential applications.

In this thesis, two kinds of luminescent CDs were successfully synthesized by employing two different approaches, respectively. At first, a series of graphene oxide quantum dots (GOQDs) were prepared from graphite powder *via* the chemical oxidation method using different reaction condition and procedures. Various techniques were used to characterize the nanoparticles, such as atomic force microscopy, transmission electron microscopy, Fourier-transform infrared spectroscopy, Ultraviolet–visible spectroscopy, X-ray photoelectron spectroscopy, X-ray diffraction, Raman spectroscopy and photoluminescence spectroscopy. The resultant GOQDs had a size distribution from 30 to 120 nm in diameter and abundant oxygen-containing functional groups. The GOQDs showed bright green-yellow fluorescence with a quantum yield (QY) of 0.41%. With the help of further hydrothermal treatment, the QY could be increased to 5.15%. By changing the reaction condition and modifying the experimental procedure, the difference in the structure of all GOQDs was investigated, and their relationship between the structure and PL properties was analyzed. It has been confirmed that some oxygen-containing functional groups like ketone and carboxyl groups are able to influence the PL properties. Cell viability and photodynamic therapeutic effect of the GOQDs were also investigated. Low toxicity and high production of reactive singlet oxygen make the GOQDs have potential in applications in bioimaging and photodynamic therapy.

Another series of carbon dots samples were synthesized with three different phenylenediamine monomers *via* a coupling process with the help of potassium persulfate. The coupling process of the three isomers of phenylenediamine was

significantly different, resulting in different structures of carbon nanodots (CNDs). These three kinds of CNDs had a size distribution from 30 to 100 nm in diameter and exhibited blue, green, yellow and orange, even light red fluorescence, which make them promising in various imaging fields.

Acknowledgements

Firstly, I would like to sincerely thank my supervisors, Prof. Biqiong Chen, Dr. Simon Hayes and Dr. Joel Foreman for their help and guidance in my studies. I really appreciate Prof. Biqiong Chen, who gave me the chance to have an opportunity to study in Sheffield and give me too much help during the study. Her spirit of hard working leave a deep impression on me. I also would say thanks again to Dr. Simon Hayes, who becomes my main supervisor during the last period. He is very nice and provides me with many good suggestions.

I would appreciate Prof. Kang Sun and Dr. Ke Tao, for the help of ROS and cell work at Shanghai Jiao Tong University. Meanwhile, I need to thank Dr. Peter Laity and Dr. Chris Holland, who kindly allow me to use their UV-Vis spectroscopy, Dawn Bussey, who gave me training and much help on AFM work, Dr. Peng Zeng for the assistance with TEM characterization, and Dr. Deborah B Hammond for XPS characterization.

I want to say thank you to my dear parents. Thank you very much. I love you. Without your support, I could not have this chance and could not insist on. Besides, I would say many thanks to my families. All of them have given me so much love, care and support. They are my strong backing.

I am very lucky that I have met so many nice colleagues and close friends during the whole PhD study: Richard, Martin, Yongzhe, Tongfei, Yasemin, Yahui, Sungkwon, Andreas, Ehssan, Zaid, Ahmed, Carina, Jessie, Yuansheng, Meng, Yang, Kai, Hanxiao, Hongwei, Shiyun and many more. Many thanks to them.

At last, I will say thank you to everyone who ever helps me.

Contents

List of Figures

List of Tables

1 Introduction and overview of the thesis

1.1 Introduction

Carbon element is one of the most common elements in nature and it appears in a large number of materials including graphite, coal, diamond, carbon fibers and polymers.[1] In the last three decades, researchers have put a lot of efforts in carbon-based nanomaterials, such as carbon nanotubes and graphene because of their excellent mechanical, thermal and electrical properties.[2–8] Recently, luminescent carbon-based dots (CDs), a new form of carbonaceous nanomaterials, have received extensive attention because of their outstanding properties including good photoluminescence (PL) properties, easy synthesis, low cost, environmental friendliness, abundance of raw materials, good water dispersibility and relatively good biocompatibility.[9–15] Until now, researchers have carried out much work regarding the synthesis methods, properties, photoluminescent mechanism and applications of CDs, and have received much progress.[16–22]

Generally, CDs contain two kinds of carbonaceous nanomaterials including graphene-based quantum dots and carbon nanodots (CNDs).[23] Graphene-based quantum dots, including graphene quantum dots (GQDs) and graphene oxide quantum dots (GOQDs) have graphene lattice structure and are mainly derived from graphene-based materials, such as graphene sheets, graphite powder and graphite oxide *via* top-down approaches including chemical oxidation and electrochemical method.[14,24–27] Carbon nanodots can be regarded as a kind of "polymers", which are synthesized with small carbonaceous molecules *via* bottom-up approaches, *e.g.* hydrothermal method and self-polymerization.[28–30] CDs have much difference in size, structure and PL properties. While there have been various explanations about their PL mechanism, there is still a need to continue the research in CDs and their fundamental PL mechanism.

The overall aims of this work are to prepare luminescent CDs with enhanced and tunable photoluminescent properties and gain a better understanding of the PL mechanism for future applications of CDs in healthcare such as bioimaging and photodynamic therapy. Their objectives are as follows:

(1) To prepare and characterize GOQDs with tunable photoluminescent properties by varying the raw materials, preparation procedure and reaction conditions.
(2) To enhance the quantum yield of GOQDs by applying a hydrothermal treatment and varying the treatment conditions.
(3) To investigate the cell toxicity and photodynamic therapeutic effects of GOQDs.
(4) To summarize the PL mechanism and some influence factors of GOQDs.
(5) To develop a new route to prepare CNDs with tunable photoluminescent properties and study their structure-property relationships.

1.2 Overview of the thesis

This thesis is divided into seven chapters. The Chapters are organized as follows:

Chapter 1 makes a brief introduction and overview of the thesis.

Chapter 2 presents a literature review of the luminescent carbon-based dots regarding their preparation methods, properties, and applications.

Chapter 3 presents the experimental methods including materials and various characterization and analysis techniques used in this thesis.

Chapter 4 is concerned with photoluminescent graphene-based nanoparticles derived from graphite powder *via* different reaction conditions. Photoluminescent graphene-

based nanoparticles are studied in three steps. The first step is to investigate a basic kind of GOQDs derived from graphite powder using methods available in the literature with some modifications. The second step is to change the preparation conditions (reaction time and reaction temperature) to make a comparison and analyze the changes in the structure and PL properties. The last step is to further study GOQDs by modifying the preparation procedures (changing acid dosage and reaction time). Some resultant modified GOQDs (GOQDs-M) show better PL behaviour. At the end of this chapter, cell toxicity and photodynamic therapy effect of GOQDs are also investigated.

Chapter 5 is concerned with the hydrothermal treatment of graphene oxide quantum dots and the regulation of their photoluminescence properties. It builds upon the previous chapter by using the basic kind of GOQDs as raw materials. By changing the condition of hydrothermal treatment, different hydrothermal GOQDs (GOQDs-H) were obtained and their structure and PL properties were analyzed. Combined with the results and conclusion in the previous chapter, the mechanism of PL in graphene-based nanoparticles is illustrated.

Chapter 6 is on the preparation and characterization of luminescent carbon nanodots with varying PL properties. The bottom-up method is used to prepare carbon nanodots derived from phenylenediamine. The resulting carbon nanodots show good PL properties and their emission range is across the visible light spectrum. Meanwhile, different kinds of carbon nanodots derived from different isomers are significantly different in PL properties. The coupling process and oxygen-containing functional groups are the main factors affecting PL properties.

Chapter 7 summarises the main conclusions of the work in this thesis and proposes directions for future work on the basis of the results in this thesis.

2 Literature review

2.1 Introduction

Luminescent carbon-based dots refer to carbon particles with nanoscale size and fluorescent properties, including graphene quantum dots, graphene oxide quantum dots and carbon nanodots. Since the first report in 2004 that luminescent CDs were accidentally obtained during the purification of single-walled carbon nanotubes *via* the arc-discharge method[31], the study of luminescent CDs has attracted more and more attention. Due to their exceptional and outstanding properties, such as obvious luminescence, relatively good biocompatibility, the abundance of raw materials in nature, low cost, simple preparation process, and potential applications, researchers have focused on this kind of materials for since then.[19,23,32–36]

At the same time, single-layer graphene (2-dimension) was firstly obtained by Geim and Novoselov from the University of Manchester by using a sticky tape to mechanically peel the layers of graphene from bulk graphite.[37] Graphene is a single layer of sp^2-hybridized carbon atoms arranged in a hexagonal lattice structure. Because of its special structure, graphene possesses excellent mechanical, thermal and electronic properties. It is the strongest material ever tested, with Young's modulus of 1 TPa and intrinsic strength of 130 GPa.[38] Its thermal conductivity could reach 5300 $W \cdot m^{-1} \cdot K^{-1}$ at room temperature.[39] It shows remarkable electron mobility at room temperature with measured values over 15000 $cm^2 \cdot V^{-1} \cdot s^{-1}$.[5] Due to these excellent properties and abundant raw material, graphene has been widely studied for many applications, such as energy storage, polymer composites and healthcare.[40–46]

Pristine graphene is a zero-bandgap semiconductor material because its valence and conduction bands overlap slightly at the Dirac Point.[47] In theory, there is no transition between the valence and conduction bands. The electron transport can be

unrestricted in the atomic monolayer. Therefore, it is impossible to observe the luminescence properties in pristine graphene.

However, researchers have tried to make use of quantum confinement effect to change the energy level structure of graphene. In principle, the bandgap of graphene can be increased from 0 eV by modifying its size.[48] Along with the reduction in the size of the particle to be comparable to the wavelength of the electron, graphene gradually produces quantum confinement effect.[49] The valence and conduction bands become discrete and bandgap appears.[50] Once the bandgap exists and becomes large enough, the electron can transit between the valence and conduction bands under a specific condition, and then the luminescent properties can be observed if the electron transport happens. Therefore, luminescent graphene-based nanoparticles, including functional graphene nanoparticles (GNPs), graphene quantum dots (GQDs) or graphene oxide quantum dots (GOQDs), derived from graphene-based raw materials, are a new class of nanomaterials that have fluorescence in addition to other properties. GQDs have graphene lattice structure with nanoscale size and usually possess less than 10 layers of graphene.[51] The feature of luminescence properties makes it possible to replace traditional semiconductor quantum dots as contrasting agents for imaging.[52] Meanwhile, their advantages of low toxicity, low cost, large specific surface area, easy functionalization and simple synthetic methods make them highly suitable for biomedical applications.

Compared with GQDs which were mainly prepared from carbonaceous compounds, such as graphite powder[53], candle shoot[54] and C_{60}[55], some CNDs can be considered to be "polymers" which are synthesized from oligomeric species or monomers as the carbon sources, such as ammonium citrate[56], phenylenediamine[57], and glucose[58]. Hundreds of other raw materials have also been reported for the preparation of CNDs including egg[59], honey[60], sugar[61] and citric acid[62]. For example, Guan *et al*.[63] reported that folic acid molecules dissolved in diethylene glycol were treated in microwave to

prepare CNDs. This one-step microwave-assisted approach just needs 40 seconds. Transmission electron microscopy (TEM) shows that the as-prepared blue luminescent CNDs have an average size of around 4.5 nm (see Figure 2.1). The CNDs possess about 18.9% of quantum yield. Zhuo *et al.*[64] used citric acid and glutathione as precursors to prepare CNDs at 200 ˚C for 10 min. The resultant water-soluble CNDs have diameters of 2.5-3 nm and can emit blue fluorescence with a high quantum yield of about 80% (see Figure 2.2).

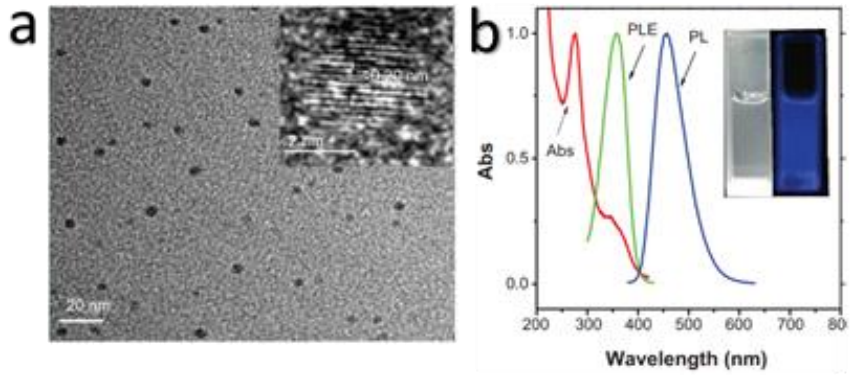

Figure 2.1. (a) TEM image of CNDs and (b) UV-Vis absorption and PL emission spectra of CNDs.[63]

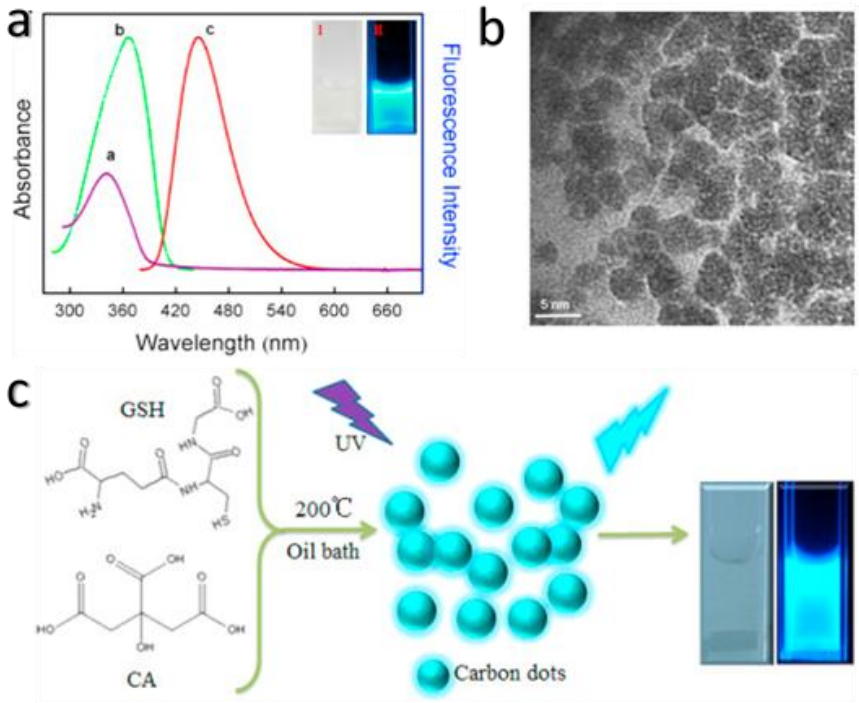

Figure 2.2. (a) UV-Vis absorption and PL emission spectra of CNDs, (b) TEM image of CNDs and (c) schematic illustration of synthesizing CNDs.[64]

CNDs, typically composed of carbon, oxygen, hydrogen and nitrogen, are usually spherical structures. Some of them have apparent lattice structure, which shows the effect of quantum size dependence.[65] For other carbon nanodots with less lattice structure, surface functional groups have much influence on the luminescence properties.[66] Many methods can be used for preparing carbon nanodots, including laser ablation[65], arc discharge[67], electrochemical approach[68], plasma treatment[69] and pyrolytic process[64].

Photoluminescence (PL) is one of the most attractive properties for a functional material. Researchers have tried to use different raw materials and different approaches to synthesize CDs with a higher PL efficiency and tunable PL. So far, much significant progress has been obtained. In this review, I will mainly review some of the latest research in GQDs and CNDs in the aspects of synthesis approaches, properties and applications.

2.2 Synthesis strategies of luminescent carbon dots

In order to obtain size-controllable, high-quality CDs with high PL performance, a variety of approaches have been studied and modified. According to the relationship between the raw materials and products, these synthetic approaches can be mainly classified into top-down or bottom-up methods.[27,70–72] For the former strategy, the cutting of carbonaceous materials from the big size into the small size is essential. As mentioned in the introduction, GQDs can be seen as fragments of graphene. Preparing and cutting of graphene into small parts using chemical or physical methods belong to top-down approaches. Conversely, bottom-up approaches involve the synthesis of luminescent carbon dots from small conjugated carbon atoms or molecules to assemble the large and complicated polymer. Raw materials and synthesis conditions such as reaction time, reaction temperature, and further treatment can affect the structure and properties of CDs.

2.2.1 Top-down approaches

Chemical oxidation method

Chemical oxidation method is an easy process in large-scale production for broad applications of luminescent graphene-based nanoparticles from many kinds of carbonaceous materials. Bulk graphene-based materials, such as graphite[73], carbon nanotubes[74], graphene oxide (GO)[75,76] or carbon fibers[24] are treated in harsh conditions including concentrated acids, strongly oxidizing environment, and high reaction temperature. With the help of strong acids, such as nitric acid and sulphuric acid, the bulk raw materials could break down into small parts. Meanwhile, high concentration acid oxidizes the raw materials and produces abundant oxygen functional groups, for instance, -OH, -COOH and epoxy groups, which make CDs have good water dispersibility. However, the disadvantage of this method is that the excess amount of oxidants (mainly strong acids) is difficult to be removed from the solution or the

generated powders. The nanoparticles need to be purified by removing the excess oxidants and after the reaction, which involves several techniques such as neutralization, filtration, centrifugation and dialysis. Besides, it is difficult to precisely control the size distribution and morphology of the product.

Liu *et al*.[75] successfully prepared GQDs and GOQDs by using chemical exfoliation of graphite nanoparticles (GNPs), which had a diameter of 4 nm. To study of the PL origin of nano-sized graphene, GQDs and GOQDs were produced as single-layered and less than 4 nm in lateral size. However, the former just had sp^2 carbon crystalline structure and the latter were rich with oxygen functional groups on the surface. Bright blue and green emissions of GQDs and GOQDs could be seen separately. They concluded that blue luminescence of GQDs originates from intrinsic states in the sp^2 carbon crystalline structure and green fluorescence of GOQDs comes from defect states with oxygen functional groups.

Peng *et al*.[24] synthesized GQDs derived from carbon fibers. After mixed acids (H_2SO_4/HNO_3=3:1 v/v ratio) treatment and chemical exfoliation of traditional pitch-based carbon fibers for 24 h, GQDs were obtained with a size range of 1-10 nm in diameter and zigzag edge structure. While increasing reaction temperature from 80 to 120 °C, the emission colour of an aqueous suspension of GQDs could be tuned from yellow to blue (see Figure 2.3). This work provided insights into the preparation of GQDs with different colours by changing the reaction condition.

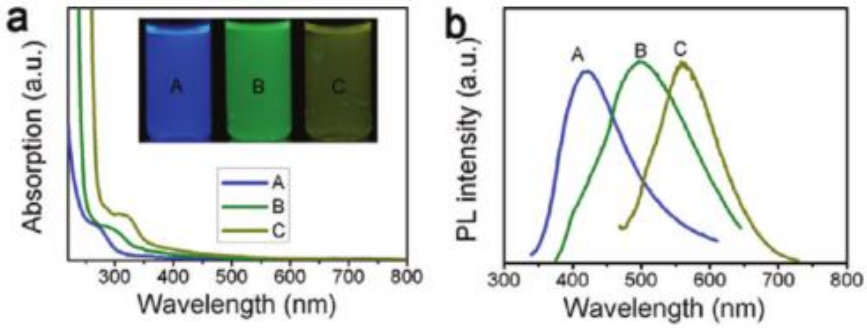

Figure 2.3 (a) UV-Vis spectra of GQDs, and (b) PL spectra of GQDs A, B, and C, corresponding to the reaction temperatures at 120, 100, and 80 °C, respectively.[24]

Using the similar mixed acid treatment method, Tao *et al.*[73] chose graphite, single and multiwalled carbon nanotubes as starting materials for treating in a harsh oxidation condition (H_2SO_4/HNO_3=3:1 v/v ratio) for 24 h at 80 ℃ to prepare photoluminescent carbon dots. Carbon dots with diameters of 3-4 nm were produced and could emit strong yellow fluorescence under UV irradiation.

Dong *et al.*[77] used carbon black as raw material. Only nitric acid (high concentration) was used as the oxidant agent and the mixture was refluxed for 24 h to prepare single- and multi-layer graphene quantum dots. After the reaction, the acid was removed by centrifugation and evaporated at 200 ℃. Both suspensions of the resulting graphene quantum dots (GQDs1 and GQDs2) could emit green and yellow colour separately under a UV beam of 365 nm, as shown in Figure 2.4. The GQDs1 was single-layered and its average diameter was about 15 nm. After further washing and dispersion in water, GQDs2 with an average diameter of 18 nm were obtained and found to have multi-layers. The difference in layers and size made them show different emission ranges.

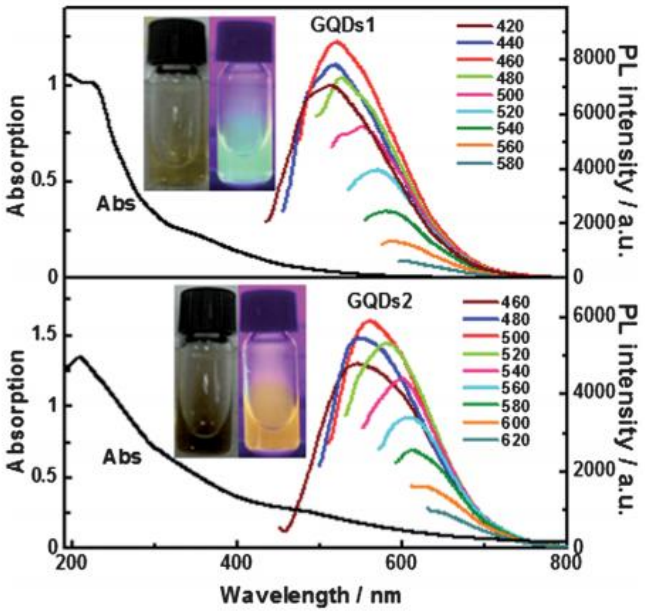

Figure 2.4. UV-vis absorption and PL emission spectra of GQDs in water suspension.[77]

Tian *et al*.[78] reported that nanosized carbon particles were prepared by nitric acid treatment of natural gas soot for 12 h. The carbon nanoparticles have an average diameter of 4.8 nm with crystalline lattices through TEM (see Figure 2.5), and emit photoluminescence with a quantum yield of about 0.43%.

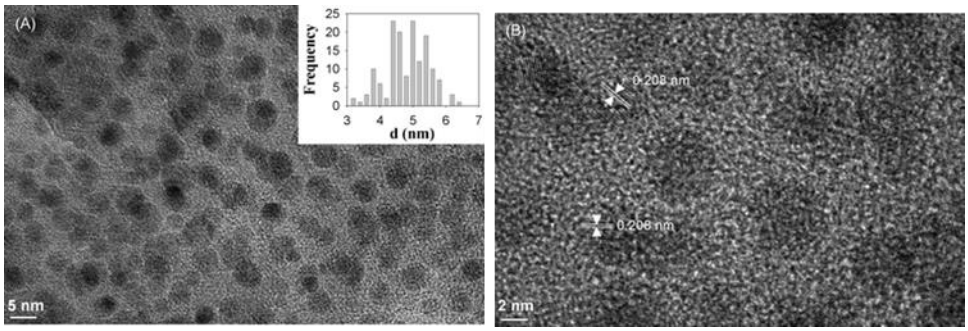

Figure 2.5. TEM images of carbon nanoparticles at (A) low and (B) high resolution.[78]

Hydrothermal method

The hydrothermal method is regarded as another common and simple treatment route to "cut" the raw material and prepare CDs. Usually, the reaction happens in an autoclave and the reaction temperature is over 150 ℃.[25,79] Under the high temperature and pressure, the precursor can be broke into small pieces quickly. Therefore, compared with the acidic method, this method can reduce reaction time considerably, be easily controlled, and cause little harm to the environment.

Pan *et al*.[25] developed a hydrothermal method to prepare GQDs with strong blue emission. Pre-oxidized graphene sheets were oxidized in an acid environment and transferred into an autoclave and heated at 200 ℃ for 10 h. According to the X-ray diffraction (XRD), Fourier-transform infrared (FTIR) spectroscopy, X-ray photoelectron spectroscopy (XPS) and UV-Vis spectroscopy, the authors investigated what happened during the oxidation-hydrothermal process and the mechanism of strong blue emission. When treated in acid, epoxy groups preferred to form a line on a carbon lattice and lead to a break of the C-C bonds with more stable carbonyl pairs appearing. These defects surrounded by graphene sheets were easily attacked and epoxy groups

may break up continuously. In addition, O atoms were removed during the hydrothermal process allowing the eventual production of GQDs. They proposed that the strong luminescence may come from the high concentration of free zigzag sites with a carbine-like triplet ground state because of small diameter (5-13 nm) and it was supported by the observed pH-dependent PL (see Figure 2.6).

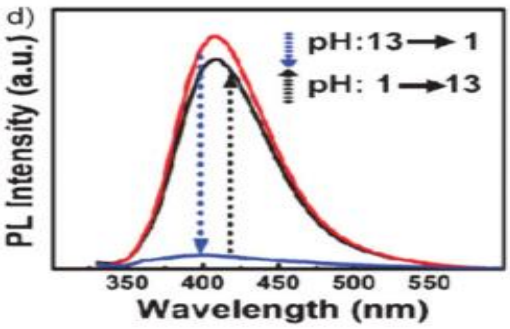

Figure 2.6 pH-dependent PL spectra when pH is switched between 13 and 1.[25]

Microwave-assisted method

While acidic and hydrothermal methods have been used to prepare luminescent graphene-based nanoparticles by many researchers. They still have some disadvantages, such as the long reaction process. To reduce the reaction time, higher-energy technologies have been used to synthesize GQDs. Because of the rapid heating source and energy, microwave-assisted synthesis of GQDs has been reported.[80,81] Chen *et al.*[82] reported that a very fast method to prepare GOQDs, as shown in Figure 2.7. GO in aqueous suspension was put in a Teflon vessel with two kinds of strong acids (H_2SO_4 and HNO_3). Under the condition of microwave irradiation at 200 ℃, it just took 5 min to obtain the GQDs with an average diameter of 3 nm. Atomic force microscopy image shows that the height is less than 0.7 nm, which means the GOQDs have a single-layer structure.

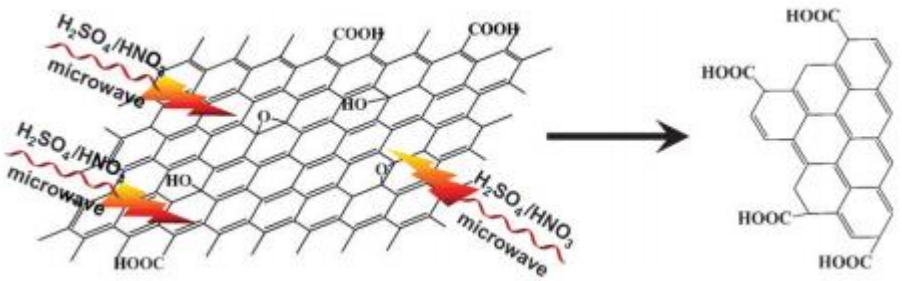

Figure 2.7. Schematic representation of the cutting route from GO to GOQDs by the effect of both acids and microwave.[82]

Oxygen plasma treatment

As mentioned in the previous, pristine graphene does not have a bandgap, so PL cannot be observed. However, using oxygen plasma treatment, PL was induced in single-layer graphene by Gokus *et al*.[83] Graphene was prepared with microcleavage of graphite on a silicon substrate and was treated by oxygen/argon RF plasma for a certain amount of time (1-6 s). The results presented that single-layer graphene exhibited strong PL, with a broadband at red range (500-800 nm). The PL emission should origin from electron quantum confinement in smaller sp^2 clusters, which were produced during oxygen plasma etching. However, multi-layer graphene remain no PL emission even after treatment. This can be considered that untreated layers below would quench PL emission from the topmost layer because treatment is layer by layer from top to bottom.[83]

Electrochemical synthesis

Zhou *et al*.[74] firstly prepared blue luminescent CDs by using the electrochemical synthesis of multi-walled carbon nanotubes, which was used as the working electrode in the electrochemical cell. A Pt wire acted as counter electrode, and an $Ag/AgClO_4$ was the reference electrode. A cyclic current between −2.0 and 2.0 V was applied in a solution containing tetrabutylammonium perchlorate, which led to the colourless solution changing to yellow and finally brown, indicating the formation of CDs peeled

from the multi-walled carbon nanotubes and their accumulation in solution. Using this method, CDs have a narrow size distribution of around 2.8 nm in diameter. Tan *et al*.[84] prepared small-sized red fluorescent GQDs with a diameter of approximately 3 nm by electrochemical peeling of graphite in 0.01 M $K_2S_2O_8$ aqueous solution at a potential of 3V. Deng *et al*.[85] used alcohols as precursors to prepare carbon nanodots through the electrochemical synthesis in NaOH/EtOH solution at a potential of 3.0-9.0 V for 3-4 h. The resultant CDs displayed different size, within a diameter of 2.1-4.3 nm, due to the various applied potential. A bright blue luminescence could be observed for the CDs, but the brightness of CDs was changed following changing the applied potential, indicating that the size of CDs affects the quantum yield.

In addition to choosing different raw materials as the electrode, changing the electrolyte and synthetic condition also can fabricate different CDs with tunable PL emission.[86,87] The advantages of electrochemical synthesis are simple and easy-controllable. Usually, no complicated purification or passivation procedures is needed.

2.2.2 Bottom-up approaches

For the bottom-up approaches, the suitable organic precursors are generally regarded as nanoscale “seeds” to be assembled together into CDs under certain conditions, such as heat.[23,88] The provided energy can result in transformation and connection between the molecular structure. Compared with top-down approaches, the bottom-up class have some advantages including diversified and low requirements of carbon sources, and relatively precise-control over the size and the structure of the products.

A bottom-up self-assembly method for preparing GQDs has been developed by Liu *et al*.[89] with hexa-peri-hexabenzocoronene (HBC) as precursors. Figure 2.8 shows the whole process for the preparation of GQDs. After self-assembly, pyrolysis, oxidative exfoliation, surface functionalization, and reduction, blue luminescent GQDs with a diameter of around 60 nm and 2-3 nm thickness were synthesized. Optical property

characterization indicated that the GQDs possess a PL quantum yield of 3.8%. Although this research provides a new method to prepare GQDs with a bottom-up approach, the complete synthetic process is still relatively complicated.

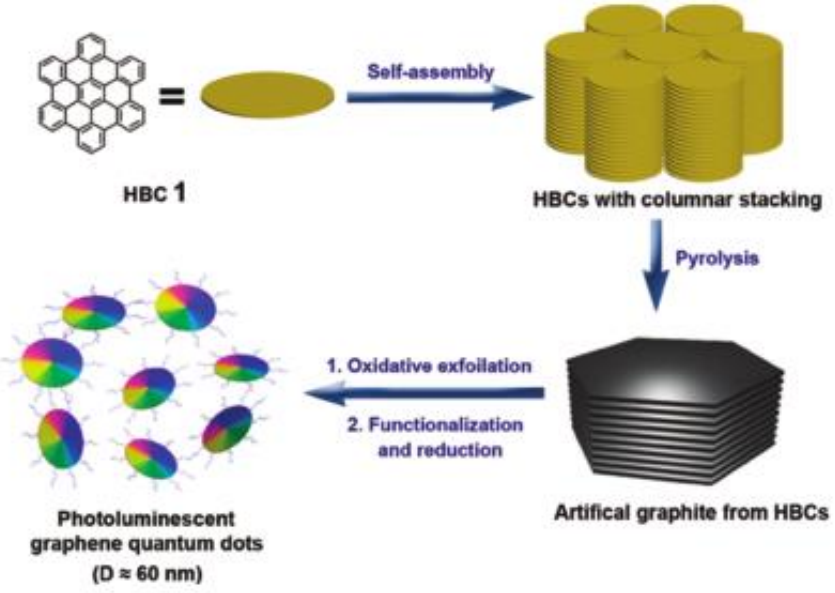

Figure 2.8 Schematic for the preparation of photoluminescent GQDs by using HBC as carbon source.[89]

Hydrothermal and microwave-assisted methods also can be used in the bottom-up approaches. In 2010, Zhang *et al*.[90] reported a new and simple hydrothermal method to prepare CDs by using L-ascorbic acid as precursors. L-ascorbic acid dissolved in ethanol was heated in an autoclave at 180 ℃ for 4 h, and the resultant water-dispersible CDs with a diameter of about 2 nm exhibited a relatively good photoluminescence efficiency (6.79%). Yang *et al*.[56] synthesized highly photoluminescent CDs with a quantum yield of 13.5% through the hydrothermal carbonization of ammonium citrate at a temperature of 160 ℃ for 6 h. Through the characterization of TEM, the CDs are approximately 2.14 nm in diameter with a nearly spherical shape.

To further reduce the reaction time, some researchers report that the microwave-assisted method is also used in the bottom-up class. Liu *et al*.[91] fabricated CDs by using glutaraldehyde and poly(ethylenimine) under microwave irradiation at 180 ℃ for 15 min. The fluorescence emissions of the CDs were in the range of 464 to 556 nm,

depending on usage of the amount of the glutaraldehyde. Zhai *et al*.[92] chose citric acid and various amine molecules as precursors to prepare CDs by heating in a microwave oven (700 W) for 2-4 min and obtained a red colour suspension. The CDs had a narrow size distribution of around 2.5 nm in diameter and exhibited PL emission in the range of 460-530 nm with a quantum yield of 30.6%. By comparison with different amine molecules, researchers summarized that N-doping can contribute to the fluorescence enhancement.

2.3 Properties

2.3.1 Morphology and structure

The morphology of the CDs, including the latter size and height, is affected by synthetic methods. Most CDs are the quasi-spherical or disk shape and typically less than 10 nm in diameter.[24,63,93–95] However, a larger diameter of GQDs has also been reported. For example, Shen *et al*.[96] collected GQDs with a diameter of 25 nm. Liu *et al*.[89] reported that their GQDs was around 60 nm in diameter. The height of GQDs generally is less than 5 nm, corresponding to no more than 10 layers of graphene.[27,97,98] AFM and high-resolution transmission electron microscopy (HRTEM) are two common techniques to characterize and evaluate the morphology, size distribution and height of synthesized CDs. X-ray diffraction (XRD) and Raman spectroscopy can be used to assist the investigation of the crystalline structure of some GQDs. Some reported that GQDs derived from graphite-based materials still maintain the crystalline structure.[99–101] Two broad peaks at 2θ around 5° and 25° correspond to the (100) and (002) planes.[24,102] For Raman spectra, two peaks at around 1350 cm^{-1} and 1580 cm^{-1} are attributed to the disordered D band and the crystalline G band, respectively. The relative intensity (I_D/I_G) of the D band and G band is used to investigate the degree of graphitization and crystallization for GQDs. For example, the I_D/I_G for GQDs derived from carbon fibers is 0.91.[24] On the contrary, the structure of CNDs synthesized from small molecules *via* bottom-up method is mainly related to its precursor's structure. In general, CDs fundamentally consist of C, O, and H elements. Sometimes, N-doping was used to help enhance PL efficiency.[92] Therefore, XPS is a good technique to identify the elemental composition and surface functional groups of CDs. FTIR can be used for qualitative analysis of functional groups. Similar results are reported that the presence of COOH, C=O, C-O-C, and OH bonds indicates that the oxygen-containing functional groups were introduced to GOQDs during the oxidation.[25,27,100,103–106] The oxidation level of GOQDs can be evaluated from C:O atomic ratio obtained from XPS spectra. For

example, the C:O atomic ratio of GOQDs prepared with the hydrothermal method, mixed acids oxidation method and electrochemical method was 2.54, 3.22 and 3.70, respectively.[24,98,107] The resulting indicates that different methods can obtain various CDs with different structure and elemental composition.

2.3.2 Optical properties

Typically, CDs exhibit strong optical absorption in the UV region (200-250 nm) due to the π-π^* transition of C=C bonds with a tail extending into the visible range.[10,84,108,109] GOQDs have oxygen-containing functional groups, so they show one more shoulder peak in the range between 250-390 nm, which can be regarded as the n-π^* transition of C=O bonds.[106,110] Photoluminescence is one of the most important and fascinating properties of CDs. So far, different sized CDs with different PL emission colours, mainly in the visible light region including blue, green, yellow and red, have been reported *via* various synthetic methods.[11–14,93,111–114] The size of CDs is considered to be a factor, affecting the PL colours. Li *et al*.[115] obtained CDs with different size (from 1.2 nm to 3.8 nm). They found that small-sized CDs emitted UV light, medium-sized gave visible light, and larger sized exhibited near-infrared light. Synthetic method is another influencing factor. CDs derived from hydrothermal treatment usually give UV or blue light.[16,18,22,25,116] Oxidation method usually produces CDs with PL emission colours in the visible region.[10,114,117–119] Quantum yield is also an important parameter to characterize the PL efficiency of CDs. The PL quantum yields reported for CDs vary significantly.[10,28,33,63,78,120] For organic compounds, the most common luminescence is due to π^*–π and π^*–n transitions.[121] The σ^*–σ transitions is not normally seen because of their high energy. The aromatic structure is very common in organic compounds. Therefore, fluorescence in most luminescent organic compounds is much strong. For inorganic compounds, the luminescence transition is relate to the energy levels of the ligands or the metal ions.[121] Ligands involve ion or molecule (functional groups). The inorganic compounds usually do not have many effective ligands, so the corresponding

absorption and emission are relatively weak. Generally, the quantum yield of GQDs is very low (less than 1%).[122] Some results are increased to over 20% by changing the methods[90], element doping[123] and surface passivation[124]. Besides that, other factors also can affect the quantum yield, such as pH[125], temperature[126] and solvent[127]. Overall, the exact mechanism of photoluminescence and the relation between the optical property and the synthetic methods remain unsettled.

2.4 The mechanism of photoluminescence

The photoluminescence mechanism of carbon materials has been a hot topic for researchers since its first discovery. There is no consistent explanation for the photoluminescence mechanism for the luminescent carbon materials because of the wide variety of materials reported so far, including graphene quantum dots, carbon dots, carbon nanodots and polymer dots. The chemical structure of the carbon dots obtained by different preparation methods is not the same. In general, the possible photoluminescence mechanisms of carbon dots mainly include quantum confinement effect of conjugate π structure[12], edge state and defect state[128], sp^2 localized electron-hole pairs[129] and excitation radiative recombination[130]. The exact mechanisms responsible for the photoluminescence of CDs remain to be elucidated clearly.

Quantum confinement effect

Quantum confinement can be described that once the diameter of a material is of the same magnitude as the de Broglie wavelength of the electron wave function or even smaller, the energy spectrum becomes discrete (see Figure 2.9).[131] As a result, a bandgap appears and becomes size-dependent. Their optical properties change substantially from those of bulk materials.

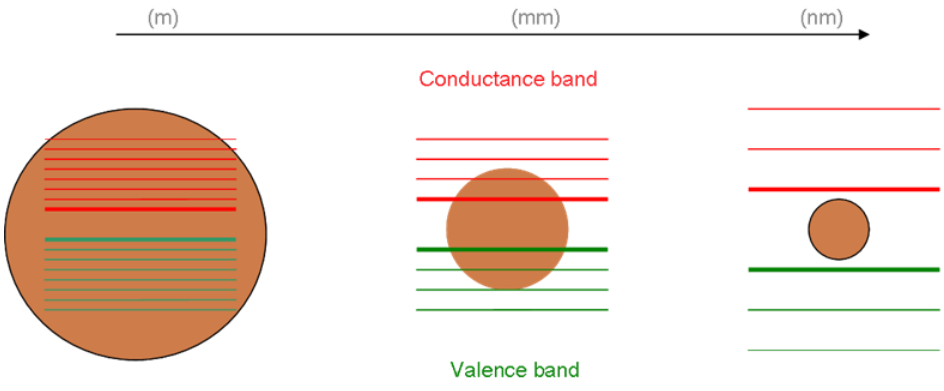

Figure 2.9. An illustration of the quantum confinement effect.

In theory, the bandgap will become larger and result in blueshift in light emission as the size of the particles decreases. Mahasin *et al.*[132] used density-functional theory

and time-dependent (DFT) calculations to simulate and speculate the relationships between the size and PL properties. The results confirm the theory. As shown in Figure 2.10, the GQDs experience emission colour changes from deep UV to near-infrared when the size increases from 0.46 to 2.31 nm.

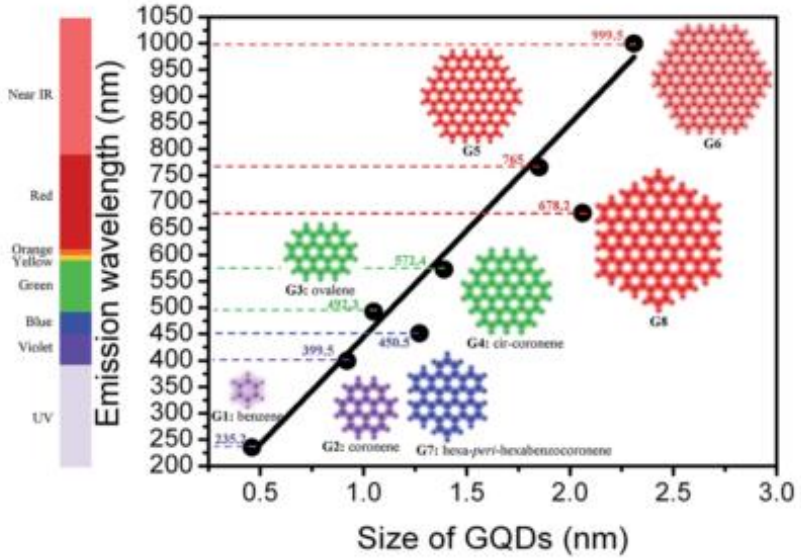

Figure 2.10. Calculated emission wavelength (nm) using DFT method in vacuum as a function of the diameter of GQDs.[132]

As mentioned above, quantum confinement in graphene depends on its size. Hence, bandgap should be highly size-dependent, that is, the larger the size is, the longer wavelength it emits.[132] However, according to previous studies, GQDs or GNPs from different methods can emit different PL colours without size dependence. Small GQDs (1~5 nm) hydrothermally derived from GO emitted green colour.[133] On the contrary, Pan *et al*.[25] also used almost the same procedure to prepare GQDs with strong blue emission. The only difference between these two preparation procedures is the reduction temperature, which makes a different PL colour. Therefore, size is not the only factor that affects the PL.

GQDs can be considered as small parts or fragments of graphene.[26,27,134] They shrink from two-dimension to zero-dimension when the size reduces to a certain extent

(usually below 50 nm in diameter).[135,136] Like traditional quantum dots (QDs), such small spatial dimensions confine electronic transport and lead to quantum confinement.[47,137,138] As a result, GQDs have a non-zero bandgap and have fluorescence properties. This bandgap can be tuned by changing the size or modifying the surface structure of GQDs.[139,140] Recently, some researchers also prepared graphene nanoparticles with fluorescence, but their diameter is larger than 50 nm.[89]

Radiative recombination of electrons and holes

Photoluminescence can be summarized as a light emission process that comes from any form of matter after excitation by photons.[141] The schematic of PL mechanism is shown in Figure 2.11. Typically, when a light that provides photons with an energy larger than bandgap excites a semiconductor, an electron from a molecule, atom or nanostructure will be not stable after receiving the energy from the photon. This unstable electron will be excited to a higher quantum state in the conduction band. After internal conversion in the excited state, it relaxes to its ground state and recombines with holes by emitting the energy *via* a photon of light.

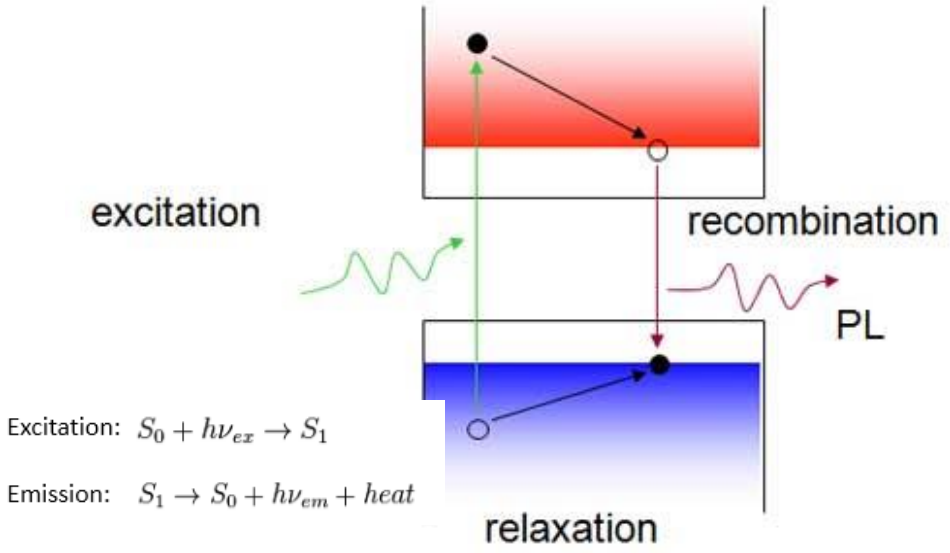

Figure 2.11 The mechanism of PL process.

Goki Eda *et al*.[129] prepared blue photoluminescence from chemically derived GO. They concluded that the mechanism of blue PL was the radiative recombination of

electron-hole pairs generated within localized states. The energy bandgap between the π and π* states resulted from the size of sp^2 clusters. In order to investigate the mechanism of PL with the isolated sp^2 clusters, the sheets of GO were progressively reduced by controlling the time of exposure to hydrazine and then the fractions of sp^2 clusters were different. The PL intensity was found to vary with different reduction periods of time. Based on their experiment results, they proposed that the area of the large sp^2 cluster did not change when GO was reduced, however, the transport between these large clusters was mediated by the increase of the smaller sp^2 clusters. The growth of small sp^2 clusters leads to percolation between the larger sp^2 clusters (see Figure 2.12).

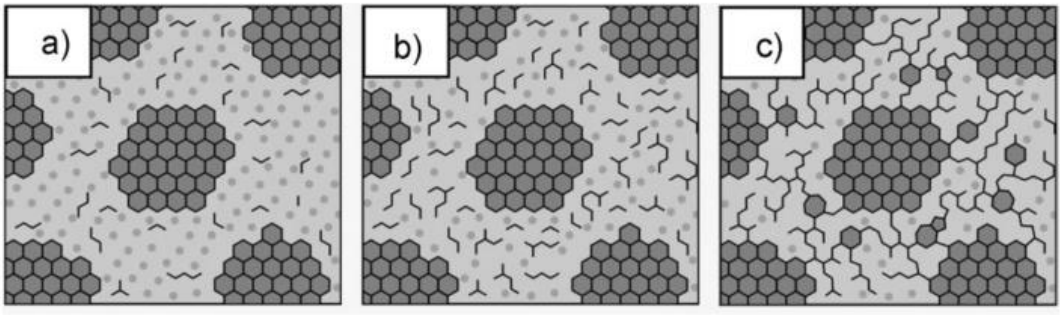

Figure 2.12 Structural models of GO at different stages of reduction.[129]

Surface states and edge states

The luminescence of carbon dots is controlled by the surface state and the edge state.[142] The edge structures of these materials are special or the polar groups are usually introduced at the edges during the preparation process, and these edge structures or the connected chemical groups have a great impact on luminescence. Peng *et al*.[25] used hydrothermal method to prepare GQDs and attributed that the observed blue luminescence may originate from zigzag sites with a carbene-like triplet ground state. Through experimental and theoretical calculations, Jin *et al*.[137] found that the edge grafted-NH_2 group can cause a red-shift of light emission. More connections of the -NH_2 groups could make more obvious redshift.

2.5 Applications

Compared with the traditional metal-containing quantum dots, luminescent carbon dots, such as GQDs and CNDs, have a good potential for biological applications because they have important significant features: they can have good distribution in water of PL properties, no heavy-metal element and show relatively low cytotoxicity at a certain concentration level, which is required for cell imaging.[143] Nurunnabi *et al*.[144] prepared GQDs from carbon fibers and reported that no acute toxicity or morphological changes were noted from *in vitro* cytotoxicity studies. The results showed that GQDs were distributed over the entire body through the systemic circulation. Tao *et al*.[73] prepared GQDs from multiwalled carbon nanotubes and investigated *in vivo* toxicology of GQDs in mice over three months. No apparent sign of toxic effect on mice was shown. By using a radiolabeling method, *in vivo* biodistribution of GQDs was studied and results suggest that the GQDs mainly accumulated in liver or spleen, which was similar to other studies on *in vivo* behaviours of nanomaterials. This work has been demonstrated that a certain amount of luminescent graphene-based nanoparticles can be used in biological applications without toxicity.

Bioimaging

As mentioned above, GQDs show good PL emission properties and have many advantages over traditional semiconductor quantum dots, including low or no cytotoxicity, good water dispersibility, and functionalization. Besides, carbon as raw material is low-cost and environmentally friendly. According to these reasons, researchers try to take advantage of PL properties of carbon-based materials for bioimaging in biological applications.

GQDs from multi-walled carbon nanotubes were prepared by Tao *et al*. [73] and were injected (2 mg/mL, 20 μL) into mouse subcutaneous tissue at three different places on its back for *in vivo* fluorescence imaging tests. Different excitation wavelengths were

used and those fluorescence images could be seen in Figure 2.13. Longer wavelength excitation could exhibit better signal-to-background separation and weaker emission. It is well known that, red colour has better tissue penetration,[145] which could reduce background autofluorescence and improve the signal-to-noise ratio.

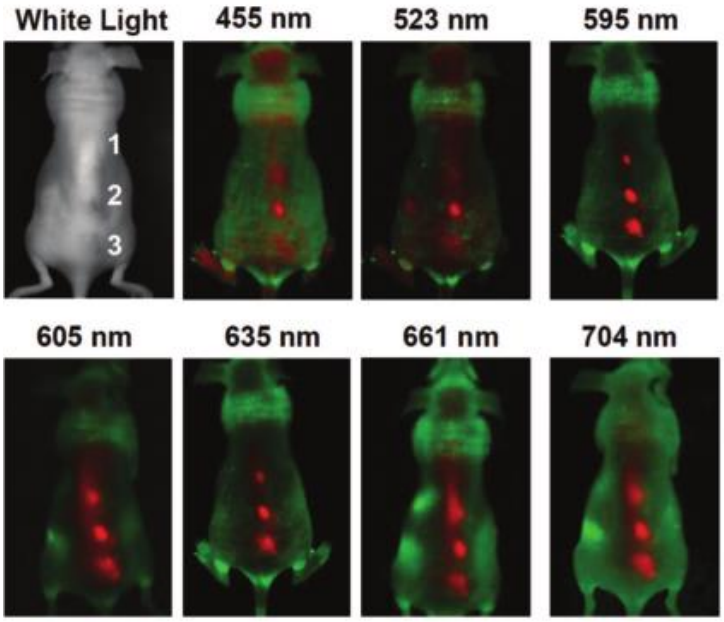

Figure 2.13. *In vivo* fluorescence imaging of a GQDs-injected mouse under different excitation wavelength.[73]

Dong *et al*.[77] prepared single-layer GQDs from XC-72 carbon black *via* chemical oxidation. Human breast cancer MCF-7 cells were incubated with GQDs sample (100 μg/mL) for 4 h. MTT assay results demonstrated that no substantial toxicity to MCF-7 cells. A bright green colour can be clearly observed on the confocal laser scanning microscope from the cells with excitation at 488 nm (see Figure 2.14). In addition, they also found that GQDs were able to label the cell membrane, nucleus, and cytoplasm. Similarly, Zhu *et al*.[146] reported GQDs were prepared with graphite powder by the solvothermal method. Up to 400 μg GQDs were added into the culture medium (10^4 cells/150 μL with Human osteosarcoma MG-63 cells). Cell activity was not affected significantly. 10 μg of GQDs were dispersed into the same culture medium environment to perform the bioimaging experiments. The green colour area inside the cells can be

observed, indicating the GQDs can well translocate into the cell's membrane and be used for bioimaging.

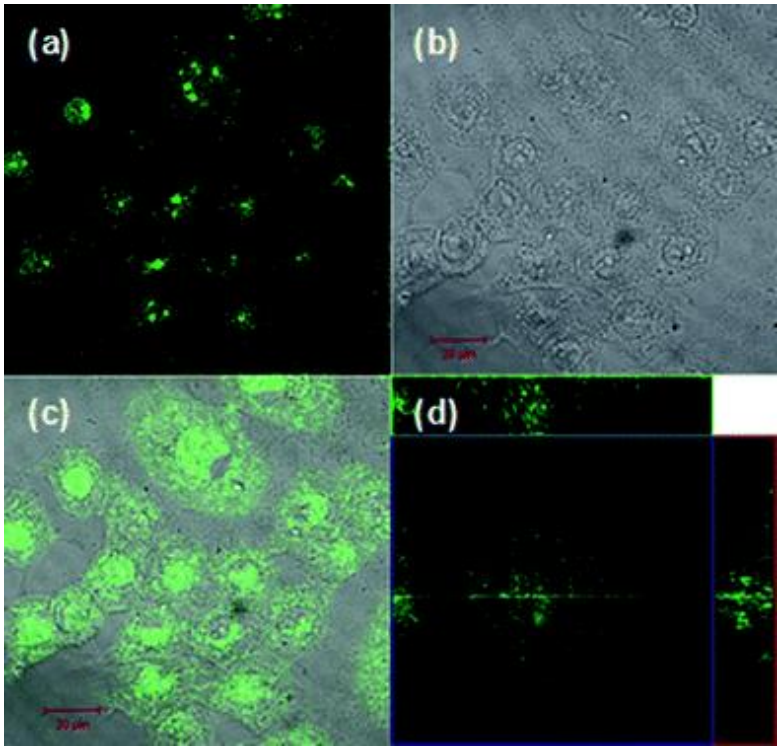

Figure 2.14. Images of MCF-7 cells labeled with GQDs taken by a confocal laser scanning microscope: (a) fluorescent image; (b) bright-field image; (c) merged fluorescent and bright-field image; and (d) section analysis.[77]

Blue fluorescent GQDs were achieved with small haloaromatic molecules *via* laser photochemistry method by Rohan *et al*.[147] Macrophages and Human hepatoma cell line (HepG2) cells were incubated with the GQDs for a certain period of time and excited at 405 nm. From the confocal microscopy images (Figure 2.15), it is obvious to see the blue colour appeared outside the macrophages cells around the membrane after 30 min and were fulfilled in the cells after 45 min incubation. In Figure 2.15c, HepG2 cells show uniform biodistribution of GQDs inside the cell and around the nucleus, indicating that GQDs can be used as fluorescent nanoprobes in cellular bioimaging. MTT assay results also demonstrated that GQDs had low cytotoxicity when the concentration of GQDs is lower than 10 μg/mL. This value is lower than those of GQDs derived from graphite-base materials.

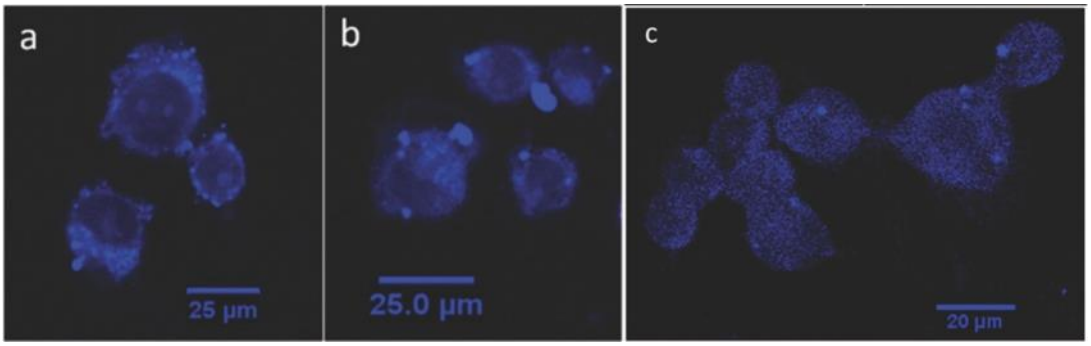

Figure 2.15. a) Macrophages after 30 min, b) macrophages after 45 min, and c) HEpG2 cells with GQDs.[147]

Biosensing

In the literature, the use of luminescent carbon dots as sensors to detect various metal ions is quite common. Generally, when CDs are dispersed in a solution with specific ions, the intensity of photoluminescence is quenched. The reason for quenching may be related to the charge transfer between the CDs and the ions, which inhibits radiative recombination.[148] Ha *et al.*[149] used graphite nanoparticles (3-4 nm in diameter) with mixed acids to prepare GOQDs. They used upconversion photoluminescence property of GOQDs to detect Cu^{2+} ions, which can accept the excited electrons of GOQDs and quench the PL. With increasing the concentration of Cu^{2+} ions, the PL intensity would decrease (see Figure 2.16).

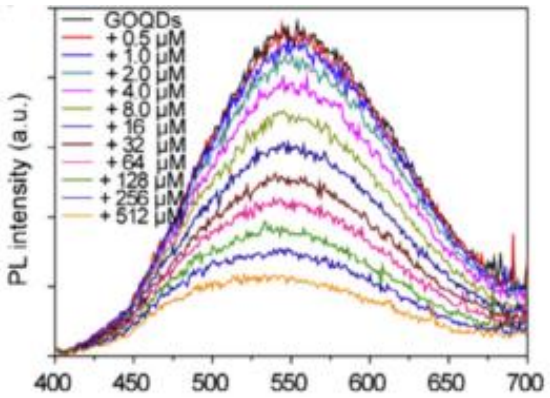

Figure 2.16 The PL spectra of the GOQDs depending on the concentration of Cu^{2+} ion [149].

Chen *et al.*[150] prepared near-IR fluorescence of GO nanosheets as a biosensor for dopamine. Dopamine could attach on the surface of GO by self-assembly with the help of multiple non-covalent interactions and PL quenching with a blue shift will exhibit

because of fluorescence resonance energy transfer. This provides a new method to sensitively and selectively detect dopamine in biological fluids.

Mercury ions (Hg^{2+}) is a kind of heavy metal ions, which may cause serious environmental pollution and toxicity to human health. Qin *et al*.[151] used flour as the carbon source to synthesis CDs *via* the microwave method. The aqueous suspension of CDs without Hg^{2+} had a strong PL peak at 442 nm. Only the presence of Hg^{2+} decreased PL intensity obviously, showing the resultant CDs were of high sensitivity and selectivity toward Hg^{2+} with a detection limit as low as 0.5 nM. Meanwhile, other ions, such as Cu^{2+}, Ag^{+}, Al^{3+} and Cr^{3+} can also be detected by other synthesized CDs.[152–154]

Drug delivery

By incorporation CDs with other nanomaterials and detecting the changes of fluorescence intensities, it is possible to track the release of drug molecules. Wang *et al*.[155] reported that the synthesized folic acid (FA)-conjugated GQDs were used to load the antitumor drug doxorubicin (DOX). The design strategy is illustrated in Figure 2.17. GQDs were prepared with carbon black following the chemical oxidation method. COOH groups of GQDs were used to graft with NH_2 group of FA. DOX was adsorbed by GQDs through π-π stacking and hydrophobic interactions. The loading efficiency of DOX on GQDs is about 68%. At pH 5.5, DOX could be released because the protonated DOX under acidic conditions increased hydrophilicity. Real-time monitoring test with HeLa cells demonstrated that DOX had released in the cells after 24 h of incubation and GQDs are novel drug carrier.

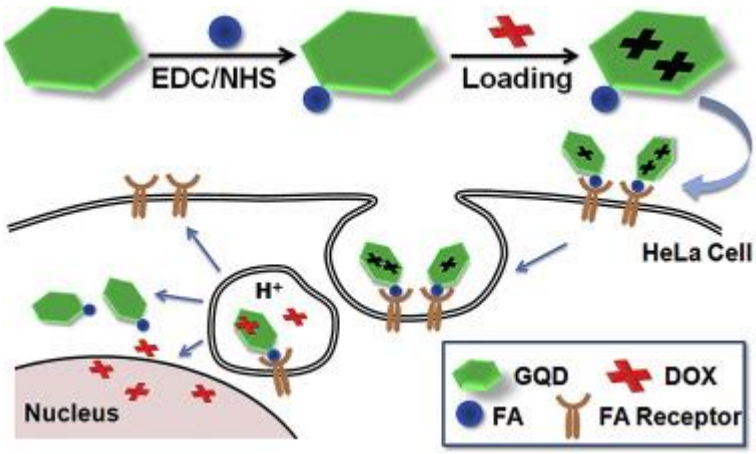

Figure 2.17. Schematic of the fabricated DOX–GQD–FA nanoassembly for DOX delivery into target cells.

Karthik *et al*.[156] synthesized a phototrigger conjugated anticancer drug with 7-(3-bromopropoxy)-2-quinolylmethyl chlorambucil (Qucbl) and fluorescent carbon dots, which were prepared by heating citric acid and urea *via* microwave-assisted method. The drug release of Qucbl-CDs was carried out by using UV light or He-Ne laser. After 30 min of irradiation, 73% or 20% of the loading drug was released, respectively.

Photodynamic therapy

Photodynamic therapy (PDT), is a form of phototherapy with the help of light and a photosensitizing chemical substance, taking advantage of molecular oxygen to elicit cell death.[157] Generally, reactive oxygen species (ROS), which produced by a photosensitizer under illumination, could kill cancerous cells.[158] Traditional PDT agents, such as porphyrin and phthalocyanines can produce singlet oxygen ($^1O_2$, an example of ROS), but they are limited by low yield, poor water dispersibility and photostability.[159] Therefore, developing a new PDT agent with a high $^1O_2$ yield is desirable. Ge *et al*.[104] successfully prepared GQDs with polyiophenes by hydrothermal method. The GQDs had a red emission peak at 680 nm and showed high $^1O_2$ generation yield with a yield of around 1.3 under irradiation with white light (different excitation wavelengths at 378, 538, 549 and 562 nm), which was almost twice as high as other PDTs.[159,160] Meanwhile, the researchers also verified that it was the energy transfer from

the GQDs to oxygen that was the cause for the sensitization of ground-state oxygen.

Zhou *et al.*[161] prepared three kinds of GQDs derivatives through the chemical oxidation method[162] and respectively eliminated carboxyl, hydroxyl, and ketonic carbonyl in order to study the relationship between oxygen functional groups and the ROS generation. Under blue laser irradiation, GQDs without ketonic groups showed the lowest ROS generation indicating that the ketonic carbonyl groups mainly affect the ROS generation.

2.6 Summary

Luminescent carbon-based dots, including graphene-based nanoparticles and carbon nanodots with fluorescent properties have become a new class of functional nanomaterials. This review has briefly summarized the common synthetic strategies, properties and applications of carbon-based dots. The structure and properties of the nanomaterials will have some differences when choosing different precursors, preparation conditions, etc. How to control the size, shape, and functional groups, which may influence PL properties, have become new challenges. The PL mechanisms of luminescent carbon-based dots also need to be investigated further and studied clearly. It can be expected that these luminescent nanoparticles will have potential in bioimaging, biosensing, photodynamic therapy, etc.

3 Experimental methods

3.1 Raw materials

For Chapters 4 and 5, reagent grades of graphite powder (<20 μm), sulfuric acid (95-98%wt), nitric acid (70%wt), sodium carbonate, sodium hydroxide, fluorescein, quinine sulfate, 0.1 M NaOH and 0.1 M H_2SO_4, dimethylsulfoxide (DMSO, 99%), 9,10-anthracenediyl-bis(methylene)dimalonic acid (ABDA) were all purchased from Sigma-Aldrich, Fisher Scientific and Alfa Aesar. Protoporphyrin IX (PPIX) and Rose Bengal (RB) were from Shanghai Jiao Tong University.

For Chapter 6, reagent grades of o-, m-, and p-phenylenediamine, potassium persulfate and ethanol were purchased from Sigma-Aldrich.

All chemicals were directly used as received without further purification. Distilled water was used throughout the whole work.

3.2 Preparation of carbon dots

Preparation of carbon dots is described in each chapter due to different methods used.

3.3 Characterizations

Atomic force microscopy (AFM) was carried out using a Veeco Dimension 3100 with the NanoScope software version 5 and Bruker OTESPA probes in tapping mode at 0.5 Hz. All the AFM samples were prepared on fresh mica substrates. To make sure the mica substrates were clean, one or two top layers of mica were removed with the help of a tape. One drop of GOQDs aqueous (~0.01 mg/mL) was dropped on the clean mica substrate which was left in a fume cupboard for a day to evaporate water. The length, height, width, standard deviation and average diameter of CDs automatically calculated by the NanoScope software. Figure 3.1 shows an example. The software can scan the obtained image and calculate the relevant information.

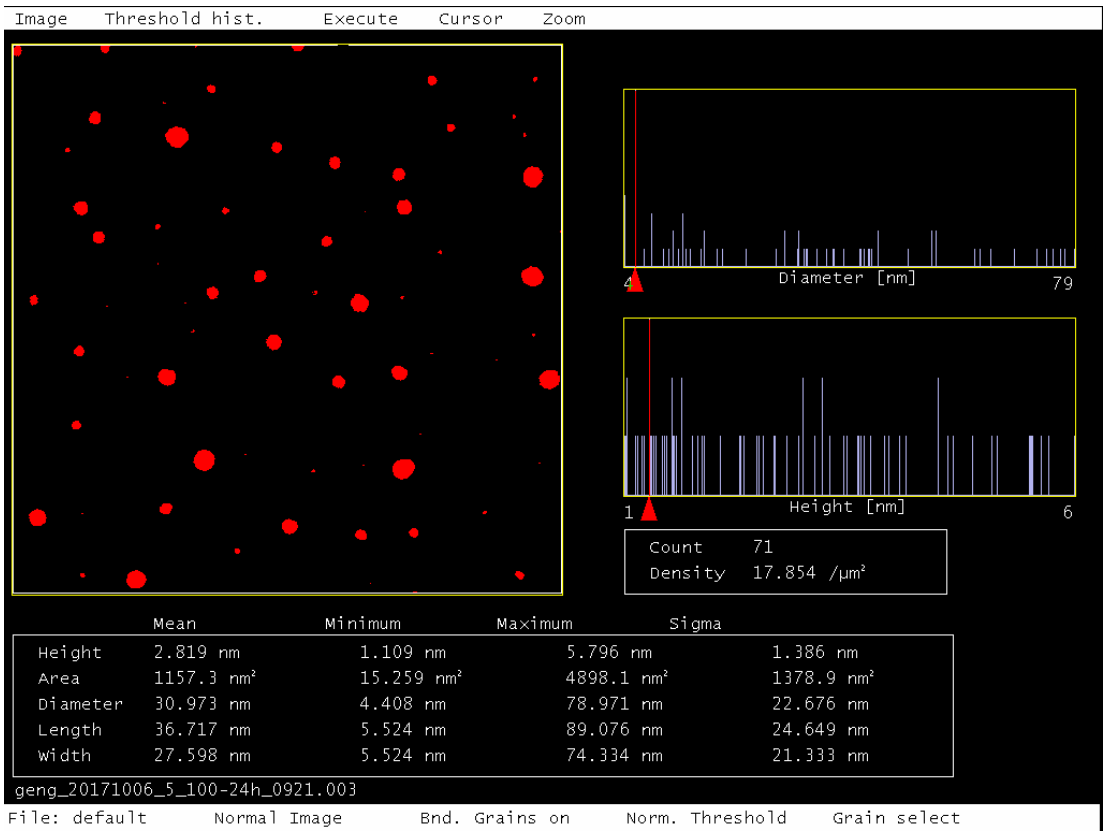

Figure 3.1. An example of the size information calculated from the NanoScope software.

High resolution TEM (HR-TEM) was operated at an accelerating voltage of 200 kV using a JEOL 2010F field emission TEM. The HR-TEM samples were prepared by soaking a holey amorphous carbon-coated copper grid (mesh size was 400 units) in a diluted suspension of carbon dots (~0.01 mg/mL) and left it in a fume cupboard to dry for 1 day.

GOQDs aqueous suspension (~0.01 mg/mL) for AFM and TEM was prepared following the procedure:

Weigh 10 mg of GOQDs in an analytical balance (Readability: 0.1 mg) and put them into a small bottle. Measure 20 mL of distilled water with a pipette (Volume: 10 mL twice) and transfer to the bottle. Put a clean stirrer bar into the bottle and stir the suspension for 1h. The obtained suspension is 0.5 mg/mL. Measure 200 μL of the obtained suspension with a pipette (Volume: 300 μL) and transfer to a centrifugation tube. Add 9.8 mL of distilled water into the tube. Stir for 30 min, sonicate for 30 min and centrifuge for 30 min. The top part suspension of the tube was used for AFM and TEM.

Fourier transform infrared (FTIR) spectra were obtained by a Perkin Elmer Spectrum 100 with a diamond attenuated total reflectance unit and the wavenumber ranged from 600 to 4000 cm^{-1} with a resolution of 1 cm^{-1}.

UV-Vis spectrometry between 250 nm to 700 nm was carried out on a Perkin Elmer Lambda 900 spectrometer with a 1 nm resolution. The polymethyl methacrylate (PMMA) cuvette has a 10 mm path length.

Raman spectroscopy was achieved with a Renishaw inVia Raman microscope using a 514.5 nm wavelength excitation laser. The scan range was from 100 cm to 3000 cm,

with a resolution of 1 cm^{-1}.

X-ray photoelectron spectroscopy (XPS) was carried out using a Kratos Ultra instrument with the monochromated aluminium source, with two analysis points per sample. The sample was prepared for analysis by pushing a small amount of powder into soft indium foil, which had been previously adhered to a sample holder using double sided carbon tape. This ensures all carbon detected was due to the sample. Survey scans were collected between 1200 to 0 eV binding energy, at 160 eV pass energy and 1.0 eV intervals. In addition, high-resolution C1s, O1s, and N1s spectra were collected, as specified, over an appropriate energy range at 20 eV pass energy and 0.1 eV intervals. The analysis area was 700 μm by 300 μm. The data collected were calibrated in intensity using a transmission function characteristic of the instrument (determined using software) to make the values instrument independent. The data were then quantified using theoretical Scofield relative sensitivity factors *via* the CasaXPS software. The data were calibrated for binding energy by making the main carbon peak C1s at 285.0 eV, and correcting all data for each sample analysis accordingly.

X-ray diffraction (XRD) was performed on a STOE Stadi P X-ray diffraction instrument (Cu Kα irradiation λ=0.154060 nm) operating at 40 kV, 35 mA and a scanning speed of $1^{\circ}\,min^{-1}$ with a step size of 0.015°.

Photoluminescent emission and excitation spectra were measured by using an LS 55 fluorescence spectrometer (Perkin Elmer) at room temperature (25 °C), and a pulsed xenon lamp excitation source. The scan speed was 200 nm/min. The PMMA cuvette has a light path of 10 mm * 10 mm. In Chapter 4 and 6, the slit widths of the excitation and emission were 10 nm. In Chapter 5, the excitation slit width was 10 nm and the emission slit width is 4.5 nm in order to obtain the data in the appropriate range.

Quantum yield was measured according to an established reliable comparative method[163]. Fluorescein in 0.1 M NaOH (literature quantum yield 0.79)[164] and quinine sulfate in 0.1 M H_2SO_4 (literature quantum yield 0.54)[165] were chosen as standard materials for 500-600 nm and 400-600 nm emission range separately. The absorbance was measured on a Hitachi-U1100 spectrophotometer. For the purpose of minimizing re-absorption effect, the absorbance in the 10 mm PMMA cuvette was kept not higher than 0.1 at the excitation wavelength. Five solutions of the standard materials or test materials with increasing concentrations were chosen, according to the following Equation 3-1:

$$\Phi_X = \Phi_{ST}\left(\frac{Grad_X}{Grad_{ST}}\right)\left(\frac{\eta_X^2}{\eta_{ST}^2}\right) \quad (3\text{-}1)$$

Φ is the fluorescence quantum yield, and the subscripts *X* and *ST* represent test and standard respectively. *Grad* is the gradient from the plot of integrated fluorescence intensity *vs* absorbance. η is the refractive index of the solvent.

The measurement of reactive oxygen species (ROS) was separated into two parts. The first characterization work in the first section in Chapter 4 was carried out by Prof. Sun Kang's group in Shanghai Jiao Tong University. ABDA was used as a chemical probe to detect singlet oxygen production during irradiation according to the decay of UV-Vis absorption at 400 nm. The GOQDs aqueous suspension (1 mL, 0.01 mg/mL) was added in a 1 mL cuvette (light path: 3 mm) with the same sample in reference cuvette. Then ABDA/ DMSO solution (0.5 mg/mL, 50 μL) were added and the absorption spectra were recorded with 365 nm irradiation every two minutes. Only one test sample was GOQDs. RB and PPIX were as comparative samples.

The characterization work in the remaining sections of Chapter 5 and 6 was carried out by the author. The sample aqueous suspension (0.5 mL, 0.25 mg/mL) was added in a 4 mL cuvette (light path: 10 mm) with the same sample in reference cuvette. Then

ABDA/DMSO solution (0.5 mg/mL, 150 μL) were added and the absorption spectra were recorded with 460 or 530 nm irradiation every five minutes. All the GOQDs, GOQDs-M and GOQDs-H samples were tested.

The measurement of cell viability test was carried out in Shanghai Jiao Tong University. HeLa cells, which are immortal cells line and commonly used in scientific research, were seeded onto 96-well plates with 1000 cells/well and incubated in a humidified atmosphere with 5% CO_2 incubator for 48 h. Then the GOQDs aqueous suspension dispersed in the culture medium with different concentration (0, 10 ppm, 20 ppm, 40 ppm, 60 ppm, 80 ppm, 100 ppm, 200 ppm, 400 ppm, 600 ppm, 800 ppm and 1000 ppm) were added to incubate for 24 h and cell viability was measured by standard Cell Counting Kit-8 (CCK8) assays. In CCK8 assays, 10 μL CCK 8 solution was added into each cell for 4 h incubation and then the absorbance at 450 nm was measured by a microplate reader (Multiskan GO, Thermo scientific),

GOQDs aqueous suspension (1 mg/mL) was prepared following the procedure:

Weigh 50 mg of GOQDs in an analytical balance (Readability: 0.1 mg) and put them into a small bottle. Measure 10 mL of distilled water with a pipette (Volume: 10 mL five times) and transfer to the bottle. Put a clean stirrer bar into the bottle and stir the suspension for 1h.

GOQDs aqueous suspension (0.5 mg/mL) was prepared following the procedure:

Weigh 25 mg of GOQDs in an analytical balance (Readability: 0.1 mg) and put them into a small bottle. Measure 10 mL of distilled water with a pipette (Volume: 10 mL five times) and transfer to the bottle. Put a clean stirrer bar into the bottle and stir the suspension for 1h.

GOQDs aqueous suspension (0.25 mg/mL) was prepared following the procedure:

Weigh 25 mg of GOQDs in an analytical balance (Readability: 0.1 mg) and put them into a small bottle. Measure 10 mL of distilled water with a pipette (Volume: 10 mL ten times) and transfer to the bottle. Put a clean stirrer bar into the bottle and stir the suspension for 1h.

GOQDs aqueous suspension (0.125 mg/mL) was prepared following the procedure:

Measure 40 mL of GOQDs aqueous suspension (0.25 mg/mL) with a pipette (Volume: 10 mL four times) and transfer to the bottle. Measure 40 mL of distilled water with a pipette (Volume: 10 mL four times) and transfer to the bottle. Put a clean stirrer bar into the bottle and stir the suspension for 1h.

GOQDs aqueous suspension (0.0625 mg/mL) was prepared following the procedure:

Measure 20 mL of GOQDs aqueous suspension (0.125 mg/mL) with a pipette (Volume: 10 mL two times) and transfer to the bottle. Measure 20 mL of distilled water with a pipette (Volume: 10 mL two times) and transfer to the bottle. Put a clean stirrer bar into the bottle and stir the suspension for 1h.

4 Photoluminescent graphene-based nanoparticles derived from graphite powder *via* different reaction conditions

4.1 Introduction

Graphite is a common material in our daily life and it has been widely used in many applications, such as batteries, pencils and lubricant. The structure of graphite is carbon layers stacking together *via* van der Waals forces, which make layers of graphite be easily segregated.[166] In each layer, the carbon atoms are arranged in a honeycomb lattice with separation of 0.142 nm, and the distance between adjacent layers is around 0.335 nm.[167] In 2004, only one layer of the graphite was collected, and that is graphene.[5] Due to its unique structure, graphene shows extraordinary mechanical, thermal and electronic properties.[39,168–170] However, its conduction bands and valence bands meet at the Dirac points, so graphene is a zero-bandgap semiconductor material, which limits its electronic and optical applications.[135]

Because the quantum confinement effect could influence and produce the bandgap, the size of graphene is considered to reduce to the nanoscale.[171–173] In general, GQDs or GOQDs are one or few-layered graphene-based nanoparticles with lateral dimensions smaller than 100 nm.[26,27,134] GOQDs, which have oxygen-containing functional groups, are expected to have new photoluminescent properties resulting from the quantum confinement effect. Compared with the heavy metal elements in the traditional semiconductor materials like CdSe, carbon and oxygen are the main elements in GOQDs. Therefore, they are relatively friendly to the environment. GOQDs are expected to be used in many applications, especially in bioimaging and photodynamic therapy.

As mentioned in the literature review, the bottom-up and top-down methods are mainly used for preparing GQDs. The bottom-up methods could be described from self-assembly of small aromatic compounds. On the contrary, the top-down methods could be considered from the chemical disintegration, including the chemical oxidation, electrochemical oxidation, hydrothermal treatment, high-resolution electron-beam and oxygen plasma treatment, of large carbonaceous materials, such as carbon nanotubes, carbon fibers, nanodiamond, and carbon nanoparticles.[10,11,14,16,24] However, some of these methods need special and complicated instruments, and some starting materials are expensive. These special conditions restrict the synthesis and yield of GOQDs.

Considering that graphite is common and low-cost, a synthesis of GOQDs from graphite *via* chemical methods would be more practical and feasible. The research method of this chapter is:

1. Prepare several kinds of GOQDs with tunable photoluminescent properties.
2. Characterize and analyze their structure and properties. Study their relation.
3. Modify the method, prepare new samples and compare the changes.

In this chapter, there are three sections. Firstly, graphite powder was used as a precursor to prepare one kind of GOQDs. Only one sample was characterized and analyzed. In the second section, a series of GOQDs were synthesized using the same experimental procedure as that of Section 1 with different reaction conditions to be specific. In the third section, the experimental procedure were further modified, and another series of GOQDs were prepared. The emission ranges of GOQDs could be tuned from blue, green and yellow to red. The relationships between photoluminescent properties, structure, and concentration, are discussed in detail at the end of the chapter.

4.2 Preparation and characterizations of the photoluminescent graphene oxide quantum dots

4.2.1 Experimental procedures

Preparation of graphene oxide quantum dots

Graphene oxide quantum dots were synthesized by a modified strong-acid oxidation method following reported approach.[24] Briefly, graphite powder (900 mg) was dispersed in concentrated sulfuric acid (100 mL), which was stirred for 1 hour followed by sonication for 30 min. The resultant suspension was poured into a three-neck round-bottom flask which contained mixed acids (80 mL sulfuric acid and 60 mL nitric acid). After 24 hours of refluxing at 100 ℃, the mixture was cooled, and a required amount of distilled water was slowly added. The pH was adjusted to around 8 with sodium bicarbonate. During this period, the reaction suspension was filtered for several times to remove the precipitated salt. Afterwards, the residual solution was collected by decantation with filter paper. The filtrate was dialyzed in a dialysis bag (MWt cut-off 3500 Da) against distilled water for more than seven days to remove excess salt. The suspension was freeze-dried to obtain GOQDs powder.

4.2.2 Results and analysis

4.2.2.1 Morphology

The prepared GOQDs were analyzed using different techniques.

The surface morphology of the GOQDs was characterized by AFM, as shown in Figure 4.1. The AFM images show that the prepared GOQDs were dot-like. By calculation from the Nanoscope software, the average lateral size of GOQDs is about 45.9 nm, and the average height was between 0.6 to 8.4 nm. Considering that the layer spacing of the single graphene sheet is about 0.7-1.0 nm,[174] the majority of nanoparticles are 1-10 layers.

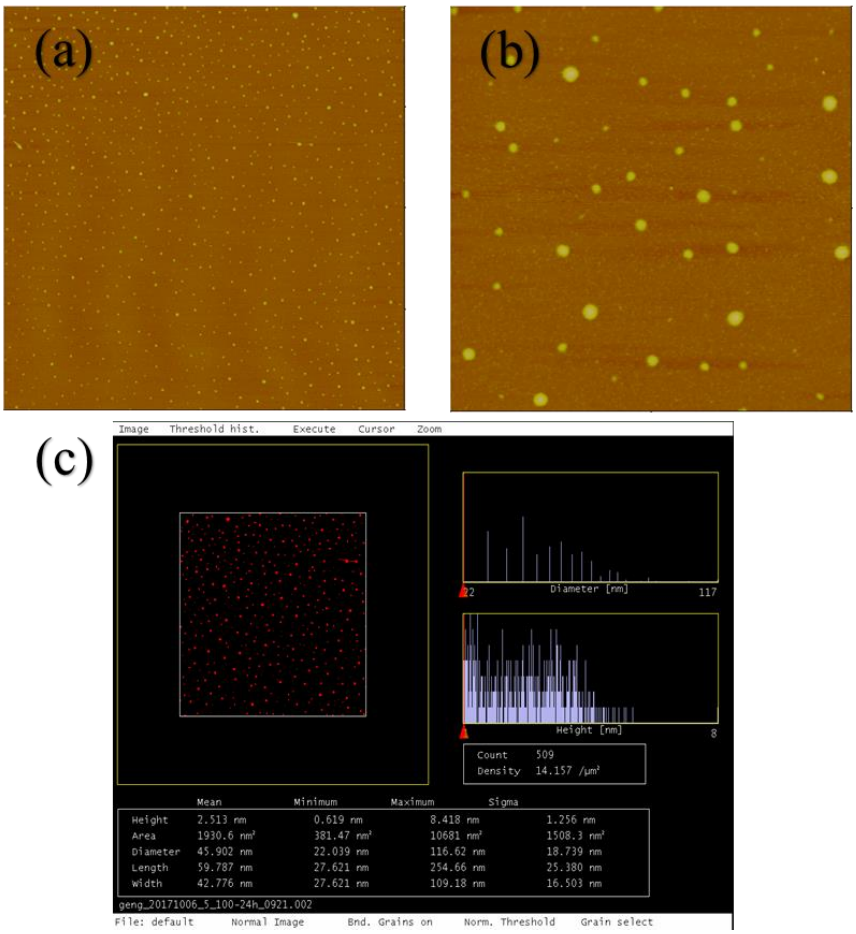

Figure 4.1. AFM images of GOQDs (a) scale: 10×10 µm; (b) scale: 2×2 µm; and (c) the size information of GOQDs in the image was calculated by the NanoScope software.

4.2.2.2 Structure

Figure 4.2a shows the XRD pattern of GOQDs and raw material of graphite powder. There is no sharp (002) peak at 2θ=26.5 ° for the GOQDs, where is the characteristic peak for graphite. However, a weak and broad diffraction peak appears at 2θ=20.9°. The broad peak is a significant indicator of amorphous materials and this could demonstrate that the crystalline structure is destroyed during the oxidation process. Because the oxygen-containing functional groups such as hydroxyl and epoxy groups were introduced on the surface, the layers became expansion and the interlayer spacing was increased. According to Bragg's law, the interlayer spacing could be calculated about 0.97 nm, which is larger than that of graphite (0.34 nm) and the layers are easily separated under sonication. As calculated by the software, the average height of GOQDs is ca. 2.5 nm, which should correspond to about three layers.

Raman spectroscopy was also used to study the GOQDs, as shown in Figure 4.2b. Graphite powder has a sharp G band at 1580 cm^{-1}. After oxidation, the D band appears at 1386 cm^{-1} and the G band broadens significantly and displays a shift to higher frequencies (blue-shift). The relative intensity ratio of D band (defect) and G band (crystalline) is about 1, which is higher than that of graphene oxide prepared by traditional Hummers methods.[175–177] The higher intensity ratio I_D/I_G indicated more defects in the carbon matrix.

The GOQDs were characterized by XPS to probe the elemental composition and chemical bonds. As seen in Figure 4.2c, the XPS spectrum of GOQDs shows three elements, including a C1s peak at 285 eV, N1s peak at 400 eV and O1s peak at 533 eV. Quantitative analysis of the XPS spectrum shows that the atomic ratio of O/C of GOQDs is 0.50, which is higher than that of graphene oxide (ca. 0.43) prepared *via* traditional Hummers methods. The high resolution scan of C1s could be curve-fitted into 5 peaks (Figure 4.2d), including 285.0 eV (C-C / C=C), 285.8 eV (C-N), 286.6 eV

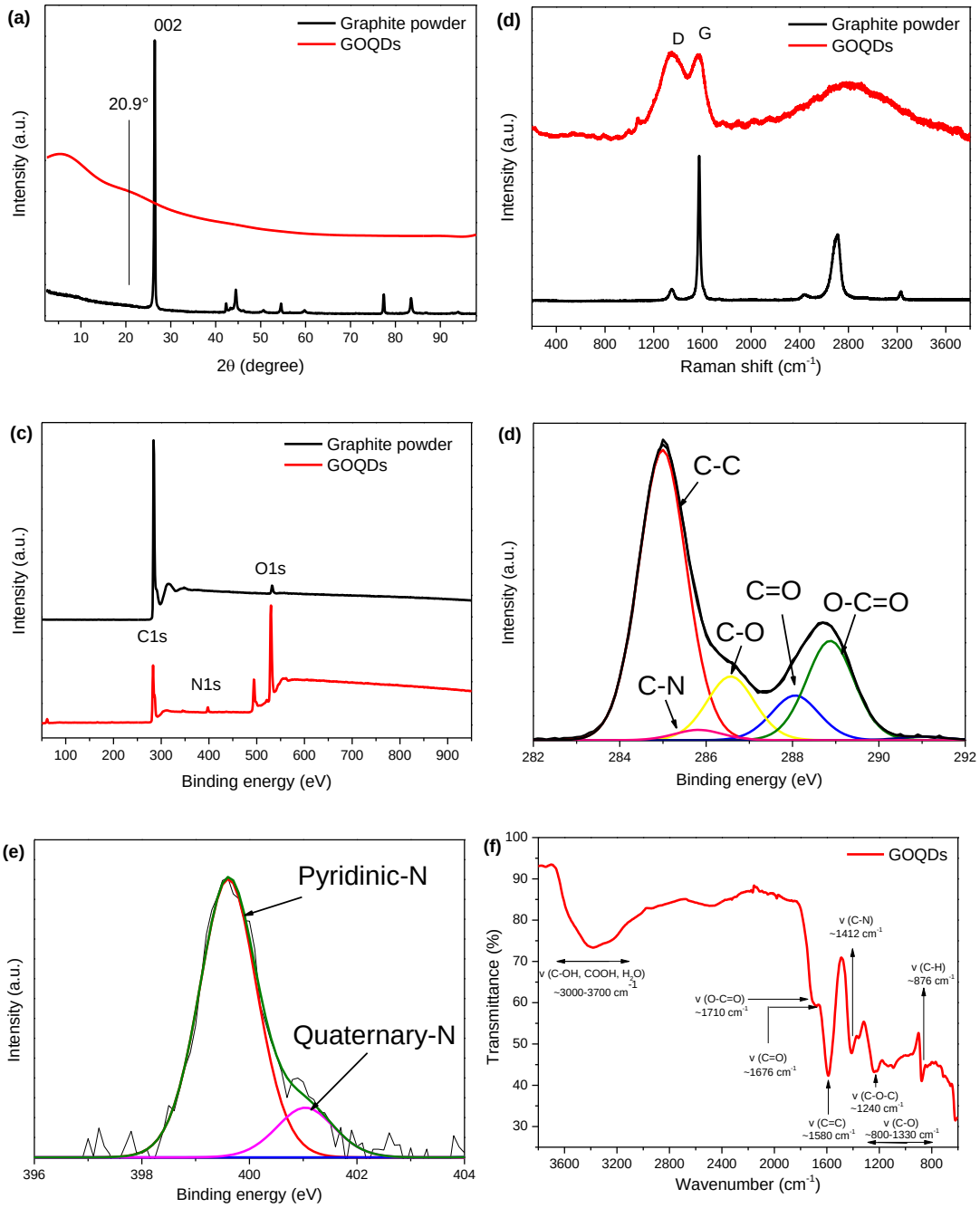

Figure 4.2. (a) XRD patterns of GOQDs and graphite powder, (b) Raman spectra of GOQDs and graphite powder, (c) XPS survey spectra of GOQDs and graphite powder, (d) high-resolution XPS C1s spectra of GOQDs, (e) high-resolution XPS N1s spectra of GOQDs and (f) FT-IR spectra of GOQDs.

(C-O-C/C-OH), 288.1 eV (C=O) and 289.0 eV (COOH). The N1s band, ranging from 396 to 404 eV (Figure 4.2e), can be deconvoluted into two peaks at 399.6 eV and 401.0 eV, representing pyridinic-like and quaternary nitrogen atoms. These indicated that the

nitrogen atoms were introduced to the graphite sheet under oxidation process and they were mainly located in the sheet edge due to the higher percentages of the pyridinic-like functionalities.

In Figure 4.2f, the FTIR spectrum of GOQDs confirms that oxygen-containing functional groups, including hydroxyl (3400 cm^{-1}), epoxy (1240 cm^{-1}), carbonyl (1676 cm^{-1}) and carboxyl groups (1710 cm^{-1}) were introduced to the surface of graphite. These functional groups make GOQDs disperse in water very well and stable for a long time. Moreover, stretching vibrations of C=C (1580 cm^{-1}) and C-N (1412 cm^{-1}) were also observed, which is consistent with the above XPS results.

4.2.2.3 Optical properties

Figure 4.3 shows photographs of the GOQDs aqueous suspensions with decreasing concentration and the colour is changed from brown to light yellow. Its clarity demonstrates that the dispersion of GOQDs in water is very good.

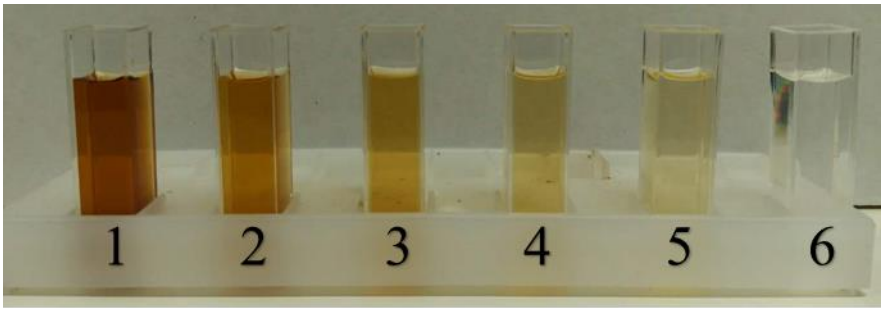

Figure 4.3. 1-5: GOQDs aqueous suspensions at 1.0, 0.5, 0.25, 0.125 and 0.0625 mg/mL. 6: water.

The optical properties of GOQDs were characterized by photoluminescence spectroscopy and UV-Vis spectroscopy. The UV-Visible spectrum (Figure 4.4a) shows a broad absorption from UV to the Visible region. Figure 4.4b shows the diagram of relative placing of different orbitals. The π-π^* transition of aromatic sp^2 domains leads to a strong absorption in the UV range. A shoulder absorption peak at around 370 nm

is observed, and could be attributed to the n-π* transition of the C-N, C-O or C=O bonds.[10,178] Compared with other graphene oxide reported in some publications, the shoulder position of GOQDs is red-shift from ca. 300 nm to 370 nm due to the increasing amount of the delocalization of π electrons. After strong oxidation, oxygen and nitrogen atoms were introduced into the graphite sheet edge, and more non-bonding orbitals were created. The compounds have massive delocalization, so the energy gaps between orbitals become small. The relationship between the wavelength λ and its energy E is:

$$E = h\frac{c}{\lambda} \tag{4-1}$$

Where h is Planck's constant and *c* is the speed of photon. The less energy needed means the longer wavelength absorbed, which made the red-shift.

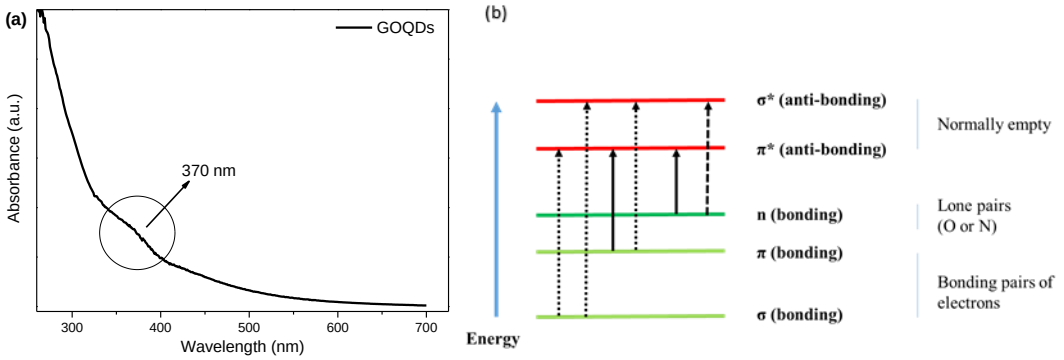

Figure 4.4. (a) UV-Vis spectrum of GOQDs and (b) the diagram of the relative placing of the different orbitals.

The resultant GOQDs can emit a wide spectrum of luminescence, including blue, green, yellow, orange and red light. Figure 4.5 shows the optical images of GOQDs under irradiation of hand-held UV, blue and green light lamps. Yellow, orange and red light paths could be seen in the cuvettes. In the photoluminescent spectra, GOQDs have optimal excitation and emission wavelengths at 470 nm and 531 nm, respectively as shown in Figure 4.6a.

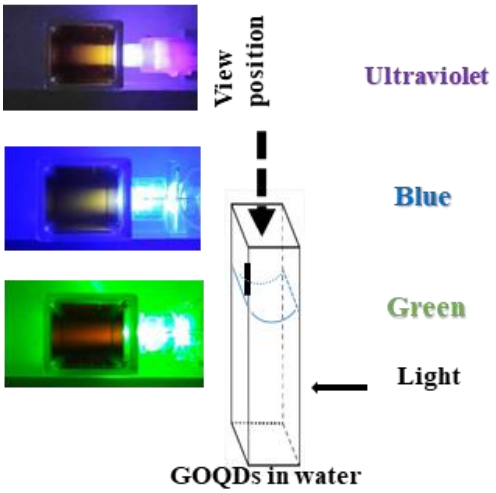

Figure 4.5. Photos of GOQDs in water excited by ultraviolet, blue and green light.

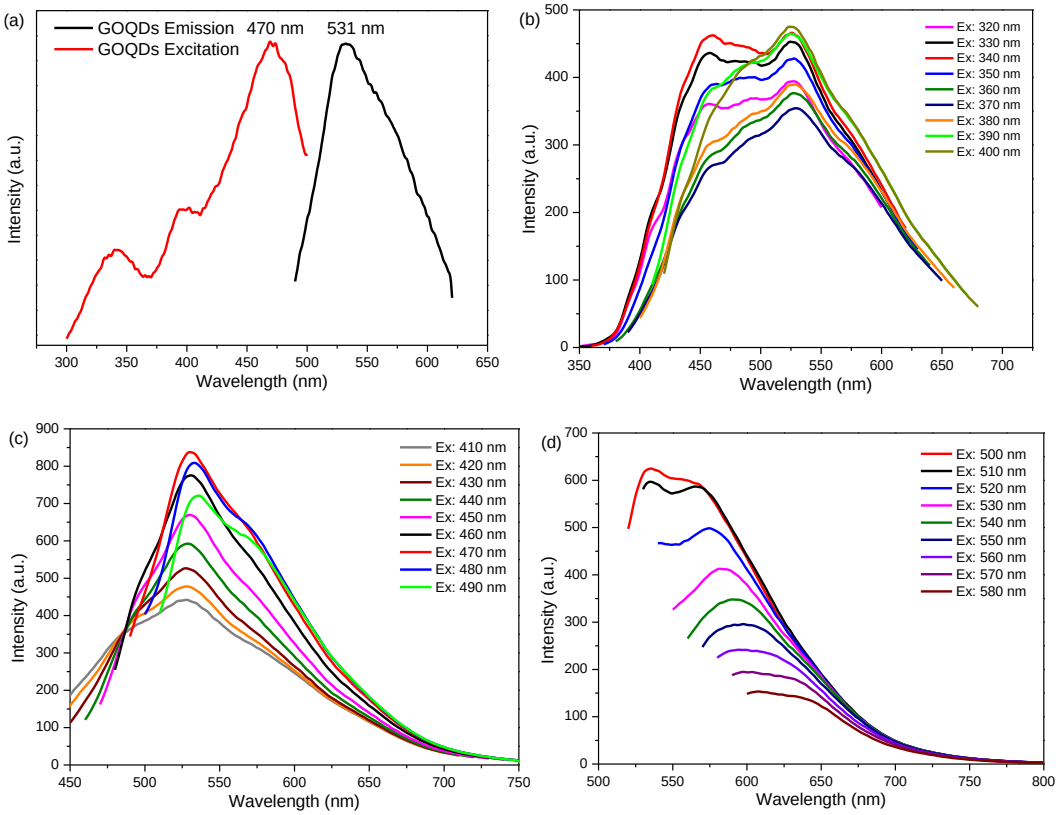

Figure 4.6. (a) Optimal excitation and emission PL spectra and (b) – (d) the excitation-dependent PL behaviour.

Fluorescent carbon materials always have excitation-dependent PL behaviours, as shown in Figure 4.6.[179–181] Under different excitation wavelengths, they could provide

different colours and change the PL intensity and wavelength position, which would be interesting for some applications. When excited under 340 nm wavelength, the GOQDs show a stronger peak at ca. 460 nm, which is blue emission, and a weak shoulder at around 531 nm, which is green emission. When increasing the excitation wavelength (redshift), the stronger peak at 460 nm becomes weaker and decreases to disappear. Meanwhile, the weak shoulder at 531 nm becomes the main peak and increases gradually (Figure 4.6b). From 410 nm to 470 nm excitation wavelength, the peak position of the emission spectrum is fixed at ca. 531 nm and the intensity increases remarkably. The strongest PL emission intensity of GOQDs appears when the materials are excited at 470 nm. At a longer excitation wavelength than 470 nm, the emission spectrum starts to redshift, and the main peak intensity gradually decreases, as shown in Figure 4.6d.

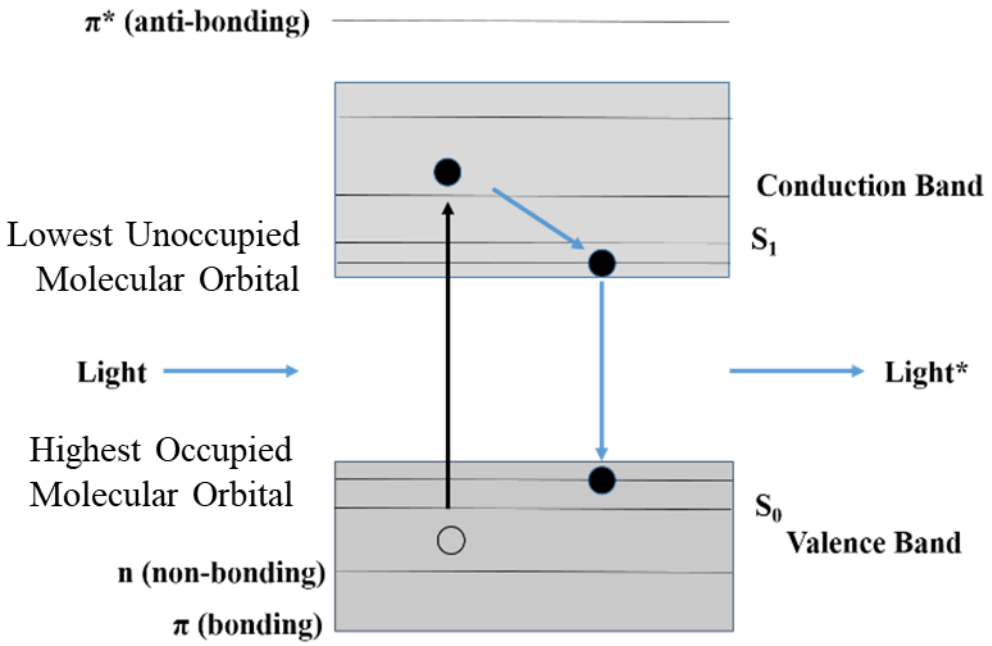

Figure 4.7. The PL mechanism of GOQDs

As seen in Figure 4.7, the PL mechanism of GOQDs could be attributed to the radiative recombination of electron and hole in a conjugation system. Strong acid oxidation brings oxygen-containing functional groups and nitrogen atoms to the surface,

as well as the fracture of C-C / C=C bonds and defects in the conjugation systems. The large conjugation system in graphite is divided into amounts of very small and individual conjugation system. Their sizes could be nanoscale and fulfill the requirement of the quantum confinement effect, which makes them possible to have PL properties. Meanwhile, oxygen or nitrogen bonding orbitals also could introduce new energy levels to the electronic band structure. Due to the wide size distribution of "small" conjugation systems and new energy levels induced, the width of bandgap can cover a broad range, leading to a wide luminescent spectrum from blue to red lights.

The relationship between PL intensity, absorbance and concentrations was studied, as shown in Figure 4.8. Five sets of different concentrations of GOQDs suspension were prepared, and four sets of representative wavelengths were selected for four colours, including green, yellow, orange and red. Firstly, the PL intensity of all four colours becomes stronger when the concentration increases from 0.0625 to 0.125 mg/mL. However, 0.125 mg/mL is the concentration that can provide the strongest PL intensity for green colour (530 nm). Afterwards, the PL intensity reduces even the concentration increases. Yellow, orange and red colours show a similar trend. PL intensity becomes stronger with increasing concentration until 0.5 mg/mL. When the concentration increases to 1 mg/mL, yellow and orange emission intensities decrease significantly, but red colour only reduces slightly. Meanwhile, the intensity of green colour is the lowest at 1 mg/mL compared to those of other colours. In Figure 4.8h, different light paths can be seen in the cuvettes. Cuvette 4 has the longest light path. However, the light path in cuvette 1, which has the highest concentration of GOQDs, is quite short. This result is similar to be specific PL intensity from the instrument.

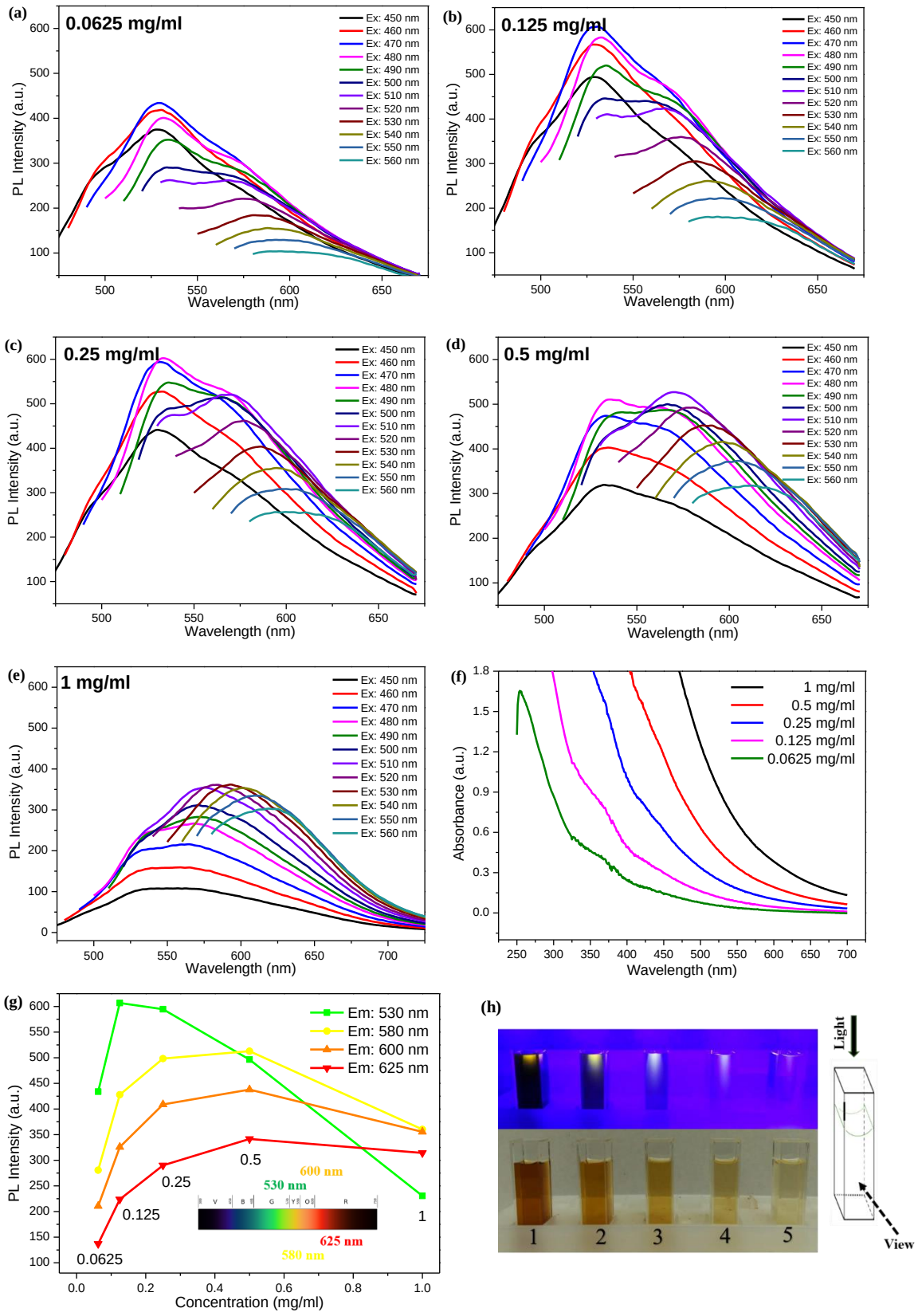

Figure 4.8. (a)-(e) The emission spectra of GOQDs-1 suspensions at 0.0625, 0.125, 0.25, 0.5 and 1 mg/mL excited by various excitation wavelengths, respectively, (f) the UV-Vis spectra of GOQDs-1 suspensions at

0.0625, 0.125, 0.25, 0.5 and 1.0 mg/mL, (g) the relationship between PL intensity at 530, 580, 600 and 625 nm emission wavelengths and different concentrations. The inset shows the spectrum of visible light, and (h) the photos of GOQDs-1 suspensions at 0.0625, 0.125, 0.25, 0.5 and 1.0 mg/mL excited by the blue light.

Therefore, the relationship between PL intensity and concentration is not linear or proportional. Higher concentration is not always equivalent to stronger PL intensity. Absorbance should be considered because both excitation and emission wavelength would be absorbed by the aqueous suspension to some extent, as seen in Figure 4.8f. According to Beer-Lambert law:

$$\mathrm{A} = \log_{10}(I_0/I) = \varepsilon cL \tag{4-2}$$

where A is the measured absorbance, I_0 is the intensity of the light at a given wavelength, I is the transmitted intensity, ε is a constant known as the extinction coefficient, L is the path length through the sample and c is the concentration.

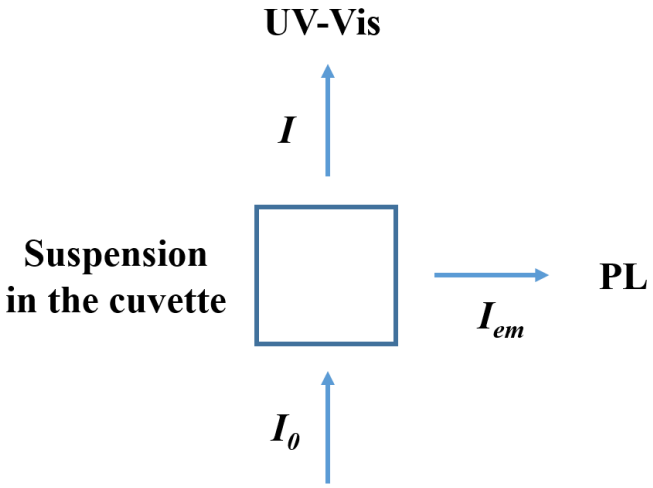

Figure 4.9. Schematic representation of the UV-Vis and PL.

Figure 4.9 shows a simple schematic representation of UV-Vis and PL in the cuvette. A part of the light is absorbed by the suspension and used to excite the electrons to generate the PL emission. The light emitted is also partly absorbed by the suspension. So the relationship between the intensity of excitation light and emission light is:

$$A_{ex} = \log_{10}(I_0/I) \tag{4-3}$$

$$I_{ex} = I_0 - I \tag{4-4}$$

$$I_{ex} \times \varphi = I_{em}^* \tag{4-5}$$

$$I_{em}^* = I_0^* \tag{4-6}$$

$$A_{em} = \log_{10}(I_0^*/I_{em}) \tag{4-7}$$

So,

$$I_{em} = (1 - 10^{-A_{ex}})10^{-A_{em}}\varphi I_0 \tag{4-8}$$

where A_{ex} is the absorbance measured at an excitation wavelength, A_{em} is the absorbance measured at an emission wavelength, I_0 is the intensity of the light at the given wavelength, I_{ex} is the intensity of the absorbed light for exciting GOQDs, I_{em}^* is the intensity of the emitted light from GOQDs aqueous suspension. I_0^* is the intensity of emitted light, which is also absorbed by the suspension. I_{em} is the intensity of the emitted light from the cuvette, and φ is a PL efficiency coefficient, which is related to the quantum yield. It can be found that the intensity of emission wavelength is affected by the absorbance of both excitation wavelength and emission wavelength. However, the Equation 4-8 is only a simple derived formula, which requires the emitted light in the GOQDs aqueous suspension just have a single wavelength. When the emission wavelength is a broad range, then different emitted wavelengths would produce the iterative effect inside the suspension and make the relationship between the PL intensities and concentrations (*via* absorbance) more complicated. Although the equation can not be used directly, it still provides an understanding between PL and UV-Vis.

As mentioned above, although some wavelengths could emit stronger light, the emission light would be partly absorbed by the aqueous suspension, so the intensity

would be weakened by the suspension. It is better to choose an appropriate concentration for different emission wavelengths to get stronger emission performance. For example, low concentration is better for green light (shorter wavelength), and high concentration is better for red light (longer wavelength).

4.2.2.4 Cell viability and ROS generation ability

As GOQDs have abundant oxygen-containing functional groups, they may have good potential in biocompatibility. To investigate the photodynamic therapy (PDT) effect of GOQDs, HeLa cells were incubated with the GOQDs for 24 h. As shown in Figure 4.10a, after 24 h incubation, the cell viability slightly decreased to 80% when the concentrations of GOQDs increased to 1 mg/mL, showing that the GOQDs sample has almost no influence on the cells and indicates the biocompatibility of the nanoparticles.

The $^1O_2$ production of GOQDs was measured by above methods with ABDA as an indicator, and the results were shown in Figure 4.10b. After irradiated by the 365 nm light for 10 min, the absorption of ABDA for GOQDs, RB, and PPIX decreased to 75%, 67%, and 91%, respectively. GOQDs show much quicker decline rate than PPIX, but slower than RB. This result demonstrates that GOQDs have better ROS-generating ability.

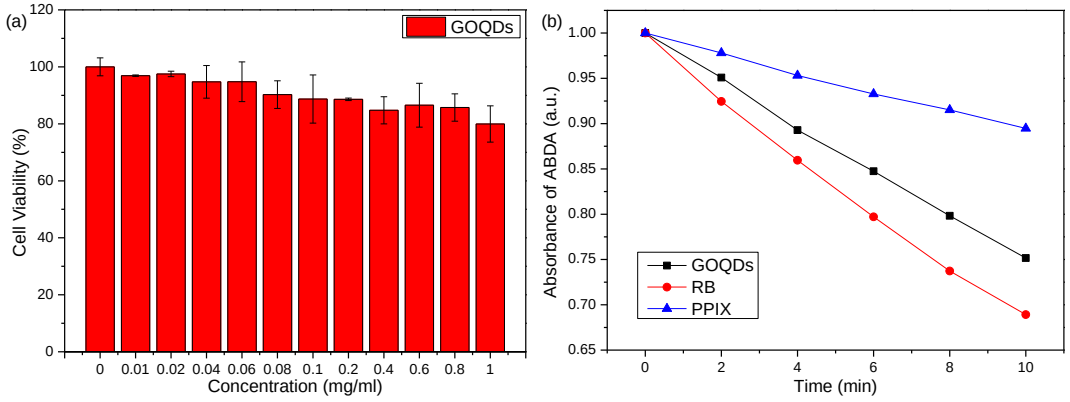

Figure 4.10. (a) Cell viability of HeLa cells incubated with different concentrations of GOQDs; (b) ROS generation of GOQDs detected by ABDA.

4.2.3 Summary

Luminescent graphene-based nanoparticles were synthesized with graphite powder following modified strong acid reaction conditions. The emission wavelengths could be tuned from blue to red. Oxygen-containing functional groups were induced to the surface, and GOQDs have possibilities to be functionalized. The coverage ratio of functional groups and the size could affect the PL properties. The concentration and absorbance would affect the PL intensity. Meanwhile, GOQDs show better ROS-generation ability and do not impose considerable toxicity to the cells.

4.3 Preparation of graphene oxide quantum dots with different reaction temperature and reaction time

4.3.1 Experimental procedures

In this section, the structural changes of GOQDs *via* controlling reaction conditions were investigated. After changing the reaction temperature and reaction time, the nanoparticle size and the content of oxygen-containing functional groups have changed, which affect the PL and ROS generation properties. With the purpose of comparison, six different samples (GOQDs-1, 2, 3, 4, 5 and 6) are arranged, and the details are shown in Table 4-1 with the reaction parameter displayed.

Table 4-1. The reaction condition of six GOQDs samples.

Sample ID	Reaction temperature / ℃	Reaction time / h
GOQDs-1	80	24
GOQDs-2	80	48
GOQDs-3	100	24
GOQDs-4	100	48
GOQDs-5	120	24
GOQDs-6	120	48

4.3.2 Results and analysis

4.3.2.1 Morphology

Figure 4.11 displays AFM images of six series of GOQDs under the same scale. Table 4-2 shows the diameter of the GOQDs obtained by the calculation from the Nanoscope software. Compared with traditional graphene oxide nanoparticles reported to be several micrometers in length, GOQDs prepared following the above method can reach less than 200 nm in length. Both Sulfuric acid and nitric acid provide the effects of "cutting" and oxidation of the carbon matrix. The role of these two kinds of the strong acid will be discussed further in the next section.

When the reaction temperature is 80 ℃, the size of GOQDs is not uniform. Large irregular shaped particles and small round dots could be seen at the same time (Figure 4.11a and 4.11b). For both GOQDs-1 and GOQDs-2, the length of large particles could be up to 160-180 nm, and small one could be 30 nm. The average length is around 70 to 80 nm. The average length of GOQDs-2 is relatively smaller than that of GOQDs-2, however, they are not much different.

When the reaction temperature is 100 ℃ and 120 ℃, it also can be found that the diameter of GOQDs produced from 48 h reaction is smaller than those produced from 24 h treatment. However, the difference in size is quite clear. The size of GOQDs under 48 h treatment is reduced to half, compared with that only with 24 h reaction time.

Time effect could explain this result that longer reaction time could help oxidation process and promote graphite sheet to split. Temperatures over 100 ℃ are more effective than lower temperature in "cutting" the graphite sheet.

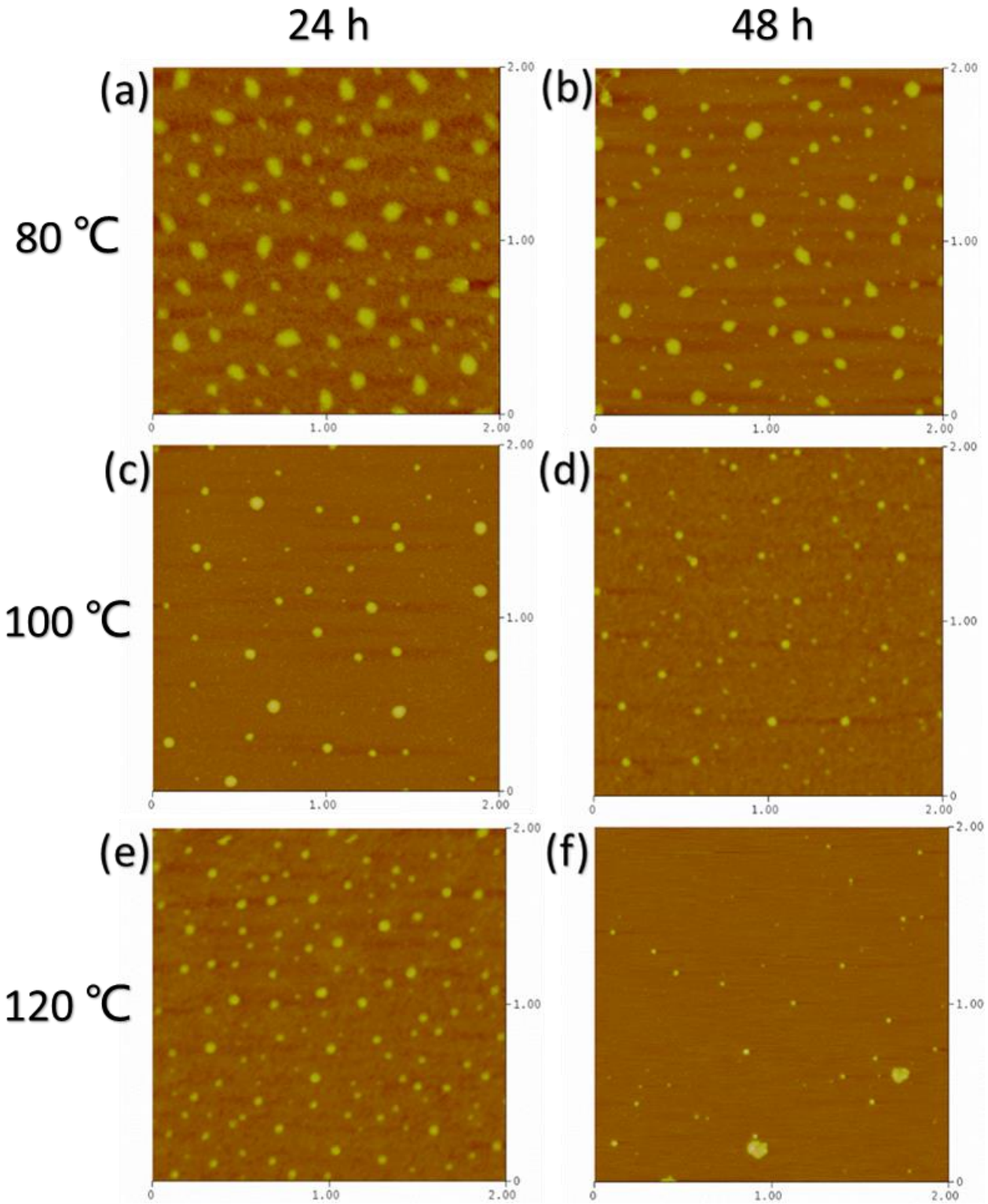

Figure 4.11. AFM images of GOQDs, Scale: 2×2 μm: (a) GOQDs-1 80 ℃ 24 h, (b) GOQDs-2 80 ℃ 48 h, (c) GOQDs-3 100 ℃ 24 h, (d) GOQDs-4 100 ℃ 48 h, (e) GOQDs-5 120 ℃ 24 h and (f) GOQDs-6 120 ℃ 48 h.

Different from the irregular shape of GOQDs produced from 80 ℃, the nanoparticles with 100 ℃ and 120 ℃ display a relatively regular and round shape. They look more like dots or discs, as shown in Figure 4.11c, 4.11d, 4.11e and 4.11f. GOQDs-3 with 100 ℃ and 24 h treatment still have some large particles. The maximum size is around 116.6 nm and average diameter is about 45.9 nm. The GOQDs-4 with 100 ℃ and 48 h reaction have an average diameter of 27.2 nm. The maximum size reduces to 57.1 nm. The GOQDs-5 (120 ℃ and 24 h) are approximately 36.1 nm in diameter. By comparison, GOQDs-5 is relatively larger than GOQDs-4, indicating that reaction time has more effect than reaction temperature on "cutting" the matrix and reducing the size (over 100 ℃).

GOQDs-6 have the highest reaction temperature (120 ℃) and longest reaction time (48 h), so the oxidation effect should be the strongest. The carbon matrix was seriously "destroyed", and its size is the smallest. The maximum diameter is around 39.9 nm, and the mean diameter reaches 15.6 nm.

Table 4-2. The diameter of GOQDs obtained from AFM images. Unit: nm

	24 h			48 h		
	mean	standard deviation	maximum	mean	standard deviation	maximum
80 ℃	78.5	38.0	177	72.8	37.0	165
100 ℃	45.9	18.7	116.6	27.2	14.1	57.1
120 ℃	36.1	17.1	69.0	15.6	10.0	39.9

4.3.2.2 Structure

The FTIR spectra displayed in Figure 4.12 reveal that all GOQDS samples possessed abundant functional groups including O-H (3400 cm^{-1}), COOH (1710 cm^{-1}), C-O-C (1242 cm^{-1}) and C-O (1090 cm^{-1}). Besides, stretching vibrations of C=C (1588 cm^{-1}), C-N (1420 cm^{-1}) and C-H (871 cm^{-1}) bonds were seen in each sample. However, the

difference between each sample is not easy to distinguish in the FTIR spectra. Therefore, XPS was used to further analyze the structural changes in detail.

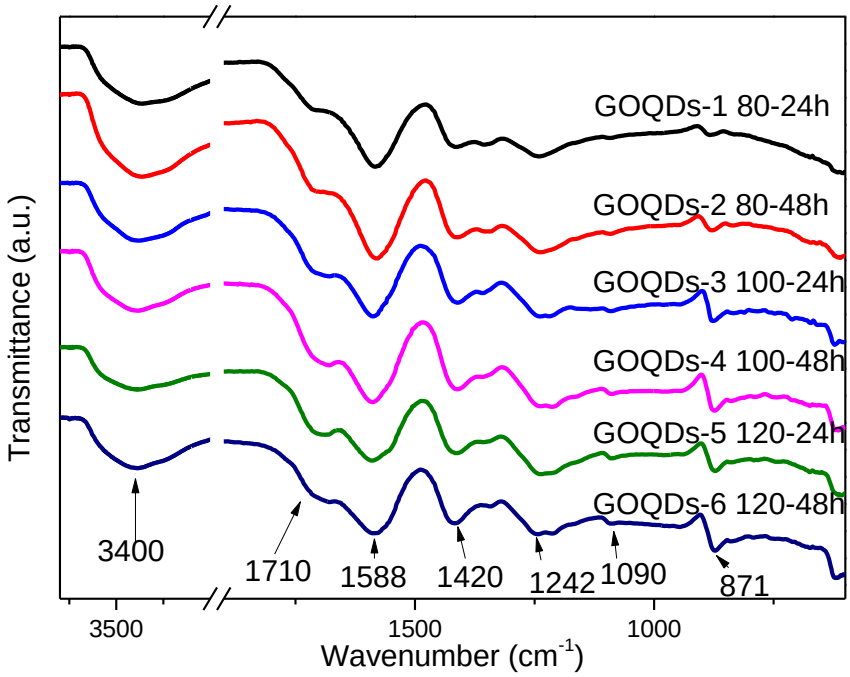

Figure 4.12. FTIR spectra of the GOQDs samples.

High-resolution scans of C1s of six GOQDs samples have been curve-fitted, and the results are shown in Figure 4.13. All GOQDs spectra consist of peaks, including C-C/C=C (285 eV), C-N (285.6 eV), C-O (286.6 eV), C=O (288.2 eV) and O-C=O (289.0 eV). The C-C/C=C bonds correspond to sp^2 or sp^3 carbons, indicating that the main matrix is still a carbon-conjugated system. The C-N bonds mean the nitrogen element was introduced to the conjugation system or replaced the carbon element during the oxidation process. It could be considered that nitrogen element comes from the effect of high concentration nitric acid. The C-O bond may originate from epoxy, basal plane phenol or edge phenol. The C=O and O-C=O reveal the presence of the aldehyde, ketone and carboxyl groups.

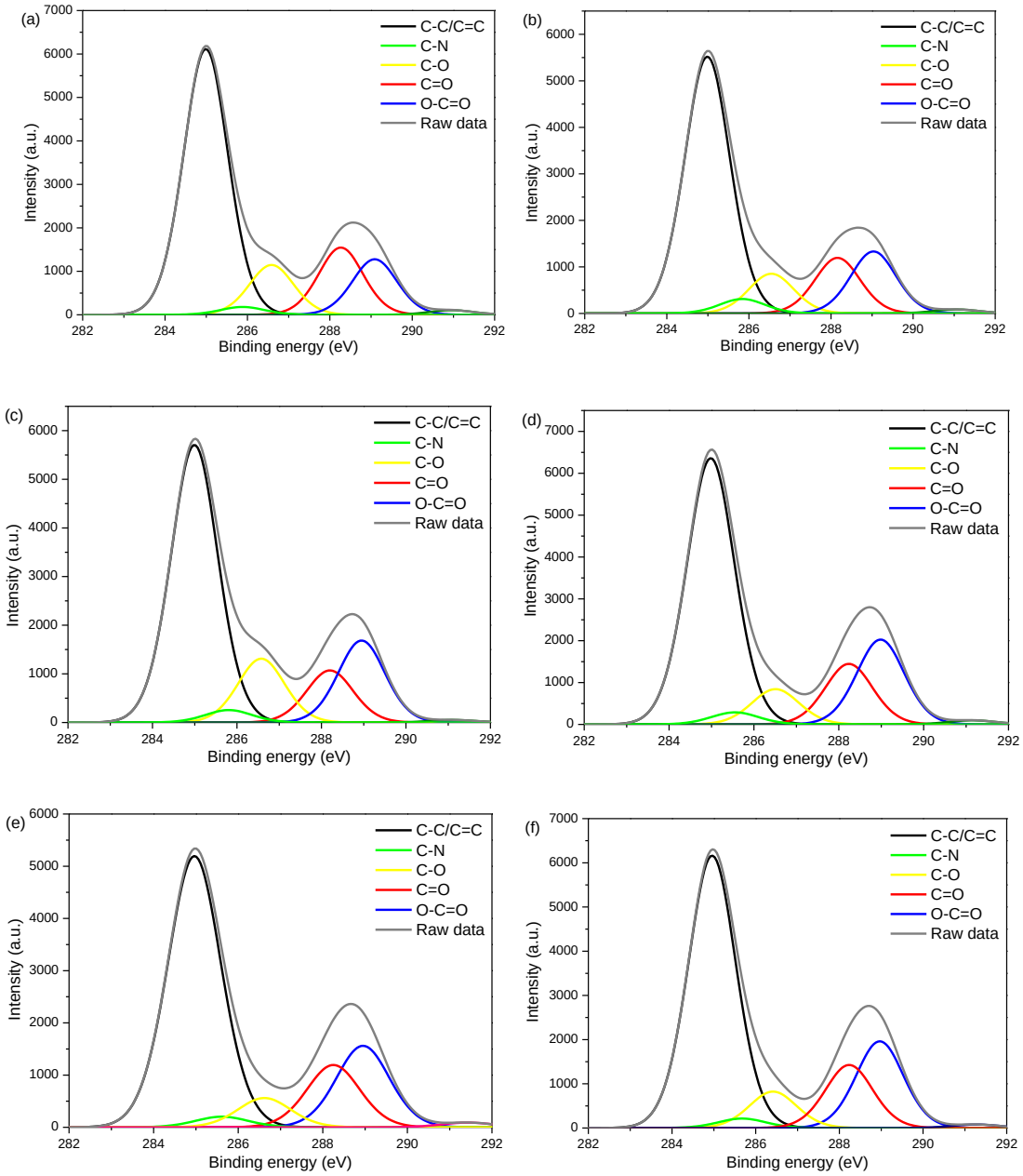

Figure 4.13. (a) - (f) High-resolution XPS C1s spectra of the GOQDs-1 to GOQDs-6, respectively.

The evolution of carbon-oxygen functional groups during the oxidation process is examined by analyzing the XPS spectra. The trend and accurate value are shown in Figure 4.14 and Table 4-3.

1. C-O bond. GOQDs-3 (100 ℃) have 12.8% content of C-O bond, which is higher than that of GOQDs-1 (80 ℃), probably corresponding to the reason of higher temperature. However, GOQDs-5 produced from the highest temperature (120 ℃)

just have 6.19% content of C-O, which is half that of GOQDs-3. For samples 2, 4 and 6 under 48 h treatment, the C-O bond has higher content when the temperature is 80 ℃. With increasing temperature, the content decreases.

2. O-C=O structure. With increasing reaction time and temperature, the COOH bond content becomes higher and reaches the highest in GOQDs-4 (100 ℃ 48 h). When the temperature is 120 ℃, the content starts to reduce. 48 h also decreases the content.

3. C=O bonds. With increasing reaction time and temperature, the content of C=O bonds gradually reduces from 15.1% in GOQDs-1 to 11.1% in GOQDs-3. However, the value slightly increases from 12.6% to 13.4% in sample 4, 5 and 6.

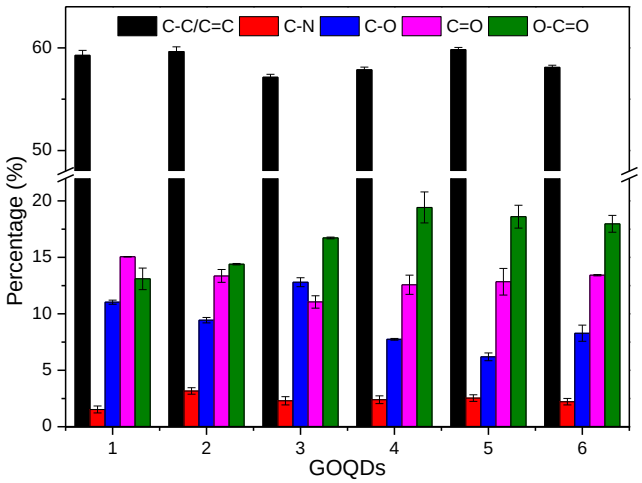

Figure 4.14. Percentage of the peaks deconvoluted from the C1s band.

Table 4-3. XPS data analyses of the C1s spectra of GOQDs samples.

	Carbon bonding composition (%)					
Sample	C-C/C=C	C-N	C-O	C=O	O-C=O	$O1_s/C1_s$
$GOQDs$-1	**59.3**	**1.5**	**11.0**	**15.1**	**13.1**	**45.6%**
$GOQDs$-2	**59.6**	**3.2**	**9.4**	**13.4**	**14.4**	**46.0%**
$GOQDs$-3	**57.1**	**2.3**	**12.8**	**11.1**	**16.7**	**50.0%**
$GOQDs$-4	**57.9**	**2.4**	**7.7**	**12.6**	**19.4**	**53.3%**
$GOQDs$-5	**59.8**	**2.5**	**6.2**	**12.8**	**18.7**	**49.9%**
$GOQDs$-6	**58.1**	**2.2**	**8.3**	**13.4**	**18.0**	**53.2%**

Results mentioned above exhibit that the changes of oxygen-containing functional groups in GOQDs are affected by reaction time and reaction temperature. To reveal this oxidation process mechanism, the formation process of oxygen-containing functional groups will be discussed.

Initially, when the temperature is 80 ℃, C-OH bonds would appear on the graphite sheet edge and the defects in the carbon-conjugated system. Besides, some carbon atoms on the surface would be oxidized to be hydroxyl. In a strong acid environment, the adjacent hydroxyl groups are dehydrated to epoxy groups. Hydroxyl and epoxy group are stable under weaker oxidation treatment (lower temperature and short time). C=O and O-C=O structure would be enrichment when the temperature and time increase, owing to C-O transfer. With the deepening of the degree of oxidation, the content of O-C=O structure on edge further increases until the edge is fully oxidized to be saturation. However, when the temperature is 120 ℃, the carboxyl groups are not stable in such a high oxidation environment. A decrease in the content of O-C=O structure is observed due to partial reduction to the ketone, and this could explain the increase in the content of C=O bonds.

As shown in Figure 4.15, the nitrogen bonding composition is also investigated, and all GOQDs samples consist of two main peaks, including pyridinic-N at 399.8 eV and quaternary-N at 401.1 eV. Quantitative analysis of the atomic ratio of (N1s) / (C1s) and the nitrogen bonding composition are displayed in Figure 4.16 and Table 4-4.

1. When the reaction temperature increases from 80 ℃ to 100 ℃ and 120 ℃, as for the samples with 24 h reaction time, the nitrogen atomic ratio increases from 1.53% in GOQDs-1 to 2.28% in GOQDs-3 and 2.55% in GOQDs-5, however, the ratio of the 48 h sample decreases from 3.16% to 2.39% and 2.24%.

2. In the oxidation process, the nitrogen atoms are introduced to the carbon-conjugated system and connected with carbon atoms. All samples have a higher content of pyridinic-N functionality, indicating that most nitrogen atoms are in the sheet edge or detect area, and less is located in the middle of the matrix.

3. When the reaction time is 24 h, the content of pyridinic-N decreases from 87.23% in GOQDs-1 to 84.83% in GOQDs-3 and 82.32% in GOQDs-5, with increasing temperature from 80 ℃ to 100 ℃ and 120 ℃.

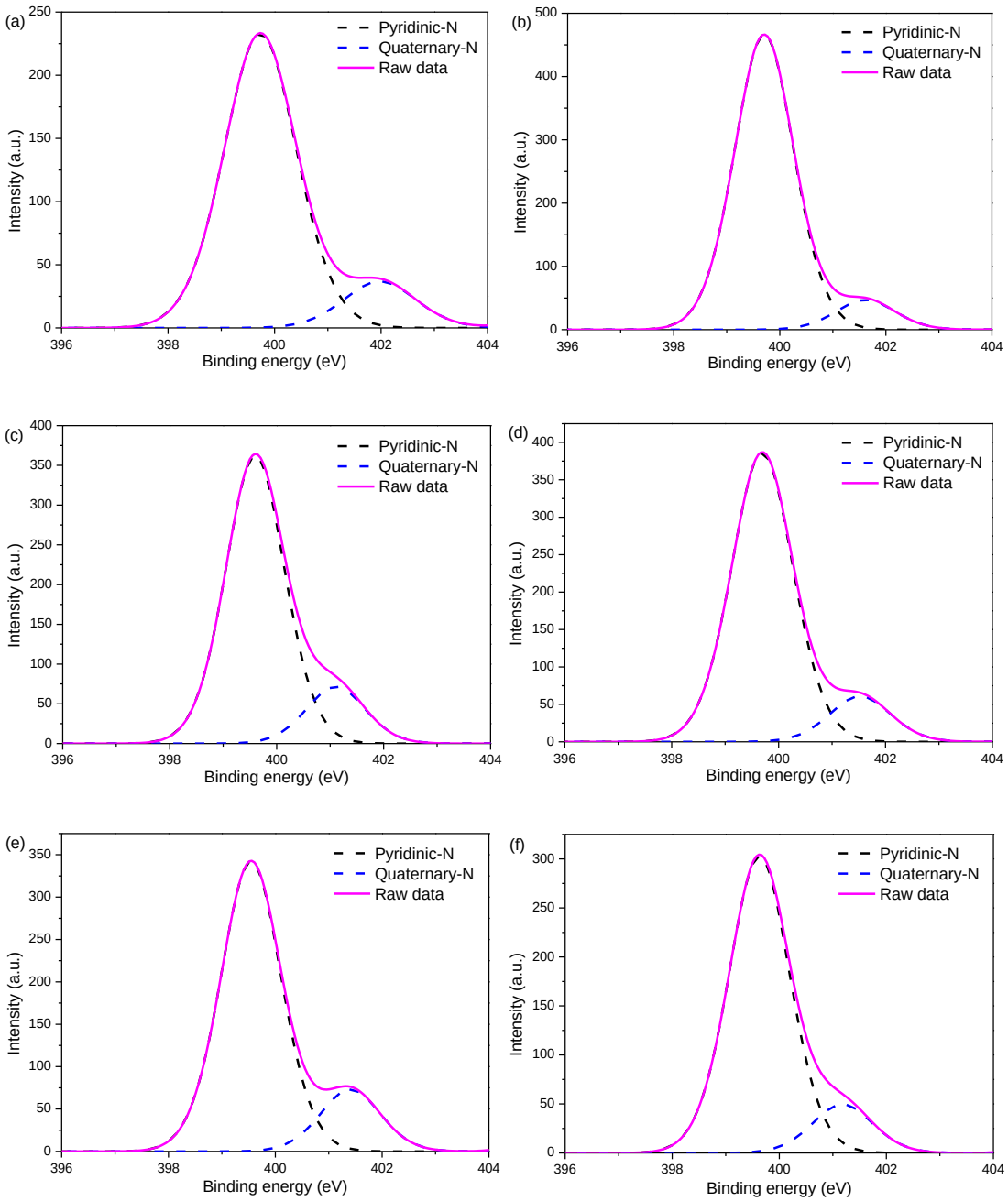

Figure 4.15. (a) - (f) High-resolution XPS N1s spectra of the GOQDs-1 to GOQDs-6, respectively.

The reason for the decrease in the content of pyridinic-N functionality could

correspond to its position. Because it is located at the edge and detects, pyridinic-N is easy to break during the oxidation process. In contrast, quaternary-N is located in the middle and connected to the carbon atoms with three C-N bonds, which is difficult to be cut. Quaternary-N is more stable than pyridinic-N, so the content becomes higher when the reaction time and reaction temperature increase.

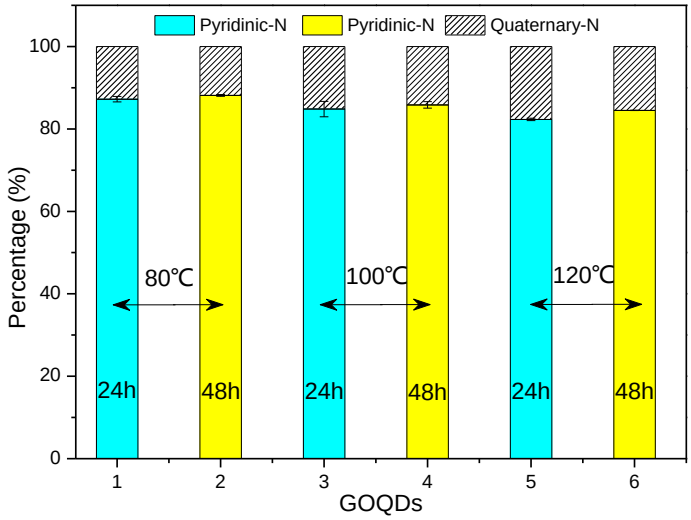

Figure 4.16. Percentage of the peaks deconvoluted from the N1s band.

Table 4-4. XPS data analyses of the N1s spectra of GOQDs samples.

	Nitrogen bonding composition (%)		
Sample	Pyridinic-N	Quaternary-N	$N1_s/C1_s$
$GOQDs$-1	**87.2**	**12.8**	**1.5%**
$GOQDs$-2	**88.1**	**11.9**	**3.2%**
$GOQDs$-3	**84.8**	**15.2**	**2.3%**
$GOQDs$-4	**85.8**	**14.2**	**2.4%**
$GOQDs$-5	**82.3**	**17.7**	**2.6%**
$GOQDs$-6	**84.5**	**15.5**	**2.2%**

4.3.2.3 Optical properties

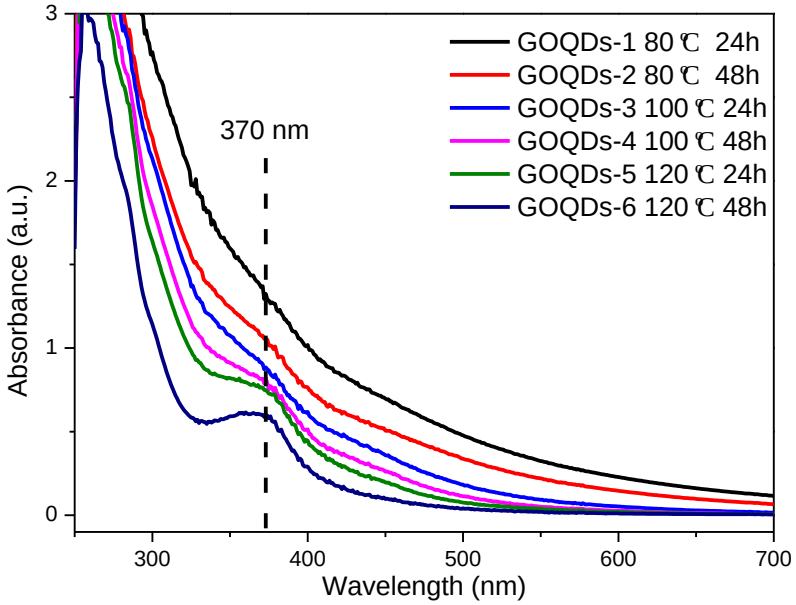

Figure 4.17. UV-Vis spectra of GOQDs-1 to 6 aqueous suspensions, respectively. The concentration is 0.125 mg/mL.

The UV-Vis absorption spectra of the six GOQDs samples with the same concentration, as shown in Figure 4.17, show a downward trend from UV to the visible region. In addition, the absorbance also decreases from the GOQDs-1 to GOQDs-6. According to Beer-Lambert Law which is expressed in terms of attenuation coefficient:

$$A = \varepsilon cL \tag{4-2}$$

A is the absorbance, ε is attenuation coefficient, c is the concentration of the light absorbing substance, and L is the length of solution the light passes through. For an equal concentration of each material and the same cuvette, the higher absorbance means the larger extinction coefficient, which is related to the number of aromatic rings or isolated aromatic domains retained[182]. The results indicate that the GOQDs-1 have more aromatic domains because the degree of oxidation is the lowest, owing to the fact that the reaction time is the shortest, and the reaction temperature is the lowest. With increasing reaction condition, the degree of oxidation becomes higher, more carbon-conjugated system is destroyed, and less aromatic domains are left. The extinction

coefficient decreases gradually, so the absorbance reduces. This result also can be shown by the different colour of the GOQDs aqueous suspension. The higher the extinction coefficient is, the darker the solution is.

Furthermore, the peak at around 370 nm becomes more and more obvious from GOQDs-1 to GOQDs-6. As mentioned above, this peak is attributed to the n-π* orbitals transition of C=O and C-N bonds. From GOQDs-1 to GOQGs-6, the average size of particles reduces. On the particle surface and edge, the aromatic domains become less and more carboxyl groups are obtained. So the ratio of the content of C=O or C-N bonds to the content of aromatic domains gradually increases, which leads to the peak more apparent.

The excitation-dependent PL behaviour of six GOQDs samples under the same concentration is displayed in Figures 4.18-4.20. The excitation wavelength starts at 450 nm, and 10 nm is increased between two neighboring test. The position of the emission peak would shift, and the intensity would increase or decrease. The trend of each sample is not the same.

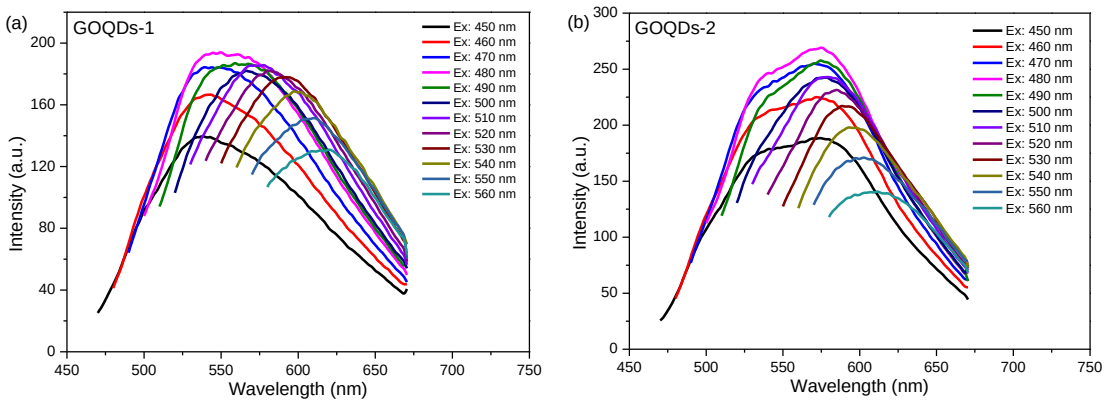

Figure 4.18. The excitation-dependent PL behaviour of (a) GQODs-1 (80 ℃ 24 h) and (b) GOQDs-2 (80 ℃ 48 h).

For the 80 ℃ reaction temperature, GOQDs-1 and GOQDs-2 samples exhibit similar emission spectra (see Figure 4.18). With increasing excitation wavelength from 450 nm to 490 nm, the position of the emission spectrum does not move, and the intensity would increase first. When the samples' suspensions are excited by the 480

nm excitation, the intensity of the peak shows the highest. Afterwards, the intensity decreases gradually. Continuously increasing the excitation wavelength, the position of the emission spectrum would red-shift, and the intensity decreases remarkably.

The highest peak position is not the same for the two sample. GOQDs-1 is at around 550 nm, while GOQDs-2 is at about 575 nm. It also can be found that the shape of these emission peaks are quite wide or the full width at half maximum (FWHM) is quite large.

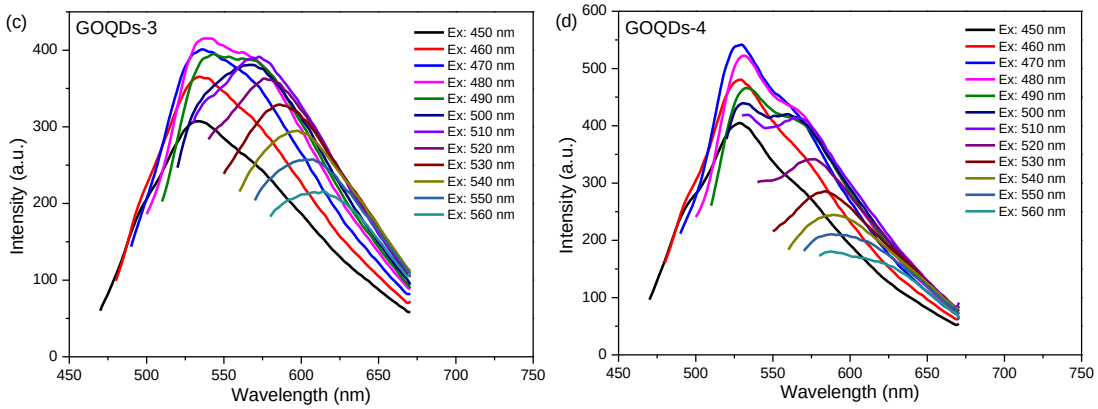

Figure 4.19. The excitation-dependent PL behaviour of (a) GQODs-3 (100 ℃ 24 h) and (b) GOQDs-4 (100 ℃ 48 h).

For the 100 ℃ reaction temperature, the similarity and difference of the PL behaviour between GOQDs-3 and GOQDs-4 can be seen in Figure 4.19. PL emission spectra also display a similar changing trend under the increasing excitation wavelength. Firstly, the spectrum increases the intensity but keeps the position; then it red-shifts to a longer wavelength and reduces the intensity. There are three difference between the two samples. The peak of the maximum emission wavelength blue-shifts from 540 nm for GOQDs-3 to 530 nm for GOQDs-4. The excitation wavelength for the maximum emission spectra reduces from 480 nm for GOQDs-3 to 470 nm for GOQDs-4. Different from the wide peak of the GOQDs-3, the maximum emission spectrum of the GOQDs-4 is quite narrow, and its shoulder peak at 563 nm is also easy to see.

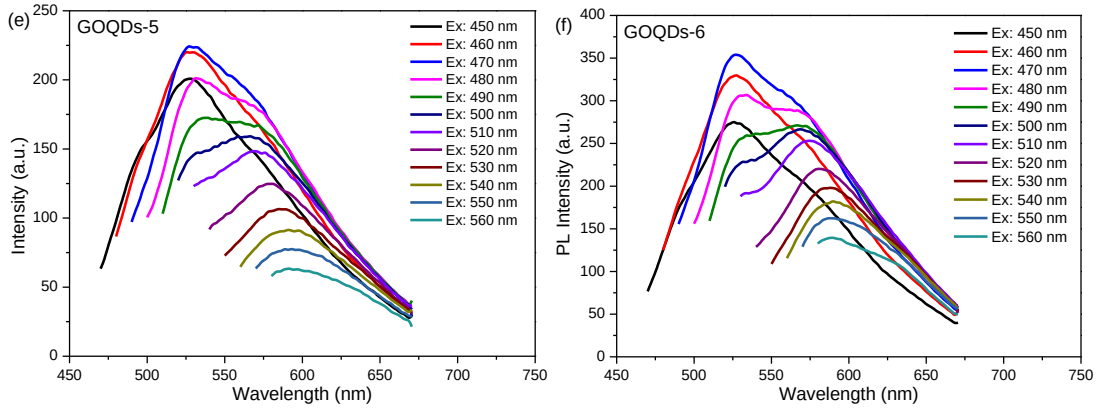

Figure 4.20. The excitation-dependent PL behaviour of (a) GOQDs-5 (120 ℃ 24 h) and (b) GOQDs-6 (120 ℃ 48 h).

For the 120 ℃ reaction temperature, GOQDs-5 and GOQDs-6 display similar PL behaviour and spectral shape to GOQDs-3 (see Figure 4.20). But the excitation wavelength for the maximum emission spectra is 470 nm, and the position of the peak is 530 nm, which are close to the results of GOQDs-4. However, the intensity of the emission spectra is lower than that of the GOQDs with 100 ℃ treatment.

As shown in Figure 4.21, the corresponding PL spectra of six GOQDs samples excited by 470 nm could be well fitted by Gaussian function, indicating that the spectrum consists of two different emission mechanisms. The two Gaussian peaks, labeled as Peak 1 and Peak 2, are located at approximately 530 nm and 565 nm, respectively. The energy gap of PL emission could be calculated by the Equation 4-1.

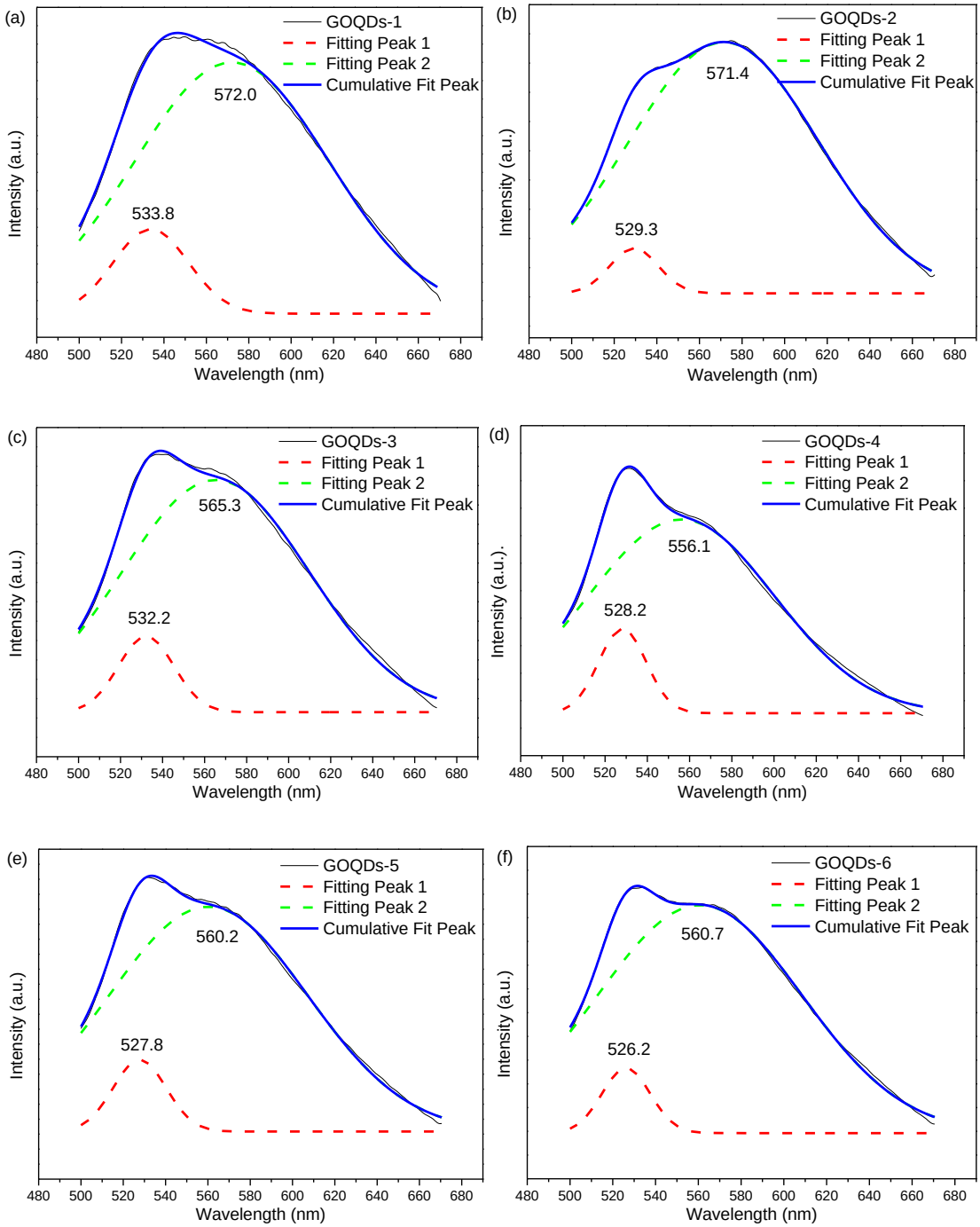

Figure 4.21. PL spectra of GOQDs excited by 470 nm with two deconvoluted Gaussian bands of Peak 1 and Peak 2 emission.

The energy gap, which produces PL emission, and the carbon bonding percentage for GOQDs samples are displayed together in Figure 4.22. Due to the position of Peak 2 blue-shifting from 572.0 nm for GOQDs-1 to 556.1 nm for GOQDs-4, and reversely red-shifting to 560.7 nm for GOQDs-6, the energy gap of PL emission increases from 2.169 eV to the highest 2.231 eV, then decreases to 2.213 eV. As previous described,

the value of COOH group in GOQDs samples is shown in Table 4-5. By analyzing these two values together, it could be found that the trend of the energy gap of Peak 2 PL emission of GOQDs is quite similar to the tendency of the percentage of COOH group in GOQDs samples. Hence, we could make a hypothesis that the evolution of PL emission at around 570 nm is related to the oxygen-containing functional groups on the GOQDs, primarily as a result of the content of the O-C=O structure.

Table 4-5. The percentage of COOH group of six GOQDs samples.

GOQDs Sample	1	2	3	4	5	6
COOH group percentage (%)	13.1	14.4	16.7	19.4	18.7	18.0

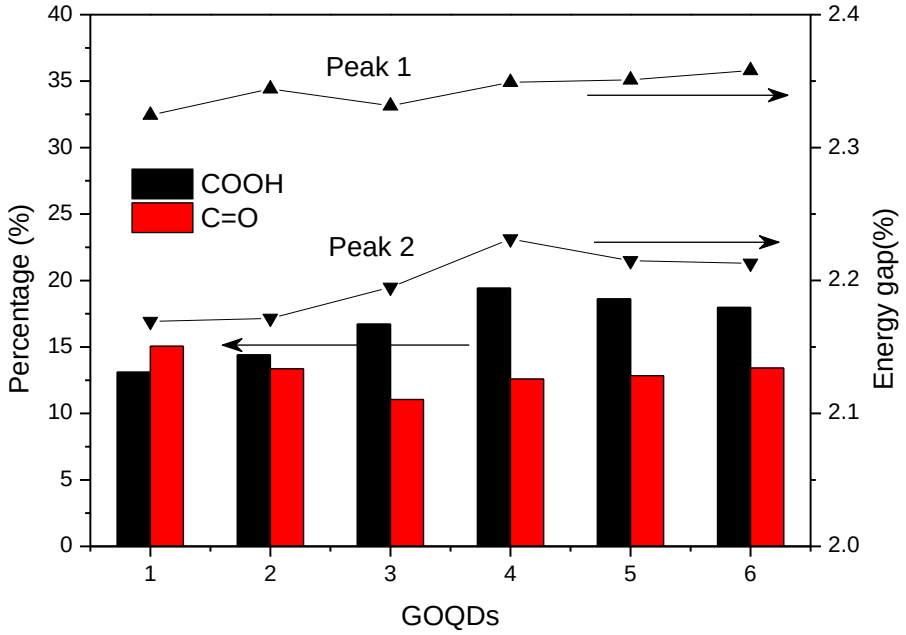

Figure 4.22. Energy gap and content of carbon bonding of six GOQDs samples.

The quantum yield (QY) of GOQDs for 500-600 nm range is calculated following the standard methodology, and the results are different due to the different reaction conditions, as shown in Figures S1 (a) - (f). When the reaction temperature is 100 ℃, the QY of GOQDs-3 and GOQDs-4 is higher than that of other samples with 80 ℃ and 120 ℃. However, it can be found that GOQDs samples with 100 ℃ have comparably lower C=O content. In Figure 4.23, we can notice that the trend of the quantum yield of GOQDs is opposite to the tendency of the percentage of C=O bonding in GOQDs

samples.

The carbonyl group belongs to the electron withdrawing groups, which remove electron density from π-conjugation system and tend to inhibit the fluorescence. Hence, the quantum yield of GOQDs for 530 nm green colour would be related to oxygen-containing functional groups on the GOQDs, mainly as a result of the content of the C=O bonding.

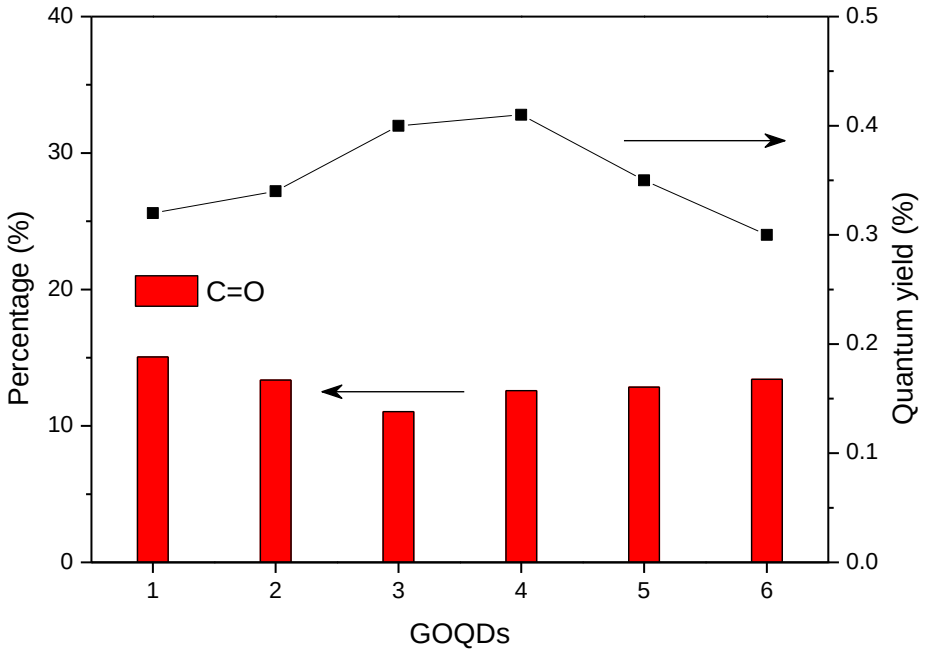

Figure 4.23. QY and percentage of C=O bonding of six GOQDs samples.

4.3.2.4 ROS generation ability

In the first section, ROS generation ability of the GOQDs is measured *via* comparing with PPIX and RB as a reference. GOQDs show much quicker releasing ability of reactive oxygen species than PPIX. In this part, six GOQDs samples are compared under two kinds of visible light irradiation, and different samples display the different results. In Figure 4.24a, all samples quickly reduce the absorbance of ABDA under 30 min blue light irradiation. GOQDs-3, 4 and 5 have almost the same decline rate. In contrast, the absorbance of GOQDs-1 and 2 declines more slowly probably because of the fewer oxygen-containing functional groups owing to the lower reaction temperature.

The ratios of O1s and C1s for these two GOQDs samples are 45.6% and 46.0%, at least 5% less than others. However, GOQDs-6 with 120 ℃ and 48 h reaction condition also has a very slow decline rate, yet its oxidation degree is much higher. It only has better ROS generation ability than GOQDs-1. When using the 530 nm green light, all samples show weaker ROS production ability than blue light. GOQDs-1 reduces the absorbance from 1 to 0.97 after 30 min irradiation, and its rate is fast. Interestingly, this result is opposite to the previous, where GOQDs-1 is the slowest under blue light. GOQDs-2 and 4 perform similar tendency, and a little better than GOQDs-3. The slowest releasing rate of ROS is GOQDs-5 and 6.

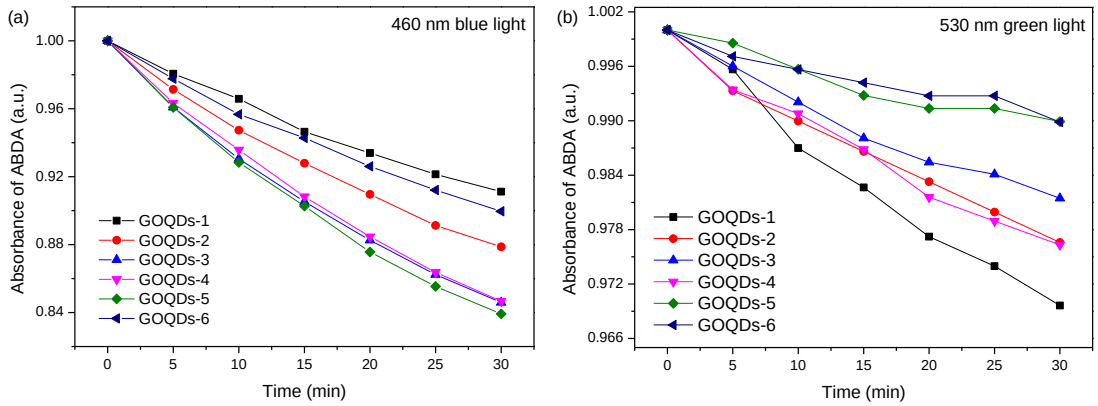

Figure 4.24. ROS generation of six GOQDs samples under (a) 460 nm blue light and (b) 530 nm green light irradiation detected by ABDA.

From the above results, it could be found that ROS generation ability is related to the oxygen-containing functional groups and the wavelength of irradiation light. Usually, higher oxidation degree, owing to the higher reaction temperature and longer reaction time, means more oxygen-containing functional groups on the surface or at the edge, and it could improve the releasing rate of the ROS. The chosen light wavelength for irradiation is another factor for determining the ROS ability. For GOQDs samples, blue light performs much better than green light, which may correspond to the higher absorbance than the former.

4.3.3 Summary

In this section, six GOQDs samples are prepared following the method mentioned in the previous section by changing the reaction condition, including the time and temperature. The structure and the tendency of different carbon and nitrogen bonding are analyzed in detail, primarily focusing on the effect of the reaction condition. PL properties are mainly investigated. The excitation-dependent PL behaviour, emission mechanism of 570 nm yellow light, and quantum yield are analyzed in the relation to the structure changes. ROS generation ability is also discussed. Oxygen-containing functional groups and the light wavelength are considered to be primary factors to affect the ability.

4.4 Preparation of graphene oxide quantum dots under a modified approach with different acid dosage and different reaction time

4.4.1 Experimental procedures

In this section, the graphene oxide quantum dots were prepared under a modified chemical oxidation approach. Different from the previous approach that the sulfuric acid and nitric acid were mixed together at the beginning, this time the reaction was separated into two steps. Firstly, the graphite powder was stirred in the sulfuric acid under 100 ℃ environment for 24 h. The solution remains colourless. The second step was adding the nitric acid, then the flask was suddenly filled with yellow colour, which came from the volatile NO_2 gas. The second step lasted 10 h, 24 h and 48 h, respectively. After this step, three new series of GOQDs were synthesized.

Another three GOQDs samples also followed this modified approach to prepare. However, only 60 mL sulfuric acid and 20 mL nitric acid were added to 0.9 g graphite powder. The acid dosage was two third less than previous samples. The amount of the acid was considered to be a factor affecting the oxidation process and the properties of the GOQDs samples.

To make a comparison, graphite powder was only treated with sulfuric acid at 100 ℃ for 24 h and no nitric acid was used. This batch was set to investigate the different role of these two kinds of acid during the reaction.

The reaction parameter of the modified GOQDs is shown in Table 4-6.

Table 4-6. The reaction parameter of the modified GOQDs.

Sample ID	Step 1		Step 2	
	Graphite powder / g	H_2SO_4 / mL	HNO_3 / mL	Reaction time / h
	100 ℃			
GOQDs-M1	0.9	180	60	10
GOQDs-M2		180	60	24
GOQDs-M3		180	60	48
GOQDs-ML4		60	20	10
GOQDs-ML5		60	20	24
GOQDs-ML6		60	20	48
GO-C7		180		

All the reaction temperature is 100 ℃. M means modified, L means less acid dosage. C means comparison.

GO-C7 is a comparative sample. Graphite powder was stirred in the sulfuric acid under 100 ℃. After 24 h, the solution was light yellow colour, and some precipitated black particles could be noticed. After separation and washing, the deposited powder was analyzed by FTIR. The light yellow solution was neutralized with the base and the salts were removed by the dialysis bags.

4.4.2 Results and analysis

4.4.2.1 Morphology

The AFM images and size information of modified GOQDs with using normal acid dosage are shown in Figure 4.25 and Table 4-7. GOQDs-M1 have many big size dots in the image. At the same time, small size particles also exist. This result can be explained by the reason of the short reaction time. The “cutting” process was only partly executed, especially on the edge. Therefore, the separated parts are very small, even less than 10 nm. The most remaining particles are still very huge in diameter, larger than 120 nm. When extending the reaction time to 24 h, the uniformity of the diameter becomes much better than that of the 10 h samples. The massive particles disappear, and the maximum size in diameter of GOQDs-M2 could reduce to approximately 70 nm. When running 48 h reaction, the diameter further decreases and average size in diameter of GOQDs-M3 could be approximately 11 nm.

The AFM images and size information of modified GOQDs with using less acid dosage are shown in Figure 4.26 and Table 4-8. Even though the acid dosage is just one-third of the normal method, the “cutting” results are quite similar to them. With increasing reaction time, the particle diameter becomes much evener. All three samples’ average size in diameter is slightly bigger than that of the standard acid dosage samples.

The average height of GOQDs-M and GOQDs-ML is between 1-3 nm, which is similar to the GOQDs.

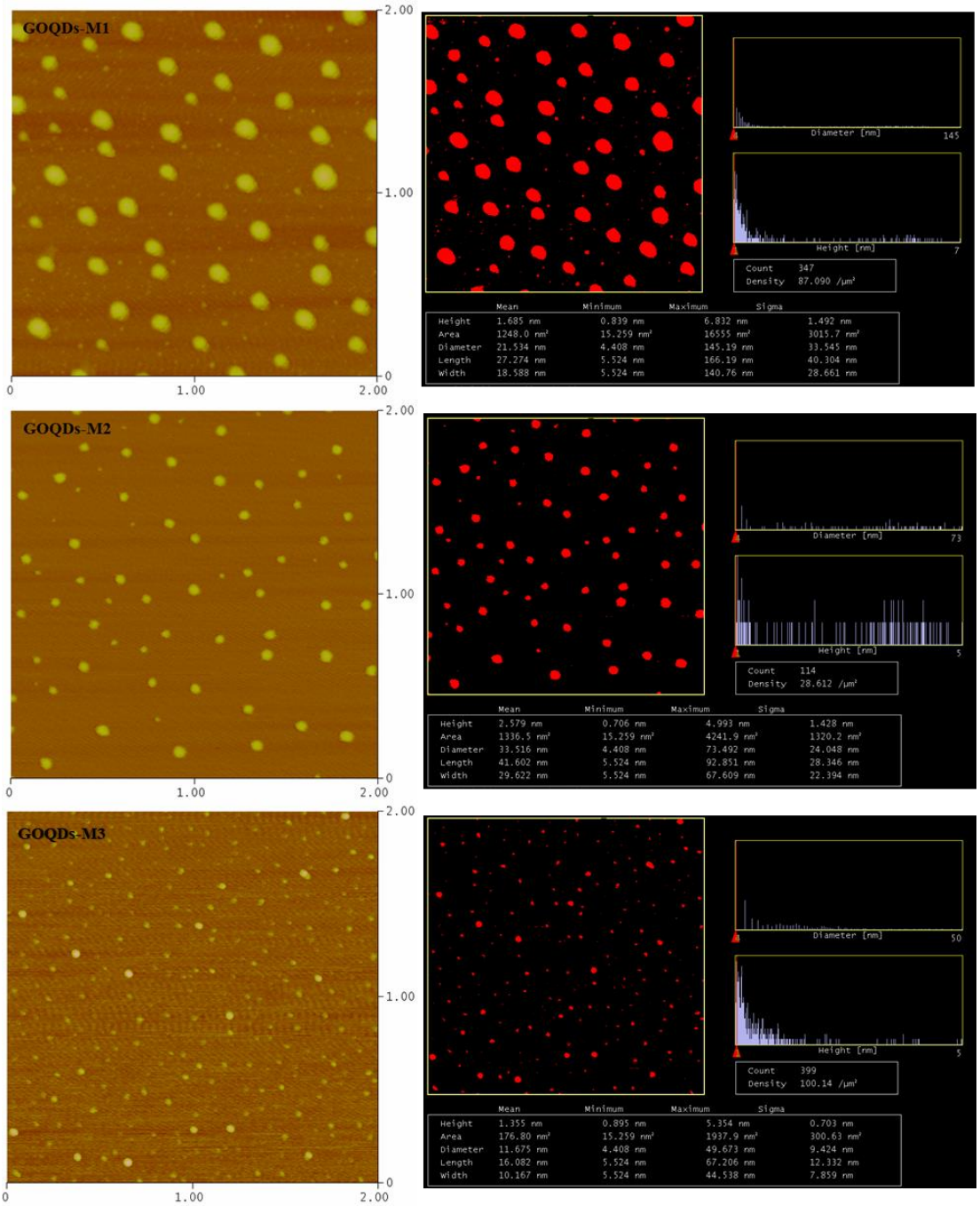

Figure 4.25. The AFM images and size information of GOQDs-M. Scale: 2 µm x 2 µm.

Table 4-7. The diameter of the GOQDs-M. Unit: nm

	mean	standard deviation	maximum
GOQDs-M1	21.5	33.5	145.2
GOQDs-M2	33.5	24.0	73.5
GOQDs-M3	11.7	9.42	49.7

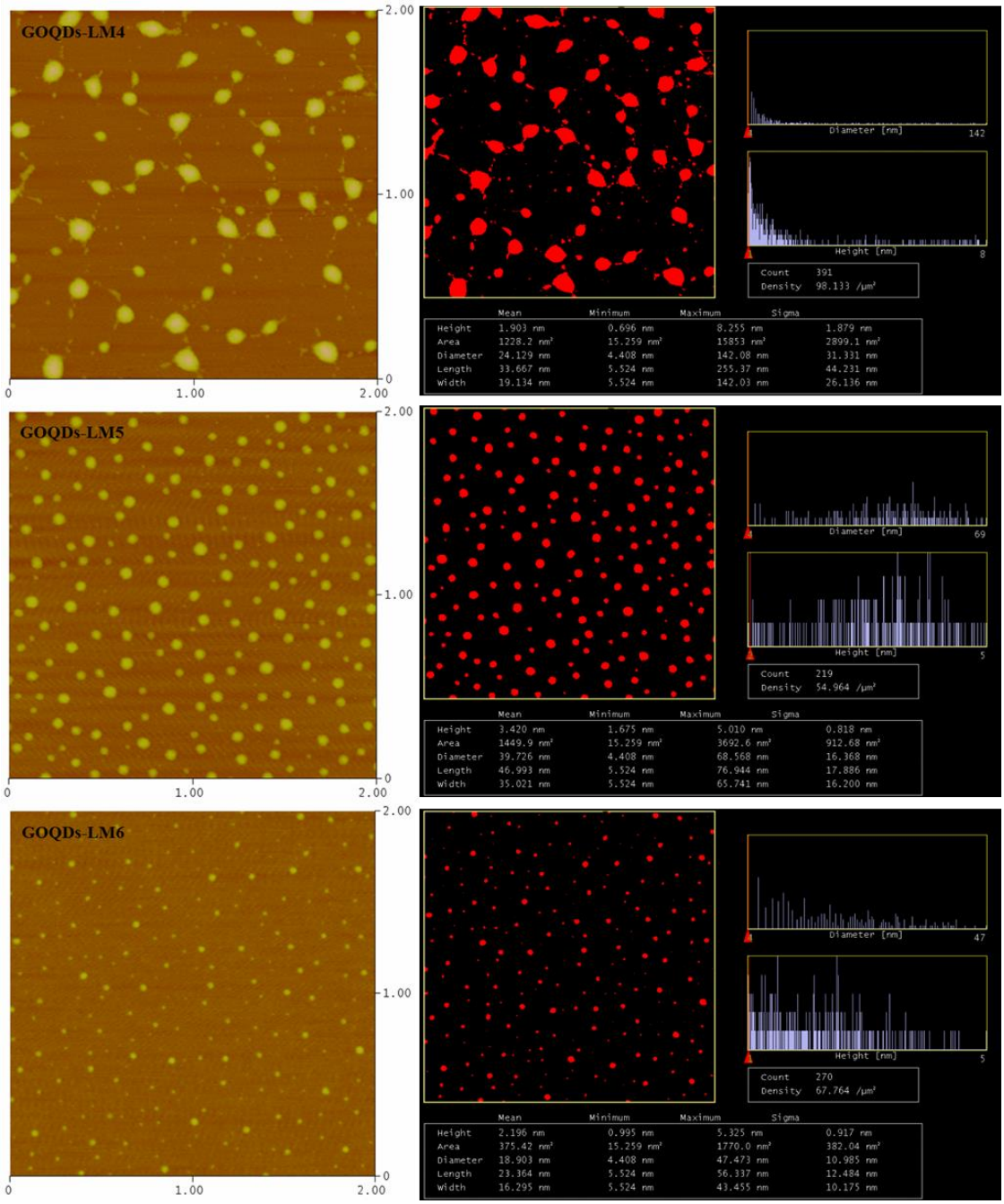

Figure 4.26. The AFM images and size information of GOQDs-ML. Scale: 2 µm x 2 µm.

Table 4-8. The diameter of the GOQDs-ML. Unit: nm

	mean	standard deviation	maximum
GOQDs-ML4	24.1	31.3	142.1
GOQDs-ML5	39.7	16.4	68.6
GOQDs-ML6	18.9	10.9	47.5

Interestingly, not only can the round dots be seen in the image of GO-C7, but also two long strip shape flakes appear, as shown in Figure 4.27. The maximum length is about 308.7 nm, the width is around 65.2 nm, and the height is approximately 1.3 nm. Both of them look like smaller single-layer graphene oxide sheets. These large size sheets do not appear in previous GOQDs samples.

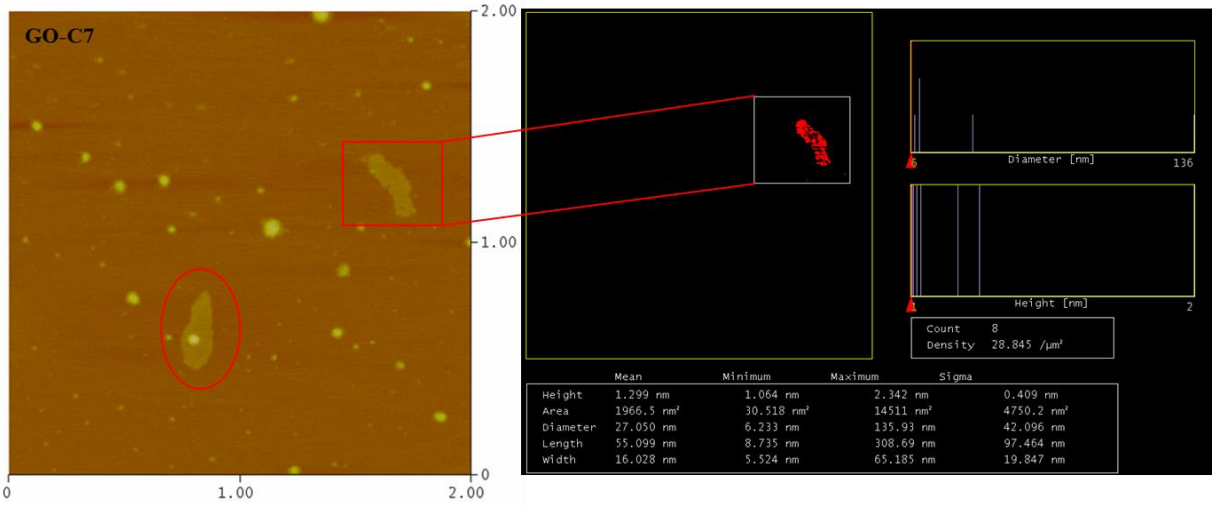

Figure 4.27. The AFM images and size information of GO-C7. Scale: 2 µm x 2µm.

The role of sulfuric acid in the reaction needs to be discussed. The modified Hummers' method[182], which uses sulfuric acid, is the most common approach to prepare graphene oxide. Dimiev *et al.*[168] explained the mechanism of the graphene oxide formation and considered that sulfuric acid would insert into the layers of the graphite and convert graphite into a graphite intercalation compound at the beginning of the whole process. In this work, sulfuric acid has a similar effect. Figure 4.28 shows a simple schematic of the mechanism of H_2SO_4 molecule. Under the high concentration condition, H_2SO_4 was very difficult to be ionized and mainly existed in the form of H_2SO_4 molecular. During the 24 h stirring, the H_2SO_4 molecule or tiny amount of HSO_4^- ions become fully inserted into the space between the layers, and then made the layer spacing larger. In the meantime, unlike the room temperature or 35 ℃ reaction in the modified Hummers method, here the reaction was maintained at 100 ℃. The high

temperature enabled the sulfuric acid to oxidize and cut the graphite sheet, even without the help of other oxidizing agents. The appearance of the smaller size dots could reveal that the place of the graphite sheet to be cut may happen at the edge, which means the oxidation effect was not strong enough to directly split in the middle. Due to the larger space of the intercalated layers, the Van der Waals forces among them became weaker. Both the heat from the high temperature in the reaction and the sonication after washing were easy to separate the graphite oxide layers.

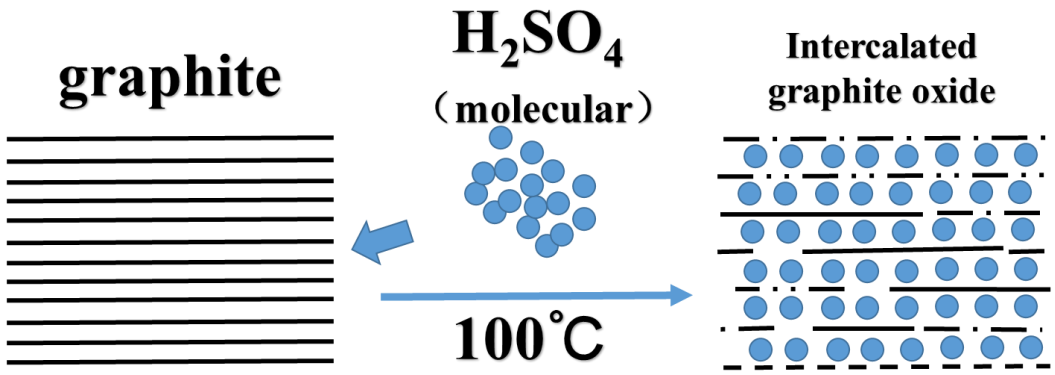

Figure 4.28. The schematic of the conversion from graphite to intercalated graphite oxide.

4.4.2.2 Structure

The FTIR spectra displayed in Figure 4.29 suggest that all GOQDs-M and GOQDs-ML samples have similar abundant functional groups including O-H (3400 cm^{-1}), COOH (~1710 cm^{-1}), C=O (~1679 cm^{-1}), C-O-C (~1240 cm^{-1}) and C-O (1090 cm^{-1}), even though GOQDs-ML have a less acid dosage. Besides, stretching vibrations of C=C (1585 cm^{-1}), C-N (1415 cm^{-1}) and C-H (875 cm^{-1}) bonds can be found in each sample. XPS would assist us to further evaluate the structure difference in detail.

However, GO-C7 has a different FTIR spectrum, as shown in Figure 4.29b. The absorption band at 1628 cm^{-1} could be assigned to the C=C stretch, and the peak at 1040 cm^{-1} is attributed to a C-O stretching. The stretching vibrations of C-OH at ~3400 cm^{-1}

could be observed. Contributions in the 1120 – 1160 cm^{-1} region may arise from C-O or C-OH functional groups. No obvious carbonyl or carboxyl groups are found in the spectrum, which may be due to the low content and could be investigated by XPS later.

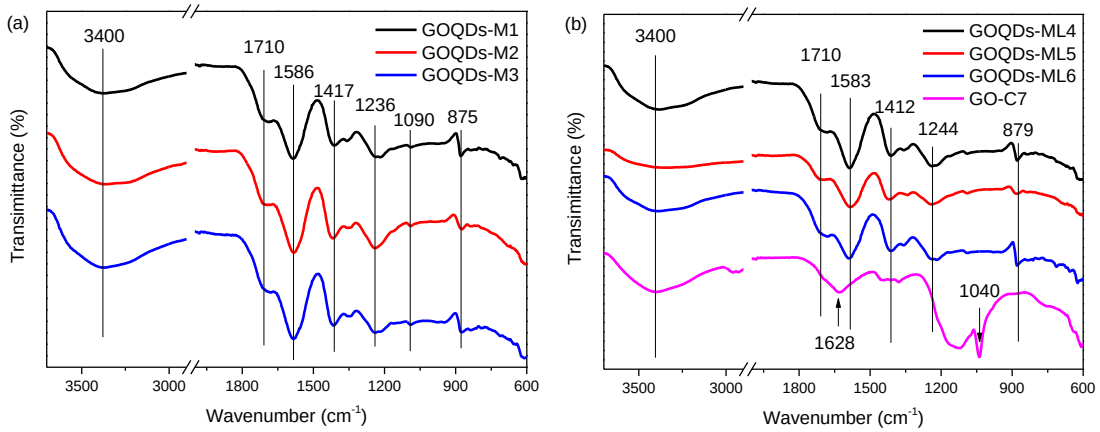

Figure 4.29. FTIR spectra of the GOQDs-M (a), GOQDs-ML and GO-C (b).

The C1s XPS spectra of the GOQDs-M and the carbon bonding composition are displayed in Figure 4.30 and Table 4-9. GOQDs-M1 only has 10 h reaction time with nitric acid, but they process a very high degree of oxidation. There are almost 16% content of C=O bond and 19% content of O-C=O structure in GOQDs-M1, which are higher than those of all the previous GOQDs samples. When the reaction time is extended to 24 h, the content of C-C / C=C bond suddenly increases by 5%, and the content of C=O bond decreases to about 10%. The C-O and O-C=O maintain almost the same proportion. When the reaction time is 48 h, the GOQDs-M3 has a similar content of the C-C / C=C, C-N and C-O bond to GOQDs-M2. However, the content of the C=O bond rises to 14.5%, and O-C=O structure drops from 19% to 16%.

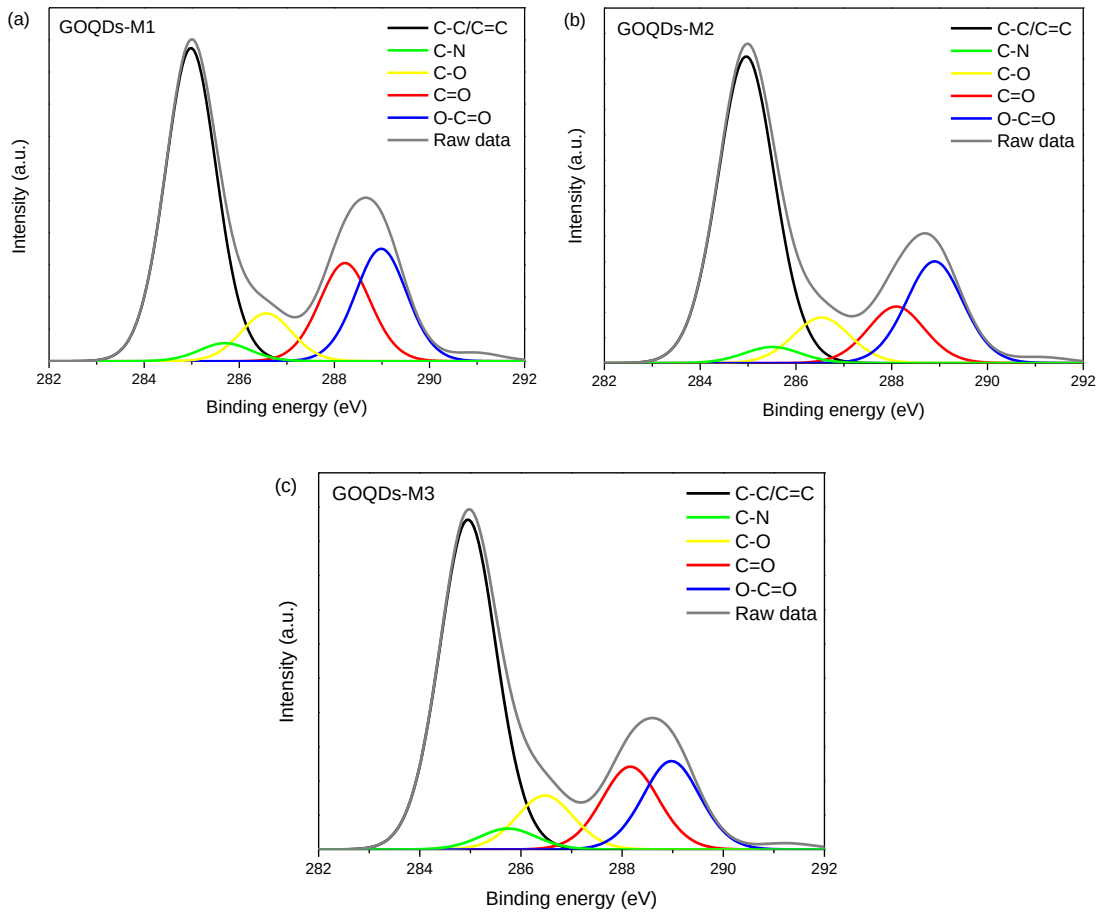

Figure 4.30. The C1s XPS spectrum of the GOQDs-M.

Table 4-9. The carbon bonding composition of the GOQDs-M

	Carbon bonding composition （%）					
Sample	C-C/C=C	C-N	C-O	C=O	O-C=O	O1s/C1s
GOQDs-M1	53.6	3.4	7.8	15.9	19.3	57.4%
GOQDs-M2	58.2	3.2	8.6	10.8	19.4	48.0%
GOQDs-M3	57.2	3.9	8.4	14.5	16.0	47.6%

The C1s XPS spectra of the GOQDs-ML and the comparable sample GO-C7 are shown in Figure 4.31. The carbon bonding composition is in Table 4-10. It could be noted that the GO-C7 without adding nitric acid has a less content of oxygen-containing functional groups, such as about 10% C-O bond, 5% C=O bond and 3% O-C=O structure. The C-C / C=C retains 81%, revealing that the main structure of GO-C7 is

still carbon skeleton. The above information is consistent with the FTIR result and demonstrates that the oxidation effect of the 100 ℃ concentrated sulfuric acid on graphite powder is not strong enough. Some hydroxyl or epoxy groups could be introduced to the graphite sheets. However, the content of the carbonyl or carboxyl groups is very low. Although the reaction time is 24 h, the transition from the hydroxyl or epoxy groups to the carbonyl or carboxyl groups does not take place.

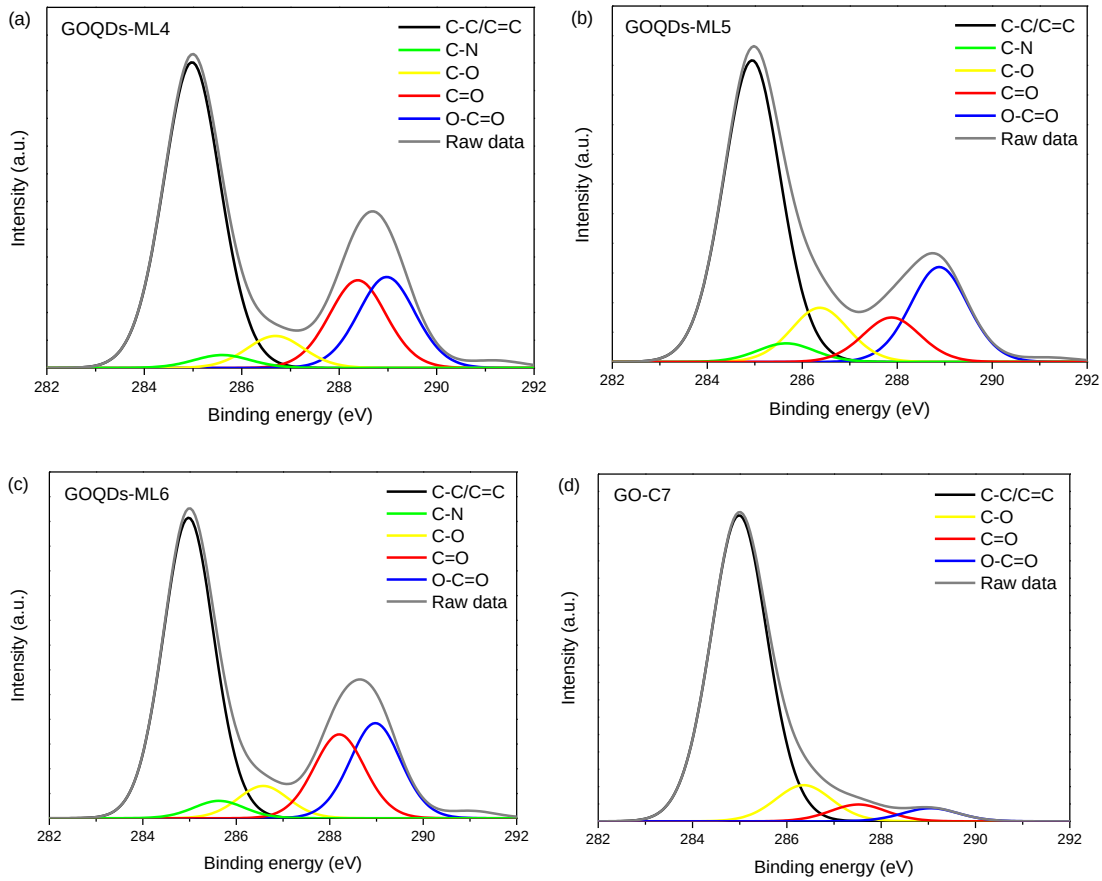

Figure 4.31. The C1s XPS spectrum of GOQDs-ML (a)-(c) and GO-C7 (d).

Table 4-10. The carbon bonding composition of GOQDs-ML and GO-C7.

	Carbon bonding composition （%）					
Sample	C-C/C=C	C-N	C-O	C=O	O-C=O	O1s/C1s
GOQDs-ML4	57.9	2.1	6.4	17.2	15.7	55.5%
GOQDs-ML5	59.1	3.7	10.6	7.3	19.3	46.0%
GOQDs-ML6	56.9	3.3	5.9	16.0	17.9	54.4%
GO-C7	81.1	0	10.4	5.1	3.4	23.1%

Compared with the fewer oxygen-containing functional groups of GO-C7, nitric acid introduces abundant oxygen-containing functional groups to the GOQDs-ML samples, even though the nitric acid dosage was less than the previous one in the experiment. Just after the 10 h reaction, GOQDs-ML4 possesses 17% C=O bond and 16% O-C=O, which are slightly less than those of the GOQDs-M1 (10 h). But they are still 3.4 and 4.7 times of those of the GO-C7. Meanwhile, the appearance of these oxygen-containing functional groups, the content of the carbon skeleton of GOQDs-M samples drops to about 58%. There is a similar phenomenon between GOQDs-M and GOQDs-ML samples, that is, the ratio of the C=O bond of the GOQDs-ML sample declines after the 24 h reaction, but shows the increment after the 48 h reaction. In the meantime, the percent of the C-C / C=C and O-C=O structure displays opposite changing tendency.

From above two batches of the GOQDs-M samples, some conclusion can be obtained as follows:

1. The oxidation effect of sulfuric acid on the graphite was not strong enough for "cutting" the carbon matrix. The main carbon skeleton remained, and a small fraction of oxygen-containing functional groups (mostly are hydroxyl and epoxy) appear on the graphite sheet.

2. The additional nitric acid made the oxidation process remarkably occur. A large number of oxygen-containing functional groups emerged, even though only using 1/3 nitric acid dosage.

3. The changing tendency of the percentage of the C=O bond performs "V" shape with the reaction time.

4.4.2.3 Optical properties

Firstly, the UV-Vis spectra of the GOQDs-M, GOQDs-ML, and GO-C7 aqueous suspensions are shown in Figure 4.32. It is easy to distinguish that the GO-C7 from other GOQDs samples. The curve of the GO-C7 has a peak at 255 nm, which belongs to π to π* transition, then smoothly declines. While others drop obviously in the UV region. The absorbance of the GO-C7 is much lower than GOQDs-M and GOQDs-ML in the region from 250 nm to 450 nm, but higher after 500 nm. These differences may result from the relative complete carbon skeleton of the GO-C7, and less oxygen-containing functional groups also lead to no noticeable shoulder peak. On the contrary, abundant oxygen-containing functional groups absorb lights intensely in the UV region and still have a shoulder peak near 370 nm, which is assigned to the transition of n to π*. For each batch of samples, a longer reaction time makes the absorbance lower.

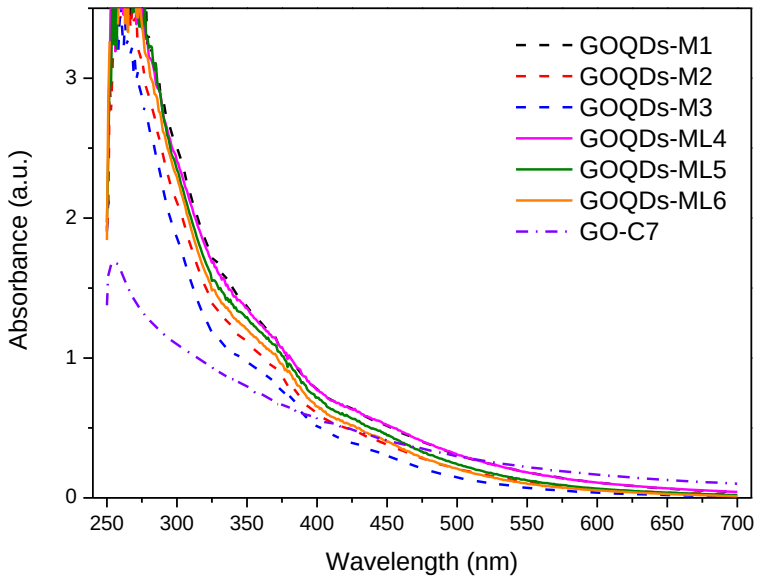

Figure 4.32. UV-Vis spectra of GOQDs-M (1-3), ML (4-6) and GO-C7 aqueous suspension, respectively. The concentration is 0.125 mg/mL.

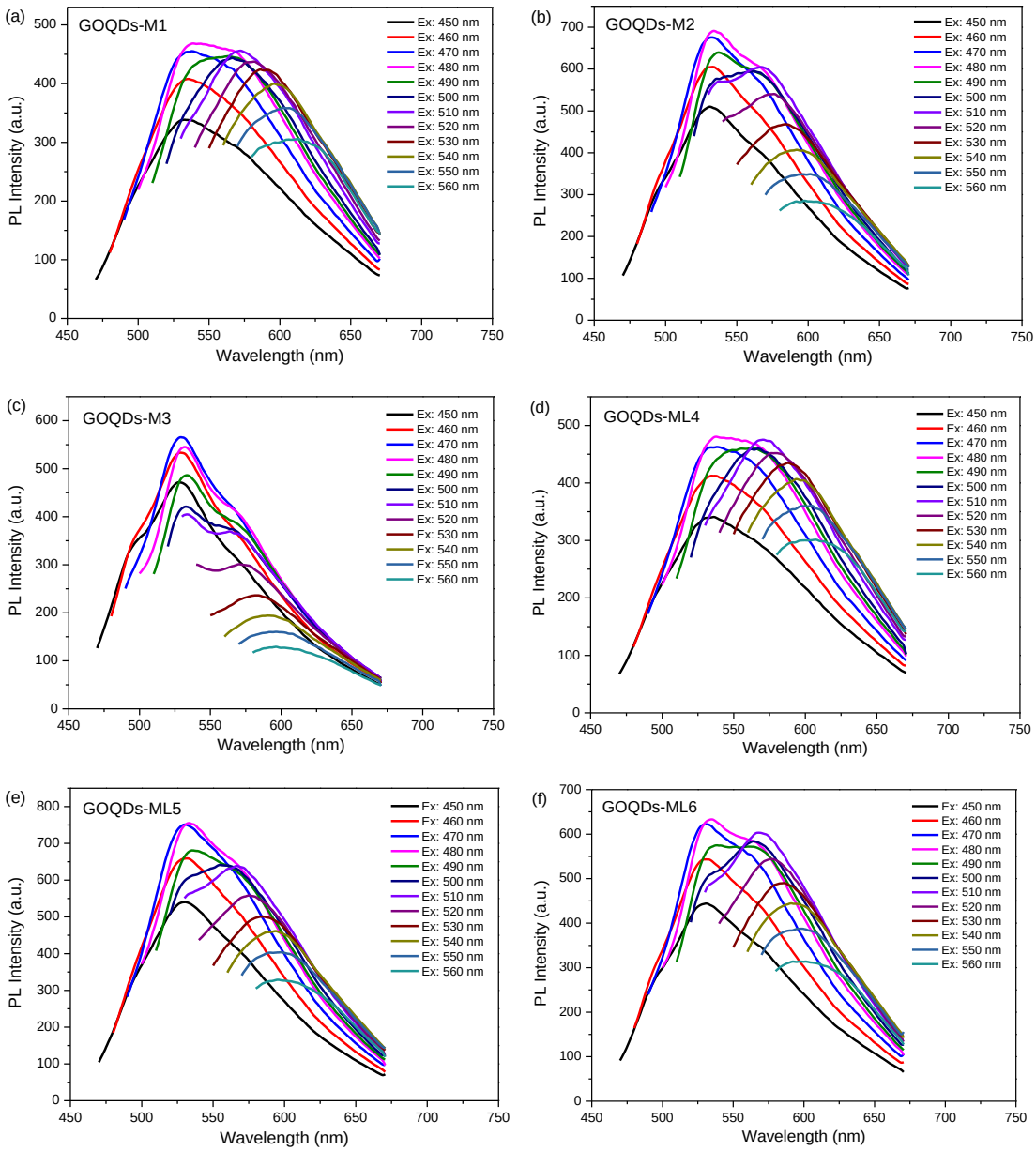

Figure 4.33. The excitation-dependent PL behaviour of GOQDs-M (a) M1-10h, (b) M2-24h and (c) M3-48h; GOQDs-ML (d) ML4-10h, (e) ML5-24h and (f) ML6-48h.

The excitation-dependent PL behaviour of GOQDs-M and GOQDs-ML samples under the same concentration is displayed in Figure 4.33. For all six samples, the peaks' positions of the emission spectra are almost fixed, and the PL intensity rises when the excitation wavelength is tuning from 450 nm to 470 nm. The emission spectrum from 480 nm excitation starts red-shifting and becomes wide, which could be possible to deconvolute into two peaks. For each batch, the emission spectra from the 10 h reaction

sample look like broader, which may correspond to the much difference in the particle size. Following the longer reaction time, the particle size becomes close, so the FWHM of the emission spectra gradually decreases.

The PL intensity of the emission spectra on different wavelength was paid attention. Like in previous GOQDs samples, the maximum PL intensity for all the emission spectra of GOQDs-M appears at near 530 nm when the excitation wavelength is 480 nm. By comparing this value between different samples, one could find the various emission effects at a particular region. In each batch, GOQDs-M2 and GOQDs-ML4, namely both with 24 h reaction time, could emit the strongest PL intensity at around 530 nm (green light).

Meanwhile, some samples could show very close PL intensities in other emission regions. For example, GOQDs-M1 and GOQDs-ML4 possess very close PL intensities at about 530 nm and 575 nm when the excitation wavelengths are 480 nm and 510 nm, respectively. Hence, we also could estimate the different emission effects on different colours, such as green, yellow and orange, by comparing the PL intensity at the same excitation wavelength.

In Figure 4.34a and 4.34b, 470, 510 and 560 nm excitation wavelengths are chosen, which correspond to emission of green, yellow and orange colours, respectively and then the PL intensities for these three colours are compared, with the following features noted:

1. For the green colour (470 nm excitation), the PL intensity emitted from GOQDs-M rises first and then drops, and as a result, the highest value appears in 24 h reaction samples. GOQDs-ML samples show a similar phenomenon, but the PL intensity is relatively higher than that of GOQDs-M.

2. For the yellow colour (510 nm excitation), GOQDs-M samples still show the same

changing tendency as for the green colour. GOQDs-M1 (10 h reaction) has almost the same intensity as for its green colour emission. When the reaction time is extended, the PL intensity difference between green colour and yellow colour starts to expand. GOQDs-M3 (48 h reaction) shows obvious reduction in the PL intensity of the yellow colour emission. On the contrary, GOQDs-ML6 (48 h reaction) keeps a similar PL intensity to that of GQODs-ML5 (24 h reaction).

3. For the orange colour (560 nm excitation), GOQDs-M samples gradually reduce the PL intensity when the reaction time increases from 10 h (M1) to 48 h (M3). However, the PL intensity of three GOQDs-ML samples are almost the same.

4. If making the horizontal comparison (the same reaction time), it will find that GOQDs-ML samples emit a stronger PL intensity than that of GOQDs-M.

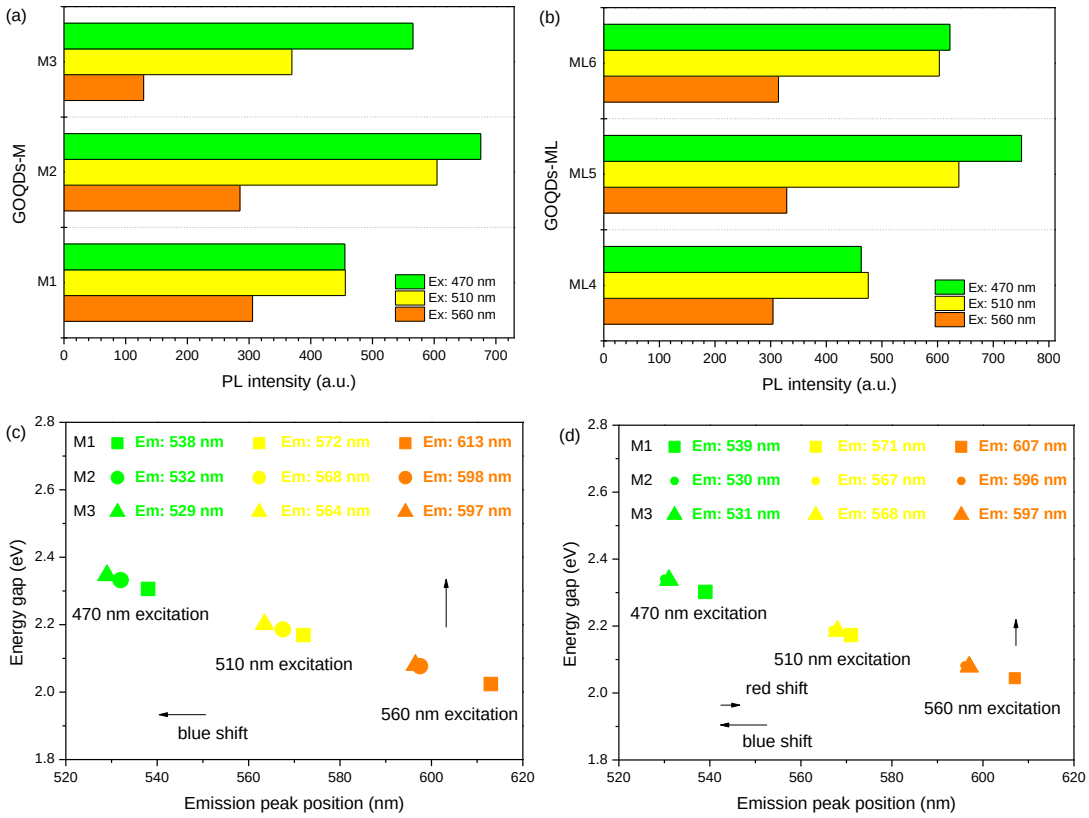

Figure 4.34. The PL emission (green, yellow and orange) intensity under a certain excitation (a) GOQDs-M and (b) GOQDs-ML and the energy gap and PL emission (green, yellow and orange) peak position under a certain excitation (c) GOQDs-M (d) GOQDs-ML.

The three colour emission peak positions under the same excitation wavelength are studied and displayed in Figure 4.34c and 4.34d. For GOQDs-M samples, when using a fixed excitation wavelength, all the three colour emission peak positions show blue-shift for the M1 (10 h) to M3 (48 h). For GOQDs-ML samples, the emission peak position also blue-shifts for the ML4 (10 h) to ML5 (24 h). But the peak position of the ML6 (48 h) is almost the same or even slightly red-shifts. As we know, the emission peak position is related to the energy gap between the excited state (S_1) and the ground state (S_0). When the peak position performs blue shift, it means that the energy gap becomes larger. According to the above results, a longer reaction time gradually makes the peak position blue-shift, that is, the energy gap becomes wider.

Like in previous GOQDs samples, the emission spectrum of the GOQDs-M and GOQDs-ML under the 480 nm excitation also could be deconvoluted into two peaks, as shown in Figure 4.35. For GOQDs-M samples, both peak 1 and peak 2 positions shift to a short wavelength. For GOQDs-ML samples, the peak positions start to blue-shift, and then red-shift. Two peaks belong to green and orange colour ranges, respectively. The results of the peak position changes are consistent with the above. It could be noted in Figure 4.35h, the change of trend on the energy gap of the peak 2 (around 560 nm region) and the O-C=O structure content of the GOQDs-ML sample are quite close. According to the hypothesis mentioned in the previous section, the oxygen-containing functional groups on the GOQDs, especially the percentage of the O-C=O structure, would change the energy gap between the excited state and the ground state, namely shifting the peak position of PL emission at around 570 nm.

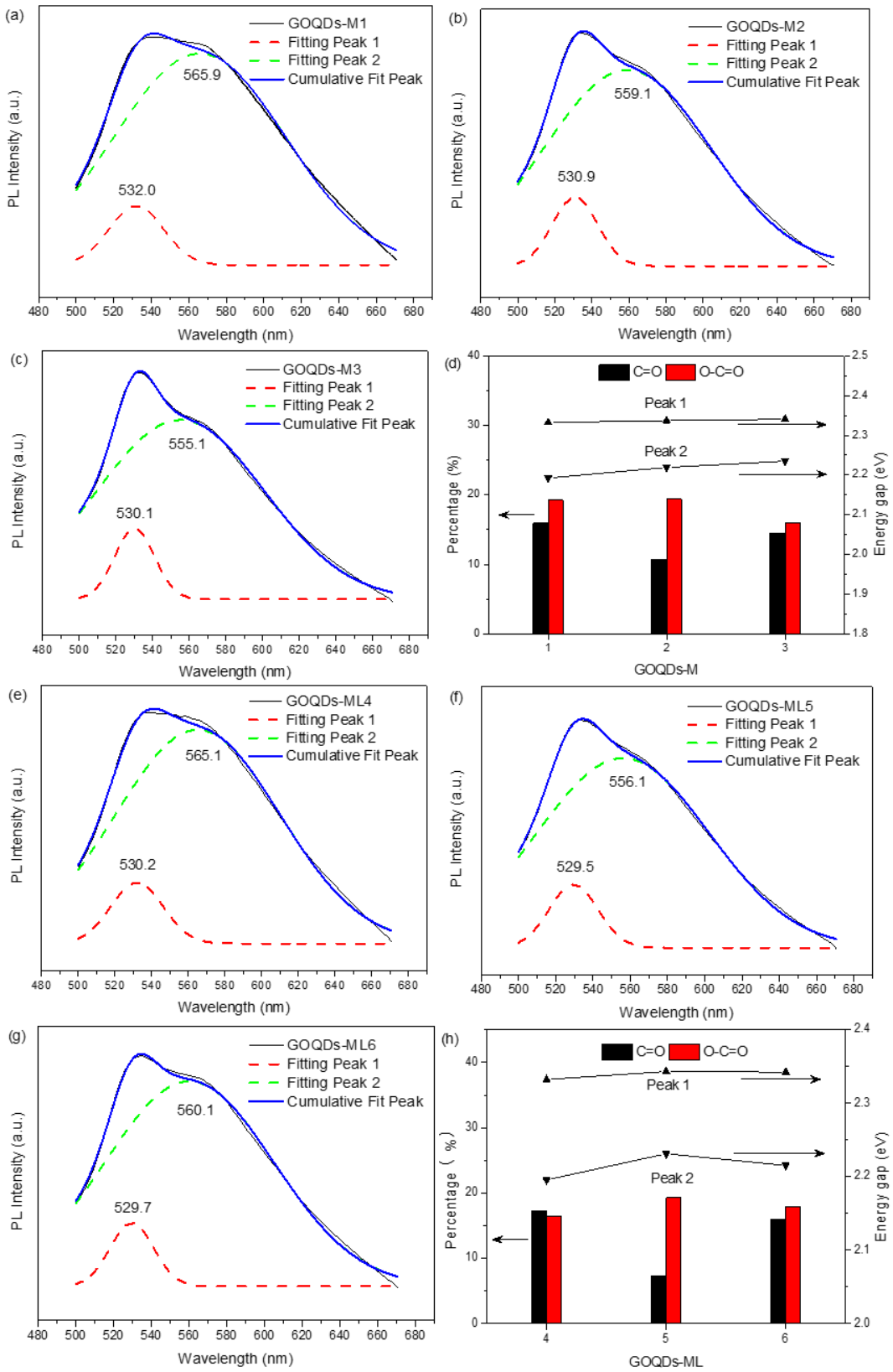

Figure 4.35. PL spectra of GOQDs-M (a) – (c) and GOQDs-ML (e) – (f) with two deconvoluted Gauss-like bands of Peak 1 and Peak 2 emission; Energy gap and content of carbon bonding of GOQDs-M (d) and GOQDs-ML (h) samples.

However, GOQDs-M3 sample does not seem to follow this hypothesis. Compared with that of other two samples, the peak 2 emission wavelength of the GOQDs-M3 is the shortest, so the content of the O-C=O structure should be highest. But from the XPS analysis results (Table 4-10), its content is lower than that of the GOQDs-M2. Because of the longest reaction time, the carboxyl groups at the edge had been saturated. Some of them were even reduced to other structures or removed. The formation of the more complicated structures may reduce the energy gap, so the peak position turns back to red-shift. This could indicate that there are still other influencing factors that affect the PL emission of the peak 2.

The quantum yield results of the GOQDs-M and GOQDs-ML for 500-600 nm range are displayed in Table 4-11. It is noted that the quantum yield of GOQDs-M samples could increase from 0.34% to 0.44% when the nitric acid treatment time increases from 10 h to 24 h, and it is higher than that of GOQDs-4 (0.41%), which is the highest of resultant GOQDs in this work. According to the XPS analysis results (Table 4-10), the percentage of the C=O bonding remarkably reduces from 15.9% to 10.8%. Extending the nitric acid treatment time to 48 h, the C=O content increases to 14.5% again, but the QY reduces to 0.39%. The changes of these two factors are related to some extent.

In another series of GOQDs-M, the conclusion about the relationship could be testified again. For the less nitric acid treatment samples, the 24 h reaction leads to the lowest C=O ratio and highest QY. The changes of QY with the reaction time are the same. However, the QY is relatively higher than that of the GOQDs-M samples for the same reaction time. The QY of GOQDs-ML5 increases to 0.54%, compared to the GOQDs-M2 with 0.44%. This means the use of less nitric acid could have a better effect on producing the GOQDs with higher QY.

Table 4-11. The quantum yield results of the GOQDs samples. (Emission range from 500-600 nm)

sample	QY	sample	QY
GOQDs-1	0.32%	GOQDs-M1	0.34%
GOQDs-2	0.34%	GOQDs-M2	0.44%
GOQDs-3	0.40%	GOQDs-M3	0.39%
GOQDs-4	0.41%	GOQDs-ML4	0.41%
GOQDs-5	0.35%	GOQDs-ML5	0.54%
GOQDs-6	0.30%	GOQDs-ML6	0.40%

4.4.2.4 Cell viability and ROS generation ability

In Figure 4.36, modified GOQDs-M samples under blue and green light irradiation show similar ROS generation abilities to those of the previous GOQDs samples. Under the blue light irradiation, the absorption intensity of ABDA for all these six samples could decrease to ~80% - 85% while the green light makes the intensity reduce just by ~2% - 5%. We could find that GOQDs-ML samples produce more ROS than GOQDs-M. UV-Vis results indicate that the absorbance of GOQDs-ML samples is higher than that of GOQDs-M samples. Higher absorbance means more energy could be transferred into the atomic oxygen on the surface of the GOQDs samples, and then makes oxygen susceptible to radical formation.

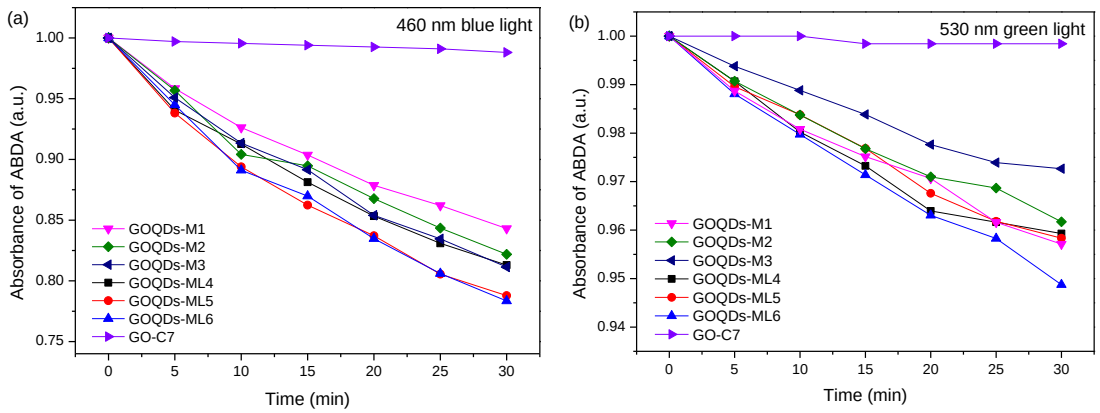

Figure 4.36. ROS generation of six modified GOQDs-M samples under (a) 460 nm blue light and (b) 530 nm green light irradiation detected by ABDA.

Zhou *et al*.[161] considered that the oxygen-containing functional groups, especially ketonic carbonyl groups, are the main factors affecting the ROS generation ability of GQDs. In this section, the GO-C7 as a comparable sample also was measured for the ROS generation ability. Both the two kinds of light can only produce a tiny amount of ROS due to fewer oxygen-containing functional groups. This result indicates that the oxygen-containing functional groups have a strong relationship with ROS generation ability of GOQDs. However, the key factor to produce ROS cannot be considered only from the ketonic carbonyl groups on the GOQDs from the results in this work. XPS analysis has revealed the composition of the oxygen-containing functional groups. GOQDs-ML5 has a relatively low concentration of C=O bonds, but it performs a similar ROS effect to that of GOQDs-ML6. Carboxyl groups (COOH) also have C=O structure, which could not only provide electrons to make oxygen become superoxide anion, but also supply hydroxyl radicals.

From the above results, GOQDs-ML5, which was prepared following a modified method and less nitric acid dosage, exhibits better PL behaviour and ROS generation ability. Therefore, GOQDs-ML5 were also chosen to undergo cell viability tests. As shown in Figure 4.37 the cell viability slightly decreased to ~80% when the concentrations of GOQDs is not higher than 0.8 mg/mL, showing that GOQDs-ML5 also have almost no influence on HeLa cells and indicate the biocompatibility of the nanoparticles.

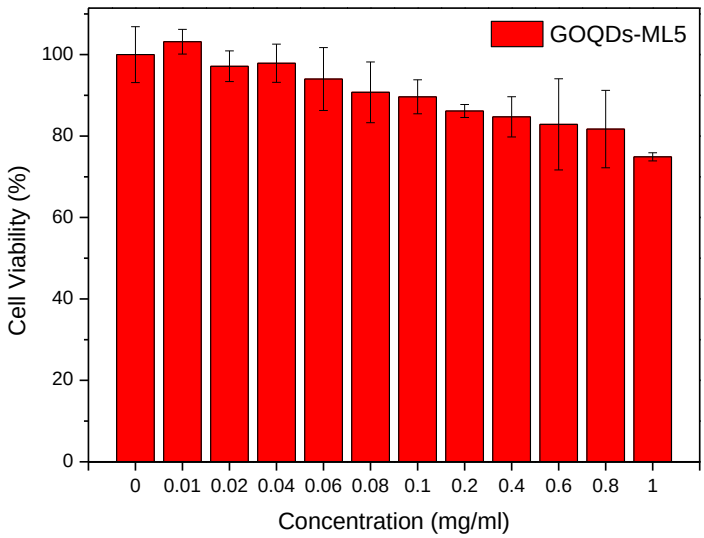

Figure 4.37. Cell viability of HeLa cells incubated with different concentrations of GOQDs-ML5.

4.4.3 Summary

In this section, six GOQDs-M samples were prepared following the modified method. Sulfuric acid was first used to treat the graphite powder in order to get intercalated graphite oxide. The H_2SO_4 molecule or HSO_4^- ions inserted into the layers. A greater layer spacing made graphite sheets separate efficiently by the 100 ℃ heat. Meanwhile, the strong oxidizing H_2SO_4 molecular also help oxidize the graphite sheet. A small amount of oxygen-containing functional groups appeared during the sulfuric acid treatment, mainly hydroxyl and epoxy groups. After 24 h and 100 ℃ sulfuric acid treatment, the epoxy groups on the graphite sheets were easily attacked when the high concentration nitric acid was added. Therefore, the smaller size and high oxidization degree of nanoparticles were obtained even using the less nitric acid dosage.

The structure and the changes of different carbon bonds of the modified GOQDs samples are analyzed to study the effect of the reaction time and nitric acid dosage. PL properties are primarily investigated. The excitation-dependent PL behaviour, especially the three colour emission peak positions, and PL intensity are compared and discussed. Quantum yield results can increase to some extent. Modified GOQDs samples still have very good ROS generation ability under blue light, and show weak influence on the cells.

4.5 Conclusion

In this chapter, three sections are designed to study the GOQDs step by step. In the first section, a single kind of GOQDs was prepared followed reported method with some changes and then examined from the structure to the properties. In the second step, six different samples were prepared by varying the reaction time and temperature. By making a comparison among these samples, the changes of the structure and the relationship between the structure and the optical properties (mainly PL behaviour) are investigated. In the last step, the experimental procedure was further revised. Two kinds of strong acid were separately added in order. The mechanism of the oxidation process and the role of these two types of acid were tried to be explained. The modified procedure could take advantage of the high concentration sulfuric acid to separate, cut and partially oxidize the graphite powder first, then more efficiently oxidization occurred after adding the nitric acid. Less acid dosage also could prepare GOQDs with good PL properties. Some samples have higher quantum yield or better ROS generation ability.

4.6 Supporting information

1. QY of GOQDs

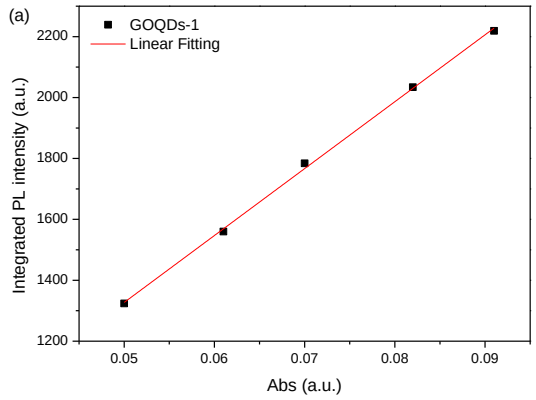

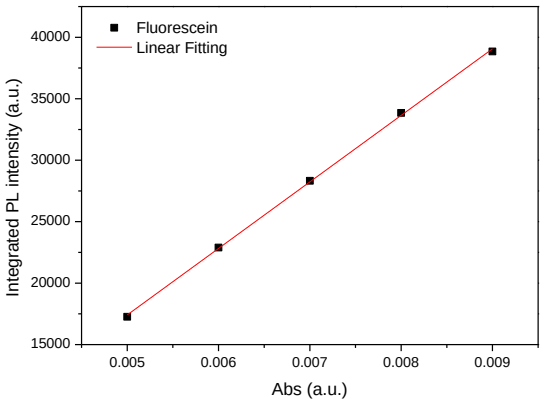

	GOQDs-1					Fluorescein				
Abs	0.091	0.082	0.070	0.061	0.050	0.009	0.008	0.007	0.006	0.005
Integrated PL	2219	2034	1784	1560	1324	38849	33848	28325	22895	17263
Slope	21970					5412500				
QY	0.32%					79%				

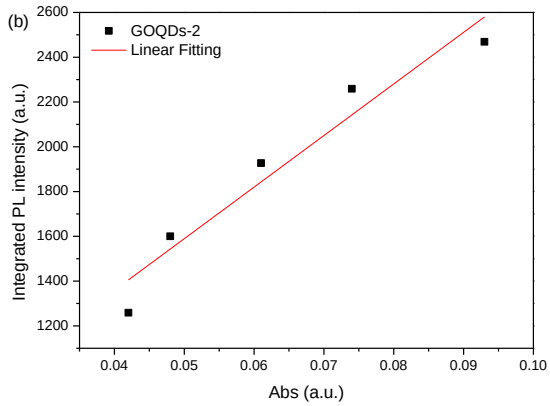

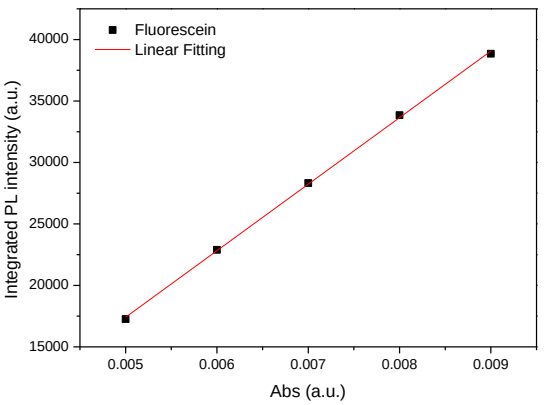

	GOQDs-2					Fluorescein				
Abs	0.093	0.074	0.061	0.048	0.042	0.009	0.008	0.007	0.006	0.005
Integrated PL	2469	2259	1927	1600	1259	38849	33848	28325	22895	17263
Slope	23039					5412500				
QY	0.34%					79%				

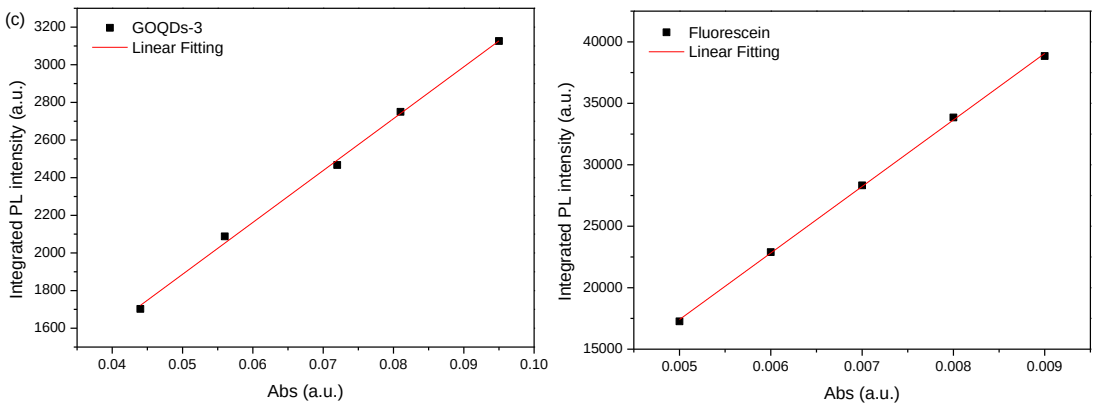

	GOQDs-3					Fluorescein				
Abs	0.095	0.081	0.072	0.056	0.044	0.009	0.008	0.007	0.006	0.005
Integrated PL	3126	2750	2467	2088	1703	38849	33848	28325	22895	17263
Slope	27558					5412500				
QY	0.40%					79%				

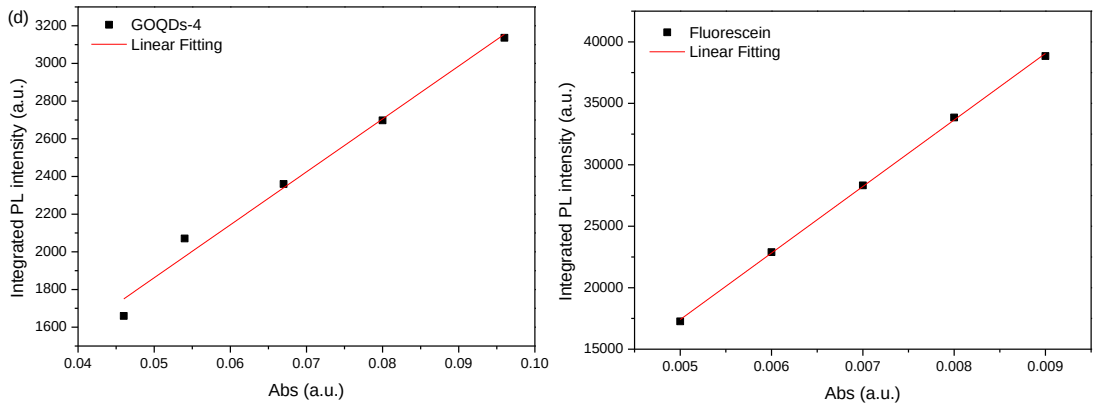

	GOQDs-4					Fluorescein				
Abs	0.096	0.080	0.067	0.054	0.046	0.009	0.008	0.007	0.006	0.005
Integrated PL	3136	2689	2360	2071	1660	38849	33848	28325	22895	17263
Slope	28095					5412500				
QY	0.41%					79%				

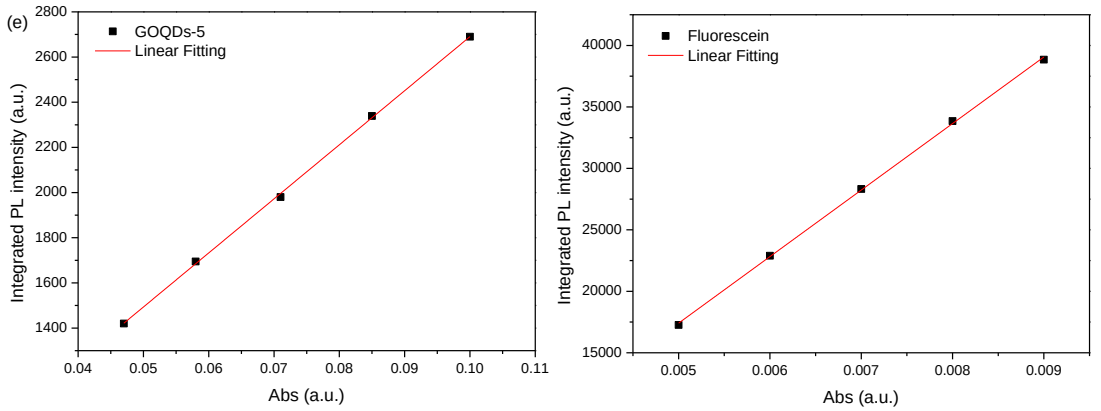

	GOQDs-5					Fluorescein				
Abs	0.1	0.085	0.071	0.058	0.047	0.009	0.008	0.007	0.006	0.005
Integrated PL	2690	2331	1992	1685	1420	38849	33848	28325	22895	17263
Slope	23942					5412500				
QY	0.35%					79%				

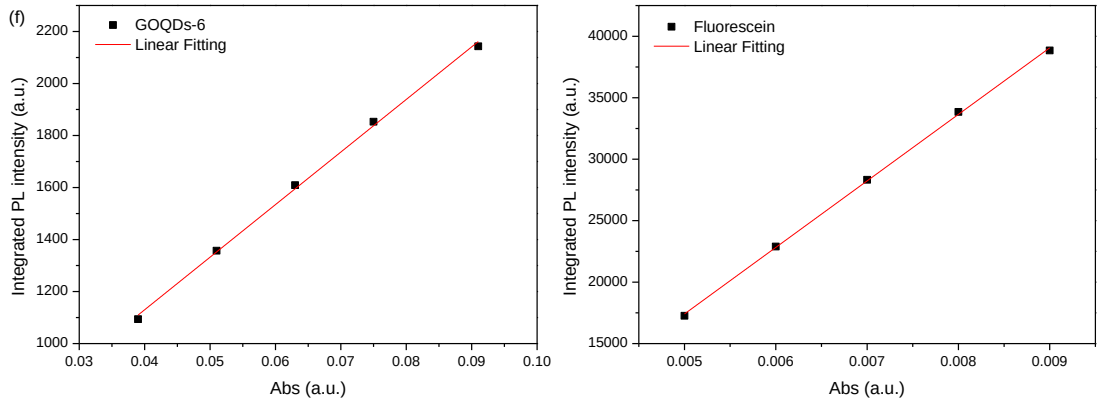

	GOQDs-6					Fluorescein				
Abs	0.091	0.075	0.063	0.051	0.039	0.009	0.008	0.007	0.006	0.005
Integrated PL	2143	1853	1609	1357	1094	38849	33848	28325	22895	17263
Slope	20218					5412500				
QY	0.30%					79%				

Figure S 1. (a) - (f) Plots of integrated PL intensity of GOQDs-1 to GOQDs-6 and fluorescein (reference standard material) as a function of absorbance at 470 nm and relevant raw data.

2. QY of GOQDs-M

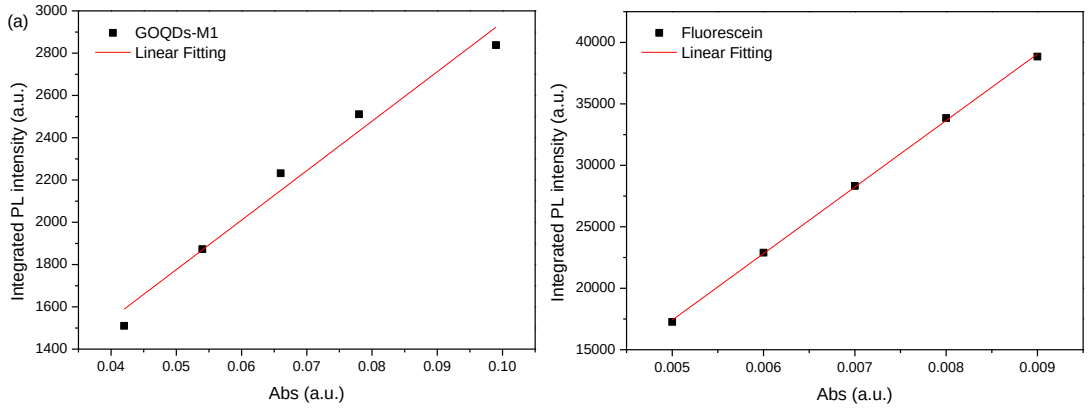

	GOQDs-M1					Fluorescein				
Abs	0.099	0.078	0.066	0.054	0.042	0.009	0.008	0.007	0.006	0.005
Integrated PL	2838	2511	2232	1873	1510	38849	33848	28325	22895	17263
Slope	23407					5412500				
QY	0.34%					79%				

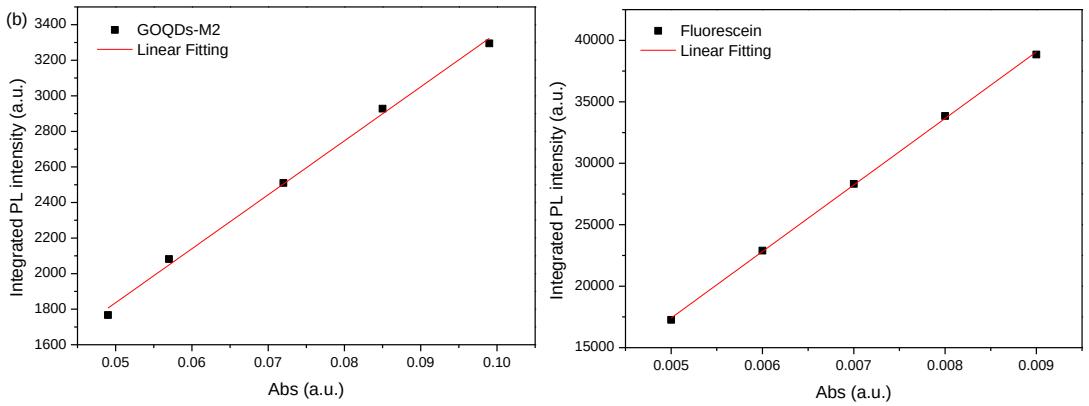

	GOQDs-M2					Fluorescein				
Abs	0.099	0.085	0.072	0.057	0.049	0.009	0.008	0.007	0.006	0.005
Integrated PL	3295	2928	2510	2082	1767	38849	33848	28325	22895	17263
Slope	30357					5412500				
QY	0.44%					79%				

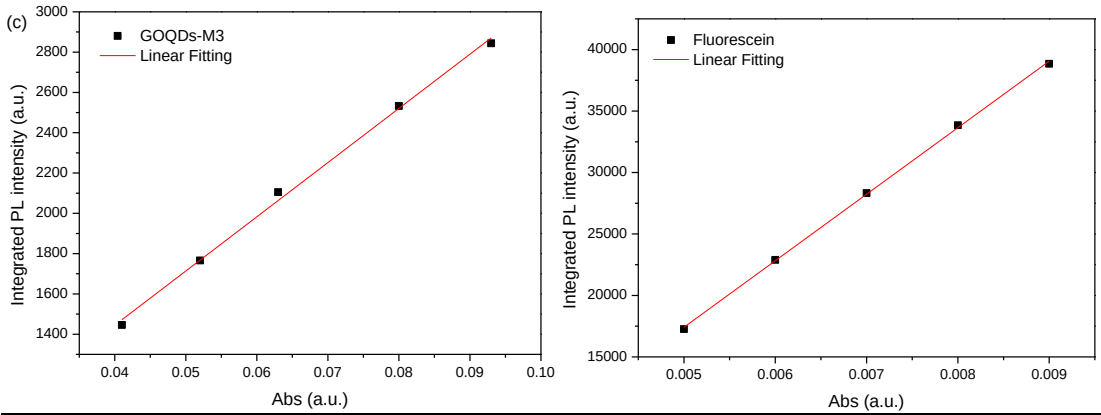

	GOQDs-M3					Fluorescein				
Abs	0.093	0.080	0.063	0.052	0.041	0.009	0.008	0.007	0.006	0.005
Integrated PL	2844	2533	2105	1766	1446	38849	33848	28325	22895	17263
Slope	26898					5412500				
QY	0.39%					79%				

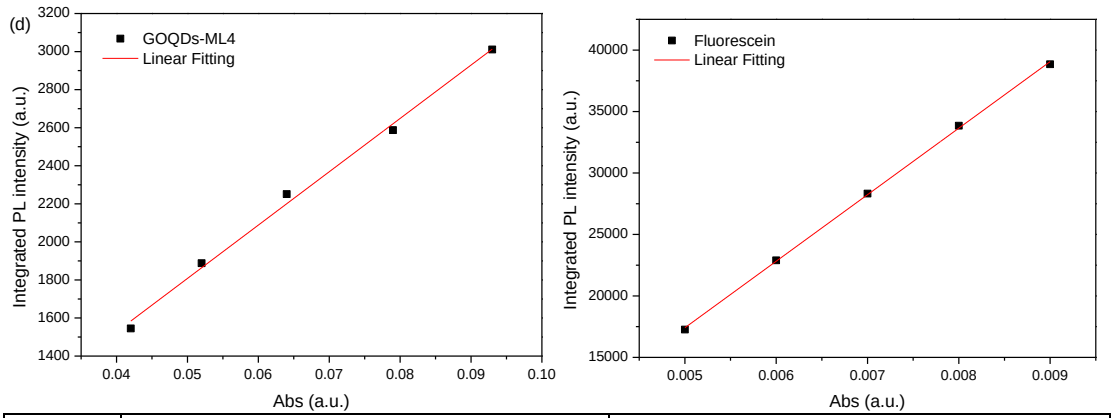

	GOQDs-ML4					Fluorescein				
Abs	0.093	0.079	0.064	0.052	0.042	0.009	0.008	0.007	0.006	0.005
Integrated PL	3011	2587	2251	1888	1545	38849	33848	28325	22895	17263
Slope	28025					5412500				
QY	0.41%					79%				

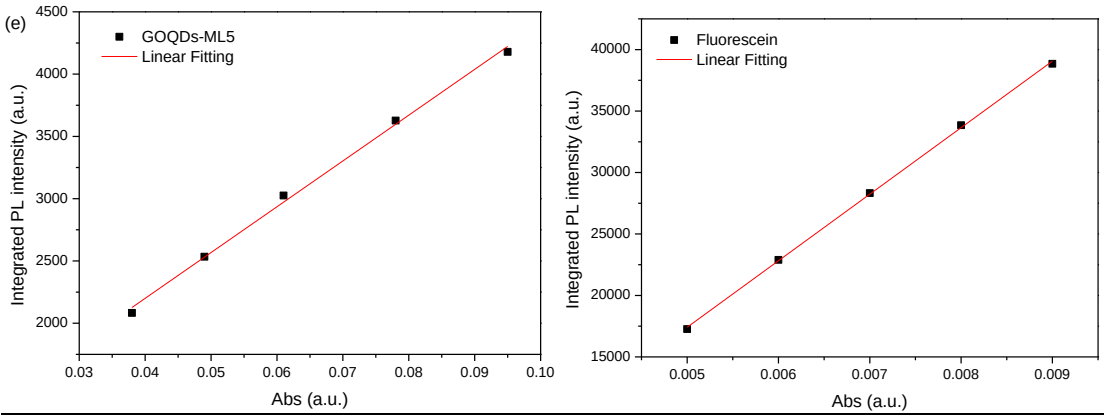

	GOQDs-ML5					Fluorescein				
Abs	0.095	0.078	0.061	0.049	0.038	0.009	0.008	0.007	0.006	0.005
Integrated PL	4179	3627	3025	2534	2083	38849	33848	28325	22895	17263
Slope	36769					5412500				
QY	0.54%					79%				

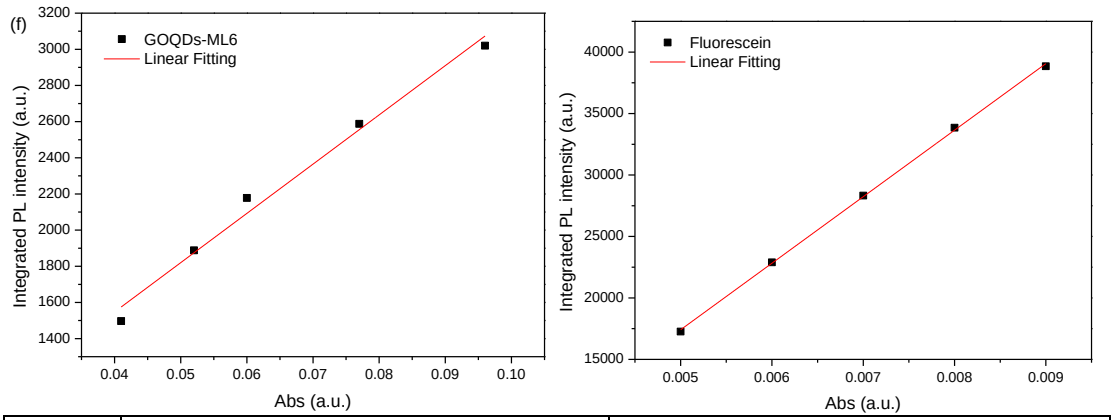

	GOQDs-ML6					Fluorescein				
Abs	0.096	0.077	0.060	0.052	0.041	0.009	0.008	0.007	0.006	0.005
Integrated PL	3020	2588	2178	1888	1497	38849	33848	28325	22895	17263
Slope	27245					5412500				
QY	0.40%					79%				

Figure S 2. (a) - (f) Plots of integrated PL intensity of GOQDs-M, GOQDs-ML and fluorescein (reference standard material) as a function of absorbance at 470 nm and relevant raw data.

5 Hydrothermal treatment of graphene oxide quantum dots and the regulation of their photoluminescence properties

5.1 Introduction

Several series of GOQDs samples were successfully prepared followed the modified chemical oxidation method by changing the reaction condition and procedure step. GOQDs have abundant oxygen-containing functional groups and they mainly show PL emission range of green and yellow colour. The size of the GOQDs is around 70-120 nm, which is relatively larger than other CDs reported in the literature.[24,77,117]

For reducing the size of the GOQDs and studying the thermal stability of different oxygen-containing functional groups, hydrothermal method was used to further treat the GOQDs samples. As mentioned in some publications, the hydrothermal method has been used to prepare GQDs from graphene oxide.[130,183,184] Due to the harsh reaction condition (high temperature and high pressure), the graphene oxide sheets could be cut to smaller sheets easily. Meanwhile, the reduction effect of this method also will remove or reduce some oxygen-containing functional groups. After the reaction, some precipitate could be seen in some work, which means the oxygen-containing functional groups are all removed.

The generated GOQDs, which were prepared by the modified chemical oxidation method in Chapter 4, have more oxygen-containing functional groups than graphene oxide sheets. Considering that the size in diameter of some GOQDs is still large and not uniform, the object in this chapter is taking use of the hydrothermal method to reduce the size and get more nanodots. Enough amount of oxygen-containing functional groups make sure that the treated GOQDs can remain well disperse in water after the

reaction. Not only will the size be smaller, but also the treatment could remove some oxygen-containing functional groups. Different hydrothermal treatment conditions are set to prepare different samples. According to the reported publications,[25,79,110,128,130,184] 180 ℃ and 200 ℃ are the common parameter of similar hydrothermal methods. Considering the temperature limit of the heating oven and the expected differentiation of results, 180 ℃ and 240 ℃ with three different heating time (3 h, 6 h and 12 h) were chosen to prepare six new series of GOQDs-H. Characterized and analyzed new samples. By comparing their difference in structure and PL properties, the mechanism of PL in GOQDs can be analyzed and summarized.

5.2 Experimental procedures

In this chapter, graphene oxide quantum dots were first prepared as raw materials following the basic chemical oxidation method mentioned in the Chapter 4. The reaction temperature was 100 ℃ and the reaction time was 24 h. After the salts were removed *via* dialysis, GOQDs aqueous suspension with a concentration of about 0.2 mg/mL was obtained. The GOQDs aqueous suspension (60 mL) was transferred to a polytetrafluoroethylene-lined pressurising vessel (150 mL) and heated in the oven at 180 ℃ or 240 ℃ for 3 h, 6 h or 12 h, respectively (Table 5-1). After cooling to room temperature, the suspension was filtered through a 0.22 μm nylon membrane. The filtered suspension was freeze-dried to obtain partially reduced GOQDs-H powder.

Table 5-1. The reaction condition of six GOQDs-H samples.

Sample ID	Heating temperature / ℃	Heating time / h
GOQDs-H1	180	3
GOQDs-H2	180	6
GOQDs-H3	180	12
GOQDs-H4	240	3
GOQDs-H5	240	6
GOQDs-H6	240	12
GOQDs	Raw material	

H means hydrothermal treatment.

5.3 Results and analysis

5.3.1 Morphology

The AFM images of partially reduced GOQDs-H obtained with 180 ℃ heating temperature are shown in Figure 5.1 and the diameter is also calculated by the NanoScope software, as shown in Table 5-2. For the raw material GOQDs, the size in diameter is around 53.5 nm and height is about 1.4 nm. The results and irregular shape feature of this batch are quite similar to those of the GOQDs mentioned in the first section of chapter 4. Under the 180 ℃ heating temperature in the pressurising vessel, GOQDs-H1 with 3 h reaction time seems not to have a noticeable difference in diameter. The big particles size slightly reduces and the average diameter is about 52.5 nm, which is almost the same as the raw GOQDs. Increasing the heating time to 6 h, the diameter of the GOQDs-H2 samples is around 35.6 nm. The size becomes smaller and more uniform, and the shape changes to be round. For the sample with 12 h heating, the average diameter continues to decrease to around 25 nm. However, some big particles still could be found in the image. Due to the limit of the calculation by AFM software, the small size particles (less than 10 nm) are difficult to measure, but these tiny dots could still be easily noticed in the images, especially for GOQDs-H2 and H3.

Table 5-2. The diameter of the GOQDs-H (180 ℃). Unit: nm.

	mean	standard deviation	maximum
GOQDs-H1	52.5	32.9	108.2
GOQDs-H2	35.6	16.6	72.6
GOQDs-H3	25.2	12.2	70.3
GOQDs	53.5	22.3	118.6

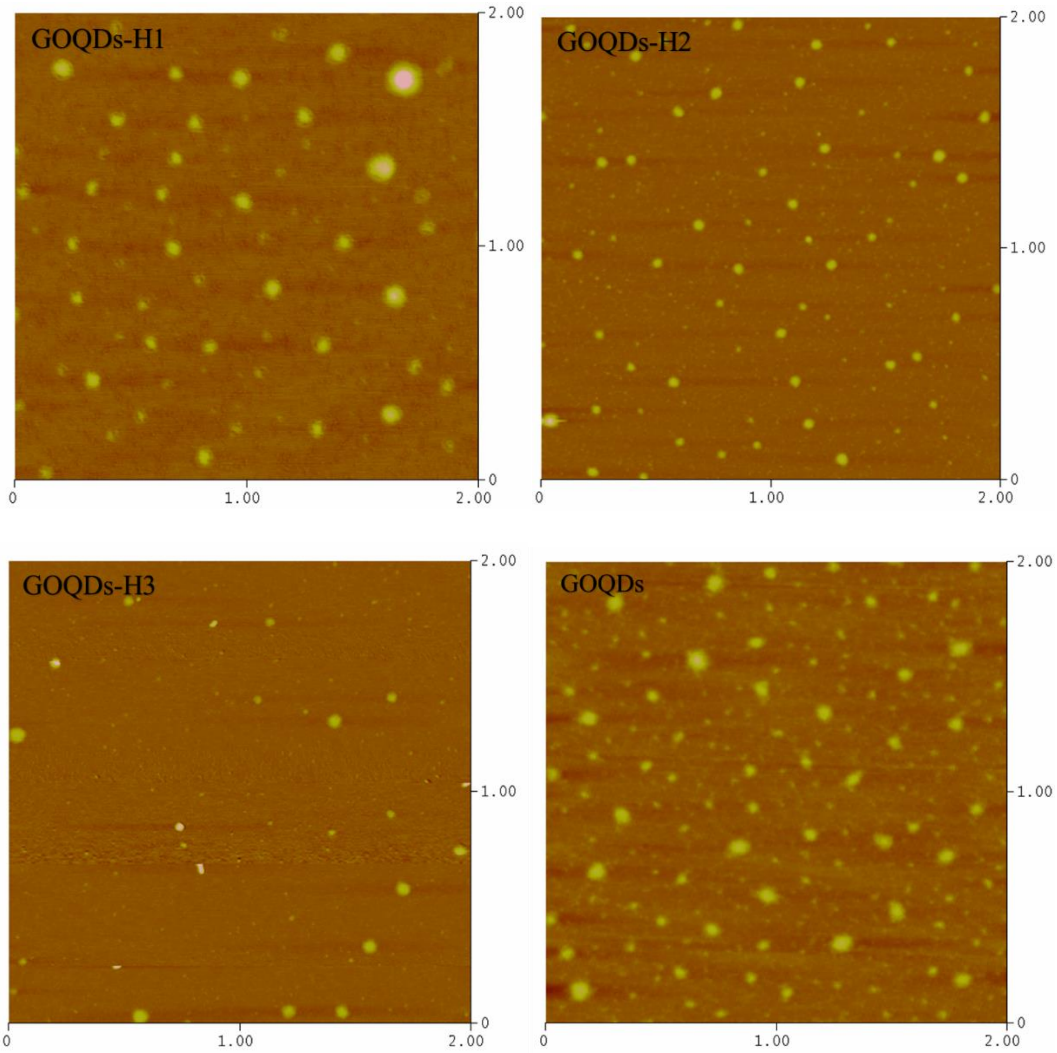

Figure 5.1. The AFM images of the GOQDs- H1 (180 ℃ 3 h), H2 (180 ℃ 6 h) H3 (180 ℃ 12 h) and raw material GOQDs. Scale: 2 μm × 2 μm.

The AFM images and diameter of other three partially reduced GOQDs-H samples obtained with 240 ℃ heating temperature are shown in Figure 5.2 and Table 5-3. Different from the H1 sample, GOQDs-H4 also just have 3h heating time, but the diameter remarkably decreases to 41.6 nm. The maximum size of the generated dots is just 69.7 nm, which is almost half of the maximum size of the raw materials. For 6 h and 12 h heating time, the cutting effect is more apparent and it can be reflected from the diameter results. The average diameter is 25.6 nm and 18.9 nm, respectively.

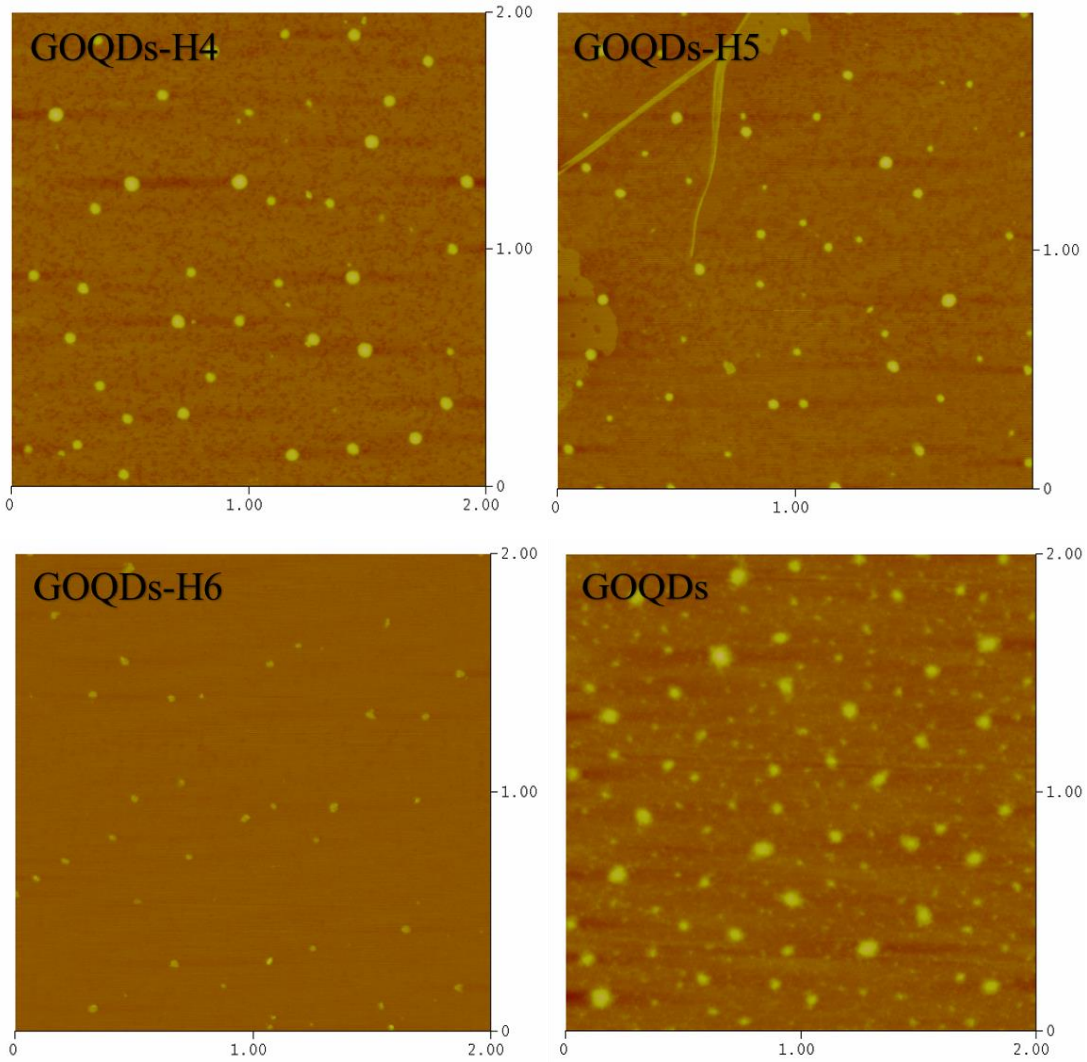

Figure 5.2. The AFM images of the GOQDs-H4 (240 ℃ 3 h), H5 (240 ℃ 6 h) H6 (240 ℃ 12 h) and raw material GOQDs. Scale: Scale: 2 μm × 2 μm.

Table 5-3. The diameter of the GOQDs-H (240 ℃). Unit: nm.

	mean	Standard deviation	maximum
GOQDs-H4	41.6	20.7	69.7
GOQDs-H5	25.6	14.4	63.9
GOQDs-H6	18.9	12.4	48.5
GOQDs	53.5	22.3	118.6

Like many other publications,[33,183,185,186] the AFM results in this chapter also demonstrate that hydrothermal treatment is a way to cut the graphene nanoparticles further. In this work, the different heating parameters were set to prepare different samples for making a comparison and studying the cutting effect. For 180 ℃, short heating time does not show much effect, however, more than 6 h heating time can lead to the apparent changes. For 240 ℃, higher temperature makes the cutting effect more efficiently, so just 3 h was enough for some large size dots to crack into smaller ones.

The high-resolution transmission electron microscope (HR-TEM) images of two GOQDs-H samples (Figure 5.3a - 5.3d) indicate that the high crystallinity of the lattice spacing of 0.21 nm is consistent with that of in-plane lattice spacing of graphene, which is similar to those of many other reported GOQDs. Especially, the hexagonal honeycomb structures and crystalline lattice are clearly visible in the circular and square markings of Figure 5.3b, 5.3c and 5.3d. However, the similar crystalline carbon structures are not easily seen in the image of the raw material GOQDs (see Figure 5.3e), which may be due to the higher content of the oxygen-containing functional groups on the basal plane. After hydrothermal treatment, some of the oxygen-containing functional groups on the basal plane were reduced so that the crystalline carbon structure could be restored. Therefore, the hexagonal honeycomb structures resulting from original graphene carbon skeleton structure could be displayed again.

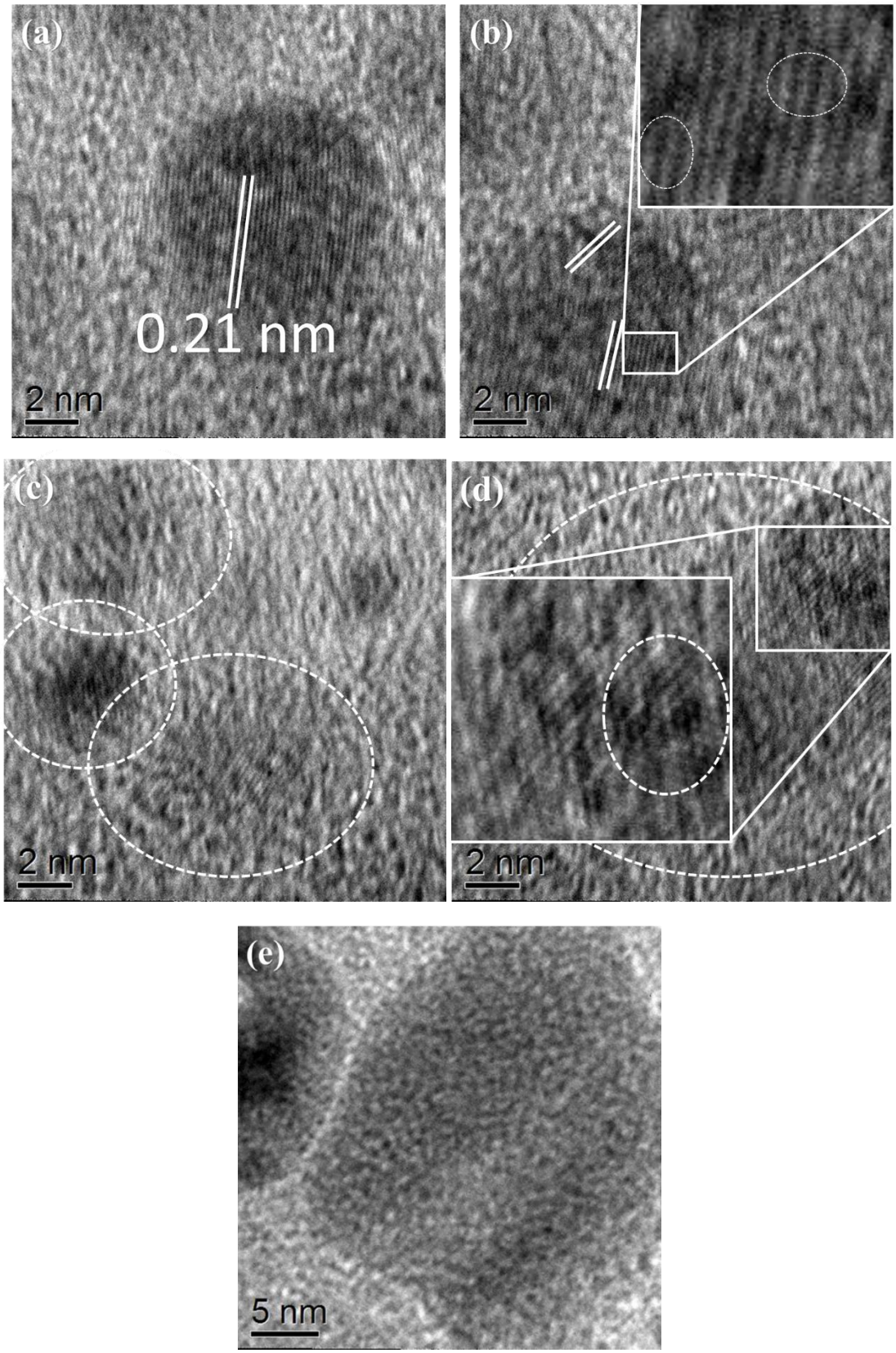

Figure 5.3. (a-b) HRTEM images of GOQDs-H3 obtained with 180 ℃ and 12 h; (c-d) HRTEM images of GOQDs-H4 obtained with 240 ℃ and 3 h; (e) HRTEM image of raw material GOQDs.

5.3.2 Structure

In Figure 5.4, two sets of GOQDs-H samples of the FTIR spectra (hydrothermal temperature: 180 ℃ and 240 ℃) were compared with the raw material GOQDs, separately. When the hydrothermal temperature is 180 ℃, the FTIR spectrum almost has no obvious change (see Figure 5.4a), compared to raw material, except the transmittance intensity of the peaks at 2936, 1333, 1245 and 879 cm^{-1}. The peak at around 1245 cm^{-1} could be attributed to the epoxy groups (C-O-C). With increasing reaction time, the transmittance intensity of the peak is reduced gradually, which may correspond to the loss of epoxy groups under hydrothermal treatment. In the meantime, the transmittance intensity of the peaks at around 2936, 1333 and 879 cm^{-1} become stronger with extended the reaction time. 2936 and 879 cm^{-1} belong to C-H stretching, and 1333 cm^{-1} band comes from C-O stretching. From the changes of these bands, we can find that hydrothermal treatment at 180 ℃ can partly change the structure. Epoxy groups and carbon skeleton could be cut, which leaves more C-H or C-O structure at the edge.

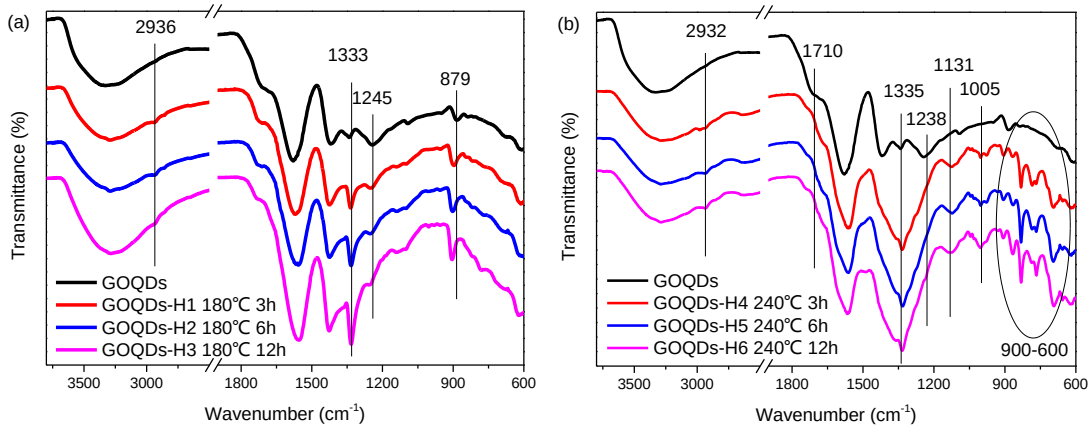

Figure 5.4. FTIR spectra of the GOQDs-H samples obtained with heat treatment at (a) 180 ℃ and (b) 240 ℃.

When the hydrothermal temperature is 240 ℃, the FTIR spectrum of shows the obvious difference after 3 h hydrothermal treatment (see Figure 5.4b). The peak of carboxylic acids (COOH structure) at 1710 cm^{-1} shifts to about 1730 cm^{-1} which

corresponds to the ester (COO structure). The peak of epoxy group at 1238 cm^{-1} disappears, and the peak of C-O stretching at around 1335 cm^{-1} becomes stronger, which again demonstrates the epoxy groups (C-O-C structure) could be split to C-O structure by hydrothermal treatment and a higher temperature (240 ℃) has a more apparent splitting effect. Besides, C-H stretching at near 2936 cm^{-1}, 1005 cm^{-1} and the region of 900-600 cm^{-1} becomes more noticeable. The stronger splitting effect by the hydrothermal treatment could also explain these changes.

High-resolution scans of C1s of the six GOQDs-H samples have been curve-fitted, and the results are shown in Figure 5.5. Even though the GOQDs samples were treated in the pressurising vessel and partly reduced, all GQODs-H spectra still could be deconvoluted into those peaks, including C-C/C=C (~285 eV), C-N (~285.6 eV), C-O (~286.6 eV), C=O (~288.2 eV) and O-C=O (~289.0 eV). The XPS results demonstrate that the oxygen-containing functional groups still exist on the surface or at the edge, which is consistent with the previous FTIR results. The values of the different oxygen-containing functional structure of the six GOQDs-H samples could be found in Figure 5.6 and Table 5-4.

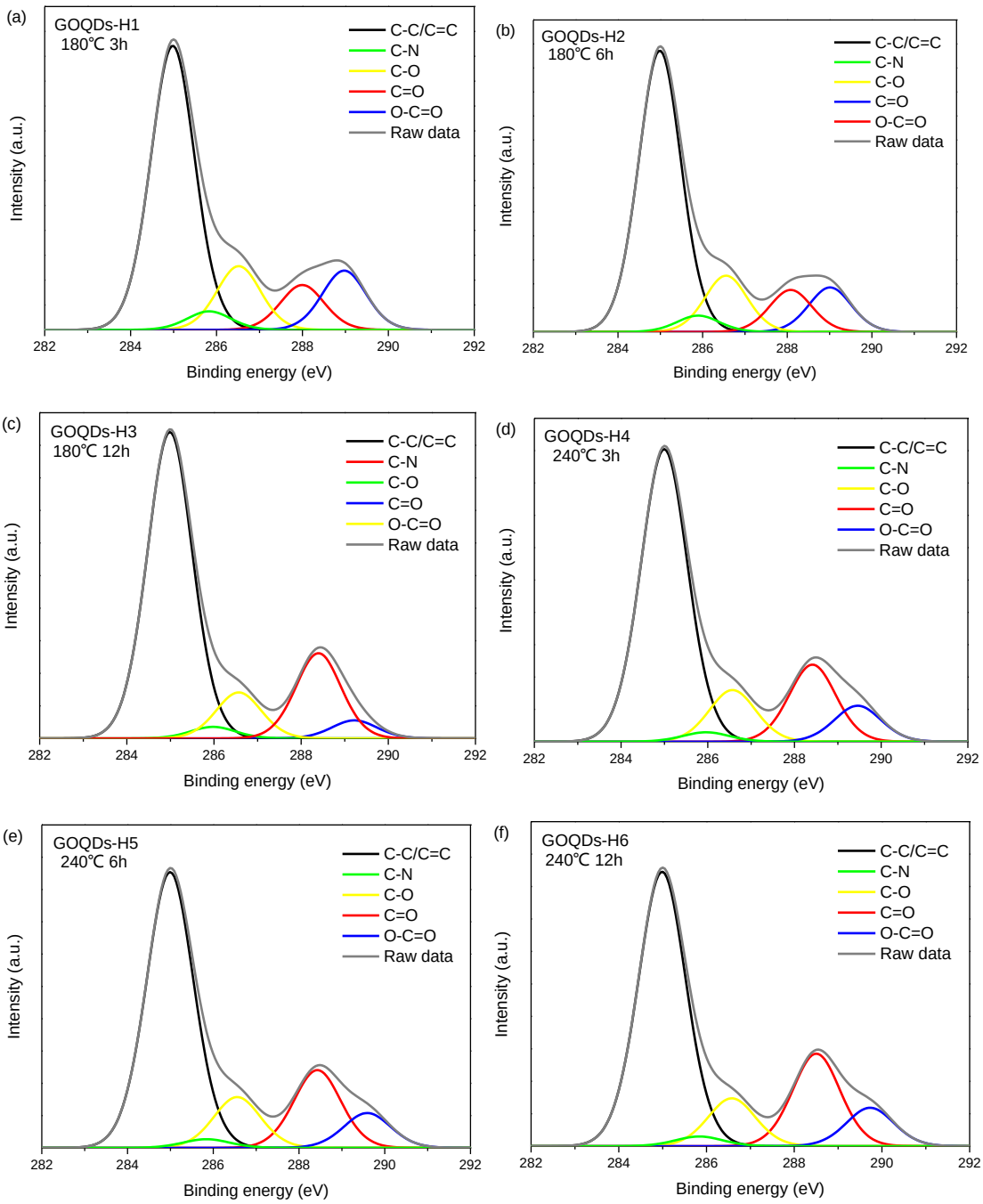

Figure 5.5. (a) - (f) High-resolution XPS C1s spectra of the GOQDs-H samples, respectively.

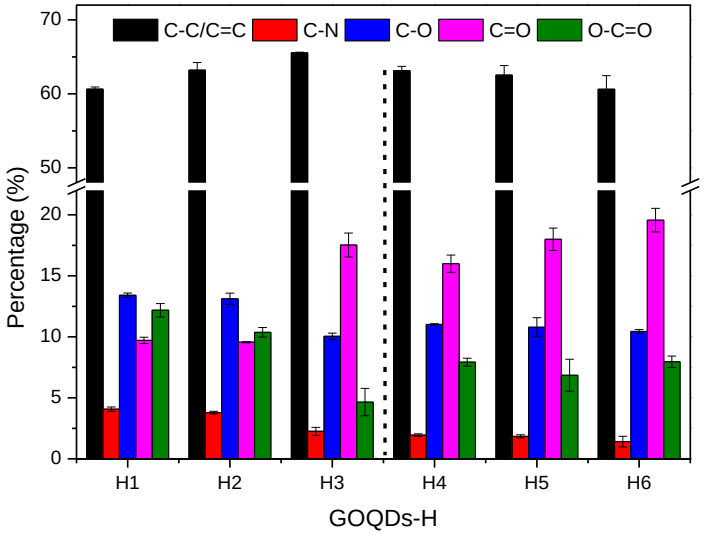

Figure 5.6. The percentage of the peaks deconvoluted from the C1s spectra.

Table 5-4. XPS data analyses of the C1s spectra of the GOQDs-H samples.

	Carbon bonding composition (%)					
Sample	C-C/C=C	C-N	C-O	C=O	O-C=O	O1s/C1s
GOQDs-H1	**60.6**	**4.1**	**13.4**	**9.7**	**12.2**	**39.2%**
GOQDs-H2	**63.2**	**3.8**	**13.0**	**9.6**	**10.4**	**37.8%**
GOQDs-H3	**65.5**	**2.3**	**10.0**	**17.5**	**4.7**	**37.2%**
GOQDs-H4	**63.2**	**1.9**	**11.0**	**16.0**	**7.9**	**48.2%**
GOQDs-H5	**62.5**	**1.8**	**10.8**	**18.0**	**6.9**	**51.2%**
GOQDs-H6	**60.6**	**1.4**	**10.4**	**19.6**	**8.0**	**53.5%**

When the hydrothermal temperature is 180 °C, the content of the carbon matrix (C-C/C=C) of all three samples is more than 60%, which is higher than that of the GOQDs and GOQDs-M samples in the previous chapter (all are between 57% and 60%). With the increase of the hydrothermal treatment time from 3 h to 12 h, the content of the carbon matrix rises from 60.6% to 65.5%. In the meantime, the reduction effect of the hydrothermal treatment could be reflected in the ratio of the O1s and C1s. The O1s/C1s

ratio of the raw GOQDs sample is about 50%. 180 ℃ and 3 h treatment make the value decrease to 39.2%, and become lower when the treatment time is extended. The changes of the above mentioned two values could be explained by the removal of the oxygen-containing functional groups. Besides, the carbon bonding composition between the carbon and oxygen changes when the treatment time increases from 3 h to 12 h. To summarize for setting the temperature at 180 ℃:

1. C-O bond. From GOQDs-H1 to GOQDs-H3, the content of C-O bonds slightly decreases from 13.4% to 13.0% and 10.0%. According to the FTIR results, the decreasing content could be considered as the epoxy groups, due to epoxy group is easy to split to C-O, as previously mentioned the FTIR analysis. The remaining content could be the C-OH structure.

2. O-C=O structure. From GOQDs-H1 to GOQDs-H2, the content slightly decreases from 12.2% to 10.4%, and significantly decrease to 4.7% when the treatment time increases to 12 h (GOQDs-H3). The above information means that O-C=O structures are more stable and need more treatment time or a higher temperature to be reduced or broke than epoxy groups.

3. C=O bonds. From GOQDs-H1 to GOQDs-H2, the content remains almost unchanged. However, GOQDs-H3 sample has about 17.53% C=O bonds, which is almost double of that of the GOQDs-H1 or GOQDs-H2 sample. The changes trend of the C=O bonds with the reaction time is just opposite to that of the O-C=O structure.

From the above analysis, we could draw some conclusion for 180 ℃ hydrothermal treatment effects. Due to the high temperature and pressure in the pressurizing vessel, the oxygen-containing functional groups on the surface and at the edge could be partially removed. The carbon matrix remains, and its content rises with a longer period

of treatment time. The maximum content of carbon matrix is 12 h treatment time. The epoxy groups are not stable at 180 ℃ and could be quickly removed in short treatment time. The O-C=O and C=O structures are more stable. Therefore, longer treatment time (more than 6 h) is needed to transform the majority of O-C=O structure transform to the C=O structure.

When the hydrothermal temperature is 240 ℃, the content of the carbon matrix (C-C/C=C) of all three samples is also more than 60%. When the treatment time is 3 h, GOQDs-H4 has 63.2% carbon matrix, which is higher than that of the GOQDs-H1 (180 ℃ 3 h). A higher hydrothermal temperature makes the reduction effect more efficiently. With the increase of the hydrothermal treatment time from 3 h to 12 h, the content of the carbon matrix decreases from 63.2% to 60.6%, which is opposite to the variation trend of that of the 180 ℃ hydrothermal treatment samples. To explain this phenomenon, we could also consider the size of the nanoparticles. Due to the higher hydrothermal temperature, the cutting effect is much more apparent, and the size of the nanoparticles is much smaller than that of the samples with a lower hydrothermal temperature. The large raw nanoparticle sheet is cut into several small pieces. The cutting effect of the 3 h treatment has been already quite apparent. After 6 h or 12 h treatment, the size of the nanoparticle sheets is much smaller. The oxygen-containing functional groups still exist at the edge. Therefore, the ratio of the carbon matrix gradually decreases.

The changes of the carbon bonding composition between the carbon and oxygen with the increase of the treatment time from 3 h to 12 h at 240 ℃ are summarized as:

1. C-O bond. The content of the C-O bond in GOQDs-H4 (3 h) is about 11.0%, which is lower than that of the GOQDs-H1 (180 ℃ 3 h) and is quite close to the value of the GOQDs-H3 (180 ℃ 12 h). When more treatment time is used, the content would slightly decrease. As mentioned in the previous part, the epoxy groups are not stable

under the 180 ℃ hydrothermal treatment. Therefore, 240 ℃ is able to cut the epoxy groups more quickly. 3 h hydrothermal treatment time could be enough, and the effect is almost the same as the 12 h treatment with the low temperature.

2. O-C=O structure. Different from the high content of the GOQDs-H1 and GOQDs-H2, the GOQDs-H4 has just 3 h hydrothermal treatment time, but only leaves 7.9% content of O-C=O. From the above comparison, we can draw a conclusion that the O-C=O structure is much stable at 180 ℃ and more treatment time (such as longer than 6 h) is needed to change it. However, it is easy to be transformed or removed at 240 ℃ and short treatment time (like 3 h) would be enough.

   Another two samples with a longer treatment time have a similar content of O-C=O. GOQDs-H6 sample still has 7.9% content of O-C=O, which is higher than that of the GOQDs-H3. The value we expect should be lower. This could be explained by the fact that the more new edges appeared after the carbon matrix had been cut into small sheets. In the meantime, the new edge is the defect part, which is easy to be oxidized to the new O-C=O structure under a higher temperature and a higher pressure. So the content of the GOQDs-H6 (12 h) is even higher than that of the GOQDs-H5 (6 h).

3. C=O bonds. When the hydrothermal treatment time is only 3 h, the content of C=O significantly increases to 16.0%, which is much higher than that of the GOQDs-H1 (180 ℃ 3 h) and is quite close to the result of the GOQDs-H3 (180 ℃ 12 h). With increasing the treatment time to 6 h, the content could continuously rise to about 18%.

From the above analysis, we could draw some conclusions for the 240 ℃ hydrothermal treatment effect. Due to the higher temperature and higher pressure in the pressurizing vessel, the cutting effect on the carbon matrix is more apparent, and the

size of the nanoparticles is much smaller. Meanwhile, the C-OH structure coming from the attacked epoxy groups or the new edge from the smaller nanoparticle sheets cut from, the bigger carbon matrix could become new defect parts, where are more straightforward to be oxidized at 240 ℃ high temperature in the pressurizing vessel. The 240 ℃ and 3 h hydrothermal treatment effect is quite close to the results of the sample with 180 ℃ and 12 h treatment.

Compared with the GOQDs and GOQDs-M samples in the last chapter, we could find the most obvious variation of the structure of the GOQDs-H samples after hydrothermal treatment is the higher contents of the carbon matrix and C=O structure. These changes of the structural composition would affect the PL properties, and the details would be discussed later.

As shown in Figure 5.7, the nitrogen bonding composition is also investigated, and all GOQDs-H samples still consist of two main peaks, including pyridinic-N at around 399.8 eV and quaternary-N at about 401.2 eV. Quantitative analysis of the atomic ratio of (N1s) / (C1s) and the nitrogen bonding composition are displayed in Figure 5.8 and Table 5-5. From the above C-N content and the N1s/O1s ratio results, we could find that C-N bond is not stable and easy to break under the hydrothermal treatment. Besides, compared with the GOQDs samples, the C-N bonding composition occurs to change after hydrothermal treatment. The content of the pyridinic-N increases up to over 92%, and even to 95% if the hydrothermal temperature is 240 ℃. Therefore, the nanoparticles have less quaternary-N structure. We could speculate that the quaternary-N structure is less stable than pyridinic-N under hydrothermal treatment, and it is easier to break to cut the carbon matrix.

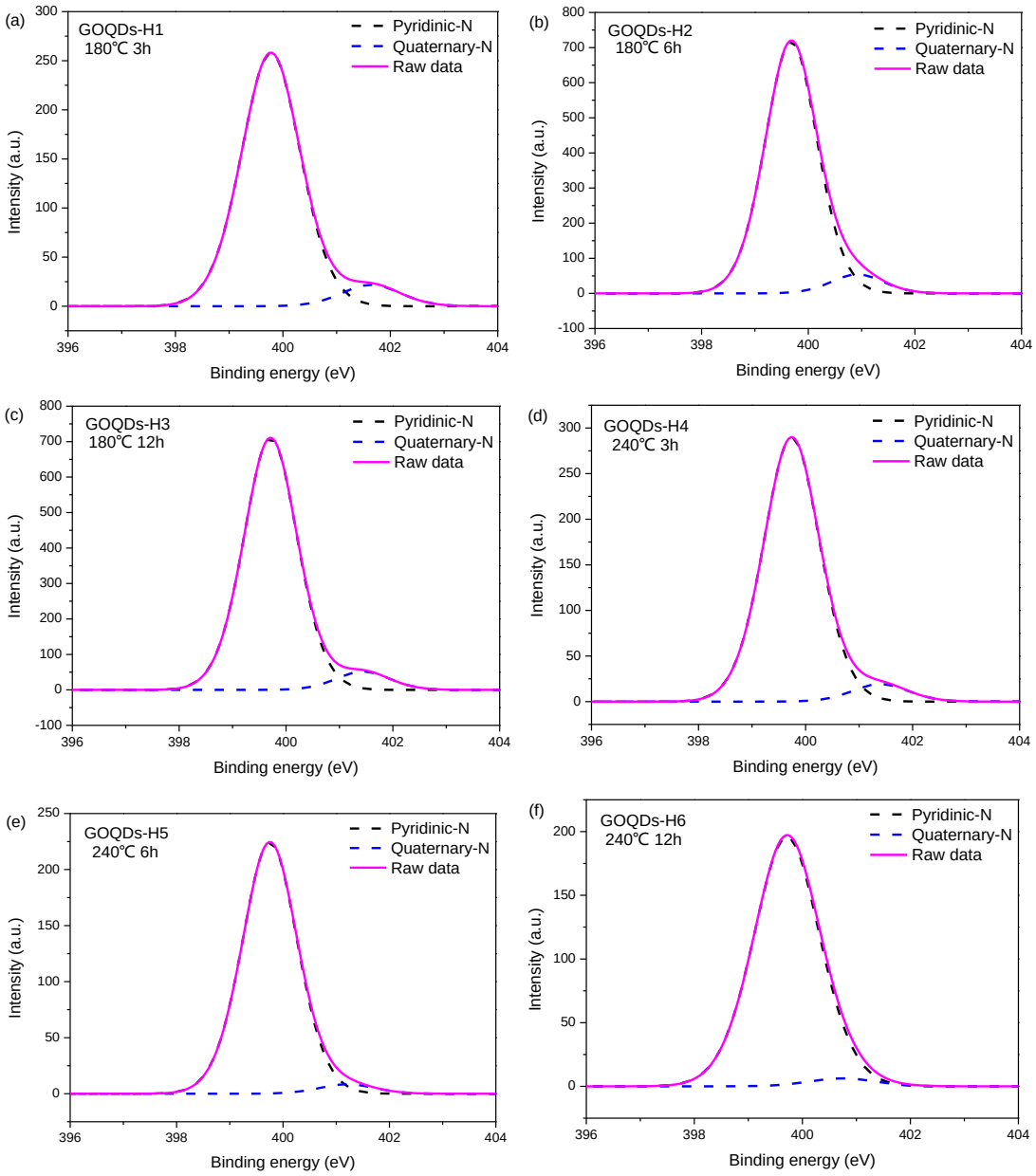

Figure 5.7. (a) - (f) High-resolution XPS N1s spectra of the GOQDs-H samples, respectively.

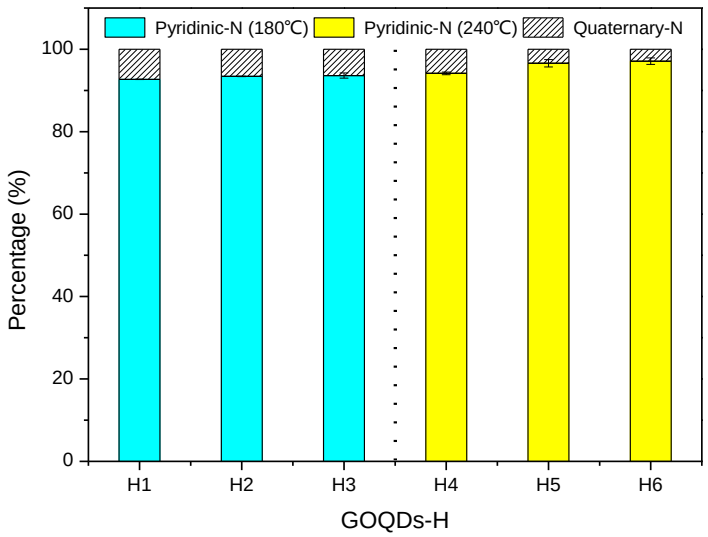

Figure 5.8. The percentage of the peaks deconvoluted from the N1s spectra.

Table 5-5. XPS data analyses of the N1s spectra of the GOQDs-H samples.

	Nitrogen bonding composition (%)		
Sample	Pyridinic-N	Quaternary-N	N1s/C1s
GOQDs-H1	**92.7**	**7.3**	**4.1%**
GOQDs-H2	**93.4**	**6.6**	**3.8%**
GOQDs-H3	**93.6**	**6.4**	**2.2%**
GOQDs-H4	**94.1**	**5.9**	**1.9%**
GOQDs-H5	**96.6**	**3.4**	**1.8%**
GOQDs-H6	**97.1**	**2.9**	**1.8%**

5.3.3 Optical properties

Figure 5.9 shows a photograph of the GOQDs-H aqueous suspensions at 0.125 mg/mL. Compared with the raw GOQDs sample, GOQDs-H1 shows lighter yellow colour. From H1 to H6, the colour is changed from light yellow to almost transparent. Its clarity demonstrates that the dispersion of the GOQDs-H in water is still very good. After two weeks, a tiny amount of the precipitate could be seen in GOQDs-H5 and H6 aqueous suspensions.

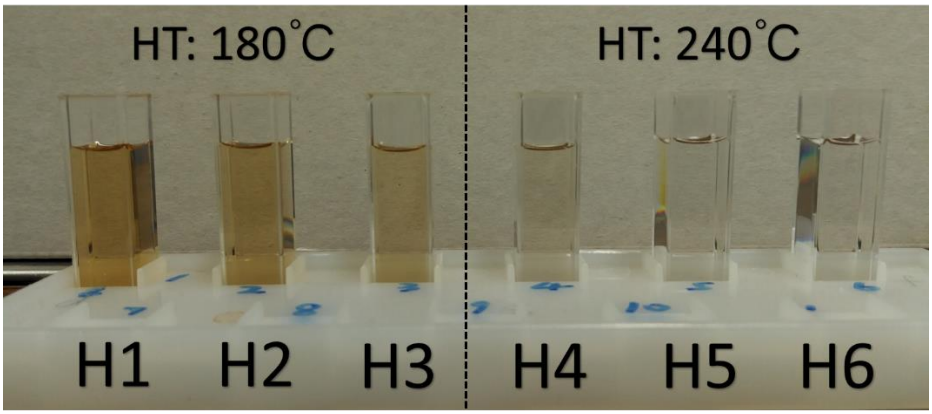

Figure 5.9. The GOQDs-H aqueous suspensions (0.125 mg/mL).

The UV-Vis spectra of the GOQDs-H samples aqueous suspension are shown in Figure 5.10. When the hydrothermal temperature is 180 ℃, the curve shape of the GOQDs-H samples is similar to that of the raw GOQDs sample, but the absorbance is slightly lower. Comparing these three samples, the whole absorbance would decline with increasing hydrothermal treatment time. A weak shoulder absorption peak at around 370 nm, which is attributed to the n-π^* transition of the C-N, C-O or C=O bonds, is still obvious in all three samples. When the hydrothermal temperature is 240 ℃ and the treatment time is just 3 h, the absorbance of the GOQDs-H4 suddenly decreases. The long treatment time makes the samples show low absorbance. Unlike the shoulder absorption peak appearing at around 370 nm in the raw GOQDs sample, these three

GOQDs-H samples obtained with 240 ℃ have a visible broad absorption peak at approximately 300 nm. In chapter 4, we speculate that the red-shift of the shoulder peak from 300 nm to 370 nm results from the increasing amount of delocalization due to the substantial oxidation. In this chapter, hydrothermal treatment provides a certain degree of reduction effect, which removes some oxygen-containing functional groups and reduces the size of the carbon matrix. Therefore, the amount of delocalization is less, and the shoulder peak returns back from 370 nm to 300 nm.

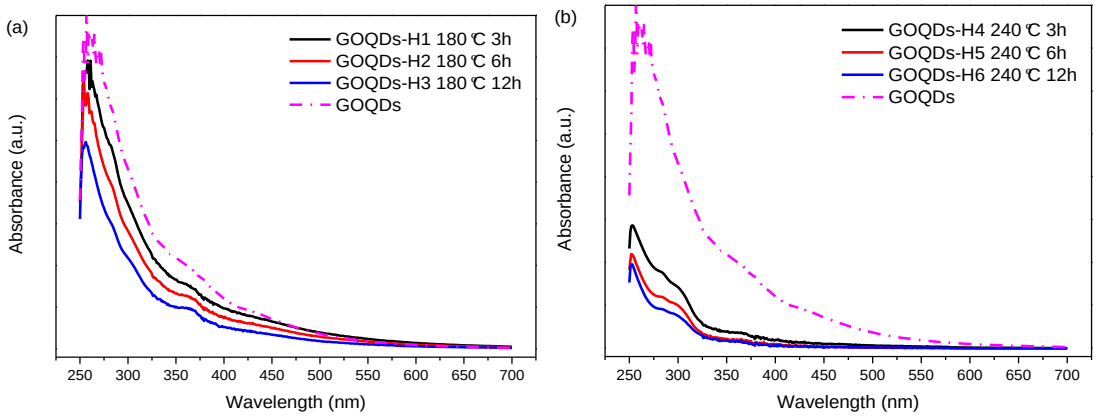

Figure 5.10. UV-Vis spectra of the GOQDs-H samples obtained with (a) HT: 180 ℃ and (b) HT: 240 ℃ aqueous suspensions, respectively. The concentration is 0.125 mg/mL.

The excitation-dependent PL behaviour of GOQDs-H samples under the same concentration are displayed in Figure 5.11. By comparing with the raw GOQDs sample, the PL behaviour of GOQDs-H is quite different, especially for the shift of the maximum emission peak. For the raw GOQDs sample, the maximum emission peak usually appears at around 530 nm when the excitation wavelength is 460 or 470 nm. However, after hydrothermal treatment, the GOQDs-H samples produce the strongest PL intensity at around 440 nm when the excitation wavelength is 320 nm. The difference of the PL behaviour could correspond to the changes in the structure of the GOQDs due to the high temperature and high pressure under the hydrothermal treatment.

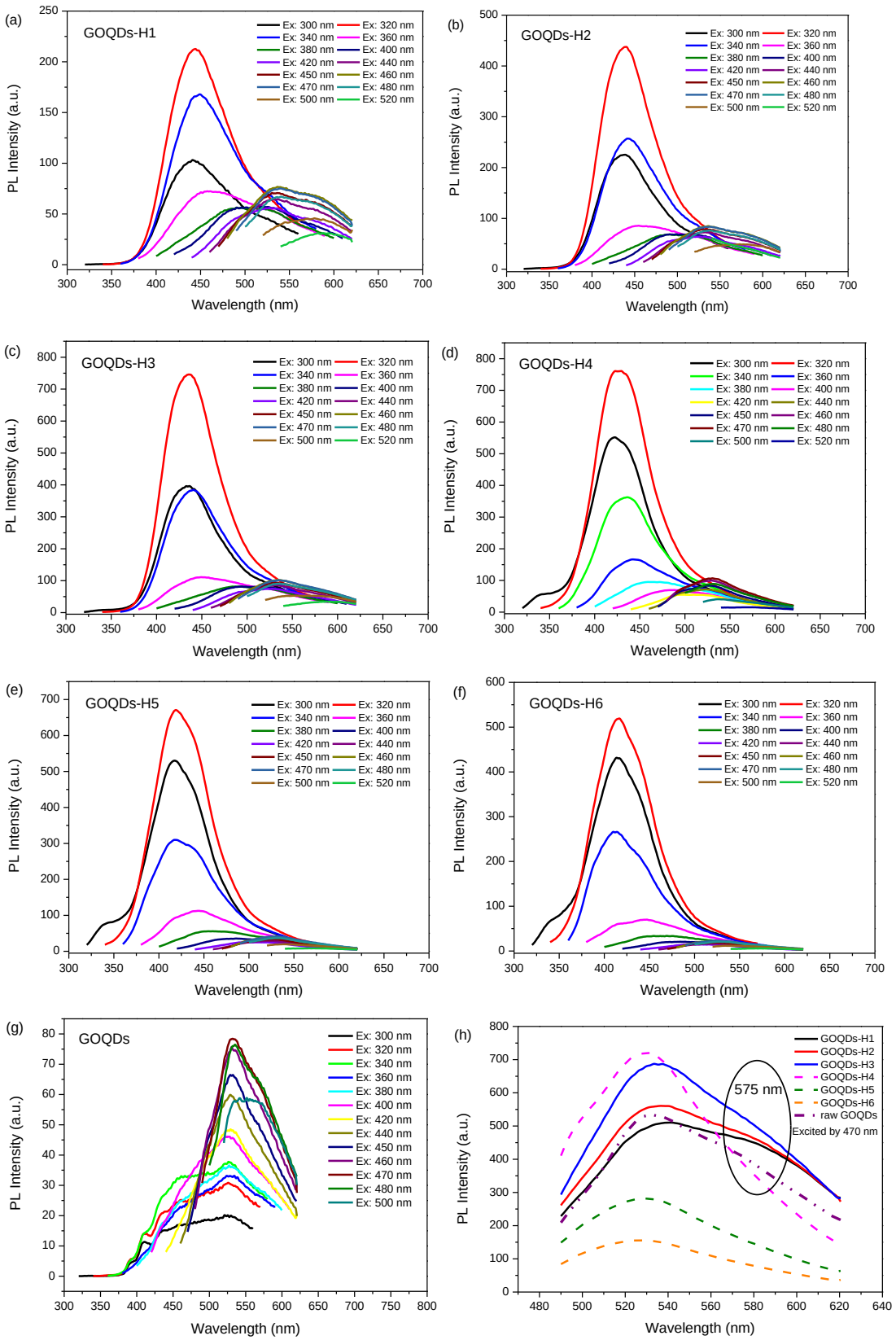

Figure 5.11. The excitation-dependent PL behaviour of (a)-(f) GOQDs-H and (g) raw materials GOQDs; (h) the emission spectra of GOQDs-H and GOQDs excited by 470 nm.

For all six samples, the PL behaviour is quite similar. To study the PL behaviour clearly, the results will be divided into four parts to see the changes. When the excitation wavelength is tuning from 300 nm to 360 nm, the emissions peak position is almost fixed at the violet colour region (420-470 nm). The PL intensity gradually starts to rise firstly, and then to decrease. The maximum PL intensity of the emission spectrum always appears when the excitation wavelength is 320 nm. When the excitation wavelength is from 380 nm to 420 nm, the region of the emission spectrum shifts to 470-500 nm region, which belongs to the blue colour and the emission spectra are much broader. When the excitation wavelength is from 440 nm to 480 nm, the emission spectrum continues to redshift to the green colour region (520-550 nm). The last part is the yellow colour region at around 570 nm when the excitation wavelength is 500nm or 520 nm.

As mentioned in the previous chapter, the PL spectrum of the GOQDs could be deconvoluted into two peaks, and one of them at around 570 nm is related to the oxygen-containing functional groups on the GOQDs, primarily as a result of the presence of the O-C=O structure. When excited by 470 nm, the emission spectra of all the samples are shown in Figure 5.11h. The range at around 575 nm still needs to be noticed. It could be easily found that raw materials GOQDs and GOQDs-H (180 ℃) have weak shoulders at around 575 nm. However, when the hydrothermal temperature is 240 ℃, there is no apparent peak in that range. Considering the low content of the O-C=O structure of the GOQDs-H (240 ℃), this result could testify again that the yellow colour range at about 575 nm is related to the O-C=O structure.

By comparing these six samples, we can find that the trend of the emission spectrum changes with the excitation wavelength is quite similar. However, the emission intensity and the peak positions change. Therefore, four excitation wavelengths (320, 380, 460 and 500 nm) are chosen to excite the samples, and four emission wavelengths with the maximum PL intensity belonging to four colour regions

are obtained and analyzed, as shown in Figure 5.12.

When the hydrothermal temperature is 180 ℃, the four excitation wavelengths can achieve violet, blue, green and yellow colours, separately (see Figure 5.12a). Among these four colours, the PL intensity of the violet colour is the maximum, which is about 3-5 times stronger than other colours. With increasing hydrothermal treatment time to 6 h or 12 h, the PL intensity of blue, green and yellow colours just slightly enhances. However, the violet colour under 320 nm excitation wavelength significantly strengthens its PL intensity, which is over 10 times stronger compared to the PL intensities of other colours when the hydrothermal treatment time is 12 h.

When the hydrothermal temperature is 240 ℃, the same four excitation wavelengths can lead to emission of violet, blue, and green colours, separately. The emission spectrum at the excitation wavelength of 500 nm mostly belongs to the green area instead of the yellow colour. The PL intensity of the violet colour is still the strongest, which is about 23 times stronger than others when the hydrothermal treatment time is 3 h. Different from the H1-H3 samples, the PL intensity of all the colours would decreases with prolonging the hydrothermal treatment time. In particular, the green colour of the GOQDs-H6 sample is very weak. The reason for the weak intensity is related to the specific hydrothermal treatment. 240 ℃ can deeply change the structure of GOQDs-H, resulting in the weakening of the green colour PL emission. The details will be discussed later.

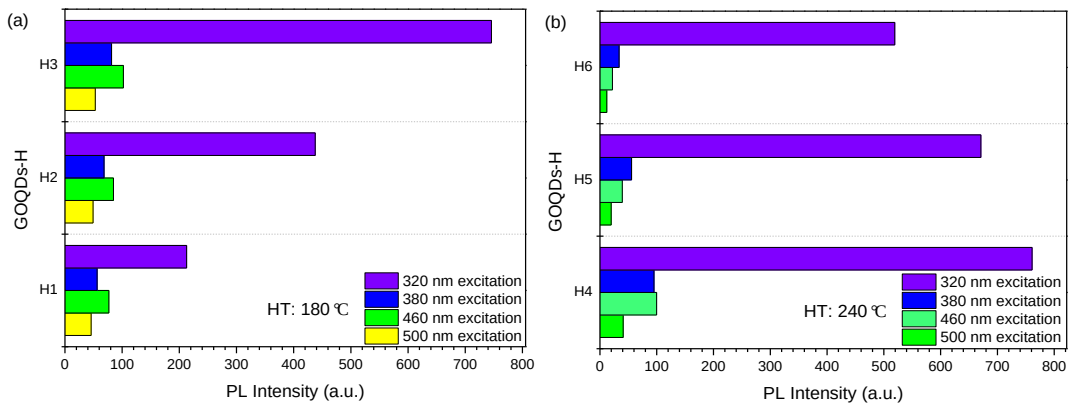

Figure 5.12. The PL emission (violet, blue, green and yellow) intensity under a certain excitation (a) GOQDs-H 180 ˚C and (b) GOQDs-H 240 ˚C.

From the above results of the PL intensity, the two batches show different tendencies, which could partially explained by connecting with the previous structure analysis. For example, the violet colour may correspond to the carbon matrix. If this is the case, the content of the carbon matrix will affect the PL intensity of the violet colour region. To demonstrate this inference, the content of the carbon matrix and violet colour PL intensities are analyzed together in Figure 5.13a. The maximum PL intensity of the emission spectrum excited by 320 nm increases when the carbon matrix content of the GOQDs-H samples under 180 ℃ hydrothermal temperature rises. The same trend happens for the 240 ℃ sample batch, as shown in Figure 5.13b.

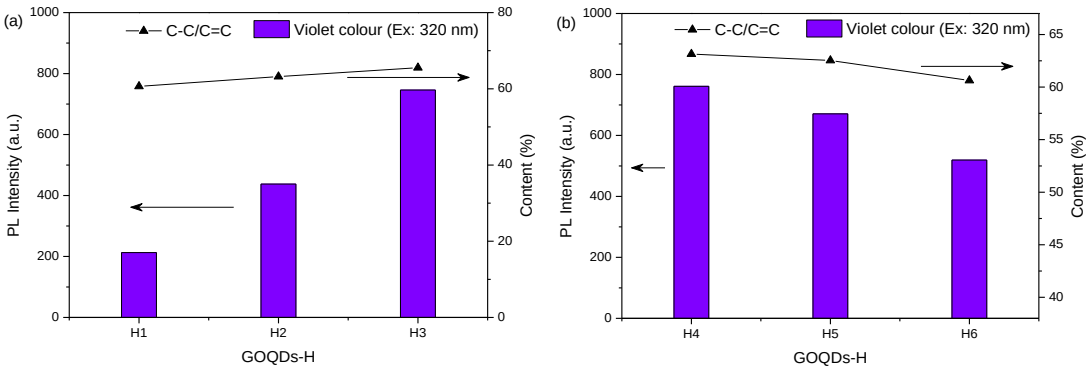

Figure 5.13. The maximum PL intensity excited by 320 nm and the carbon matrix content of the GOQDs-H samples under (a) 180 ˚C and (b) 240 ˚C.

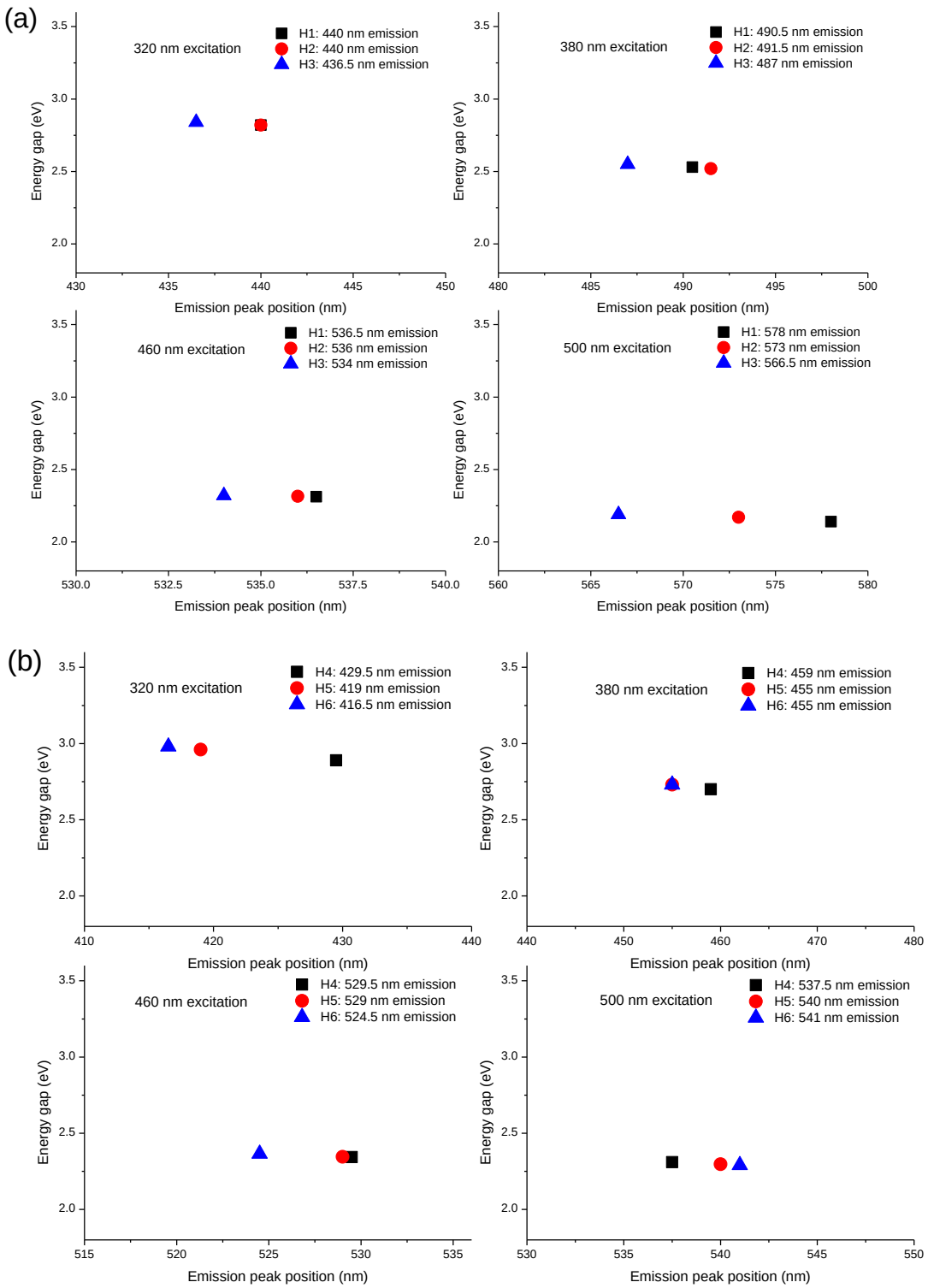

Figure 5.14. The energy gap and PL emission (violet, blue, green and yellow) peak position under a certain excitation (a) GOQDs-H 180 ˚C and (b) GOQDs-H 240 ˚C.

In Figure 5.14, 320, 380, 460 and 500 nm excitation wavelengths are used, which

correspond to the emission of violet, blue, green, and yellow colour region respectively. The maximum PL intensity of the emission spectrum is also shown in Figure 5.14. The corresponding energy gap could be calculated and compared. In the same batch, we can find that the peak position blue-shifts when the hydrothermal treatment time increases from 3 h to 12 h. Therefore, the energy gap between the excited state (S1) and the ground state (S0) becomes larger. If making the comparison between the samples with the same hydrothermal treatment time, we can find that the sample with the higher hydrothermal temperature has a shorter emission wavelength, that is, a greater energy gap.

Higher hydrothermal temperature and more prolonged treatment time remove more oxygen-containing functional groups. It could be considered that the width of the excited state (S1) should depend on the content of the oxygen-containing functional groups. The less content makes the width narrower, and so the energy gap increases.

The quantum yield results for 400-500 nm emission range of the GOQDs-H are displayed in Table 5-6. Compared with the reference standard material Quinine Sulfate, the GOQDs-H samples have a quantum yield of about 2-5%, which is much higher than that of the raw GOQDs materials (<0.05%) and is similar to some publications results.[25,101,187] When the hydrothermal temperature is 180 ℃, just 3 h treatment time could significantly raise the quantum yield to 2.14%. With the extension of the treatment time, the quantum yield could be up to 3.20% (6 h) or 4.15% (12 h). In contrast, the highest quantum yield result for the batch with the 240 ℃ hydrothermal temperature is about 5.15% when the hydrothermal treatment time is 3 h. More prolonged time would make the value lower.

Table 5-6. The quantum yield results of the GOQDs-H samples excited by 320 nm excitation (Emission range from 400-500 nm).

sample	QY	sample	QY
GOQDs-H1	2.14%	GOQDs-H4	5.15%
GOQDs-H2	3.20%	GOQDs-H5	4.22%
GOQDs-H3	4.51%	GOQDs-H6	2.99%

The quantum yield results for 500-600 nm emission range of the GOQDs-H are shown in Table 5-7. Compared with the reference standard material Fluorescein, the GOQDs-H samples have a quantum yield of about 0.44% to 2.35%, which is again higher than that of the raw GOQDs materials (~0.40%). When the hydrothermal temperature is 180 ℃, 3 h or 6 h treatment time just slightly raise the quantum yield to 0.44% or 0.59%. The longest time 12 h lead to the highest value of about 0.94%. When the hydrothermal temperature is 240 ℃, just 3 h treatment time could significantly raise the quantum yield to 2.35%. Longer treatment time also makes the quantum yield lower.

Table 5-7. The quantum yield results of the GOQDs-H samples excited by 470 nm excitation (Emission range from 500-600 nm).

sample	QY	Sample	QY
GOQDs-H1	0.44%	GOQDs-H4	2.35%
GOQDs-H2	0.59%	GOQDs-H5	1.31%
GOQDs-H3	0.94%	GOQDs-H6	1.01%

From the above results, we could find that the quantum yield results for both 400-500 nm and 500-600 nm ranges of the GOQDs-H have significantly increased, and the trend under the different hydrothermal temperatures with the changes of the treatment time is the same. The hydrothermal treatment could remove some oxygen-containing functional groups and increase the content of the carbon matrix, which has sp^2 hybridization structure. It could be considered that relatively more sp^2 hybridization structure could help increase the quantum yield. Besides, the impact of the 240 ℃

hydrothermal treatment is relatively higher than that of 180 ℃. However, perhaps due to less content of the COOH groups, the dispersion stability of the GOQDs-H (240 ℃) is not as good for the GOQDs-H (180 ℃). The very high concentrations of the GOQDs-H (240 ℃) could not be prepared. Therefore, even though they have a better quantum yield, the PL intensity under the same concentration is not stronger than that of GOQDs-H (180 ℃).

5.3.4 Mechanism analysis

It could be considered that relatively more sp^2 hybridization structure could provide more "routes", which can allow more electrons to "move". After excited by the light, the electrons in the ground state would jump to the excited state, that is, π to π^* transition. Due to more "routes", the efficiency of the transitions between different energy levels would rise. The emission spectra range depends on the excited state. According to the previous analysis and hypothesis, the mechanism of the PL behaviour of the GOQDs and GOQDs-H is shown in Figure 5.15. G1 states are sp^2 hybridization structure in carbon matrix. G2 states are C=O structure, such as aldehyde or ketone groups. G3 states are O-C=O structure, such as carboxylic acid or ester groups.

Before hydrothermal treatment, GOQDs have relatively more oxygen-containing functional groups and less carbon matrix with sp^2 hybridization structure. Therefore, when excited by 320 nm, the electrons would jump to the higher energy excited states. Due to the less content of the C-C/C=C structure, the G1 states is relatively narrow, so fewer electrons could drop back to the G1 states and go *via* the R1 route. When excited by 470 nm, the electrons could jump and drop back G2 or G3 states. Due to the relatively more content of the C=O structure, the electrons prefer to drop from G2 states to ground state *via* the R2 route. Therefore the emission spectrum has a maximum PL intensity at around 530 nm. Meanwhile, some electrons could drop to the G3 states and emit around 575 nm light when they are using the R3 route back to the ground state. (See Figure 5.15a)

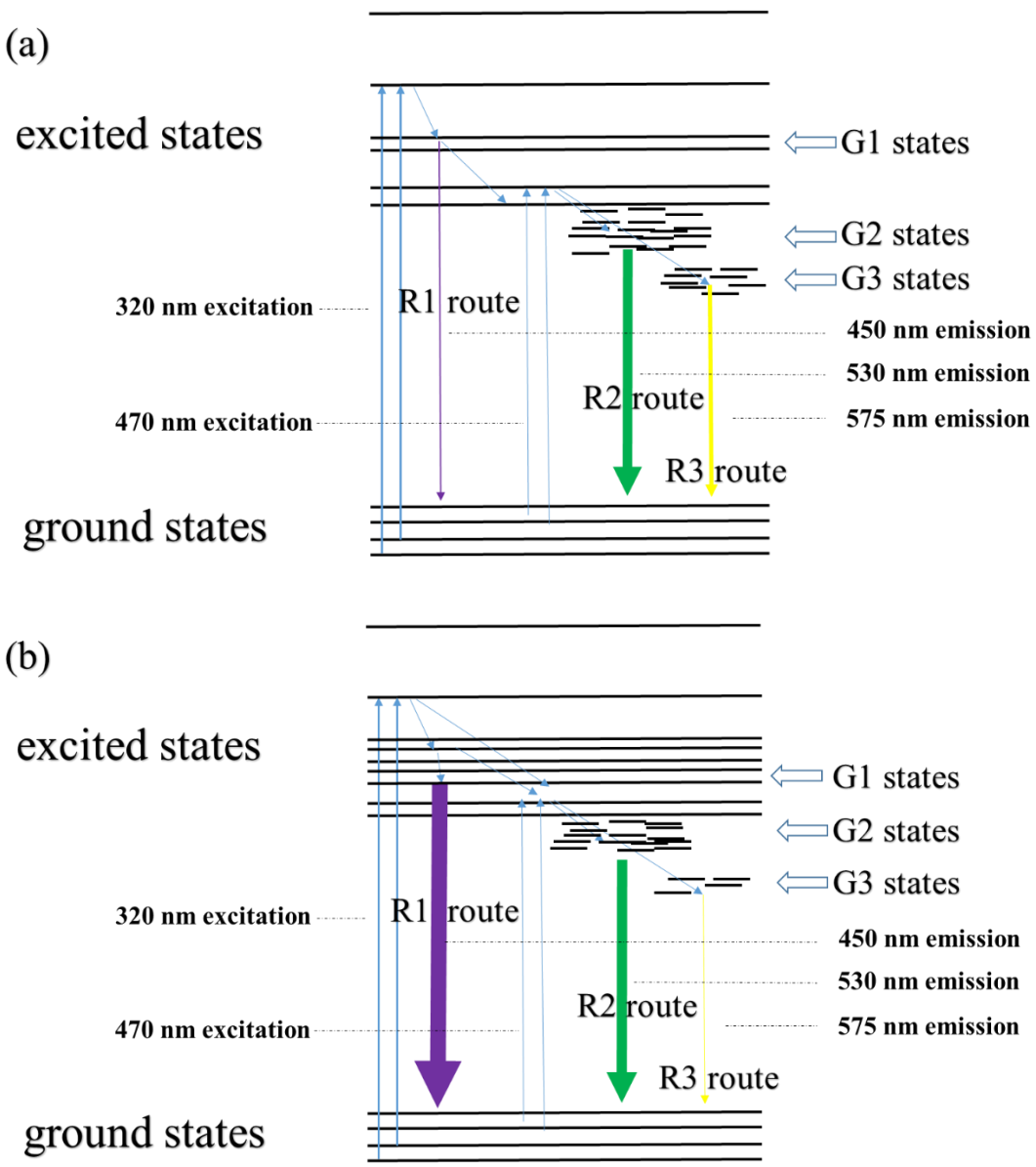

Figure 5.15. The mechanism of PL behaviour of the GOQDs (a) and GOQDs-H (b).

After hydrothermal treatment, the structure and the ratio of the oxygen-containing functional groups of the GOQDs-H alter, so the width of the corresponding states also changes, as shown in Figure 5.15b. The increasing of the content of the carbon matrix results in the wider of the G1 states. When excited by 320 nm, more electrons could fall in the G1 states and go down to the ground states *via* the R1 route. The G2 states become wider because some epoxy and O-C=O structures are change to the C=O structure. So the quantum yield for the green colour range is obviously increasing. The content of the

O-C=O structure reduces, which affect the G3 states. Fewer electrons drop in the G3 states, and only weak yellow colour light could be emitted *via* the R3 route.

Actually, the mechanism of PL behaviour is much complicated. The excited states of different functional groups usually overlaps, and the routes of the electrons between different energy levels are diverse. The PL behaviour is affected by many factors at the same time. Each kind of structure is analysed and simply processed so that the mechanism could be understood more easily.

5.3.5 Cell viability and ROS generation ability

The investigation of the photodynamic therapy (PDT) effect of the GOQDs-H was carried out in the same condition as the characterization in previous chapter. As shown in Figure 5.16a, after 24 h incubation, the HeLa cell viability slightly decreased to 75% when the concentrations of GOQDs-H3 increased to 0.8 mg/mL, which could indicate that the GOQDs-H3 sample also has almost no influence on the cells and have a potential in the biocompatibility of the nanoparticles.

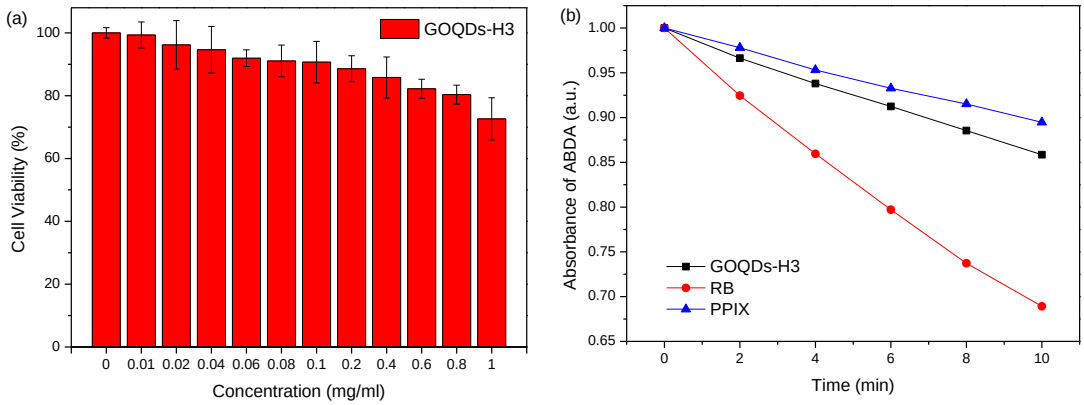

Figure 5.16. (a) Cell viability of HeLa cells incubated with different concentrations of GOQDs-H3; (b) ROS generation of GOQDs-H3 detected by ABDA.

The $^1O_2$ production of GOQDs-H3 was measured by the same method mentioned above with ABDA as an indicator, and the results were shown in Figure 5.16b. After irradiated by the 365 nm light for 10 min, the absorption of ABDA for GOQDs-H3, RB, and PPIX decreased to about 86%, 67%, and 91%, respectively. GOQDs-H3 show much quicker decline rate than PPIX, and slower than RB. This result demonstrates that GOQDs-H3 also have the better ROS-generating ability.

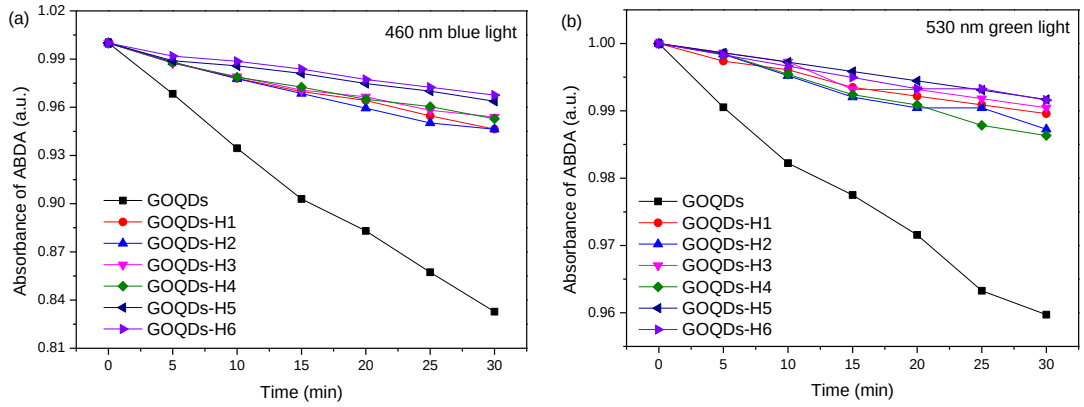

Figure 5.17. ROS generation of the GOQDs-H samples under (a) 460 nm blue light and (b) 530 nm green light irradiation detected by ABDA.

In Figure 5.17, ROS generation of the GOQDs-H samples under 460 nm blue light and 530 green light irradiation is displayed. Compared with the raw material GOQDs, the ROS generation ability of GOQDs-H samples is apparently reduced. This could be explained by the less content of the oxygen-containing functional groups due to the hydrothermal treatment. GOQDs-H5 and H6 have relatively lower ROS generation. According to the analysis in the previous chapter, carboxyl acid groups may be the main factor to determine the ROS generation. Considering that the worse performance of the dispersion stability, it could be attributed to the same reason, that is, the less content of the COOH groups.

5.4 Conclusion

In this chapter, the GOQDs as raw materials are further treated by the hydrothermal method. Different temperature and different treatment time are set to compare and analyse the effect on the GOQDs structure and PL behaviours. Firstly, the difference of the hydrothermal temperature would affect the changes of the oxygen-containing functional groups. Lower temperature at 180 ℃ can have apparent changes when the treatment time is long enough. Higher temperature at 240 ℃ could cut the nanoparticles much more quickly, and more groups would be reduced or removed within a short period. Some publications used a similar method and got GQDs samples, which were almost totally reduced and no oxygen-containing functional groups were left. However, the most samples prepared in this work still have a lot of oxygen-containing functional groups and have good dispersion. This could be explained by the two reasons. Firstly, the raw materials used in this work are GOQDs. They have more groups than graphene oxide, which is always used in other hydrothermal research. Another reason may be the equipment. The pressurizing vessel in this work is a small chamber and it is heated in the heating oven. The gas pressure could not be added manually. The pressure may be less than others work, which lead to the weak reduction effect of the hydrothermal treatment.

Because of the changes in the structure and the content of the oxygen-containing functional groups, the PL behaviour of the GOQDs-H has much difference to that of the GOQDs. GOQDs-H still has a wide emission range, including from violet to yellow colour. It could be also found that the performance of the PL intensity and the quantum yield are both increased. Due to the weak hydrothermal effect, the GOQDs-H still can be dispersed in water well and generate ROS.

Finally, with the help of the structure analysis in the previous and this chapter, the structural changes and the PL behaviour are linked, then the mechanism of PL is simply

concluded.

5.5 Supporting information

1. QY of GOQDs-H (Range 400-500 nm)

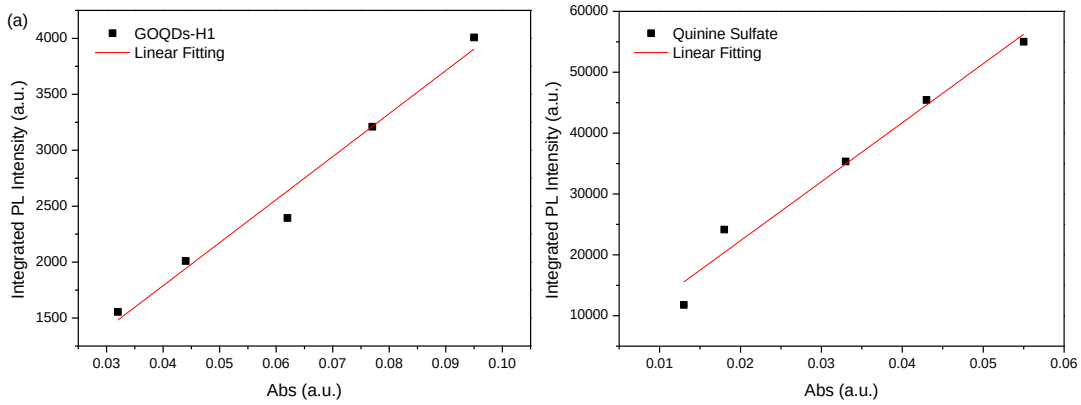

	GOQDs-H1					Quinine Sulfate				
Abs	0.095	0.077	0.062	0.044	0.032	0.013	0.018	0.033	0.043	0.055
Integrated PL	4008	3210	2394	2010	1555	11777	24163	35338	45453	55004
Slope	38449					968915				
QY	2.14%					54%				

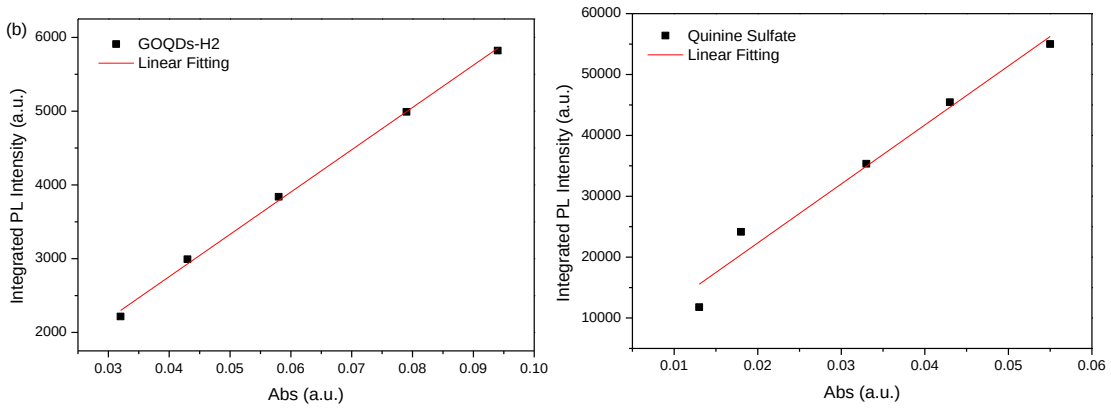

	GOQDs-H2					Quinine Sulfate				
Abs	0.094	0.079	0.058	0.043	0.032	0.013	0.018	0.033	0.043	0.055
Integrated PL	5822	4991	3840	2993	2216	11777	24163	35338	45453	55004
Slope	57343					968915				
QY	3.20%					54%				

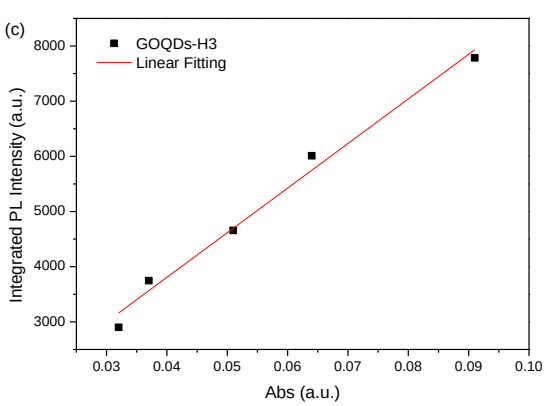

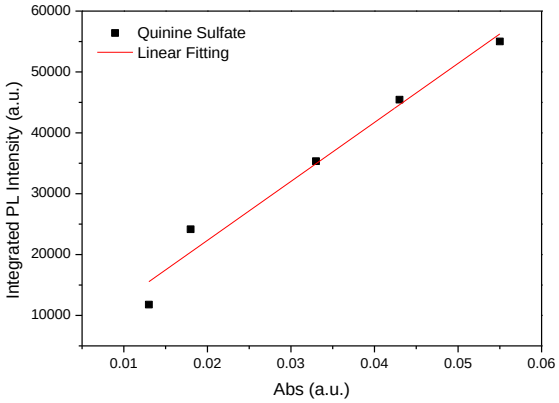

	GOQDs-H3					Quinine Sulfate				
Abs	0.091	0.064	0.051	0.037	0.032	0.013	0.018	0.033	0.043	0.055
Integrated PL	7786	6010	4658	3747	2901	11777	24163	35338	45453	55004
Slope	80848					968915				
QY	4.51%					54%				

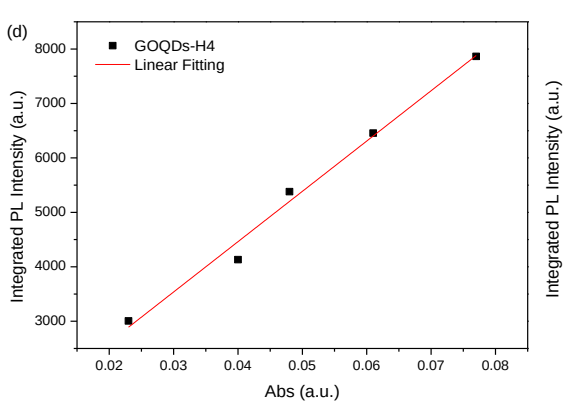

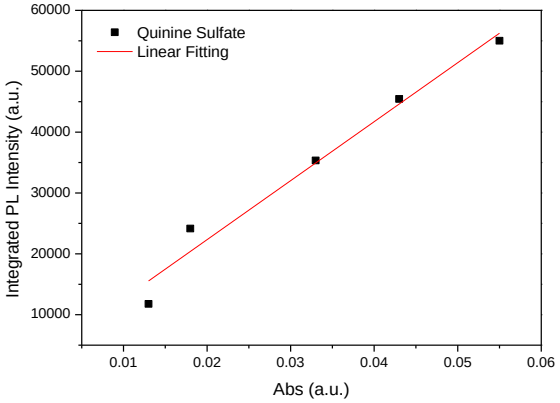

	GOQDs-H4					Quinine Sulfate				
Abs	0.077	0.061	0.048	0.040	0.023	0.013	0.018	0.033	0.043	0.055
Integrated PL	7864	6456	5380	4131	3005	11777	24163	35338	45453	55004
Slope	92409					968915				
QY	5.15%					54%				

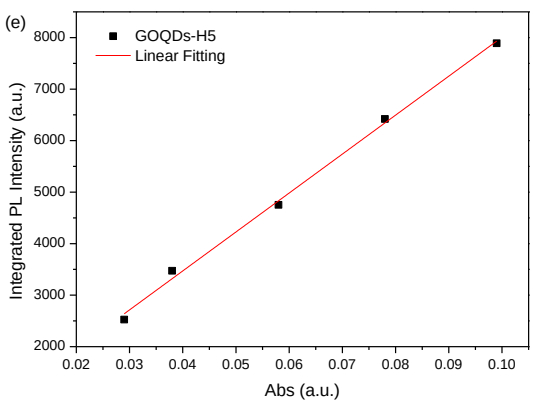

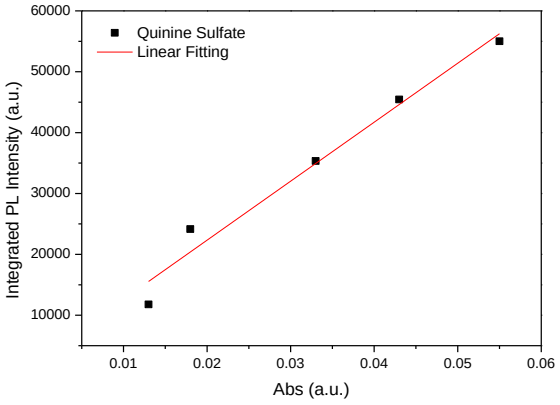

	GOQDs-H5					Quinine Sulfate				
Abs	0.099	0.078	0.058	0.038	0.029	0.013	0.018	0.033	0.043	0.055
Integrated PL	7891	6421	4753	3474	2526	11777	24163	35338	45453	55004
Slope	75629					968915				
QY	4.22%					54%				

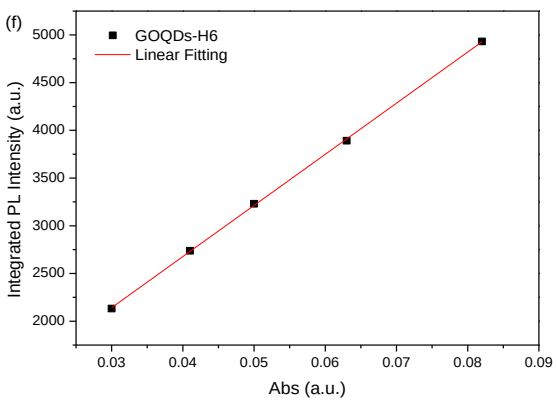

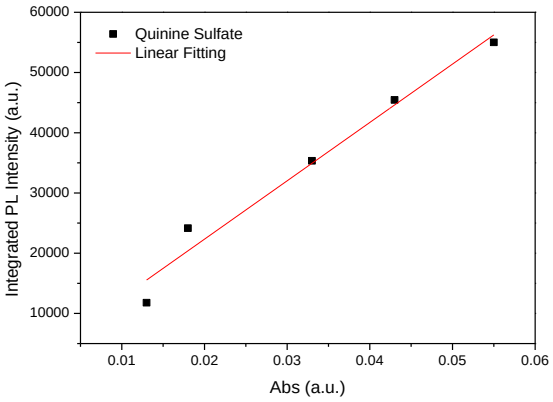

	GOQDs-H6					Quinine Sulfate				
Abs	0.082	0.063	0.050	0.041	0.030	0.013	0.018	0.033	0.043	0.055
Integrated PL	4931	3891	3231	2738	2132	11777	24163	35338	45453	55004
Slope	53574					968915				
QY	2.99%					54%				

Figure S 3. (a) - (f) Plots of integrated PL intensity of GOQDs-H1 to GOQDs-H6 and Quinine Sulfate (reference standard material) as a function of absorbance at 320 nm and relevant raw data.

2. QY of GOQDs-H (Range 500-600 nm)

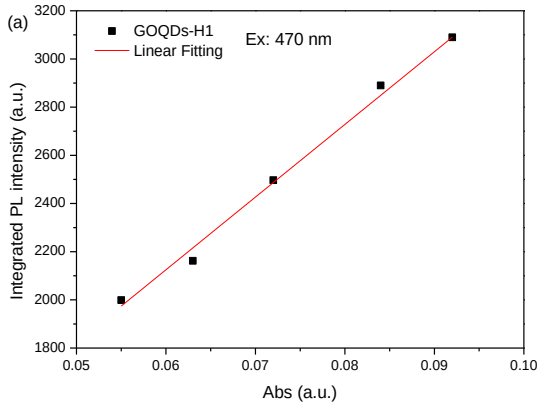

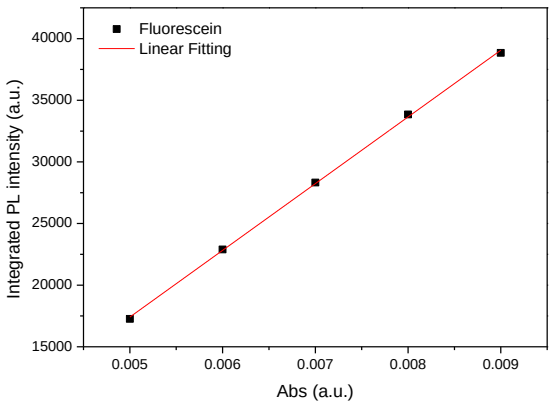

	GOQDs-H1					Fluorescein				
Abs	0.092	0.084	0.072	0.063	0.055	0.009	0.008	0.007	0.006	0.005
Integrated PL	3090	2854	2480	2214	1978	38849	33848	28325	22895	17263
Slope	30145					5412500				
QY	0.44%					79%				

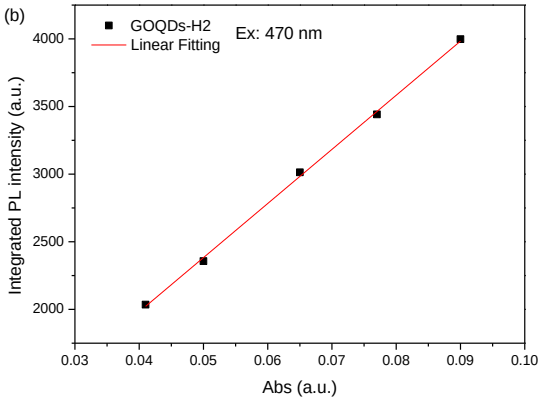

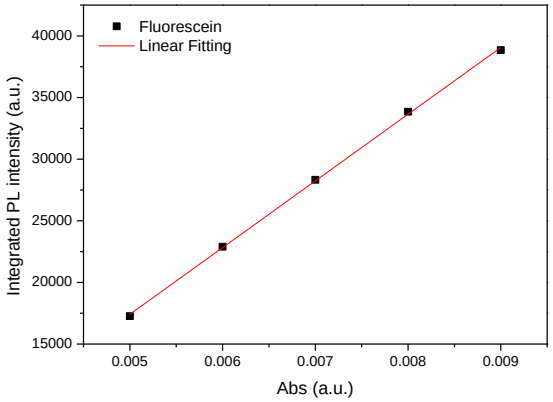

	GOQDs-H2					Fluorescein				
Abs	0.090	0.077	0.065	0.050	0.041	0.009	0.008	0.007	0.006	0.005
Integrated PL	3988	3458	2987	2370	2032	38849	33848	28325	22895	17263
Slope	40422					5412500				
QY	0.59%					79%				

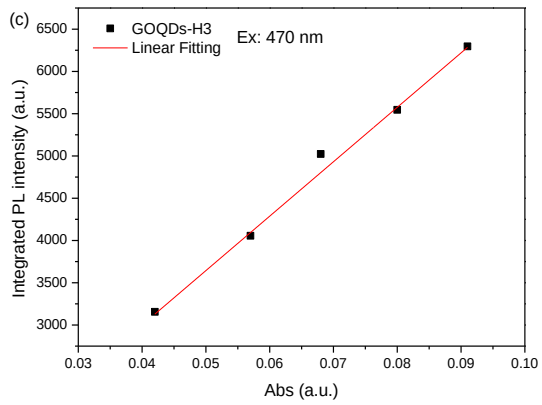

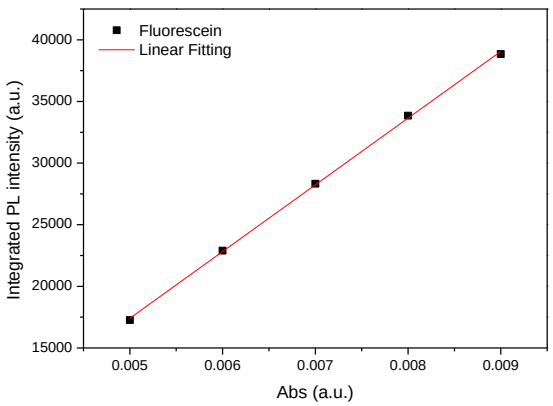

	GOQDs-H3					Fluorescein				
Abs	0.091	0.080	0.068	0.057	0.042	0.009	0.008	0.007	0.006	0.005
Integrated PL	6281	5592	4983	4086	3135	38849	33848	28325	22895	17263
Slope	64402					5412500				
QY	0.94%					79%				

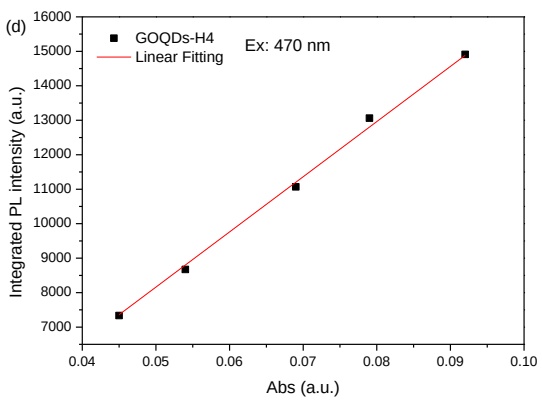

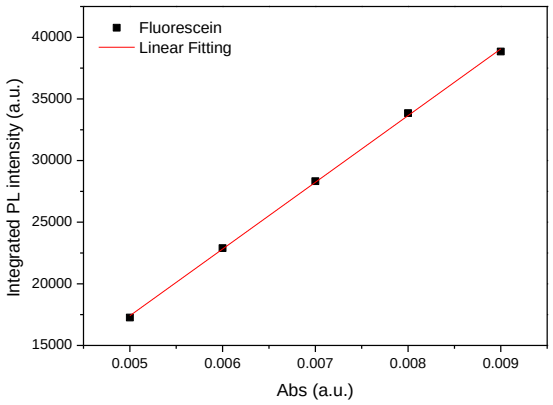

	GOQDs-H4					Fluorescein				
Abs	0.092	0.079	0.069	0.054	0.045	0.009	0.008	0.007	0.006	0.005
Integrated PL	14912	13061	11068	8673	7334	38849	33848	28325	22895	17263
Slope	161005					5412500				
QY	2.35%					79%				

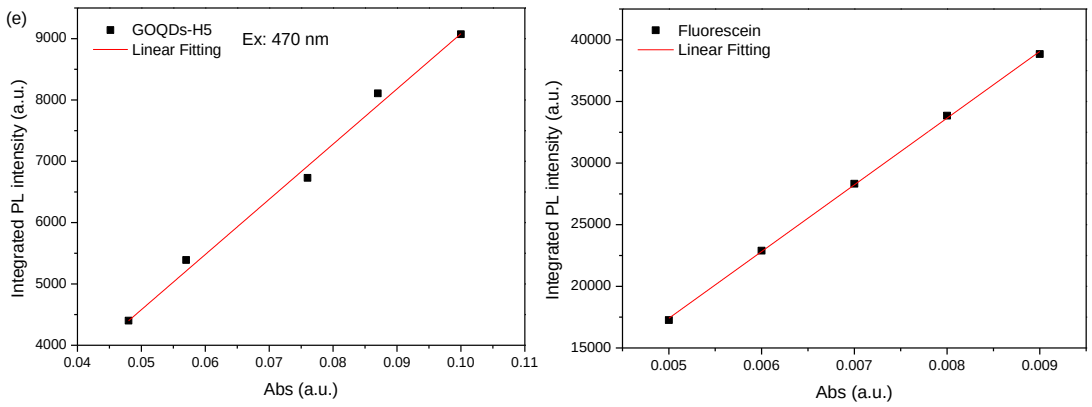

	GOQDs-H5					Fluorescein				
Abs	0.1	0.087	0.076	0.057	0.048	0.009	0.008	0.007	0.006	0.005
Integrated PL	9072	8108	6730	5390	4401	38849	33848	28325	22895	17263
Slope	89752					5412500				
QY	1.31%					79%				

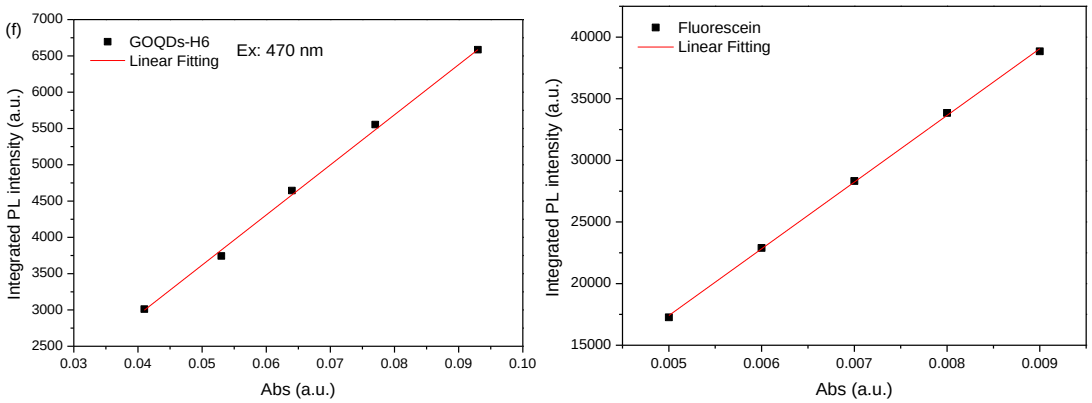

	GOQDs-H6					Fluorescein				
Abs	0.093	0.077	0.064	0.053	0.041	0.009	0.008	0.007	0.006	0.005
Integrated PL	6585	5502	4633	3744	3012	38849	33848	28325	22895	17263
Slope	69198					5412500				
QY	1.01%					79%				

Figure S 4. (a) - (f) Plots of integrated PL intensity of GOQDs-H1 to GOQDs-H6 and Fluorescein (reference standard material) as a function of absorbance at 470 nm and relevant raw data.

6 Preparation and characterization of the luminescent carbon nanodots derived from phenylenediamine: from controllable fabrication to tunable photoluminescence properties

6.1 Introduction

In chapter 4 and 5, several series of luminescent GOQDs nanoparticles derived from graphite powder were successfully prepared with chemical oxidation method and hydrothermal treatment. The resultant GOQDs can show yellow and green fluorescence, and GOQDs-H can exhibit bright blue and yellow fluorescence. These new class of nanomaterials is considered to have good photoluminescence properties and be potentially used in health care. However, some of the disadvantages of these nanomaterials from the difficulty in complicated reaction (*e.g.* using a lot of strong acids) and long-wavelength (red colour region). Therefore, the development of a new method for the preparation of water-soluble, multicolour PL materials and a relatively simple reaction is still highly desirable.

Luminescent carbon nanodots derived from small molecules like citric acid, glucose and sucrose as the carbon source *via* bottom-up approaches have been investigated.[58,79,188–190] Phenylenediamine, which has three kinds of isomers: o-phenylenediamine (o-PD), m-phenylenediamine (m-PD) and p-phenylenediamine (p-PD), are important precursors for synthesizing heterocyclic compounds and polymers.[191] Several reports have mentioned that phenylenediamine was used as raw materials *via* the hydrothermal method for preparing luminescent carbon nanodots.[28,192,193] Their synthesized CNDs can exhibit blue or yellow fluorescence.

However, they rarely explain or mention how the mechanism of the synthesis. Meanwhile, it could not precisely control the product *via* the hydrothermal method. In this chapter, I will mainly focus on the preparation, structure and properties of multicolour luminescent CNDs with different colour emissions by using the three kinds of phenylenediamine isomers, through a simple polymerization method.

6.2 Mechanism of polymerization in theory

The main mechanism of the synthesis is related to electrophilic aromatic substitution.[194] In theory, the chemical polymerization of phenylenediamine by $K_2S_2O_8$ should proceed *via* a radical propagation mechanism as shown in Steps 1-3 below:

Step 1: The dissociation of potassium persulfate.

First of all, $K_2S_2O_8$ could be dissociated into anionic radicals as shown in Figure 6.1. In aqueous solution at 50 ℃, potassium persulfate could decompose into K^+ ions and $S_2O_8^{2-}$ ions. Then $S_2O_8^{2-}$ ions could decompose into persulfate ions and free radical, which behave as anionic radicals. The free radical was very able to attract the amino groups (NH_2) at the carbon location of the phenylenediamine because of electrostatic attraction.

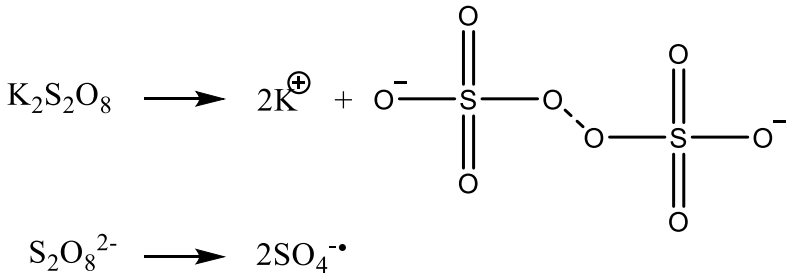

Figure 6.1. The dissociation of $K_2S_2O_8$.

Step 2: Oxidation of monomer

The oxidation of phenylenediamine to free radicals could occur and be stabilized in different resonance forms, as shown in Figure 6.2. Firstly, the free radicals would appear at the amino groups, and then it would transfer to the adjacent carbon location. It also could transfer to the nearby or opposite carbon location, due to the effect of the resonance structure in aromatic molecules. For o-PD and m-PD, the free radical may transfer to the opposite carbon location to the amino groups. However, for p-PD, the free radical would prefer to transfer to the nearby carbon location, due to the occupation of the amino groups.

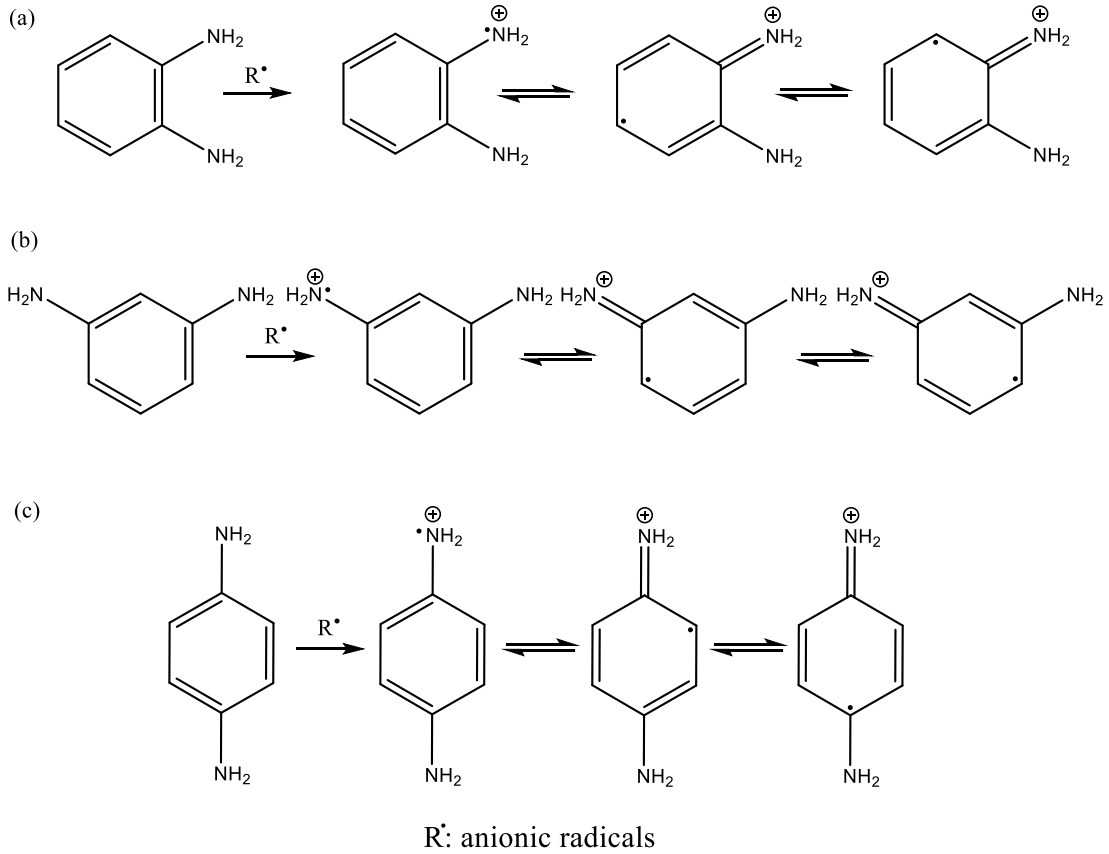

Figure 6.2. The oxidation of monomer: (a) o-PD, (b) m-PD, and (c) p-PD.

The active sites in the three kinds of phenylenediamine monomer due to the effect of free radical are different because of the different positions of the two amino groups, as shown in Figure 6.3. The amino group is ortho- and para- director in electrophilic aromatic substitution.[194] The most active sites available are ortho and para positions in each molecule.

(1) For o-PD (Figure 6.3a), the para carbon locations to the two amino groups are C-4 and C-5 point. Although the ortho carbon location at C-3 and C-6 point to the amino groups are empty, the positions at C-3 and C-6 flanked by the fewest number of substituents are favoured to be attacked by the electrophile. Therefore, C-4 and C-5 point are active sites.

(2) For m-PD (Figure 6.3b), C-4 and C-6 point are para carbon locations to amino

groups, and C-2 point is ortho carbon location. C-2 point is surrounded by two amino groups, while C-4 or C-6 point just have one group nearby. The positions flanked by the fewer number of substituents is favoured by the electrophile. Therefore, the attacking positions available are C-4 and C-6 point. However, C-4 and C-6 point still have one nearby substituent. Therefore, the active sites of m-PD are less favoured than o-PD.

(3) For p-PD (Figure 6.3c), since the para carbon location is already occupied by NH_2 group, only ortho carbon locations at C-2, C-3, C-5 and C-6 point are available, where are active sites for p-PD monomers.

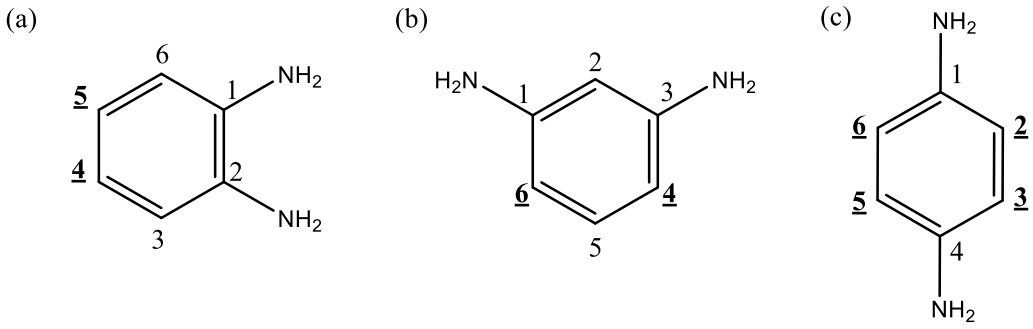

Figure 6.3. The active sites in the phenylenediamine due to the free radical: (a) o-PD, (b) m-PD, (c) p-PD.

Step 3: Head to tail coupling of monomers

According to the above analysis, the active sites in the three kinds of isomers have been known. The free radical at the amino groups could be considered as the "head", and the active sites at carbon location could be as the "tail". Theoretically, the head to tail coupling of free radicals could take place *via* elimination reaction of two free radicals, and then the monomers are connected. The possible polymerization orientations could be described as two modes.

The first mode is relatively more straightforward, which could be considered to be straight direction, as shown in Figure 6.4a, 6.5a and 6.6a. The phenylenediamine

monomers are connected one by one when their monomers are set in the same direction in order. The length of the generated material would become longer if the amount of free radical and monomers are enough. Because the direction of the generated material is one way. the structure obtained by this mode is also called ladder-like structure[195].

The second mode, which is mentioned in Figure 6.4b, 6.5b and 6.6b, is relatively complicated. When the monomers are not set in the same direction, they may not follow the first mode and do not grow in one direction in order. Therefore, the structure would not be the ladder-like structure. The monomers could be connected with others in different directions, then the generated material would become larger and larger. The process seems to be from a single point to a large surface. Due to the random directions in head to tail coupling of monomers, the mode could be called the crossing direction. To well explain this mode process, four monomers of each phenylenediamine isomers are used as an example, separately. They are coupled step by step, as shown in Figure 4b, 5b and 6b. The structure of the generated materials is quite different.

In fact, these two modes could happen at the same time. When the amount of the monomers are more, the coupling process would become more complicated and their generated structure would be more variety. In theory, the process can be controlled by adjusting the amount of free radicals. When the free radical is not excessive, the polymerization should be stopped when using all the free radicals. Then synthesized CNDs with different size *via* controlling the amount of potassium persulfate would have different structure and different PL properties.

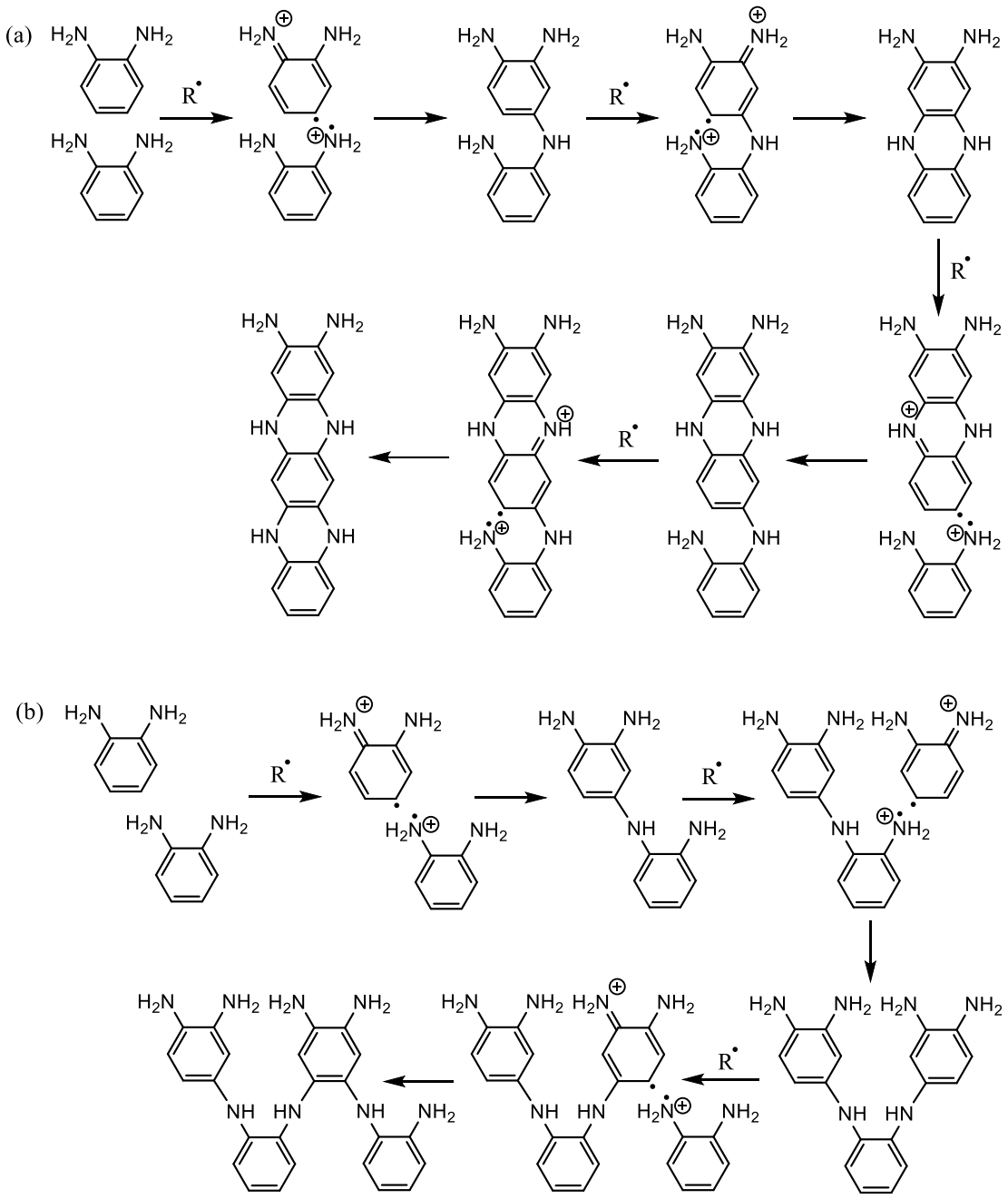

Figure 6.4. Possible coupling orientations in o-PD: (a) straight, (b) cross.

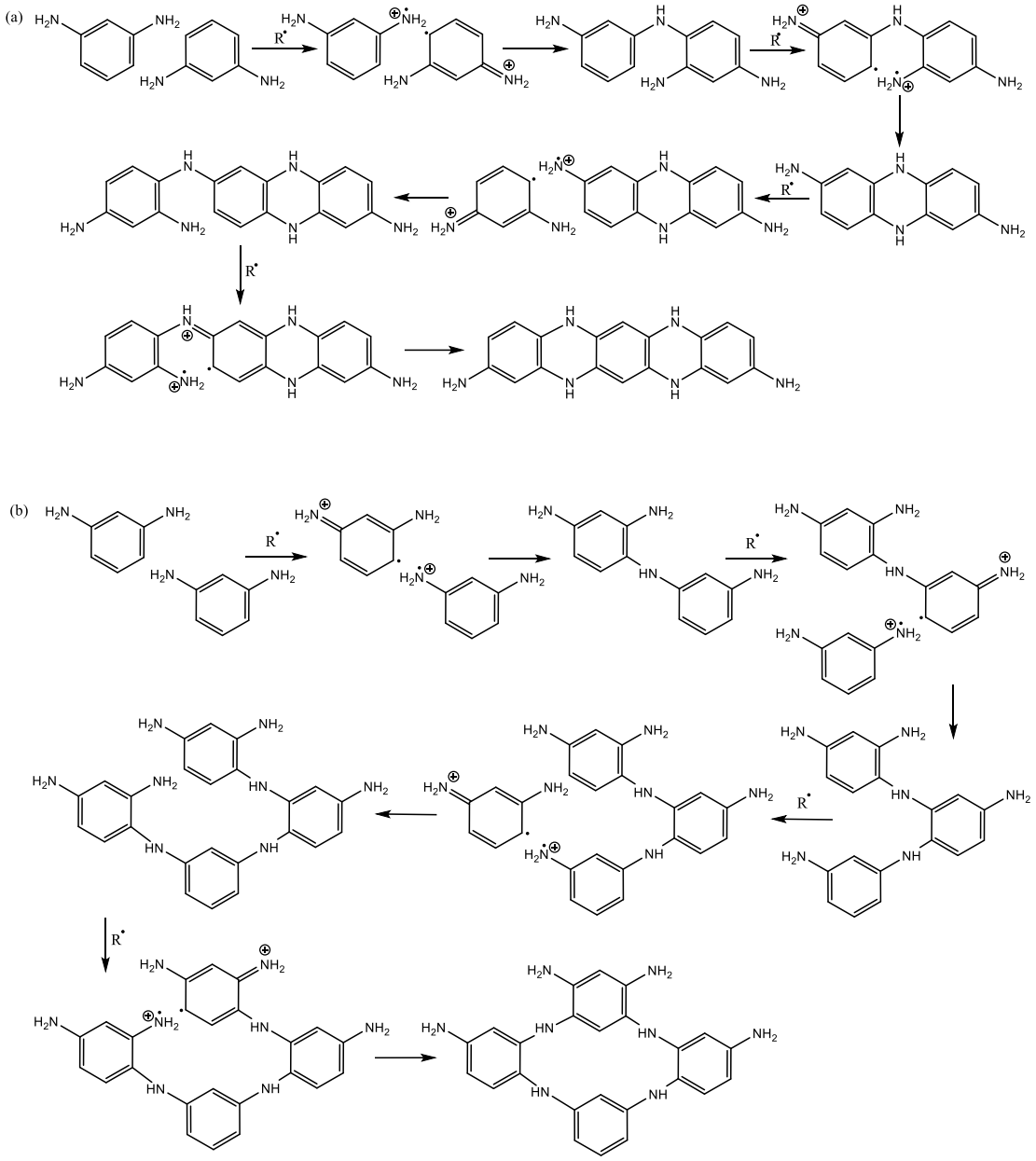

Figure 6.5. Possible coupling orientations in m-PD: (a) straight, (b) cross.

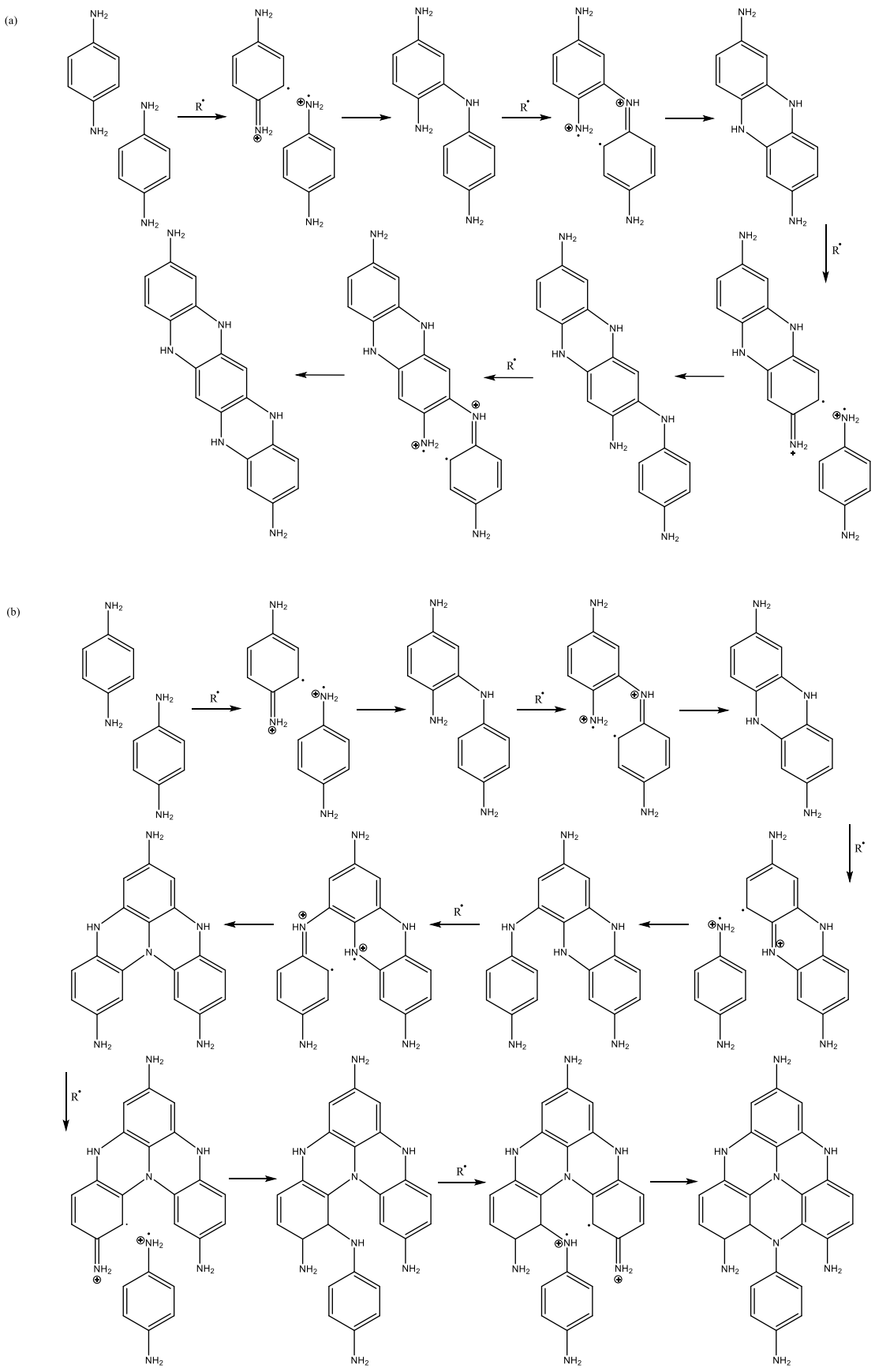

Figure 6.6. Possible coupling orientations in p-PD: (a) straight, (b) cross.

6.3 Experimental procedures

The preparation process of CNDs powder has three steps: synthesis, collect and purification.

1. Synthesis: Firstly, 0.0015 mol p-PD (m-PD or o-PD) was dissolved in 100 mL distilled water, and then the solution was transferred into a round-bottom flask. The flask was heated in a 50 ℃ oil bath for 1.5 hours. The colour of the solution changed from transparent to light pink (light blue or light yellow). Meanwhile, 0.0015 mol $K_2S_2O_8$ was dissolved in 50 mL distilled water and stirred for 0.5 hours. Then the solution was added dropwise in 2 hours. Immediately after the addition of several drops, the solution in the flask would turn dark. After all the $K_2S_2O_8$ solution was added to the flask, the mixture was stirred for 24 hours at 50 ℃.

2. Collect: The dark colour suspension with black solid was collected and separated by centrifugation under 8000 rpm for 20 min. The upper suspension was collected and filtered by the filtration paper. The bottom sediment was washed with the distilled water, shook, sonicated and centrifuged again. The suspension was freeze-dried to obtain initial CNDs powder.

3. Purification: It was necessary to remove K_2SO_4 salt that had formed from $K_2S_2O_8$ during the synthesis reaction. The initial CNDs powder was dissolved in 200 mL of the ethanol and sonicated for several minutes. Because of the insolubility of the K_2SO_4 in ethanol, the salt could be separated by filtration. Then the ethanol suspension was dried in a rotary evaporator. The ethanol was removed and the pure CNDs powder was left in the flask. To collect the powder from the inner wall of the flask, distilled water was added to dissolve the powder again. Finally, the suspension was freeze-dried to obtain relatively pure p-CNDs (m-CNDs or o-CNDs) powder.

6.4 Results and analysis

6.4.1 Morphology

The AFM images of resultant CNDs displayed in Figure 6.7 reveals that the synthesized CNDs are spherical, with an average size of around 30-40 nm in diameter (see Table 6-1). Among these three CNDs, the diameter of p-CNDs is relatively larger. The diameter of m-CNDs is relatively smaller than that of o-CNDs. We have discussed that p-PD has four active sites due to the free radicals, which is more than o-PD and m-PD. The active sites of o-PD are more favoured than that of m-PD. Therefore, the coupling process between p-PD monomers occurs most and between m-PD does least, which resulting in the difference of the size. The average thickness of CNDs is around 2-4 nm.

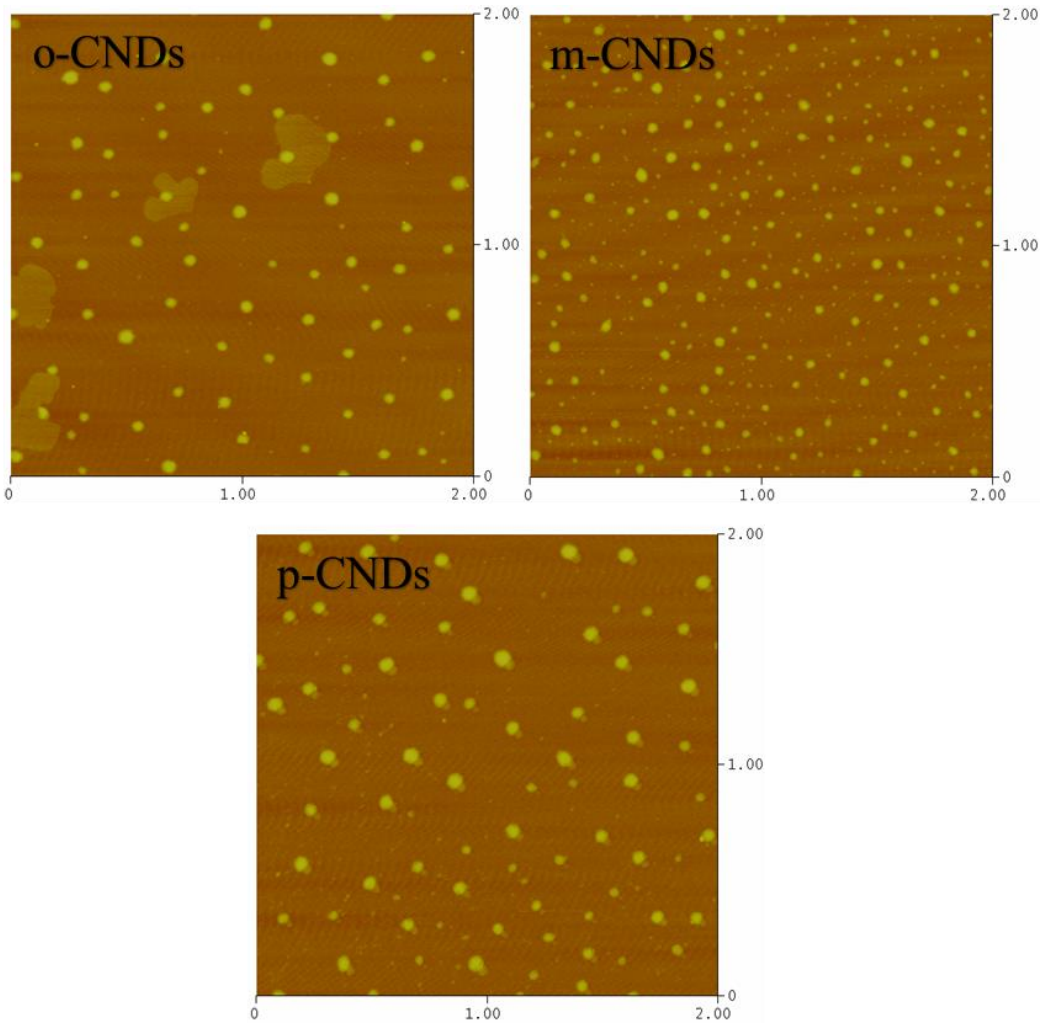

Figure 6.7. The AFM images of CNDs. Scale: 2 µm × 2 µm.

Table 6-1.The diameter of the CNDs-50. Unit: nm.

	mean	standard deviation	maximum
o-CNDs-50	37.6	25.4	92.4
m-CNDs-50	32.4	29.4	85.6
p-CNDs-50	40.2	22.4	102.5

6.4.2 Structure

The FTIR spectra of raw chemicals and their corresponding polymers are shown in Figure 6.8. The three kinds of phenylenediamine monomer have similar characteristic peaks (see Figure 6.8a). The sharp absorption peaks appear at around 3373 and 3297 cm^{-1}, which are attributed to the N-H asymmetric stretching. Peaks at around 1628 and 821 cm^{-1}, which can be regarded as the C-C stretching of the aromatic structure. The absorption peaks at 1127 and 1310 cm^{-1} are considered to be the C-N asymmetric stretching. The peaks at 1510 cm^{-1} are due to in-plane C-H bending vibration from the phenyl rings.[193,196]

After polymerization, the FTIR spectra of synthesized CNDs have some changes, as shown in Figure 6.8b. The characteristic peaks of amino groups (NH_2) at 3373 and 3297 cm^{-1} disappear. In the meanwhile, there are two new peaks at about 2853 and 2592 cm^{-1}, which could be attributed to the C-H stretching bands and N-H vibration bands, separately. C-N asymmetric stretching at 1127 and 1310 cm^{-1} disappears. On the contrary, a wide absorption peak at around 1020 cm^{-1} can be easily seen in the spectrum of the CNDs. Usually, that position would be explained to be the C-O stretching. Besides, the exist of C=O stretching bands at around 1740 cm^{-1} also demonstrates that the oxygen element was introduced to the phenylenediamine during the reaction. The appearance of oxygen-containing functional groups is able to improve the water solubility of the CNDs. The last part to be noted is the in-plane C-H bending vibration band at 1510 cm^{-1}. After the reaction, the absorption peak intensity weakens. This

change can be attributed to the loss of C-H because the phenylenediamine monomer was coupled with others through the C-H position during the polymerization.

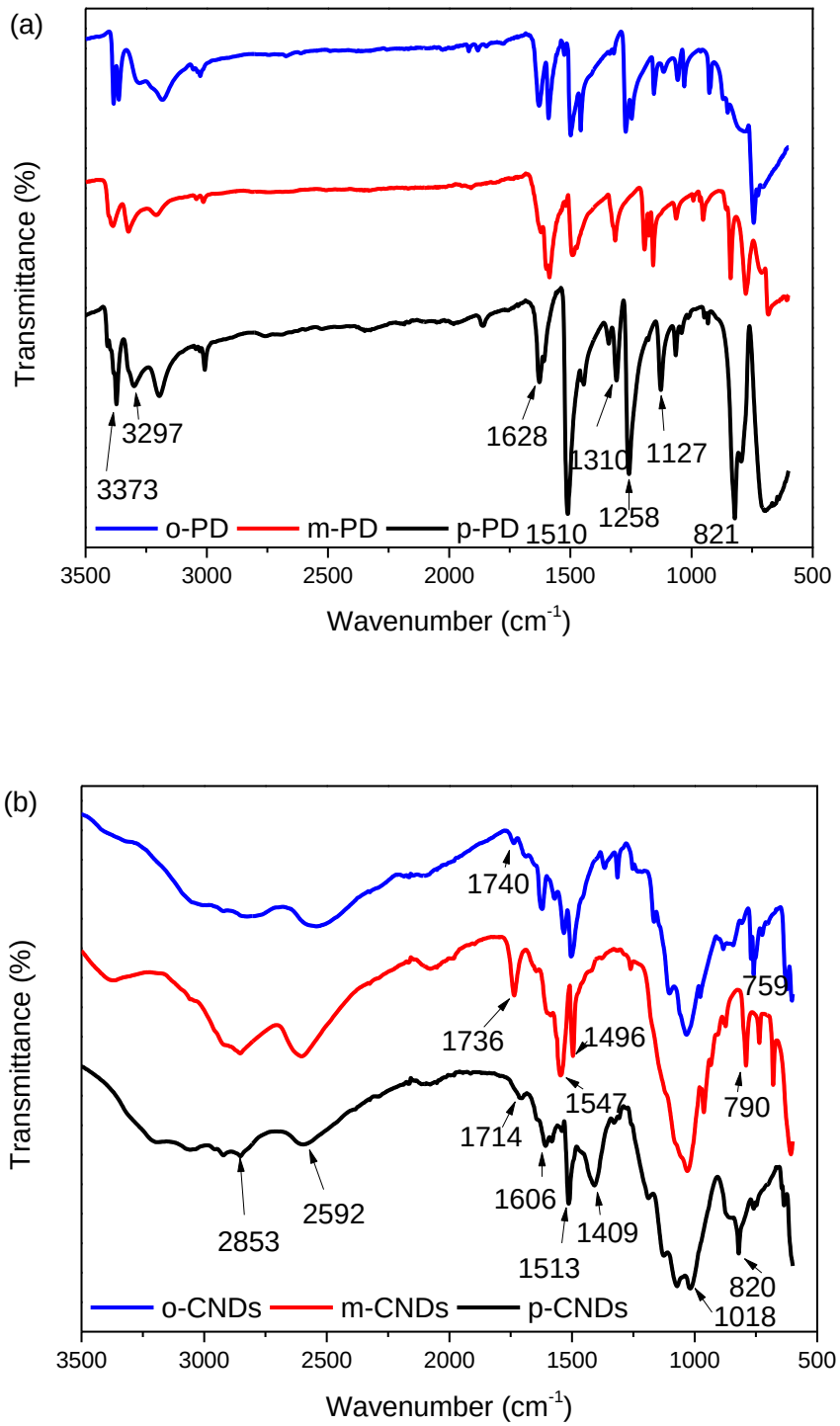

Figure 6.8. FTIR spectra of the raw chemicals: o-PD, m-PD and p-PD (a), and their corresponding CNDs o-CNDs, m-CNDs and p-CNDs (b).

By comparison, we can find much difference in the FTIR spectra between Figure 6.8a and 6.8b, demonstrating that the three kinds of CNDs were successfully prepared by the chemical polymerization with the help of potassium persulfate. In the meantime, these three kinds of CNDs also have different characteristic peaks, revealing that the structure of synthesized CNDs derived from different isomers is not the same. This is a good demonstration for the different mechanism of the isomer coupling process, which is mentioned in the previous section.

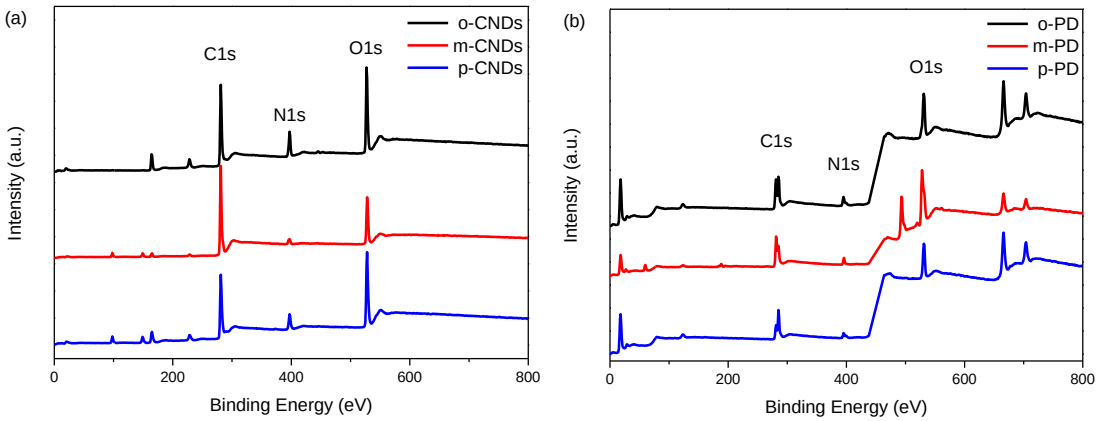

Figure 6.9. Full-range XPS spectra of CNDs (a) and raw materials (b).

Table 6-2. The atomic ratio of the C, N and O elements in raw materials (a) and synthesized CNDs (b).

(a)

Samples	C (%)	N (%)	O (%)
o-PD	70.7	7.5	21.8
m-PD	62.7	4.4	32.9
p-PD	71.6	6.4	22.0

(b)

Samples	C (%)	N (%)	O (%)
o-CNDs	68.0	26.0	6.0
m-CNDs	61.1	23.5	15.4
p-CNDs	65.9	25.8	8.3

Figure 6.9 shows the full-range XPS spectra of the CNDs and raw materials. The main binding energy peaks of C1s at 285 eV, N1s at 400 eV, and O1s at 532 eV can be seen. The atomic ratios of the main elements: C, N and O are shown in Table 6-2. The XPS surveys of the CNDs further confirm the FTIR results that oxygen was introduced to the phenylenediamines during the polymerization. In theory, the raw chemicals only have carbon, nitrogen and hydrogen elements. However, the oxygen element signals are also found in the characterization of the raw material. This result should be considered that the phenylenediamine is not stable and easily oxidized in the atmosphere, due to the very active amino groups on the aromatic structure. Usually, the oxygen would react with the amino groups and form the N-oxide structure, which contains an N-O coordinate covalent bond with two additional hydrogen, as shown in Figure 6.10. The attached oxygen increases the water solubility of phenylenediamine.

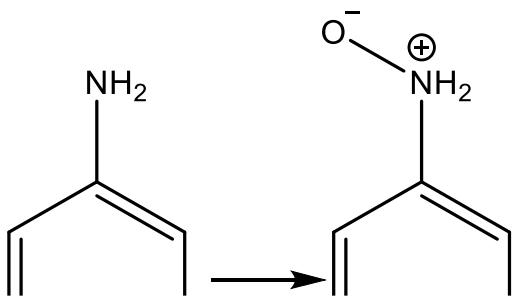

Figure 6.10. Possible N-oxide structure in phenylenediamine.

Meanwhile, the appearance of the oxygen functional groups in the FTIR results demonstrate that the oxygen element is introduced *via* another outside route. Because the potassium persulfate was used in this work, its strong oxidizing property could be the main factor for the initiation of polymerization and the introduction of the oxygen element. Besides, the amino groups on the benzene are active groups, which are easy to be attacked. To obtain a better understanding of the introduction process of the oxygen element, the Boyland–Sims oxidation process[197] can be considered to help explain it, as shown in Figure 6.11. Under the effect of the $K_2S_2O_8$, the hydroxyl is added to the aromatic hydrocarbon on the ortho or para substitution. When the oxidizing

agent has enough amount, the C=O structure can be further formed on the basis of the ortho-hydroxyl aromatic hydrocarbon, as shown in Figure 6.12.

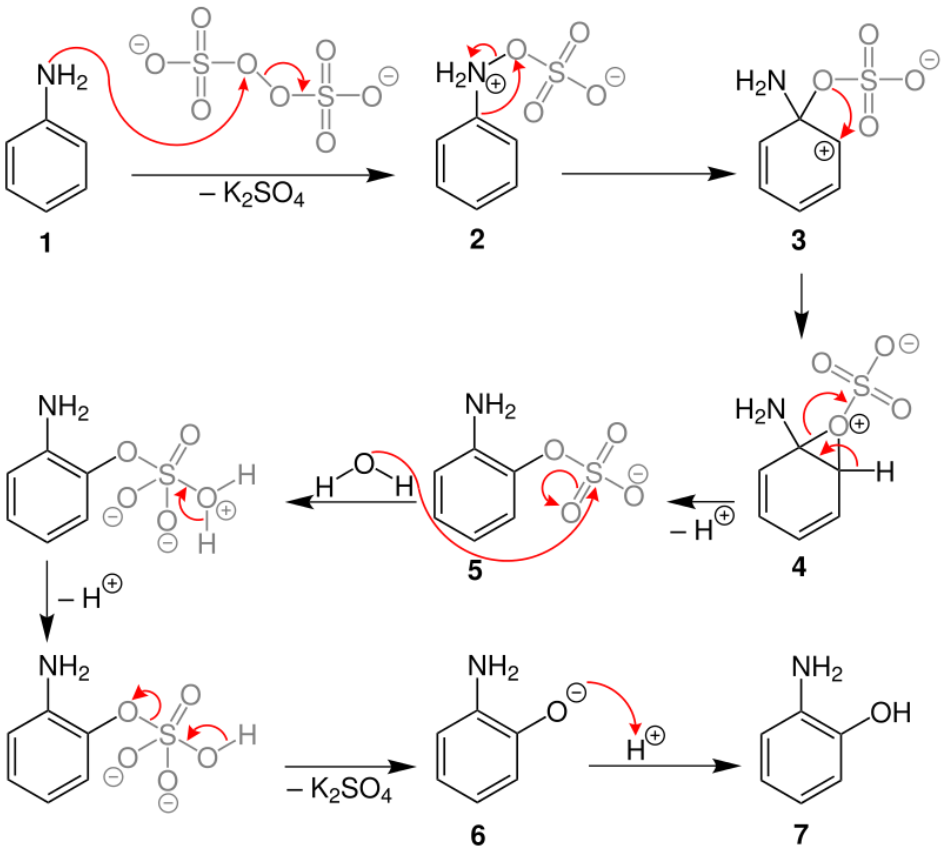

Figure 6.11. The reaction mechanism of the Boyland-Sims oxidation.[198]

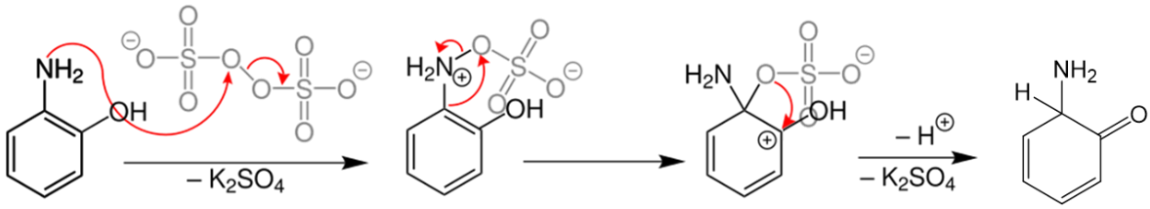

Figure 6.12. The potential formation mechanism of the C=O structure.

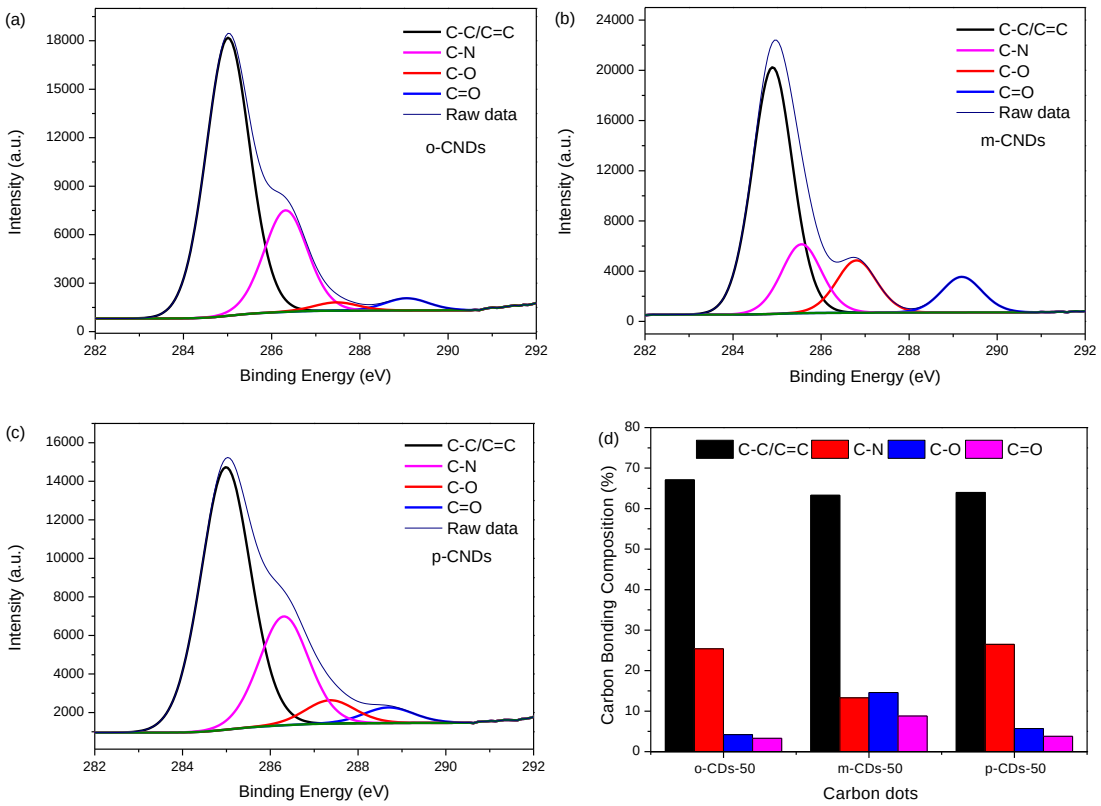

Figure 6.13. High-resolution C1s spectra of (a) o-CNDs, (b) m-CNDs and (c) p-CNDs; (d). The percentage of the peaks deconvoluted from the C1s spectra.

Table 6-3. XPS data analyses of the C1s spectra of CNDs samples.

Carbon Bonding Composition (%)				
	C-C/C=C	C-N	C-O	C=O
o-CNDs	67.1	25.4	4.2	3.3
m-CNDs	63.3	13.3	14.6	8.8
p-CNDs	64.0	26.5	5.7	3.8

Figure 6.13 shows the high-resolution C1s spectra of the CNDs, which were between 282 eV and 292 eV. These spectra could be deconvoluted into several peaks, including C-C/C=C (~285 eV), C-N (~286.2 eV), C-O (~287 eV), and C=O (~288.4 eV). The XPS results further demonstrate that the oxygen functional groups exist on

the CNDs, which is consistent with the previous FTIR results. Besides, the accurate value and changes of the different structure of the three kinds of CNDs could be found in Figure 6.13d and Table 6-3. The C-N content (13.3%) for m-CNDs is quite lower than that of the other two CNDs, which could consider that the amount of coupling connection between amino groups and carbon location in the aromatic molecules is less than that of other two isomers. In the meantime, the C-O content (14.6%) and C=O content (8.8%) are more than those of o-CNDs and p-CNDs. From the comparison of C-O and C=O content, it can be noted that m-CNDs have more oxygen-containing functional groups and less C-N bonding than o-CNDs and p-CNDs. The reason for this may be related to the different coupling process due to the different position of the -NH_2. Besides, the occupation of the oxygen-containing functional groups on the aromatic molecules could lead to the less coupling and affect the polymerization.

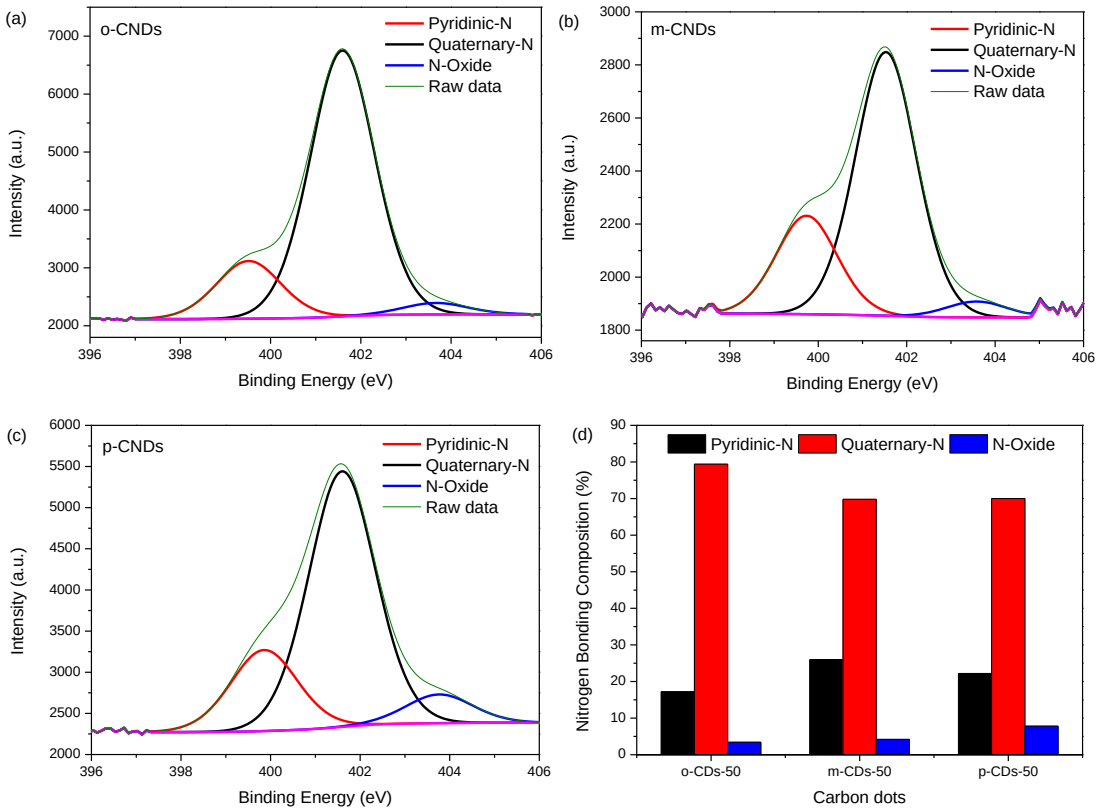

Figure 6.14. High-resolution N1s spectra of (a) o-CNDs, (b) m-CNDs and (c) p-CNDs; (d). The percentage of the peaks deconvoluted from the N1s spectra.

Table 6-4. XPS data analyses of the N1s spectra of CNDs samples.

Nitrogen Bonding Composition (%)			
	Pyridinic-N	Quaternary-N	N-Oxide
o-CNDs	17.2	79.4	3.4
m-CNDs	26.0	69.8	4.2
p-CNDs	22.2	70.0	7.8

As shown in Figure 6.14, the nitrogen bonding composition is also investigated, and the spectra consist of three main peaks (see Table 6-4), including pyridinic-N at around 399.6 eV, quaternary-N at about 401.5 eV and N-oxide at about 403.4 eV. The m-CNDs have the most pyridinic-N content (26%), which means that there are much –NH left. The o-CNDs have the most quaternary-N content (79.4%), which indicates that the amino groups could be more easily connected with other aromatic hydrocarbons and two hydrogens of the amino groups were substituted and used to couple. The reason for the different nitrogen bonding composition is still considered as the different coupling process, which is due to the different position of the amino groups ($-NH_2$).

6.4.3 Summary

According to the structural analysis from FTIR and XPS results, it can demonstrate that three kinds of CNDs derived from phenylenediamine isomers were successfully synthesized *via* the chemical polymerization method. Different from theoretical speculation, oxygen element was found in the synthesized CNDs due to the effect of the potassium persulfate and the formation of N-oxide. The different positions of the amino groups and the occupation of the oxygen-containing functional groups on the aromatic molecule can both affect the coupling process and lead to synthesize the different structure. The structure and oxygen-containing functional groups would be considered to the main factors for determining optical properties.

6.4.4 Optical properties

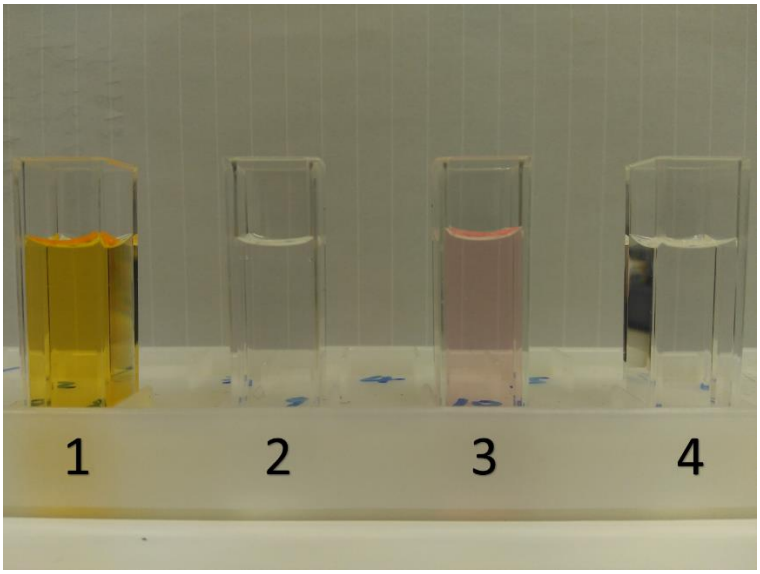

Figure 6.15. Photograph of (1) o-CNDs, (2) m-CNDs, (3) p-CNDs dispersed in water (0.08 mg/mL) and (4) distilled water.

The synthesized CNDs derived from phenylenediamine could be well dispersed in water and be stable for several days. As shown in Figure 6.15, the aqueous suspension is clear and their colours are quite different. The o-CNDs aqueous is yellow, m-CNDs is close to transparent, and p-CNDs is pink.

Figure 6.16 shows the UV-Vis absorption spectra of three synthesized CNDs and their raw materials in aqueous suspension. For the raw materials, there is an obvious peak at around 250-280 nm, which is a characteristic absorption peak of benzene ring structure. After polymerization, the three kinds of CNDs have new and different absorption peaks. For o-CNDs (Figure 6.16a), there is a new peak at around 452 nm and the peak position of benzene ring structure shifts from 280 nm to 266 nm. For p-CNDs (Figure 6.16c), a new and broad peak appears at around 517 nm and its benzene peak position moves from 278 nm to 255 nm. For m-CNDs (Figure 6.16b), its benzene peak position just shifts from 290 nm to 284 nm and there is no new peak in other range. Because of the coupling process, the carbon in the aromatic molecule was connected

with the amino groups. The delocalized system was broken, and then the amount of delocalization in benzene ring structure decreased, which moves the characterization peak to shorter wavelengths. These changes could also demonstrate that the CNDs were successfully synthesized by the coupling process.

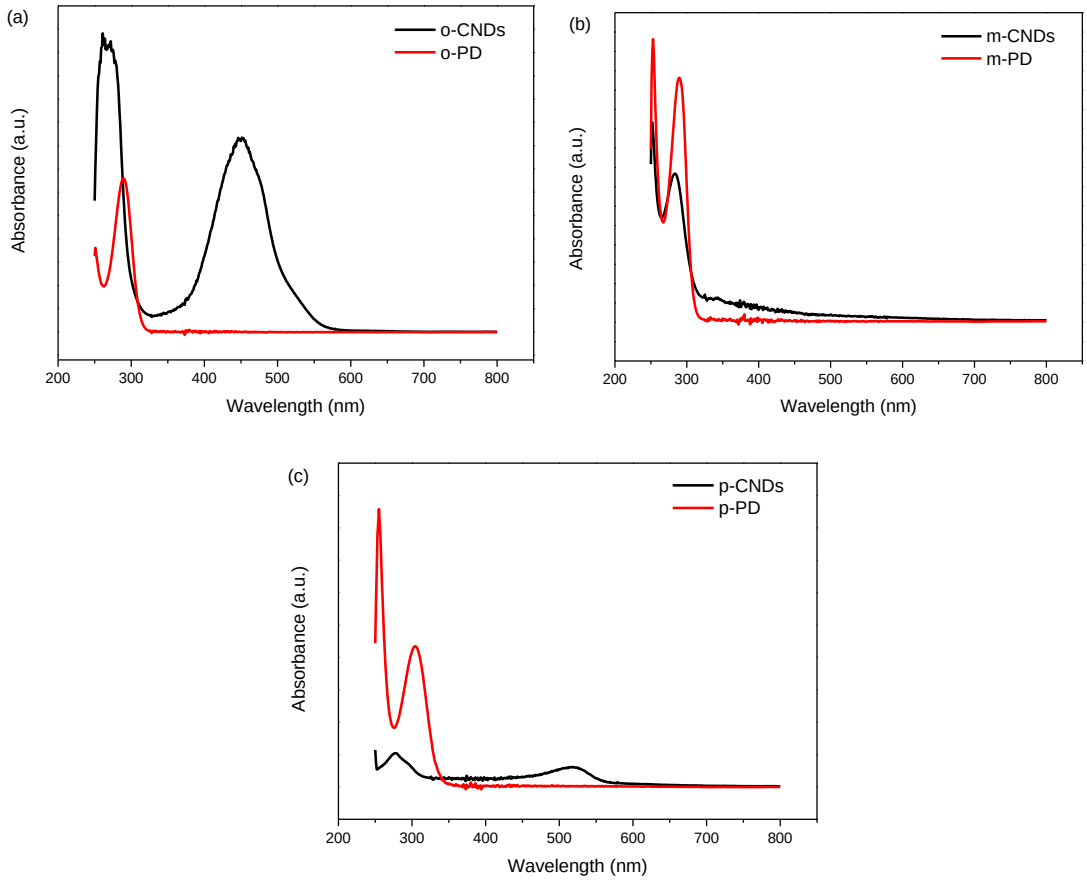

Figure 6.16. UV-Vis absorption spectra of (a) o-CNDs and raw chemicals o-PD, (b) m-CNDs and raw chemicals m-PD, (c) p-CNDs and raw chemicals p-PD in aqueous suspension.

The range between 300 and 400 nm should also be noticed. It can be found that all three kinds of synthesized CNDs have a certain degree of absorbance in that range. From the previous chapter, we can know that the broad absorption peak in that range could be attributed to the C=O structure. These results verify the existence of oxygen-containing functional groups on the synthesized CNDs again.

The PL properties of synthesized CNDs were investigated and the results are

displayed, separately. Three kinds of synthesized CNDs perform different PL behaviour.

The excitation-dependent PL behaviour of o-CNDs is displayed in three graphs according to the different excitation wavelength range. The first emission peak appears at around 570 nm when the excitation wavelength is from 360 nm to 430 nm, as shown in Figure 6.17. 380 nm excitation wavelength can produce the strongest PL emission intensity.

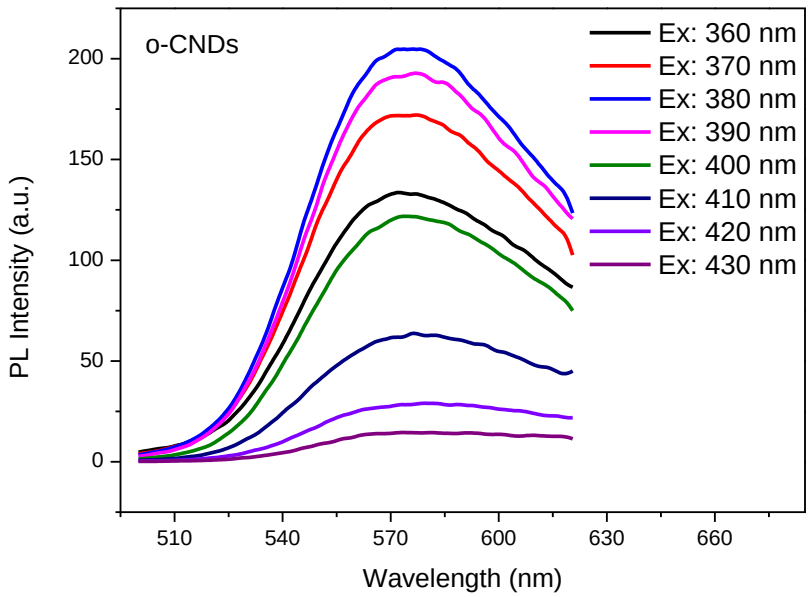

Figure 6.17. The excitation-dependent PL behaviour of o-CNDs (Ex: from 360 nm to 430 nm).

When continuing to increase the excitation wavelength, the second emission peak appears at around 580 nm, which is quite near to the first one. The emission PL intensity gradually become strong with increasing the excitation wavelength from 490 nm to 525 nm, and 525 nm excitation could make its strongest (see Figure 6.18). Meanwhile, the emission spectrum is very broad. When using 540 nm excitation wavelength, it is easy to notice that the emission spectrum consists of two peaks. One is at around 570 nm, and another is at around 610 nm.

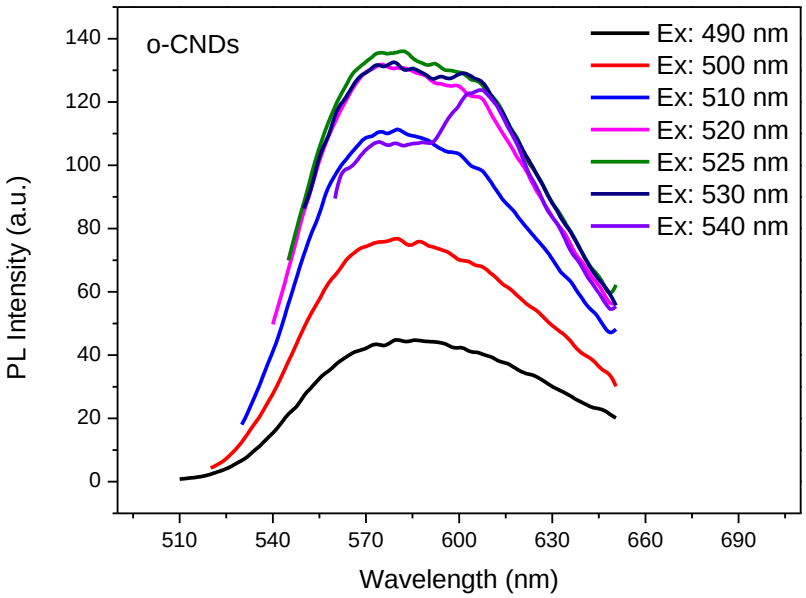

Figure 6.18. The excitation-dependent PL behaviour of o-CNDs (Ex: from 490 nm to 540 nm).

The last excitation wavelength range is from 550 to 600 nm. A relatively narrow emission peak appears at around 610 nm, and the strongest PL intensity is produced by 560 nm excitation wavelength. A quite small emission peaks appear at around 660 nm when using 600 nm excitation wavelength.

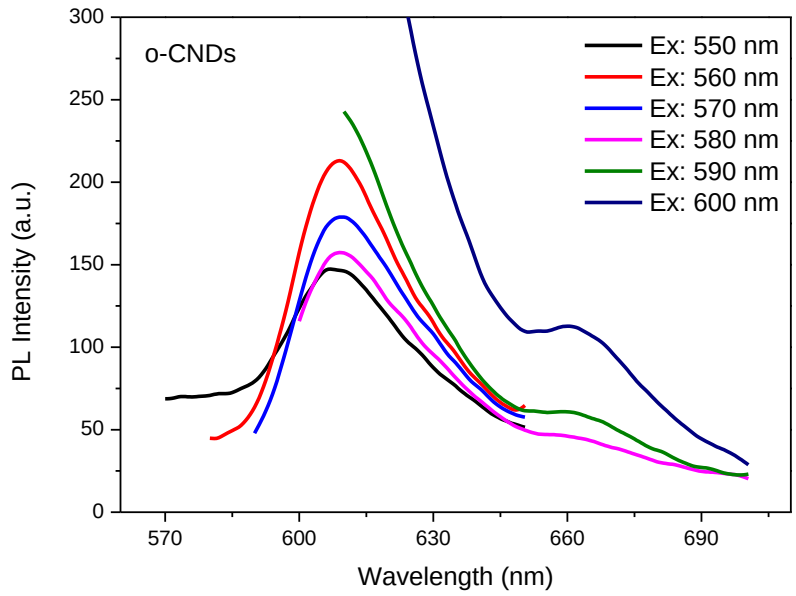

Figure 6.19. The excitation-dependent PL behaviour of o-CNDs (Ex: from 550 nm to 600 nm).

According to the PL behaviour results, it can summarize that there are two main emission peaks at around 570 nm and 610 nm for o-CNDs. Therefore, two S1 states for the two peaks exist. The possible mechanism of PL behaviour of o-CNDs derived from o-phenylenediamine is shown in Figure 6.20. S1 state is for 570 nm emission peak and S1* state represents 610 nm emission peak. In the previous chapter, a speculative conclusion is that 570 nm emission range is related to the effect of O-C=O structure. Due to the existence of C-O and C=O structure in the CNDs, it is still considered that S1 state is related to the oxygen-containing functional groups. About the S1* state for 610 nm emission, the reason is still not clear. To investigate this reason, more characterization and simulation can be done to analyze the structure and PL in the future work.

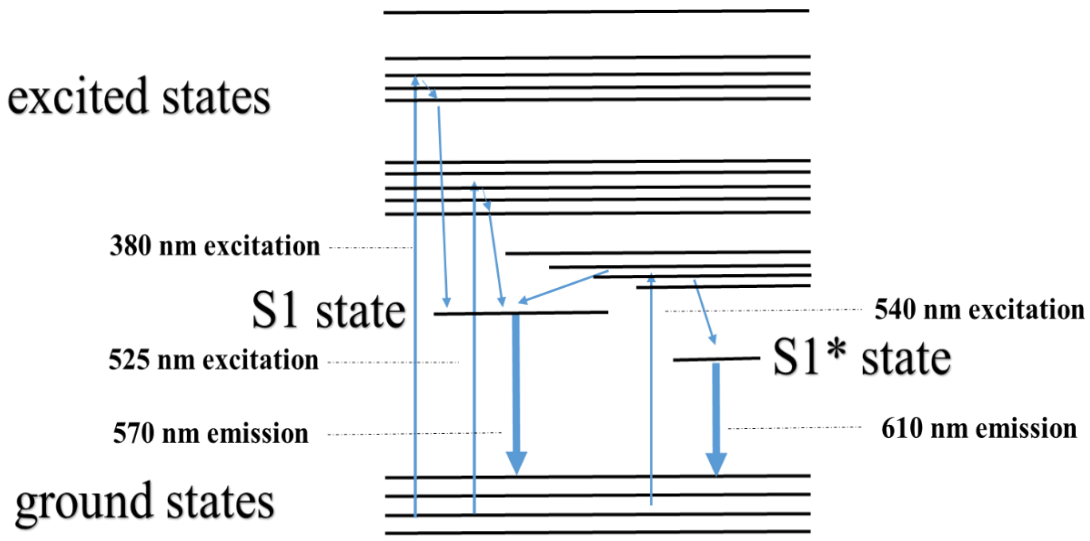

Figure 6.20. The possible mechanism of PL behaviour of o-CNDs.

The excitation-dependent PL behaviour of m-CNDs is displayed in two graphs. When the excitation wavelength is from 330 nm to 360 nm, the emission peak position is at around 450 nm (see Figure 6.21a). When increasing the excitation wavelength from 370 nm to 450 nm, the emission peak position slowly shifts from 475 nm to 520 nm, as shown in Figure 6.21b. There are no new peaks when using other excitation wavelengths.

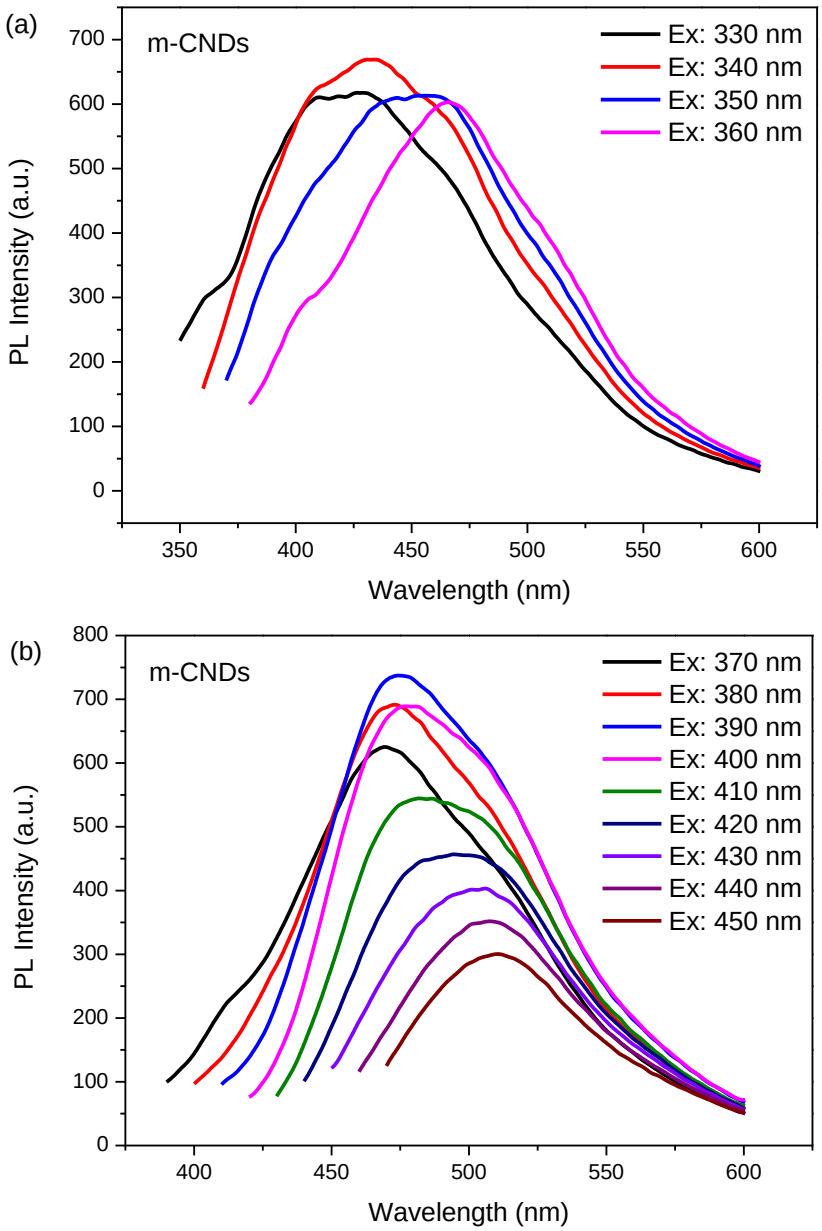

Figure 6.21. The excitation-dependent PL behaviour of m-CNDs.

The PL behaviour of this kind of CNDs is quite similar to that of the graphene oxide quantum dots treated with hydrothermal method. It is sensitive to the violet colour (330-450 nm) and can produce emission spectra with very strong PL intensity. The emission range also belongs to blue and green colour. In the previous chapter, a conclusion is stated that blue colour is related to carbon matrix and the green colour is due to C=O structure. For m-CNDs derived from m-phenylenediamine, more C=O content has been mentioned in the structural analysis, which demonstrates the C=O

structure could affect the green colour in PL behaviour once again. Meanwhile, more C=O structure occupies the carbon location on the aromatic molecule and reduce the coupling with the amino groups. More benzene ring structure could be retained, which means the delocalization system like carbon matrix is more than other two kinds of CNDs. The more content of delocalization system is, the more absorbance of violet colour is. More photons, which means more energy, could be absorbed in. Therefore, the PL intensity is much higher than that of other two kinds of carbon dots.

For p-CNDs derived from p-phenylenediamine, its PL behaviour is relatively simple. The emission peak position is only in the range between 575 and 610 nm, as shown in Figure 6.22. The emission peak with maximum PL intensity is at around 578 nm when the excitation wavelength is 530 nm. With increasing the excitation wavelength, the emission peak could slightly move to longer wavelengths (around 600 nm). Compared with o-CNDs, their PL emission peak range is close, but the PL behaviour is different. 570 nm and 610 nm emission peaks of p-CNDs are not easy to distinguish and separate, which means the excited states corresponding to these two emission peaks are close together. The reason for this is still considered to be the difference structure of the synthesized CNDs due to the different coupling process and different distribution of oxygen functional groups

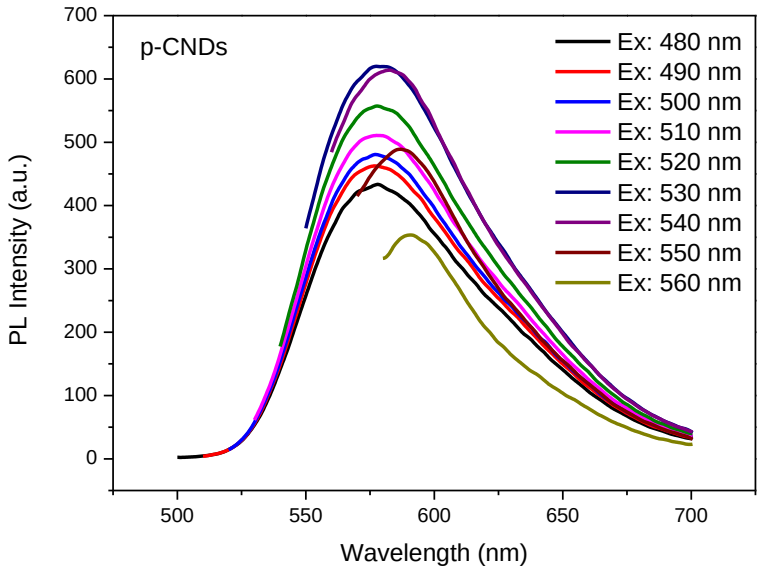

Figure 6.22. The excitation-dependent PL behaviour of p-CNDs.

6.5 Conclusion

To the best of my knowledge, this is the first time that CNDs are synthesized *via* the chemical polymerization with the help of the potassium persulfate. Compared with the hydrothermal method, this method can precisely control the synthesis in theory *via* controlling the amount of free radicals that is potassium persulfate. The optical properties of resultant CNDs derived from phenylenediamine isomers have been studied. Especially, the three kinds of CNDs perform different PL behaviour. For o-CNDs and p-CNDs, they mainly emit 570 nm to 600 nm range spectrum, which is yellow and orange colour. For m-CNDs, it could emit 420 nm to 525 nm range spectrum, which belongs to blue and green colour. The PL intensity of o-CNDs is relatively weaker than that of others. However, it could emit 620 nm and 660 nm, which belongs to red colour. The possible mechanism of PL behaviour for three kinds of generated CNDs has been investigated. Oxygen-containing functional groups have a key role in determining the PL properties. Some results also demonstrate the conclusion mentioned in the previous chapter. Moreover, the CNDs are stable in the water for several days. These features make CNDs potentially used in numerous imaging applications.

7 Conclusions and suggestions for future work

In this thesis, two kinds of luminescent carbon-based dots were successfully prepared *via* two routes.

Luminescent graphene oxide quantum dots were synthesized with graphite powder *via* chemical oxidation method. With the help of a high temperature, long reaction time and high concentration of sulfuric acid and nitric acid, graphite powder was cut into smaller pieces with a size of around 70-120 nm in diameter, and oxygen-containing functional groups were introduced onto the edge or surface of matrix including carboxyl, epoxy, ketone and hydroxyl groups. A high amount of oxygen-containing functional groups made GOQDs disperse in water very well and stable. The GOQDs emitted green and yellow fluorescence. The maximum photoluminescence emission peak occurred at around 531 nm when the excitation wavelength was 470 nm. When the excitation wavelength was longer and the concentration of GOQDs in aqueous suspension was high, weak PL emission spectra in orange or light red colour could be observed. In addition, cell viability test revealed that 1mg/mL of GOQDs aqueous suspension still make 80% HeLa cells alive, demonstrating that GOQDs did not impose considerable toxicity to cells. Meanwhile, GOQDs had the ability to produce reactive oxygen species when excited with visible light. By comparison, GOQDs showed better ROS-generation ability than a classic photosensitizer, protoporphyrin IX. Based on these features, GOQDs have potential in bioimaging and photodynamic therapy applications.

By adjusting the reaction temperature and reaction time, six series of GOQDs samples were obtained with the nanoparticle size varying between 15-80 nm. The composition of carbon bonding was also changed. Different oxygen-containing functional groups showed different stabilities for specific reaction temperature and time.

Epoxy groups were not stable and were the easiest to reduce. The content of carboxyl groups increased when the reaction temperature was higher and the reaction time was longer. However, carboxyl groups would be partially reduced to ketone when the oxidation environment was too harsh. These six series of GOQDs samples had similar PL emission ranges of green and yellow colour. However, their PL intensities were different. GOQDs-3 and GOQDs-4 samples which were produced at 100 ℃ showed stronger PL intensities compared to those prepared at 80 ℃ and 120 ℃. All the samples had a quantum yield of ~0.2-0.4% and GOQDs-4 had the highest. It was considered that the quantum yield of GOQDs for 530 nm green colour was related to their oxygen-containing functional groups on the GOQDs, specifically the content of C=O bonding. ROS generation ability was also discussed. The oxygen-containing functional groups and the light wavelength were considered to be primary factors affecting the ability.

Another six GOQDs-M and GOQDs-ML (lower nitric acid dosage) samples were subsequently prepared following the modified experimental procedures. To better separate the layers of graphite oxide, sulfuric acid was first used to treat the graphite powder to increase the interlayer spacing. A greater interlayer spacing made graphite sheets separate efficiently under the 100 ℃ heating and stirring. Meanwhile, the strong oxidizing H_2SO_4 molecular was considered to also help oxidize the graphite sheet. Hydroxyl and epoxy groups were found to be produced first. After 24 h and 100 ℃ of sulfuric acid treatment, the epoxy groups on the graphite sheets were easily broken when the high concentration nitric acid was added. Therefore, the smaller size and high oxidization degree of nanoparticles were obtained even using lower nitric acid dosage. GOQDs-M samples showed similar PL emission range to that of the previous GOQDs samples. The maximum PL emission spectra peak was located at around 530 nm. However, the PL intensities for all GOQDs-M samples were increased. GOQDs-ML samples have an obvious PL emission peak at around 570 nm, corresponding to more content of carboxyl groups. The QY of GOQDs-M increased to 0.3%-0.5%, which was slightly higher than that of GOQDs samples. From the ROS test, GOQDs-M samples

under blue and green light irradiation showed similar ROS generation abilities to those of the previous GOQDs samples.

It is the first report that the GOQDs are as raw materials and further treated by the hydrothermal method. Different treatment conditions were set to make a comparison for the analysis of their effect on the GOQDs structure and PL behaviours. Under the hydrothermal treatment, the size of the GOQDs-H could be decreased to 20-50 nm. Interestingly, oxygen-containing functional groups were still on the GOQDs-H samples, although, most carboxyl groups had been transformed to ketone groups. The peak of the PL emission moved to 420 nm, which belongs to blue colour. The QY significantly increased to 2%-5%, among which GOQDs-H3 and GOQDs-H4 had a highest QY. Due to the high temperature and long reaction time, GOQDs-H3 and GOQDs-H4 were further reduced and had more content of the carbon matrix, which has sp^2 hybridization structure. More sp^2 hybridization structure can increase the QY.

According to the analysis of the obtained results, the mechanism of PL of GOQDs was simply summarized. Carbon matrix could influence the PL emission (blue colour) at around 450 nm. PL emission at around 530 nm (green colour) and 575 nm (yellow colour) could correspond to C=O structure and O-C=O structure, respectively.

Another three series of luminescent carbon nanodots derived from phenylenediamine isomers were successfully synthesized *via* chemical polymerization with the help of potassium persulfate. To the best of my knowledge, it is the first time to discuss and speculate the mechanism of the coupling process of three kinds of phenylenediamine isomers, and prepare CNDs with potassium persulfate. The hypothetical coupling process and potential structure were analyzed according to the theory and publications. The optical properties of synthesized carbon nanodots had been studied. Especially, the three kinds of carbon nanodots performed different PL behaviours. For o-CDs-50 and p-CDs-50, they mainly emit 570 nm to 600 nm range

spectra, which correspond to yellow and orange colour respectively. For m-CDs-50, it could emit 420 nm to 525 nm range spectrum, which belong to blue and green colour. The PL intensity of o-CDs-50 is relatively weaker than that of others. However, it could emit 620 nm and 660 nm, which is red colour. Oxygen-containing functional groups were considered to be a key role in determining the PL properties. Based on the unique PL features and good water dispersibility, these carbon nanodots could have potential in various imaging applications.

Suggestions for future work

1. Try to find a method to remove a certain kind of oxygen-containing functional groups and analyze the effect of each kind of functional groups on PL properties.
2. Try to use computer simulation software to study the effect of each kind of the oxygen-containing functional groups on PL properties.
3. To increase the QY value of carbon dots by further treatment, such as introduce heterocycle structure molecules.
4. To further study the reason for the difference PL behaviour of the carbon dots derived from three isomers by using computer simulation and more characterization for structure.
5. To increase the water solubility of carbon nanodots derived from phenylenediamine by introducing suitable amount of oxygen-containing functional groups.

8 References

(1) Förster. Handbook of Chemistry and Physics. *Zeitschrift fur Phys. Chemie* **1956**.

(2) Coleman, J. N.; Khan, U.; Blau, W. J.; Gun'ko, Y. K. Small but Strong: A Review of the Mechanical Properties of Carbon Nanotube-Polymer Composites. *Carbon N. Y.* **2006**, *44* (9), 1624–1652.

(3) Baughman, R. H.; Zakhidov, A. A.; De Heer, W. A. Carbon Nanotubes - The Route toward Applications. *Science (80-.).* **2002**, *297* (5582), 787–792.

(4) Franklin, A. D. Carbon Nanotube Electronics. In *Emerging Nanoelectronic Devices*; 2015; Vol. 9781118447, pp 315–335.

(5) Geim, A. K.; Novoselov, K. S. The Rise of Graphene. *Nat. Mater.* **2007**, *6* (3),

(6) Geim, A. K. Graphene: Status and Prospects. *Science (80-.).* **2009**, *324* (5934), 1530–1534.

(7) Bonaccorso, F.; Sun, Z.; Hasan, T.; Ferrari, A. C. Graphene Photonics and Optoelectronics. *Nat. Photonics* **2010**, *4* (9), 611–622.

(8) Stankovich, S.; Dikin, D. a; Dommett, G. H. B.; Kohlhaas, K. M.; Zimney, E. J.; Stach, E. a; Piner, R. D.; Nguyen, S. T.; Ruoff, R. S. Graphene-Based Composite Materials. *Nature* **2006**, *442* (7100), 282–286.

(9) Sun, Y. P.; Zhou, B.; Lin, Y.; Wang, W.; Fernando, K. A. S.; Pathak, P.; Meziani, M. J.; Harruff, B. A.; Wang, X.; Wang, H.; et al. Quantum-Sized Carbon Dots for Bright and Colorful Photoluminescence. *J. Am. Chem. Soc.* **2006**, *128* (24), 7756–7757.

(10) Baker, S. N.; Baker, G. A. Luminescent Carbon Nanodots: Emergent Nanolights. *Angew. Chemie - Int. Ed.* **2010**, *49* (38), 6726–6744.

(11) Zhu, S.; Song, Y.; Zhao, X.; Shao, J.; Zhang, J.; Yang, B. The Photoluminescence Mechanism in Carbon Dots (Graphene Quantum Dots, Carbon Nanodots, and Polymer Dots): Current State and Future Perspective. *Nano Res.* **2015**, *8* (2), 355–381.

(12) Cao, L.; Wang, X.; Meziani, M. J.; Lu, F.; Wang, H.; Luo, P. G.; Lin, Y.; Harruff,

B. A.; Veca, L. M.; Murray, D.; et al. Carbon Dots for Multiphoton Bioimaging. *J. Am. Chem. Soc.* **2007**, *129* (37), 11318–11319.

(13) Li, H.; Kang, Z.; Liu, Y.; Lee, S.-T. Carbon Nanodots: Synthesis, Properties and Applications. *J. Mater. Chem.* **2012**, *22* (46), 24230.

(14) Zheng, X. T.; Ananthanarayanan, A.; Luo, K. Q.; Chen, P. Glowing Graphene Quantum Dots and Carbon Dots: Properties, Syntheses, and Biological Applications. *Small* **2015**, *11* (14), 1620–1636.

(15) Machado, C. E.; Vieira, K. O.; Ferrari, J. L.; Schiavon, M. A. Carbon Quantum Dots: Chemical Synthesis, Properties and Applications. *Rev. Virtual Quim.* **2015**, *7* (4), 1306–1346.

(16) Dong, Y.; Shao, J.; Chen, C.; Li, H.; Wang, R.; Chi, Y.; Lin, X.; Chen, G. Blue Luminescent Graphene Quantum Dots and Graphene Oxide Prepared by Tuning the Carbonization Degree of Citric Acid. *Carbon N. Y.* **2012**, *50* (12), 4738–4743.

(17) Yang, S. T.; Wang, X.; Wang, H.; Lu, F.; Luo, P. G.; Cao, L.; Meziani, M. J.; Liu, J. H.; Liu, Y.; Chen, M.; et al. Carbon Dots as Nontoxic and High-Performance Fluorescence Imaging Agents. *J. Phys. Chem. C* **2009**, *113* (42), 18110–18114.

(18) Sahu, S.; Behera, B.; Maiti, T. K.; Mohapatra, S. Simple One-Step Synthesis of Highly Luminescent Carbon Dots from Orange Juice: Application as Excellent Bio-Imaging Agents. *Chem. Commun.* **2012**, *48* (70), 8835–8837.

(19) Yang, S.-T.; Cao, L.; Luo, P. G.; Lu, F.; Wang, X.; Wang, H.; Meziani, M. J.; Liu, Y.; Qi, G.; Sun, Y.-P. Carbon Dots for Optical Imaging in Vivo. *J. Am. Chem. Soc.* **2009**, *131* (32), 11308–11309.

(20) Zhao, A.; Chen, Z.; Zhao, C.; Gao, N.; Ren, J.; Qu, X. Recent Advances in Bioapplications of C-Dots. *Carbon N. Y.* **2015**, *85*, 309–327.

(21) Dong, Y.; Wang, R.; Li, H.; Shao, J.; Chi, Y.; Lin, X.; Chen, G. Polyamine-Functionalized Carbon Quantum Dots for Chemical Sensing. *Carbon N. Y.* **2012**, *50* (8), 2810–2815.

(22) Liang, Q.; Ma, W.; Shi, Y.; Li, Z.; Yang, X. Easy Synthesis of Highly

Fluorescent Carbon Quantum Dots from Gelatin and Their Luminescent Properties and Applications. *Carbon N. Y.* **2013**, *60*, 421–428.

(23) Miao, P.; Han, K.; Tang, Y.; Wang, B.; Lin, T.; Cheng, W. Recent Advances in Carbon Nanodots: Synthesis, Properties and Biomedical Applications. *Nanoscale* **2015**, *7* (5), 1586–1595.

(24) Peng, J.; Gao, W.; Gupta, B. K.; Liu, Z.; Romero-Aburto, R.; Ge, L.; Song, L.; Alemany, L. B.; Zhan, X.; Gao, G.; et al. Graphene Quantum Dots Derived from Carbon Fibers. *Nano Lett.* **2012**, *12* (2), 844–849.

(25) Pan, D.; Zhang, J.; Li, Z.; Wu, M. Hydrothermal Route for Cutting Graphene Sheets into Blue-Luminescent Graphene Quantum Dots. *Adv. Mater.* **2010**, *22* (6), 734–738.

(26) Bacon, M.; Bradley, S. J.; Nann, T. Graphene Quantum Dots. *Part. Part. Syst. Charact.* **2014**, *31* (4), 415–428.

(27) Shen, J.; Zhu, Y.; Yang, X.; Li, C. Graphene Quantum Dots: Emergent Nanolights for Bioimaging, Sensors, Catalysis and Photovoltaic Devices. *Chem. Commun. (Camb).* **2012**, *48* (31), 3686–3699.

(28) Vedamalai, M.; Periasamy, A. P.; Wang, C.-W.; Tseng, Y.-T.; Ho, L.-C.; Shih, C.-C.; Chang, H.-T. Carbon Nanodots Prepared from O-Phenylenediamine for Sensing of Cu^{2+} Ions in Cells. *Nanoscale* **2014**, *6* (21), 13119–13125.

(29) Sun, X.; Lei, Y. Fluorescent Carbon Dots and Their Sensing Applications. *TrAC - Trends Anal. Chem.* **2017**, *89*, 163–180.

(30) Li, J.; Ye, Q.; Cassell, A.; Ng, H. T.; Stevens, R.; Han, J.; Meyyappan, M. Bottom-up Approach for Carbon Nanotube Interconnects. *Appl. Phys. Lett.* **2003**, *82* (15), 2491–2493.

(31) Xu, X.; Ray, R.; Gu, Y.; Ploehn, H. J.; Gearheart, L.; Raker, K.; Scrivens, W. A. Electrophoretic Analysis and Purification of Fluorescent Single-Walled Carbon Nanotube Fragments. *J. Am. Chem. Soc.* **2004**, *126* (40), 12736–12737.

(32) Deng, Y.; Zhao, D.; Chen, X.; Wang, F.; Song, H.; Shen, D. Long Lifetime Pure Organic Phosphorescence Based on Water Soluble Carbon Dots. *Chem.*

Commun. **2013**, *49* (51), 5751–5753.

(33) Chen, P. C.; Chen, Y. N.; Hsu, P. C.; Shih, C. C.; Chang, H. T. Photoluminescent Organosilane-Functionalized Carbon Dots as Temperature Probes. *Chem. Commun.* **2013**, *49* (16), 1639–1641.

(34) Wang, F.; Kreiter, M.; He, B.; Pang, S.; Liu, C. Y. Synthesis of Direct White-Light Emitting Carbogenic Quantum Dots. *Chem. Commun.* **2010**, *46* (19), 3309–3311.

(35) Bhunia, S. K.; Saha, A.; Maity, A. R.; Ray, S. C.; Jana, N. R. Carbon Nanoparticle-Based Fluorescent Bioimaging Probes. *Sci. Rep.* **2013**, *3*, 1473.

(36) Lin, L. P.; Wang, X. X.; Lin, S. Q.; Zhang, L. H.; Lin, C. Q.; Li, Z. M.; Liu, J. M. Research on the Spectral Properties of Luminescent Carbon Dots. *Spectrochim. Acta - Part A Mol. Biomol. Spectrosc.* **2012**, *95*, 555–561.

(37) Novoselov, K. S.; Geim, a K.; Morozov, S. V; Jiang, D.; Zhang, Y.; Dubonos, S. V; Grigorieva, I. V; Firsov, a a. Electric Field Effect in Atomically Thin Carbon Films. *Science* **2004**, *306* (5696), 666–669.

(38) Lee, C.; Wei, X.; Kysar, J. W.; Hone, J. Measurement of the Elastic Properties and Intrinsic Strength of Monolayer Graphene. *Science* **2008**, *321* (5887), 385–388.

(39) Balandin, A. a; Ghosh, S.; Bao, W.; Calizo, I.; Teweldebrhan, D.; Miao, F.; Lau, C. N. Superior Thermal Conductivity of Single-Layer Graphene. *Nano Lett.* **2008**, *8* (3), 902–907.

(40) Pumera, M. Graphene-Based Nanomaterials for Energy Storage. *Energy Environ. Sci.* **2011**, *4* (3), 668.

(41) Wang, Y.; Shi, Z.; Huang, Y.; Ma, Y.; Wang, C.; Chen, M.; Chen, Y. Supercapacitor Devices Based on Graphene Materials. *J. Phys. Chem. C* **2009**, *113* (30), 13103–13107.

(42) Steurer, P.; Wissert, R.; Thomann, R.; Mülhaupt, R. Functionalized Graphenes and Thermoplastic Nanocomposites Based upon Expanded Graphite Oxide. *Macromol. Rapid Commun.* **2009**, *30* (4–5), 316–327.

(43) Yoon, S.; Park, J.; Kim, E.; Kim, B. Preparations and Properties of Waterborne Polyurethane/Allyl Isocyanated-Modified Graphene Oxide Nanocomposites. *Colloid Polym. Sci.* **2011**, *289* (17–18), 1809–1814.

(44) Compton, O.; Nguyen, S. Graphene Oxide, Highly Reduced Graphene Oxide, and Graphene: Versatile Building Blocks for Carbon-Based Materials. *Small* **2010**, *6* (6), 711–723.

(45) Cai, D.; Jin, J.; Yusoh, K.; Rafiq, R.; Song, M. High Performance Polyurethane/Functionalized Graphene Nanocomposites with Improved Mechanical and Thermal Properties. *Compos. Sci. Technol.* **2012**, *72* (6), 702–707.

(46) Greco, A.; Timo, A.; Maffezzoli, A. Development and Characterization of Amorphous Thermoplastic Matrix Graphene Nanocomposites. *Materials (Basel).* **2012**, *5* (12), 1972–1985.

(47) Ponomarenko, L. a; Schedin, F.; Katsnelson, M. I.; Yang, R.; Hill, E. W.; Novoselov, K. S.; Geim, a K. Chaotic Dirac Billiard in Graphene Quantum Dots. *Science* **2008**, *320* (5874), 356–358.

(48) Kim, S.; Hwang, S. W.; Kim, M. K.; Shin, D. Y.; Shin, D. H.; Kim, C. O.; Yang, S. B.; Park, J. H.; Hwang, E.; Choi, S. H.; et al. Anomalous Behaviors of Visible Luminescence from Graphene Quantum Dots: Interplay between Size and Shape. *ACS Nano* **2012**, *6* (9), 8203–8208.

(49) Li, Y.; Jiang, X.; Liu, Z.; Liu, Z. Strain Effects in Graphene and Graphene Nanoribbons: The Underlying Mechanism. *Nano Res.* **2010**, *3* (8), 545–556.

(50) Geim, A. K.; MacDonald, A. H. Graphene: Exploring Carbon Flatland. *Phys. Today* **2007**, *60* (8), 35–41.

(51) Zhang, Z.; Zhang, J.; Chen, N.; Qu, L. Graphene Quantum Dots: An Emerging Material for Energy-Related Applications and Beyond. *Energy Environ. Sci.* **2012**, *5* (10), 8869–8890.

(52) Luo, P. G.; Sahu, S.; Yang, S.-T.; Sonkar, S. K.; Wang, J.; Wang, H.; LeCroy, G. E.; Cao, L.; Sun, Y.-P. Carbon ‘Quantum’ Dots for Optical Bioimaging. *J.*

Mater. Chem. B **2013**, *1* (16), 2116–2127.

(53) Zheng, L.; Chi, Y.; Dong, Y.; Lin, J.; Wang, B. Electrochemiluminescence of Water-Soluble Carbon Nanocrystals Released Electrochemically from Graphite. *J. Am. Chem. Soc.* **2009**, *131* (13), 4564–4565.

(54) Liu, H.; Ye, T.; Mao, C. Fluorescent Carbon Nanoparticles Derived from Candle Soot. *Angew. Chemie - Int. Ed.* **2007**, *46* (34), 6473–6475.

(55) Lan, J.; Liu, C.; Gao, M.; Huang, C. An Efficient Solid-State Synthesis of Fluorescent Surface Carboxylated Carbon Dots Derived from C60 as a Label-Free Probe for Iron Ions in Living Cells. *Talanta* **2015**, *144*, 93–97.

(56) Yang, Z.; Xu, M.; Liu, Y.; He, F.; Gao, F.; Su, Y.; Wei, H.; Zhang, Y. Nitrogen-Doped, Carbon-Rich, Highly Photoluminescent Carbon Dots from Ammonium Citrate. *Nanoscale* **2014**, *6* (3), 1890–1895.

(57) Craciun, A. M.; Diac, A.; Focsan, M.; Socaci, C.; Magyari, K.; Maniu, D.; Mihalache, I.; Veca, L. M.; Astilean, S.; Terec, A. Surface Passivation of Carbon Nanoparticles with P-Phenylenediamine towards Photoluminescent Carbon Dots. *RSC Adv.* **2016**, *6* (62), 56944–56951.

(58) Ma, Z.; Ming, H.; Huang, H.; Liu, Y.; Kang, Z. One-Step Ultrasonic Synthesis of Fluorescent N-Doped Carbon Dots from Glucose and Their Visible-Light Sensitive Photocatalytic Ability. *New J. Chem.* **2012**, *36* (4), 861–864.

(59) Wang, J.; Wang, C. F.; Chen, S. Amphiphilic Egg-Derived Carbon Dots: Rapid Plasma Fabrication, Pyrolysis Process, and Multicolor Printing Patterns. *Angew. Chemie - Int. Ed.* **2012**, *51* (37), 9297–9301.

(60) Yang, X.; Zhuo, Y.; Zhu, S.; Luo, Y.; Feng, Y.; Dou, Y. Novel and Green Synthesis of High-Fluorescent Carbon Dots Originated from Honey for Sensing and Imaging. *Biosens. Bioelectron.* **2014**, *60*, 292–298.

(61) Hill, S.; Galan, M. C. Fluorescent Carbon Dots from Mono- and Polysaccharides: Synthesis, Properties and Applications. *Beilstein J. Org. Chem.* **2017**, *13* (1), 675–693.

(62) Qu, D.; Zheng, M.; Zhang, L.; Zhao, H.; Xie, Z.; Jing, X.; Haddad, R. E.; Fan,

H.; Sun, Z. Formation Mechanism and Optimization of Highly Luminescent N-Doped Graphene Quantum Dots. *Sci. Rep.* **2014**, *4*, 5294.

(63) Xue, M.; Guan, W.; Gu, W.; Guo, C.; Su, S.; Xu, P.; Ye, L. Microwave-Assisted Polyol Synthesis of Carbon Nitride Dots from Folic Acid for Cell Imaging. *Int. J. Nanomedicine* **2014**, *9*, 5071.

(64) Zhuo, Y.; Miao, H.; Zhong, D.; Zhu, S.; Yang, X. One-Step Synthesis of High Quantum-Yield and Excitation-Independent Emission Carbon Dots for Cell Imaging. *Mater. Lett.* **2015**, *139*, 197–200.

(65) Sun, Y.; Zhou, B.; Lin, Y. Quantum-Sized Carbon Dots for Bright and Colorful Photoluminescence. *J. …* **2006**, *128* (24), 7756–7757.

(66) Jia, W.; Tang, B.; Wu, P. Carbon Dots with Multi-Functional Groups and the Application in Proton Exchange Membranes. *Electrochim. Acta* **2018**, *260*, 92–100.

(67) Bottini, M.; Balasubramanian, C.; Dawson, M. I.; Bergamaschi, A.; Bellucci, S.; Mustelin, T. Isolation and Characterization of Fluorescent Nanoparticles from Pristine and Oxidized Electric Arc-Produced Single-Walled Carbon Nanotubes. *J. Phys. Chem. B* **2006**, *110* (2), 831–836.

(68) Yao, S.; Hu, Y.; Li, G. A One-Step Sonoelectrochemical Preparation Method of Pure Blue Fluorescent Carbon Nanoparticles under a High Intensity Electric Field. *Carbon N. Y.* **2014**, *66*, 77–83.

(69) Jiang, H.; Chen, F.; Lagally, M. G.; Denes, F. S. New Strategy for Synthesis and Functionalization of Carbon Nanoparticles. *Langmuir* **2010**, *26* (3), 1991–1995.

(70) Lim S Y, Shen W, G. Z. Carbon Quantum Dots and Their Applications. *Chem. Soc. Rev.* **2013**, *44* (1), 362–381.

(71) Chen, Y.; Liang, H. Applications of Quantum Dots with Upconverting Luminescence in Bioimaging. *J. Photochem. Photobiol. B Biol.* **2014**, *135*, 23–32.

(72) Esteves da Silva, J. C. G.; Gonçalves, H. M. R. Analytical and Bioanalytical Applications of Carbon Dots. *TrAC - Trends Anal. Chem.* **2011**, *30* (8), 1327–

1336.

(73) Tao, H.; Yang, K.; Ma, Z.; Wan, J.; Zhang, Y.; Kang, Z.; Liu, Z. In Vivo NIR Fluorescence Imaging, Biodistribution, and Toxicology of Photoluminescent Carbon Dots Produced from Carbon Nanotubes and Graphite. *Small* **2012**, *8* (2), 281–290.

(74) Zhou, J.; Booker, C.; Li, R.; Zhou, X.; Sham, T. K.; Sun, X.; Ding, Z. An Electrochemical Avenue to Blue Luminescent Nanocrystals from Multiwalled Carbon Nanotubes (MWCNTs). *J. Am. Chem. Soc.* **2007**, *129* (4), 744–745.

(75) Liu, F.; Jang, M. H.; Ha, H. D.; Kim, J. H.; Cho, Y. H.; Seo, T. S. Facile Synthetic Method for Pristine Graphene Quantum Dots and Graphene Oxide Quantum Dots: Origin of Blue and Green Luminescence. *Adv. Mater.* **2013**, *25* (27), 3657–3662.

(76) Patel, M. a; Yang, H.; Chiu, P. L.; Mastrogiovanni, D. D. T.; Flach, C. R.; Savaram, K.; Gomez, L.; Hemnarine, A.; Mendelsohn, R.; Garfunkel, E.; et al. Direct Production of Graphene Nanosheets for near Infrared Photoacoustic Imaging. *ACS Nano* **2013**, *7* (9), 8147–8157..

(77) Dong, Y.; Chen, C.; Zheng, X.; Gao, L.; Cui, Z.; Yang, H.; Guo, C.; Chi, Y.; Li, C. M. One-Step and High Yield Simultaneous Preparation of Single- and Multi-Layer Graphene Quantum Dots from CX-72 Carbon Black. *J. Mater. Chem.* **2012**, *22* (18), 8764.

(78) Han, L.; Ghosh, D.; Chen, W.; Pradhan, S.; Chang, X.; Chen, S. Nanosized Carbon Particles from Natural Gas Soot. *Chem. Mater.* **2009**, *21* (13), 2803–2809.

(79) Ogi, T.; Iwasaki, H.; Aishima, K.; Iskandar, F.; Wang, W.-N.; Takimiya, K.; Okuyama, K. Transient Nature of Graphene Quantum Dot Formation via a Hydrothermal Reaction. *RSC Adv.* **2014**, *4* (99), 55709–55715.

(80) Song, L.; Cui, Y.; Zhang, C.; Hu, Z.; Liu, X. Microwave-Assisted Facile Synthesis of Yellow Fluorescent Carbon Dots from o-Phenylenediamine for Cell Imaging and Sensitive Detection of Fe^{3+} and H_2O_2. *RSC Adv.* **2016**, *6* (21),

17704–17712.

(81) Viana, M. M.; Lima, M. C. F. S.; Forsythe, J. C.; Gangoli, V. S.; Cho, M.; Cheng, Y.; Silva, G. G.; Wong, M. S.; Caliman, V. Facile Graphene Oxide Preparation by Microwave-Assisted Acid Method. *J. Braz. Chem. Soc.* **2015**, *26* (5), 978–984.

(82) Chen, S.; Liu, J.-W.; Chen, M.-L.; Chen, X.-W.; Wang, J.-H. Unusual Emission Transformation of Graphene Quantum Dots Induced by Self-Assembled Aggregation. *Chem. Commun.* **2012**, *48* (61), 7637–7639.

(83) Gokus, T.; Nair, R. R.; Bonetti, a.; Böhmler, M.; Lombardo, a.; Novoselov, K. S.; Geim, a. K.; Ferrari, a. C.; Hartschuh, a. Making Graphene Luminescent by Oxygen Plasma Treatment. *ACS Nano* **2009**, *3* (12), 3963–3968.

(84) Tan, X.; Li, Y.; Li, X.; Zhou, S.; Fan, L.; Yang, S. Electrochemical Synthesis of Small-Sized Red Fluorescent Graphene Quantum Dots as a Bioimaging Platform. *Chem. Commun.* **2015**, *51* (13), 2544–2546.

(85) Deng, J.; Lu, Q.; Mi, N.; Li, H.; Liu, M.; Xu, M.; Tan, L.; Xie, Q.; Zhang, Y.; Yao, S. Electrochemical Synthesis of Carbon Nanodots Directly from Alcohols. *Chem. - A Eur. J.* **2014**, *20* (17), 4993–4999.

(86) Bao, L.; Zhang, Z. L.; Tian, Z. Q.; Zhang, L.; Liu, C.; Lin, Y.; Qi, B.; Pang, D. W. Electrochemical Tuning of Luminescent Carbon Nanodots: From Preparation to Luminescence Mechanism. *Adv. Mater.* **2011**, *23* (48), 5801–5806.

(87) Li, H.; He, X.; Kang, Z.; Huang, H.; Liu, Y.; Liu, J.; Lian, S.; Tsang, C. H. A.; Yang, X.; Lee, S. T. Water-Soluble Fluorescent Carbon Quantum Dots and Photocatalyst Design. *Angew. Chemie - Int. Ed.* **2010**, *49* (26), 4430–4434.

(88) Yan, S.; Yang, S.; He, L.; Ye, C.; Song, X.; Liao, F. Quantum Size Effect of Poly(o-Phenylenediamine) Quantum Dots: From Controllable Fabrication to Tunable Photoluminescence Properties. *Synth. Met.* **2014**, *198*, 142–149.

(89) Liu, R.; Wu, D.; Feng, X. Bottom-Up Fabrication of Photoluminescent Graphene Quantum Dots with Uniform Morphology. *J. Am. Chem. Soc.* **2011**, *133* (39), 15221–15223.

(90) Zhang, B.; Liu, C. Y.; Liu, Y. A Novel One-Step Approach to Synthesize Fluorescent Carbon Nanoparticles. *Eur. J. Inorg. Chem.* **2010**, *2010* (28), 4411–4414.

(91) Liu, H.; He, Z.; Jiang, L. P.; Zhu, J. J. Microwave-Assisted Synthesis of Wavelength-Tunable Photoluminescent Carbon Nanodots and Their Potential Applications. *ACS Appl. Mater. Interfaces* **2015**, *7* (8), 4913–4920.

(92) Zhai, X.; Zhang, P.; Liu, C.; Bai, T.; Li, W.; Dai, L.; Liu, W. Highly Luminescent Carbon Nanodots by Microwave-Assisted Pyrolysis. *Chem. Commun.* **2012**, *48* (64), 7955–7957.

(93) Zhang, J.; Yu, S. H. Carbon Dots: Large-Scale Synthesis, Sensing and Bioimaging. *Mater. Today* **2016**, *19* (7), 382–393.

(94) Zhang, C.; Cui, Y.; Song, L.; Liu, X.; Hu, Z. Microwave Assisted One-Pot Synthesis of Graphene Quantum Dots as Highly Sensitive Fluorescent Probes for Detection of Iron Ions and PH Value. *Talanta*. 2016, pp 54–60.

(95) Wang, Y.; Hu, A. Carbon Quantum Dots: Synthesis, Properties and Applications. *J. Mater. Chem. C Mater. Opt. Electron. devices* **2014**, *2*, 6921–6939.

(96) Shen, J.; Zhu, Y.; Yang, X.; Zong, J.; Zhang, J.; Li, C. One-Pot Hydrothermal Synthesis of Graphene Quantum Dots Surface-Passivated by Polyethylene Glycol and Their Photoelectric Conversion under near-Infrared Light. *New J. Chem.* **2012**, *36* (1), 97–101.

(97) Markovic, Z. M.; Ristic, B. Z.; Arsikin, K. M.; Klisic, D. G.; Harhaji-Trajkovic, L. M.; Todorovic-Markovic, B. M.; Kepic, D. P.; Kravic-Stevovic, T. K.; Jovanovic, S. P.; Milenkovic, M. M.; et al. Graphene Quantum Dots as Autophagy-Inducing Photodynamic Agents. *Biomaterials* **2012**, *33* (29), 7084–7092.

(98) Li, Y.; Zhao, Y.; Cheng, H.; Hu, Y.; Shi, G.; Dai, L.; Qu, L. Nitrogen-Doped Graphene Quantum Dots with Oxygen-Rich Functional Groups. *J. Am. Chem. Soc.* **2012**, *134* (1), 15–18.

(99) Markovic, Z. M.; Ristic, B. Z.; Arsikin, K. M.; Klisic, D. G.; Harhaji-Trajkovic,

L. M.; Todorovic-Markovic, B. M.; Kepic, D. P.; Kravic-Stevovic, T. K.; Jovanovic, S. P.; Milenkovic, M. M.; et al. Graphene Quantum Dots as Autophagy-Inducing Photodynamic Agents. *Biomaterials* **2012**, *33* (29), 7084–7092.

(100) Wang, F.; Gu, Z.; Lei, W.; Wang, W.; Xia, X.; Hao, Q. Graphene Quantum Dots as a Fluorescent Sensing Platform for Highly Efficient Detection of Copper(II) Ions. *Sensors Actuators, B Chem.* **2014**, *190*, 516–522.

(101) Zhu, S.; Zhang, J.; Liu, X.; Li, B.; Wang, X.; Tang, S.; Meng, Q.; Li, Y.; Shi, C.; Hu, R.; et al. Graphene Quantum Dots with Controllable Surface Oxidation, Tunable Fluorescence and up-Conversion Emission. *RSC Adv.* **2012**, *2* (7), 2717–2720.

(102) Li, Y.; Hu, Y.; Zhao, Y.; Shi, G.; Deng, L.; Hou, Y.; Qu, L. An Electrochemical Avenue to Green-Luminescent Graphene Quantum Dots as Potential Electron-Acceptors for Photovoltaics. *Adv. Mater.* **2011**, *23* (6), 776–780.

(103) Yoo, J. M.; Kang, J. H.; Hong, B. H. Graphene-Based Nanomaterials for Versatile Imaging Studies. *Chem. Soc. Rev.* **2015**, *44* (14), 4835–4852.

(104) Ge, J.; Lan, M.; Zhou, B.; Liu, W.; Guo, L.; Wang, H.; Jia, Q.; Niu, G.; Huang, X.; Zhou, H.; et al. A Graphene Quantum Dot Photodynamic Therapy Agent with High Singlet Oxygen Generation. *Nat. Commun.* **2014**, *5*, 4596.

(105) Zheng, X. T.; Than, A.; Ananthanaraya, A.; Kim, D. H.; Chen, P. Graphene Quantum Dots as Universal Fluorophores and Their Use in Revealing Regulated Trafficking of Insulin Receptors in Adipocytes. *ACS Nano* **2013**, *7* (7), 6278–6286.

(106) Gu, J.; Hu, M. J.; Guo, Q. Q.; Ding, Z. F.; Sun, X. L.; Yang, J. High-Yield Synthesis of Graphene Quantum Dots with Strong Green Photoluminescence. *RSC Adv.* **2014**, *4* (91), 50141–50144.

(107) Zhang, S.; Li, Y.; Kang, Y.; Dong, Y.; Hong, S.; Chen, X.; Zhou, J.; Fedoseeva, Y. V.; Asanov, I. P.; Bulusheva, L. G.; et al. Leaky Graphene Oxide with High Quantum Yield and Dual-Wavelength Photoluminescence. *Carbon N. Y.* **2016**,

108, 461–470.

(108) Luo, P. G.; Sahu, S.; Yang, S. T.; Sonkar, S. K.; Wang, J.; Wang, H.; Lecroy, G. E.; Cao, L.; Sun, Y. P. Carbon 'Quantum' Dots for Optical Bioimaging. *J. Mater. Chem. B* **2013**, *1* (16), 2116–2127.

(109) Bourlinos, A. B.; Trivizas, G.; Karakassides, M. A.; Baikousi, M.; Kouloumpis, A.; Gournis, D.; Bakandritsos, A.; Hola, K.; Kozak, O.; Zboril, R.; et al. Green and Simple Route toward Boron Doped Carbon Dots with Significantly Enhanced Non-Linear Optical Properties. *Carbon N. Y.* **2015**, *83*, 173–179.

(110) Sun, H.; Gao, N.; Wu, L.; Ren, J.; Wei, W.; Qu, X. Highly Photoluminescent Amino-Functionalized Graphene Quantum Dots Used for Sensing Copper Ions. *Chem. - A Eur. J.* **2013**, *19* (40), 13362–13368.

(111) Sun, Y. P.; Zhou, B.; Lin, Y.; Wang, W.; Fernando, K. A. S.; Pathak, P.; Meziani, M. J.; Harruff, B. A.; Wang, X.; Wang, H.; et al. Quantum-Sized Carbon Dots for Bright and Colorful Photoluminescence. *J. Am. Chem. Soc.* **2006**, *128* (24), 7756–7757.

(112) Hola, K.; Zhang, Y.; Wang, Y.; Giannelis, E. P.; Zboril, R.; Rogach, A. L. Carbon Dots - Emerging Light Emitters for Bioimaging, Cancer Therapy and Optoelectronics. *Nano Today* **2014**, *9* (5), 590–603.

(113) Sun, H.; Wu, L.; Wei, W.; Qu, X. Recent Advances in Graphene Quantum Dots for Sensing. *Mater. Today* **2013**, *16* (11), 433–442.

(114) Wang, L.; Zhu, S. J.; Wang, H. Y.; Qu, S. N.; Zhang, Y. L.; Zhang, J. H.; Chen, Q. D.; Xu, H. L.; Han, W.; Yang, B.; et al. Common Origin of Green Luminescence in Carbon Nanodots and Graphene Quantum Dots. *ACS Nano* **2014**, *8* (3), 2541–2547.

(115) Li, L.; Wu, G.; Yang, G.; Peng, J.; Zhao, J.; Zhu, J. J. Focusing on Luminescent Graphene Quantum Dots: Current Status and Future Perspectives. *Nanoscale* **2013**, *5* (10), 4015–4039.

(116) Prasannan, A.; Imae, T. One-Pot Synthesis of Fluorescent Carbon Dots from Orange Waste Peels. In *Industrial and Engineering Chemistry Research*; 2013;

Vol. 52, pp 15673–15678.

(117) Ye, R.; Xiang, C.; Lin, J.; Peng, Z.; Huang, K.; Yan, Z.; Cook, N. P.; Samuel, E. L. G.; Hwang, C.-C.; Ruan, G.; et al. Coal as an Abundant Source of Graphene Quantum Dots. *Nat. Commun.* **2013**, *4*, 2943.

(118) Zhang, M.; Bai, L.; Shang, W.; Xie, W.; Ma, H.; Fu, Y.; Fang, D.; Sun, H.; Fan, L.; Han, M.; et al. Facile Synthesis of Water-Soluble, Highly Fluorescent Graphene Quantum Dots as a Robust Biological Label for Stem Cells. *J. Mater. Chem.* **2012**, *22* (15), 7461–7467.

(119) Xie, M.; Su, Y.; Lu, X.; Zhang, Y.; Yang, Z.; Zhang, Y. Blue and Green Photoluminescence Graphene Quantum Dots Synthesized from Carbon Fibers. *Mater. Lett.* **2013**, *93*, 161–164.

(120) Ray, S. C.; Saha, A.; Jana, N. R.; Sarkar, R. Fluorescent Carbon Nanoparticles: Synthesis, Characterization, and Bioimaging Application. *J. Phys. Chem. C* **2009**, *113* (43), 18546–18551.

(121) Encyclopedia of Spectroscopy and Spectrometry. *Choice Rev. Online* **2013**.

(122) McGuire, J. A. Growth and Optical Properties of Colloidal Graphene Quantum Dots. *Phys. status solidi - Rapid Res. Lett.* **2016**, *10* (1), 91–101.

(123) Qu, D.; Zheng, M.; Du, P.; Zhou, Y.; Zhang, L.; Li, D.; Tan, H.; Zhao, Z.; Xie, Z.; Sun, Z. Highly Luminescent S, N Co-Doped Graphene Quantum Dots with Broad Visible Absorption Bands for Visible Light Photocatalysts. *Nanoscale* **2013**, *5* (24), 12272–12277.

(124) Liu, C.; Bao, L.; Tang, B.; Zhao, J. Y.; Zhang, Z. L.; Xiong, L. H.; Hu, J.; Wu, L. L.; Pang, D. W. Fluorescence-Converging Carbon Nanodots-Hybridized Silica Nanosphere. *Small* **2016**, *12* (34), 4702–4706.

(125) Ando, Y.; Akiyama, H. PH-Dependent Fluorescence Spectra, Lifetimes, and Quantum Yields of Firefly-Luciferin Aqueous Solutions Studied by Selective-Excitation Fluorescence Spectroscopy. *Jpn. J. Appl. Phys.* **2010**, *49* (11), 117002.

(126) Ware, W. R.; Baldwin, B. A. Effect of Temperature on Fluorescence Quantum Yields in Solution. *J. Chem. Phys.* **1965**, *43* (4), 1194–1197.

(127) Nagaraja, D.; Melavanki, R. M.; Patil, N. R.; Kusanur, R. A. Solvent Effect on the Relative Quantum Yield and Fluorescence Quenching of 2DAM. *Spectrochim. Acta - Part A Mol. Biomol. Spectrosc.* **2014**, *130*, 122–128.

(128) Li, L.; Wu, G.; Yang, G.; Peng, J.; Zhao, J.; Zhu, J.-J. Focusing on Luminescent Graphene Quantum Dots: Current Status and Future Perspectives. *Nanoscale* **2013**, *5* (10), 4015–4039.

(129) Eda, G.; Lin, Y. Y.; Mattevi, C.; Yamaguchi, H.; Chen, H. A.; Chen, I. S.; Chen, C. W.; Chhowalla, M. Blue Photoluminescence from Chemically Derived Graphene Oxide. *Adv. Mater.* **2010**, *22* (4), 505–509.

(130) Zhu, X.; Xiao, X.; Zuo, X.; Liang, Y.; Nan, J. Hydrothermal Preparation of Photoluminescent Graphene Quantum Dots Characterized Excitation-Independent Emission and Its Application as a Bioimaging Reagent. *Part. Part. Syst. Charact.* **2014**, *31* (7), 801–809.

(131) Haug, H.; Koch, S. W.; Keldysh, L. V. *Quantum Theory of the Optical and Electronic Properties of Semiconductors*; 2008.

(132) Sk, M. A.; Ananthanarayanan, A.; Huang, L.; Lim, K. H.; Chen, P. Revealing the Tunable Photoluminescence Properties of Graphene Quantum Dots. *J. Mater. Chem. C* **2014**, *2* (34), 6954–6960.

(133) Pan, D.; Guo, L.; Zhang, J.; Xi, C.; Xue, Q.; Huang, H.; Li, J.; Zhang, Z.; Yu, W.; Chen, Z.; et al. Cutting Sp2 Clusters in Graphene Sheets into Colloidal Graphene Quantum Dots with Strong Green Fluorescence. *J. Mater. Chem.* **2012**, *22*, 3314.

(134) Silvestrov, P. G.; Efetov, K. B. Quantum Dots in Graphene. *Phys. Rev. Lett.* **2007**, *98* (1), 016802.

(135) Molitor, F.; Güttinger, J.; Stampfer, C.; Dröscher, S.; Jacobsen, A.; Ihn, T.; Ensslin, K. Electronic Properties of Graphene Nanostructures. *J. Phys. Condens. Matter* **2011**, *23* (24), 243201.

(136) Trauzettel, B.; Bulaev, D. V.; Loss, D.; Burkard, G. Spin Qubits in Graphene Quantum Dots. *Nat. Phys.* **2007**, *3* (3), 192–196.

(137) Jin, S. H.; Kim, D. H.; Jun, G. H.; Hong, S. H.; Jeon, S. Tuning the Photoluminescence of Graphene Quantum Dots through the Charge Transfer Effect of Functional Groups. *ACS Nano* **2013**, *7* (2), 1239–1245.

(138) Leutwyler, W.; Bürgi, S.; Burgl, H. Semiconductor Clusters, Nanocrystals, and Quantum Dots. *Science (80-.).* **1996**, *271* (5251), 933–937.

(139) Zhu, S.; Zhang, J.; Tang, S.; Qiao, C.; Wang, L.; Wang, H.; Liu, X.; Li, B.; Li, Y.; Yu, W.; et al. Surface Chemistry Routes to Modulate the Photoluminescence of Graphene Quantum Dots: From Fluorescence Mechanism to Up-Conversion Bioimaging Applications. *Adv. Funct. Mater.* **2012**, *22* (22), 4732–4740.

(140) Zhu, S.; Shao, J.; Song, Y.; Zhao, X.; Du, J.; Wang, L.; Wang, H.; Zhang, K.; Zhang, J.; Yang, B. Investigating the Surface State of Graphene Quantum Dots. *Nanoscale* **2015**, *7* (17), 7927–7933.

(141) Guo, W. Isotopomer. In *Encyclopedia of Astrobiology*; 2015; pp 1289–1290.

(142) Kuno, M.; Lee, J. K.; Dabbousi, B. O.; Mikulec, F. V.; Bawendi, M. G. The Band Edge Luminescence of Surface Modified CdSe Nanocrystallites: Probing the Luminescing State. *J. Chem. Phys.* **1997**, *106* (23), 9869–9882.

(143) Kim, T. H.; Lee, S.; Chen, X. Nanotheranostics for Personalized Medicine. *Expert Rev. Mol. Diagn.* **2013**, *13* (3), 257–269.

(144) Nurunnabi, M.; Khatun, Z.; Huh, K. M.; Park, S. Y.; Lee, D. Y.; Cho, K. J.; Lee, Y. K. In Vivo Biodistribution and Toxicology of Carboxylated Graphene Quantum Dots. *ACS Nano* **2013**, *7* (8), 6858–6867.

(145) Ash, C.; Dubec, M.; Donne, K.; Bashford, T. Effect of Wavelength and Beam Width on Penetration in Light-Tissue Interaction Using Computational Methods. *Lasers Med. Sci.* **2017**.

(146) Zhu, S.; Zhang, J.; Qiao, C.; Tang, S.; Li, Y.; Yuan, W.; Li, B.; Tian, L.; Liu, F.; Hu, R.; et al. Strongly Green-Photoluminescent Graphene Quantum Dots for Bioimaging Applications. *Chem. Commun. (Camb).* **2011**, *47* (24), 6858–6860.

(147) Gokhale, R.; Singh, P. Blue Luminescent Graphene Quantum Dots by Photochemical Stitching of Small Aromatic Molecules: Fluorescent Nanoprobes

in Cellular Imaging. *Part. Part. Syst. Charact.* **2014**, *31* (4), 433–438.

(148) Li, N.; Than, A.; Chen, J.; Xi, F.; Liu, J.; Chen, P. Graphene Quantum Dots Based Fluorescence Turn-on Nanoprobe for Highly Sensitive and Selective Imaging of Hydrogen Sulfide in Living Cells. *Biomater. Sci.* **2018**, *6* (4), 779–784.

(149) Ha, H. D.; Jang, M.-H.; Liu, F.; Cho, Y.-H.; Seo, T. S. Upconversion Photoluminescent Metal Ion Sensors via Two Photon Absorption in Graphene Oxide Quantum Dots. *Carbon N. Y.* **2015**, *81*, 367–375.

(150) Chen, J.; Yan, X.; Meng, K.; Wang, S. Graphene Oxide Based Photoinduced Charge Transfer Label-Free near-Infrared Fluorescent Biosensor for Dopamine. *Anal. Chem.* **2011**, *83* (22), 8787–8793.

(151) Qin, X.; Lu, W.; Asiri, A. M.; Al-Youbi, A. O.; Sun, X. Microwave-Assisted Rapid Green Synthesis of Photoluminescent Carbon Nanodots from Flour and Their Applications for Sensitive and Selective Detection of Mercury(II) Ions. *Sensors Actuators, B Chem.* **2013**, *184*, 156–162.

(152) Liu, S.; Tian, J.; Wang, L.; Zhang, Y.; Qin, X.; Luo, Y.; Asiri, A. M.; Al-Youbi, A. O.; Sun, X. Hydrothermal Treatment of Grass: A Low-Cost, Green Route to Nitrogen-Doped, Carbon-Rich, Photoluminescent Polymer Nanodots as an Effective Fluorescent Sensing Platform for Label-Free Detection of Cu(II) Ions. *Adv. Mater.* **2012**, *24* (15), 2037–2041.

(153) Ran, X.; Sun, H.; Pu, F.; Ren, J.; Qu, X. Ag Nanoparticle-Decorated Graphene Quantum Dots for Label-Free, Rapid and Sensitive Detection of Ag+and Biothiols. *Chem. Commun.* **2013**, *49* (11), 1079–1081.

(154) Liu, L.; Li, Y.; Zhan, L.; Liu, Y.; Huang, C. One-Step Synthesis of Fluorescent Hydroxyls-Coated Carbon Dots with Hydrothermal Reaction and Its Application to Optical Sensing of Metal Ions. *Sci. China Chem.* **2011**, *54* (8), 1342–1347.

(155) Wang, X.; Sun, X.; Lao, J.; He, H.; Cheng, T.; Wang, M.; Wang, S.; Huang, F. Multifunctional Graphene Quantum Dots for Simultaneous Targeted Cellular Imaging and Drug Delivery. *Colloids Surfaces B Biointerfaces* **2014**, *122*, 638–

644.

(156) Karthik, S.; Saha, B.; Ghosh, S. K.; Pradeep Singh, N. D. Photoresponsive Quinoline Tethered Fluorescent Carbon Dots for Regulated Anticancer Drug Delivery. *Chem. Commun.* **2013**, *49* (89), 10471–10473.

(157) Saini, R.; Lee, N. V.; Liu, K. Y. P.; Poh, C. F. Prospects in the Application of Photodynamic Therapy in Oral Cancer and Premalignant Lesions. *Cancers (Basel).* **2016**, *8* (9), 83.

(158) Dennis E.J.G.J. Dolmans1, D. F. & R. K. J. Cancer Revoked: Oncogenes as Therapeutic Targets. *Nat. Rev. Cancer* **2003**, *3* (5), 375–380.

(159) Detty, M. R.; Gibson, S. L.; Wagner, S. J. Current Clinical and Preclinical Photosensitizers for Use in Photodynamic Therapy. *J. Med. Chem.* **2004**, *47* (16), 3897–3915.

(160) Bakalova, R.; Ohba, H.; Zhelev, Z.; Ishikawa, M.; Baba, Y. Quantum Dots as Photosensitizers? *Nat. Biotechnol.* **2004**, *22* (11), 1360.

(161) Zhou, Y.; Sun, H.; Wang, F.; Ren, J.; Qu, X. How Functional Groups Influence the ROS Generation and Cytotoxicity of Graphene Quantum Dots. *Chem. Commun.* **2017**, *53* (76), 10588–10591.

(162) Ye, R.; Peng, Z.; Metzger, A.; Lin, J.; Mann, J. a.; Huang, K.; Xiang, C.; Fan, X.; Samuel, E. L. G.; Alemany, L. B.; et al. Bandgap Engineering of Coal-Derived Graphene Quantum Dots. *ACS Appl. Mater. Interfaces* **2015**, *7* (12), 7041–7048.

(163) Williams, A. T. R.; Winfield, S. A.; Miller, J. N. Relative Fluorescence Quantum Yields Using a Computer-Controlled Luminescence Spectrometer. *Analyst* **1983**, *108* (1290), 1067.

(164) Umberger, J. Q.; LaMer, V. K. The Kinetics of Diffusion Controlled Molecular and Ionic Reactions in Solution as Determined by Measurements of the Quenching of Fluorescence. *J. Am. Chem. Soc.* **1945**, *67* (7), 1099–1109.

(165) Melhuish, W. H. Quantum Efficiencies of Fluorescence of Organic Substances: Effect of Solvent and Concentration of the Fluorescent Solute. *J. Phys. Chem.*

1961, *65* (2), 229–235.

(166) Chung, D. D. L. Review: Graphite. *J. Mater. Sci.* **2002**, *37* (8), 1475–1489.

(167) Delhaes P. *Graphite and Precursors*; 2014.

(168) Dimiev, A. M.; Tour, J. M.; Science, M.; Science, C.; Science, N.; Street, M.; States, U.; Materials, A. Z. E.; Avenue, M. Mechanism of Graphene Oxide. *ACS Nano* **2014**, *8* (3), 3060–3068.

(169) Wei, W.; Qu, X. Extraordinary Physical Properties of Functionalized Graphene. *Small* **2012**, *8* (14), 2138–2151.

(170) Castro Neto, A. H.; Peres, N. M. R.; Novoselov, K. S.; Geim, A. K. The Electronic Properties of Graphene. *Rev. Mod. Phys.* **2009**, *81* (1), 109–162.

(171) Baskoutas, S.; Terzis, A. F. Size-Dependent Band Gap of Colloidal Quantum Dots. *J. Appl. Phys.* **2006**, *99* (1), 013708.

(172) Wang, Y.; Herron, N. Nanometer-Sized Semiconductor Clusters: Materials Synthesis, Quantum Size Effects, and Photophysical Properties. *Journal of Physical Chemistry*. 1991, pp 525–532.

(173) Ekimov, A. I.; Efros, A. L.; Onushchenko, A. A. Quantum Size Effect in Semiconductor Microcrystals. *Solid State Commun.* **1993**, *88* (11–12), 947–950.

(174) Zhu, Y.; Murali, S.; Cai, W.; Li, X. Graphene and Graphene Oxide: Synthesis, Properties, and Applications. *Adv. Mater.* **2010**, *22* (35), 3906–3924.

(175) Marcano, D. C.; Kosynkin, D. V.; Berlin, J. M.; Sinitskii, A.; Sun, Z.; Slesarev, A.; Alemany, L. B.; Lu, W.; Tour, J. M. Improved Synthesis of Graphene Oxide. *ACS Nano* **2010**, *4* (8), 4806–4814.

(176) Liu, Y.; Li, Y.; He, X. In Situ Synthesis of Ceria Nanoparticles in the Ordered Mesoporous Carbon as a Novel Electrochemical Sensor for the Determination of Hydrazine. *Anal. Chim. Acta* **2014**, *819*, 26–33.

(177) Alam, S. N.; Sharma, N.; Kumar, L. Synthesis of Graphene Oxide (GO) by Modified Hummers Method and Its Thermal Reduction to Obtain Reduced Graphene Oxide (RGO). *Graphene* **2017**, *06* (01), 1–18.

(178) Sciortino, A.; Cannizzo, A.; Messina, F. Carbon Nanodots: A Review—From

the Current Understanding of the Fundamental Photophysics to the Full Control of the Optical Response. *C* **2018**, *4* (4), 67.

(179) Gan, Z.; Xu, H.; Hao, Y. Mechanism for Excitation-Dependent Photoluminescence from Graphene Quantum Dots and Other Graphene Oxide Derivates: Consensus, Debates and Challenges. *Nanoscale* **2016**, *8* (15), 7794–7807.

(180) Li, M.; Cushing, S. K.; Zhou, X.; Guo, S.; Wu, N. Fingerprinting Photoluminescence of Functional Groups in Graphene Oxide. *J. Mater. Chem.* **2012**, *22* (44), 23374–23379.

(181) Yang, P.; Zhou, L.; Zhang, S.; Wan, N.; Pan, W.; Shen, W. Facile Synthesis and Photoluminescence Mechanism of Graphene Quantum Dots. *J. Appl. Phys.* **2014**, *116* (24), 244306.

(182) Marcano, D.; Kosynkin, D.; Berlin, J. Improved Synthesis of Graphene Oxide. *ACS Nano* **2010**, *4* (8), 4806–4814.

(183) Choudhary, S.; Mungse, H. P.; Khatri, O. P. Hydrothermal Deoxygenation of Graphene Oxide: Chemical and Structural Evolution. *Chem. - An Asian J.* **2013**, *8* (9), 2070–2078.

(184) Zheng, X.; Peng, Y.; Yang, Y.; Chen, J.; Tian, H.; Cui, X.; Zheng, W. Hydrothermal Reduction of Graphene Oxide; Effect on Surface-Enhanced Raman Scattering. *J. Raman Spectrosc.* **2017**, *48* (1), 97–103.

(185) Luo, P.; Qiu, Y.; Guan, X.; Jiang, L. Regulation of Photoluminescence Properties of Graphene Quantum Dots via Hydrothermal Treatment. *Phys. Chem. Chem. Phys.* **2014**, *16* (35), 19011–19016.

(186) Díez, N.; Śliwak, A.; Gryglewicz, S.; Grzyb, B.; Gryglewicz, G. Enhanced Reduction of Graphene Oxide by High-Pressure Hydrothermal Treatment. *RSC Adv.* **2015**, *5* (100), 81831–81837.

(187) Pan, D.; Guo, L.; Zhang, J.; Xi, C.; Xue, Q.; Huang, H.; Li, J.; Zhang, Z.; Yu, W.; Chen, Z.; et al. Cutting Sp 2 Clusters in Graphene Sheets into Colloidal Graphene Quantum Dots with Strong Green Fluorescence. *J. Mater. Chem.* **2012**,

22 (8), 3314–3318.

(188) Dhenadhayalan, N.; Lin, K. C.; Suresh, R.; Ramamurthy, P. Unravelling the Multiple Emissive States in Citric-Acid-Derived Carbon Dots. *J. Phys. Chem. C* **2016**, *120* (2), 1252–1261.

(189) Li, L.; Lu, C.; Li, S.; Liu, S.; Wang, L.; Cai, W.; Xu, W.; Yang, X.; Liu, Y.; Zhang, R. A High-Yield and Versatile Method for the Synthesis of Carbon Dots for Bioimaging Applications. *J. Mater. Chem. B* **2017**, *5* (10), 1935–1942.

(190) Liu, Y.; Xiao, N.; Gong, N.; Wang, H.; Shi, X.; Gu, W.; Ye, L. One-Step Microwave-Assisted Polyol Synthesis of Green Luminescent Carbon Dots as Optical Nanoprobes. *Carbon N. Y.* **2014**, *68*, 258–264.

(191) Li, X. G.; Huang, M. R.; Duan, W.; Yang, Y. L. Novel Multifunctional Polymers from Aromatic Diamines by Oxidative Polymerizations. *Chem. Rev.* **2002**, *102* (9), 2925–3030.

(192) Song, X.; Sun, H.; Yang, S.; Zhao, S.; Liao, F. Synthesis of Photoluminescent O-Phenylenediamine-m-Phenylenediamine Copolymer Nanospheres: An Effective Fluorescent Sensing Platform for Selective and Sensitive Detection of Chromium(VI) Ion. *J. Lumin.* **2016**, *169*, 186–190.

(193) Jiang, K.; Sun, S.; Zhang, L.; Lu, Y.; Wu, A.; Cai, C.; Lin, H. Red, Green, and Blue Luminescence by Carbon Dots: Full-Color Emission Tuning and Multicolor Cellular Imaging. *Angew. Chemie - Int. Ed.* **2015**, *54* (18), 5360–5363.

(194) Moodie, R. B. Electrophilic Aromatic Substitution. In *Organic Reaction Mechanisms, 1983: An Annual Survey Covering the Literature Dated December 1982 Through November 1983*; 2007.

(195) Cataldo, F. On the Polymerization of P-Phenylenediamine. *Eur. Polym. J.* **1996**, *32* (1), 43–50.

(196) Rehman, I. ur; Movasaghi, Z.; Rehman, S. *Vibrational Spectroscopy for Tissue Analysis*; 2012.

(197) Behrman, E. J. The Ortho-Para Ratio and the Intermediate in the Persulfate Oxidation of Aromatic Amines (the Boyland-Sims Oxidation). *J. Org. Chem.*

1992, *57* (8), 2266–2270.

(198) Boyland–Sims oxidation https://en.wikipedia.org/wiki/Boyland–Sims_oxidation#cite_note-5.